Luminescent glasses, optical fibers, and composites for optical sensing and photonic applications

Renato Grigolon Capelo

THESE DE DOCTORAT DE L'ETABLISSEMENT UNIVERSITE BOURGOGNE FRANCHE-COMTE

Préparée à l'Université de Bourgogne
Laboratoire Interdisciplinaire Carnot de Bourgogne (ICB), UMR 6303

Ecole doctorale n°553

École Doctorale Carnot-Pasteur

Doctorat de Science des Matériaux

Par

M. Renato GRIGOLON CAPELO

Luminescent glasses, optical fibers, and composites for optical sensing and photonic applications

Thèse présentée et soutenue à São Carlos, le 17 décembre 2024.

Composition du Jury:

Pr. ALMEIDA, Juliana	Professeure – Universidade Federal de São Carlos	Président du Jury
Pr. MESSADDEQ, Younès	Professeur – Université Laval	Rapporteur
Dr. COLAS, Maggy	Chargée de recherche – CNRS/Université de Limoges	Rapporteure
Pr. MANZANI, Danilo	Professeur – Universidade de São Paulo	Directeur de thèse
Pr. SMEKTALA, Frédéric	Professeur – Université de Bourgogne	Directeur de thèse

RENATO GRIGOLON CAPELO

Luminescent glasses, optical fibers, and composites for optical sensing and photonic applications

Revised version

The original copy is held in the reserved collection at the IQSC-USP Library.

Ph. D. thesis submitted to the Graduate Program in Chemistry at the Instituto de Química de São Carlos, Universidade de São Paulo, Brazil, and to the Graduate Program in Materials Science at the École Doctorale Carnot-Pasteur, Université de Bourgogne, France, to obtain the dual degree of Doctor of Science.

Concentration area: Analytical and Inorganic Chemistry (75135)

Supervisors: Prof. Dr. Danilo Manzani
Prof. Dr. Frédéric Smektala

São Carlos / Dijon
2024

Ficha Catalográfica elaborada pela Seção de Referência e Atendimento ao Usuário do SBI/IQSC

Capelo, Renato Grigolon
Luminescent glasses, optical fibers, and composites for optical sensing and photonic applications / Renato Grigolon Capelo. — São Carlos, 2024.
180 f.

Tese (Doutorado em Química Analítica e Inorgânica) — Instituto de Química de São Carlos / Universidade de São Paulo, 2024.
Edição revisada

Orientador: Prof. Dr. Danilo Manzani
Coorientador: Prof. Dr. Frédéric Smektala

1. Oxide glasses. 2. Optical fibers. 3. Optical sensing. 4. Photonics. 5. Luminescence. I. Título.

Sonia Alves - CRB: 4280/8

ACKNOWLEDGMENTS

Firstly, I would like to express my deepest gratitude to LaMIV, and especially to Prof. Danilo Manzani, for providing me with the opportunity to begin and complete this journey. The support and guidance I received over the years have allowed me to grow both professionally and personally, preparing me to continue moving forward. I also extend my thanks to the entire LaMIV team for their friendship and collaboration, as well as to everyone at IQSC and USP-São Carlos, which has been my second home for over a decade.

I am also grateful to the SAFIR team at the ICB Laboratory for welcoming me during this project, especially to Prof. Frédéric Smektala, who accepted me as his Ph.D. student. The invaluable expertise I gained during the year I spent in Dijon significantly contributed to the development of this research and provided me with a unique opportunity for personal growth. I would also like to thank my colleagues at ICB for their continuous support and assistance throughout this stage, as well as the special people I met in Dijon who made my time in France even better.

Special thanks go to GSOLFA group at Universidad Complutense de Madrid and to Prof. Guillermo Orellana. The final experimental phase of the project would not have been possible without the expertise and resources provided by GSOLFA. I am grateful for their warm welcome during my internship and for the opportunity to work alongside well-qualified researchers and very kind people.

I would also like to acknowledge the funding agencies that made this research possible: the Brazilian Federal Agency for Support and Evaluation of Graduate Education (CAPES), the São Paulo Research Foundation (FAPESP) - process number 2020/12280-1 and 2023/16047-8, and Campus France for the Eiffel scholarship. Their financial support was essential in carrying out this work across different countries and laboratories. Thank you for continuing to believe in science to make the world a better place.

Finally, I would like to thank my family, especially my parents, Mauro and Cida, and brother, Rafael, as well as my friends and my lovely girlfriend, Marlisa, for their constant support and encouragement throughout this journey. Their belief in me has been a continuous source of strength, especially during the most challenging moments. I am deeply grateful to all of you – thank you so much!

ABSTRACT

CAPELO, R. G. **Luminescent glasses, optical fibers and composites for optical sensing and photonic applications.** 2024. Thesis (Ph. D.) – Instituto de Química de São Carlos / École Doctorale Carnot-Pasteur, Universidade de São Paulo / Université de Bourgogne, São Carlos, 2014.

This work explores the design, synthesis, and application of luminescent glassy materials and composites for optical sensing and photonic technologies. The research focuses on developing novel optically active materials using oxide glass matrices suitable for fiber drawing, such as tellurite and phosphate glasses, which are modified to improve their optical and thermal properties. The introduction of network modifiers, particularly fluorides, results in glass systems with increased transparency and appropriate chemical stability. These matrices were doped with rare-earth ions (RE^{3+}) and nanoparticles, and they also served as substrates for the growth of luminescent coordination polymers (Ln-CPs), enabling the production of new glass@Ln-CP composites with significant potential for chemical sensing. A systematic approach was employed to characterize these glass matrices using techniques such as X-ray diffraction (XRD), Raman spectroscopy, solid-state nuclear magnetic resonance (NMR), and absorption spectroscopy, providing insights into their structural, optical, and thermal properties. The synthesis of optically active phosphate glasses co-doped with RE^{3+} demonstrated the capability to promote upconversion (UC) luminescence, highlighting their potential for photonic applications. The research also emphasizes the development of glass@Ln-CP composites, synthesized through *in situ* growth on glass substrates and optical fibers. These composites exhibit strong luminescent responses to carbonyl compounds like acetone and 2-pentanone, demonstrating their potential for chemical sensing. Furthermore, coated optical fibers enable the transmission of luminescent signals over long distances, facilitating real-time and remote detection of analytes. Thus, this thesis contributes to the development of new luminescent materials and fiber-optic-based sensors, offering a versatile platform for innovative optical sensors and photonic devices.

Keywords: oxide glasses; optical fibers; optical sensing; photonics.

RESUMO

CAPELO, R. G. **Luminescent glasses, optical fibers and composites for optical sensing and photonic applications.** 2024. Tese (Doutorado) - Instituto de Química de São Carlos / École Doctorale Carnot-Pasteur, Universidade de São Paulo / Université de Bourgogne, São Carlos, 2014.

Este trabalho explora o design, a síntese e a aplicação de materiais vítreos e compósitos luminescentes para aplicação em detecção óptica e dispositivos fotônicos. A pesquisa tem foco no desenvolvimento de novos materiais opticamente ativos usando matrizes de vidros óxidos adequadas para a fabricação de fibras ópticas, como vidros teluritos e fosfatos, que são modificadas a fim de aprimorar suas propriedades ópticas e térmicas. A introdução de modificadores de rede, particularmente fluoretos, resulta em sistemas vítreos com maior transparência e estabilidade química apropriada. Essas matrizes foram dopadas com íons terras raras (TR^{3+}) e nanopartículas, além de servirem como substratos para o crescimento de polímeros de coordenação (PC) luminescentes, possibilitando a produção de novos compósitos vidro@PC com potencial significativo para sensoriamento químico. Uma abordagem sistemática foi empregada a fim de caracterizar essas matrizes vítreas usando técnicas como difração de raios X, espectroscopia Raman, ressonância magnética nuclear em estado sólido e espectroscopia de absorção, obtendo informações detalhadas sobre suas propriedades estruturais, ópticas e térmicas. A síntese de vidros fosfatos opticamente ativos co-dopados com TR^{3+} demonstrou sua capacidade de promover a luminescência por conversão ascendente (*upconversion*), atestando seu potencial como material hospedeiro para aplicações em fotônica. A pesquisa também destaca o desenvolvimento de compósitos vidro@PC, sintetizados por meio de crescimento *in situ* em monólitos de vidro e fibras ópticas. Esses compósitos exibem respostas luminescentes significativas a compostos carbonílicos, como a acetona e a 2-pentanona, demonstrando seu potencial para sensoriamento químico. Além disso, as fibras ópticas recobertas permitem a transmissão dos sinais luminescentes por longas distâncias, viabilizando a detecção de maneira remota e em tempo real. Assim, esta tese contribui para o desenvolvimento de novos materiais luminescentes e sensores baseados em fibras ópticas, oferecendo uma plataforma versátil para novos tipos de sensores ópticos e dispositivos fotônicos.

Palavras-chave: vidros óxidos; fibras ópticas; sensoriamento óptico; fotônica.

RESUMÉ

CAPELO, R. G. **Luminescent glasses, optical fibers and composites for optical sensing and photonic applications.** 2024. Thèse (Doctorat) - Instituto de Química de São Carlos / École Doctorale Carnot-Pasteur, Universidade de São Paulo / Université de Bourgogne, São Carlos, 2014.

Ce travail explore la conception, la synthèse et l'application de matériaux vitreux luminescents et de composites pour la détection optique et les technologies photoniques. La recherche se concentre sur le développement de nouveaux matériaux optiquement actifs utilisant des matrices de verre oxydé adaptées à la fabrication de fibres optiques, telles que les verres tellurites et phosphates, qui sont modifiés pour améliorer leurs propriétés optiques et thermiques. L'introduction de modificateurs de réseau, en particulier des fluorures, aboutit à des systèmes vitreux avec une transparence accrue et une stabilité chimique appropriée. Ces matrices ont été dopées avec des ions de terres rares (TR^{3+}) et des nanoparticules, et elles ont également servi de substrats pour la croissance de polymères de coordination (PC) luminescents, permettant la production de nouveaux composites verre@PC avec un potentiel significatif pour la détection chimique. Une approche systématique a été employée pour caractériser ces matrices de verre à l'aide de techniques telles que la diffraction des rayons X, la spectroscopie Raman, la résonance magnétique nucléaire à l'état solide et la spectroscopie d'absorption, fournissant des informations sur leurs propriétés structurelles, optiques et thermiques. La synthèse de verres de phosphate optiquement actifs co-dopés avec des ions TR^{3+} a démontré leur capacité à promouvoir la luminescence par conversion ascendante (*upconversion)*, mettant en évidence leur potentiel pour les applications photoniques. La recherche met également en avant le développement de composites verre@PC, synthétisés par croissance *in situ* sur des substrats en verre et des fibres optiques. Ces composites montrent de réponses luminescentes aux composés carbonylés comme l'acétone et le 2-pentanone, démontrant leur potentiel pour la détection chimique. De plus, les fibres optiques revêtues permettent la transmission de signaux luminescents sur de longues distances, facilitant la détection en temps réel et à distance des analytes. Ainsi, cette thèse contribue au développement de nouveaux matériaux luminescents et de capteurs à base de fibres optiques, offrant une plateforme polyvalente pour des capteurs optiques innovants et des dispositifs photoniques.

Mots clés: verres d'oxyde; fibres optiques; détection optique; photonique.

CONTENTS

CHAPTER I:

Introduction to optically active glasses, optical fibers and lanthanide coordination polymers

General introduction and relevance

The development of new luminescent materials has drawn significant attention over the past few decades due to their broad range of applications in photonics (1,2). Particularly, luminescent materials based on rare-earth ions (RE^{3+}), have shown promising potential in diverse fields such as telecommunications (3,4), light-emitting devices (5), and bioimaging (6). In this context, the incorporation of RE^{3+} into glass matrices has been extensively explored, owing to the numerous advantages offered by these host materials. Generally, glasses are chemically and thermally stable, exhibit good optical transparency, and can accommodate a wide variety of dopants, including RE^{3+}, without significantly altering their structure (7,8). Moreover, the amorphous nature of glass allows for the homogeneous distribution of lanthanide ions, minimizing quenching effects (9,10). These properties make glass matrices excellent candidates for enhancing the performance of lanthanide-doped materials, particularly in applications requiring long-term stability, such as lasers, amplifiers, and sensors.

Lanthanide-doped glasses are widely studied due to their sharp emission lines and high quantum efficiency (8). The unique electronic structure of lanthanides, with 4f electrons shielded by the outer 5s and 5p orbitals, minimizes interaction with the host lattice, allowing them to retain their luminescent properties across various glass matrices (11,12). These characteristics make lanthanide-doped glasses valuable for advanced photonic applications, particularly when incorporated into optical fibers, where they enable the propagation and amplification of luminescent signals over long distances (13).

Commercial optical fibers are generally based on silica glass compositions, which feature a broad transparency window from ultraviolet (UV) to near-IR, high characteristic temperatures, and high phonon energy (~1100 cm^{-1}). However, silica glasses also have limited RE^{3+} solubility compared to other oxide glasses, limiting their applications (14). Thus, other glass matrices have been used for optical fiber production, such as tellurite (15), germanates (16), phosphates (17), and heavy-metal oxide (HMO) glasses (18). These matrices are referred as “soft glasses” due to their low characteristic temperatures and difference in rheological properties comparing to silica and silicates. They present unique optical properties advantageous for applications requiring lower processing temperatures, higher linear and nonlinear refractive indices, lower phonon energies, and broader transparency windows in the mid-IR (0.35 - 6 μm). Additionally, incorporating fluorides and synthesizing oxyfluoride

glasses can shift the absorption edge to higher energies, facilitating the design of lasers and efficient emitting materials (19,20).

The most remarkable characteristic of optical fibers is their ability to guide light over long distances with minimal loss. This property has revolutionized telecommunications, enabling the rapid transmission of signals (21,22). Moreover, this light-guiding ability facilitates their use in remote sensing applications, where the sensing element can be located far from the detection system (23). The fabrication of optical fibers from lanthanide-doped glasses has further advanced the development of fiber-optic sensors, enabling the detection of various chemical species and physical parameters such as temperature, pressure (24,25). Chalcogenide-based optical fibers, for example, are notable for their ability to transmit light in the mid-infrared region, where many organic molecules and gases exhibit strong absorption bands, making them well-suited for applications in environmental monitoring and industrial safety (26).

Chemical sensors based on optical absorption offer faster response times, high selectivity, and excellent detection capabilities compared to semiconductor or electrochemical sensors, allowing for real-time detection without sample degradation (27). However, some sensing platforms require chemosensor agents to enhance interactions with the evanescent field and gaseous analytes, generating optical responses such as absorption or luminescence. In this context, coordination polymers (CPs) represent a promising class of materials for applications in gas sensing and the detection of volatile organic compounds (VOCs). Recently, luminescent CPs containing RE^{3+} as the metallic center (Ln-CPs) have been employed for sensing nitroaromatic explosives, such as nitrobenzene and 2-nitrotoluene, in both aqueous and vapor phases (28,29).

The emission mechanism of Ln-CPs typically occurs by the "antenna effect" of the ligands, which absorb energy and assisted by vibronic coupling, transfer energy to the metal, resulting in luminescence of the lanthanide ion (30,31). Optical sensing with these materials is based on changes in the luminescence intensity when analytes interact with the CP, disturbing the energy transfer from the excited state of the ligands to the emitting center. In addition, the use of this class of compounds in sensor devices is supported by their ease of functionalization on surfaces of different materials, along with their significant permanent porosity – a fundamental condition for the interaction with gaseous analytes (32-34).

Thus, the aim of this thesis was to develop new luminescent materials and optical sensors based on “soft glass” matrices, such as tellurite, phosphate, and HMO glasses. Specifically, systematic studies were conducted on various glass compositions with suitable properties for optical fibers production, with the goal of developing new composites that integrate these glass substrates with luminescent Ln-CPs. These composites were used in sensing tests, where they were exposed to different organic analytes, and their luminescence behavior was monitored to evaluate their performance as optical sensors.

Next, several theoretical aspects about the main topics covered in this work will be presented, as well as key concepts and previous studies that contribute to the formulation of this research project. This introductory chapter is organized into three main research topics: (i) glass systems: definitions and key properties; (ii) fundamentals of optical fibers; and (iii) Ln-CPs for optical sensing.

1. Glass systems: definitions and main properties

Glass is one of the first materials mastered by humans and was fundamental for developing modern civilization, used both in everyday items, such as windows and bottles, and in advanced technologies, such as displays, lasers, and optical fibers. This widespread use of glass in modern society is even an argument for classifying current times as the Age of Glass. However, defining what glass truly is remains a subject of considerable interest and debate.

In a recent work, Zanotto and Mauro brought the following definition*: “Glass is a nonequilibrium, non-crystalline state of matter that appears solid on a short time scale but continuously relaxes towards the liquid state.”* (35) This may seem complex, but the essential is to understand that glass is a material that is out of thermodynamic equilibrium and has a non-crystalline structure, without long-range order (LRO). Furthermore, glasses also show the phenomenon of glass transition, which is the point where a supercooled liquid passes into the glassy state. This phenomenon occurs in a condition of rapid cooling of the melt, as represented in Figure I.1, which prevents the liquid structure from organizing itself in a crystalline form and removes energy for the free movement of atoms in the system (increasing viscosity). Therefore, the glass formation depends on the cooling rate, taking the system from the metastable equilibrium until the glass transition region, where the structure is frozen by increasing the viscosity and the structural relaxation time (36).

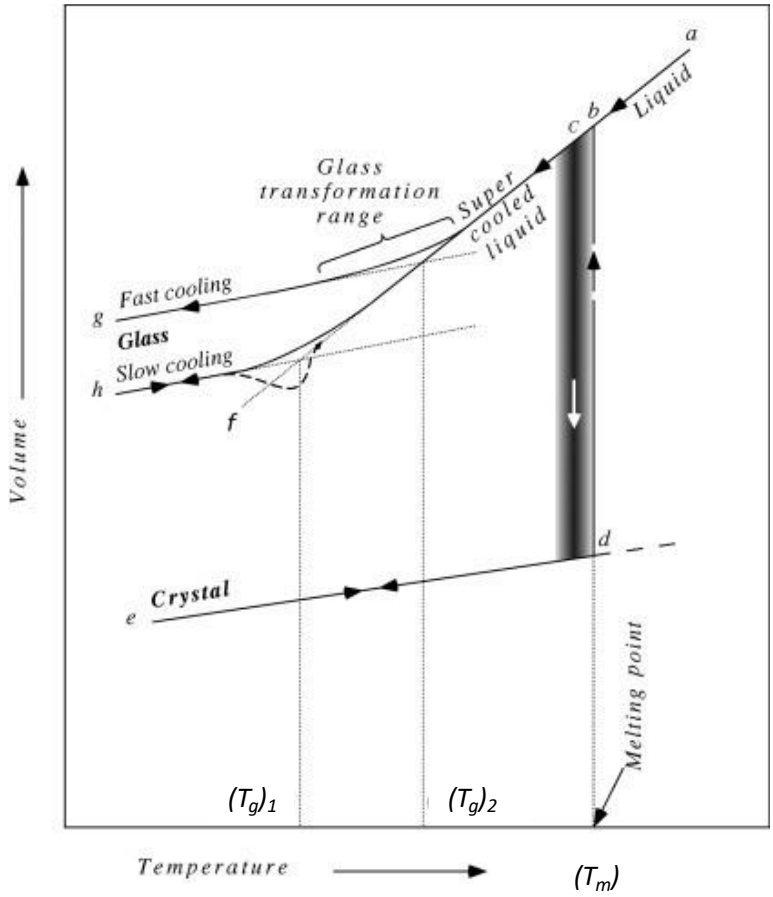

Figure I.1 - Schematic plot of volume versus temperature for a glass-forming material illustrating four distinct phases: liquid, supercooled liquid, glass, and crystalline states. T_m = melting point, and T_g = glass transition temperature.
Source: reproduced from VARSHNEYA AND MAURO (37).

In contrast to crystalline materials, glasses do not have a LRO structure. However, relatively uniform coordination polyhedral, like SiO_4, AlO_4, BO_4, and TeO_4, can be found in the oxide glass corresponding to a short-range order (SRO). Generally, these polyhedra are classified according to the number of bridging oxygen atoms, connecting them to neighboring polyhedra. These structural units can influence the extent of polymerization of the 3D network and thus define the optical, mechanical, and thermal properties of the glass matrix (36).

Although almost all elements of the periodic table can form glasses, most glasses used in commercial and technological applications are composed of silica-based matrices as the main component. Silicate glasses present a high chemical and thermal stability, large transparency window and appropriate mechanical properties for fiber production (38). However, these glasses also demand high melting temperature, which could be a manufacturing issue, in addition to their high phonon energy and the consequent short IR transmission, with a cut-off around 3.2 um. Thus, other families of oxide glasses have been used in several applications,

especially for developing new optical fibers. An example of an alternative glass type are the HMO glasses, which have lower phonon energies and characteristic temperatures than silicates, in addition to offering better stability and milder synthesis conditions compared to other glass families, such as fluoride and chalcogenide glasses (39).

Although HMO glasses are not typically used in large-scale production due to their higher raw material costs, as well as lower chemical durability and mechanical strength compared to silicate glasses, they present unique and advantageous properties in IR transmittance. This makes them attractive as host materials for mid-IR laser sources and other mid-IR applications (39). For a better understanding of the structural and optical properties of glasses, concepts related to thermal stability, as well as the transparency range of this material will be defined in the following topics.

1.1. *Thermal properties of glasses*

One of the most relevant properties of glasses is their thermal stability against crystallization. In a practical approach, this parameter reveals the working temperature range of the glass, which can be essential information for many applications, such as the optical fibers pulling. Although it is essential, the definition of this property is relatively simple. The first definition was proposed by Dietzel as a modest formula, $\Delta T = T_X - T_g$, where T_X is the onset temperature of crystallization and T_g the glass transition temperature (40). Hruby, in turn, proposed the H_f criterion, $H_f = (T_X - T_g)(T_m - T_P)$, where T_m is the melting temperature and T_P is the crystallization maxima temperature (41). Both formulas are commonly accepted as thermal stability criteria, but the T_m is often above the equipment threshold temperature, making ΔT the most used criterion for this purpose (42).

The characteristic temperatures of glasses are obtained by thermal analysis, which shows physical and chemical changes that occur in the material with the increase in temperature and allows determining the value of phase transformation temperatures, as shown in Figure I.2. Thermal analysis generally involves increasing the temperature of the material and recording the variations in heat flow, which can be exothermic (heat release) or endothermic (heat absorption) (43).

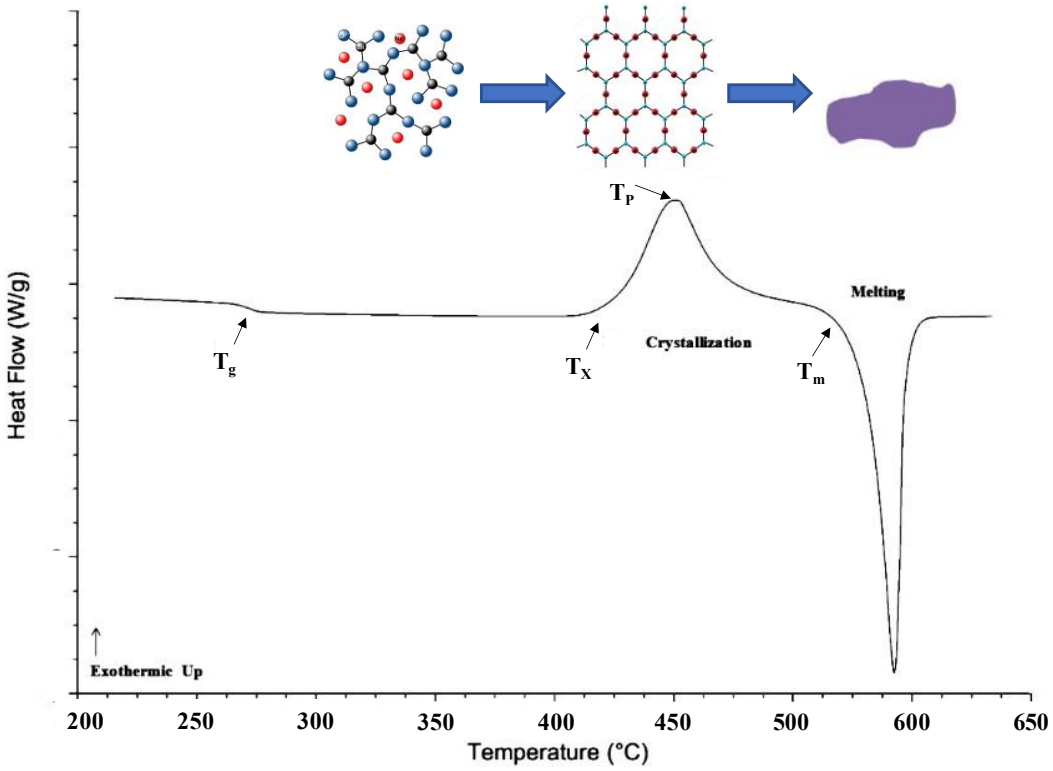

Figure I.2 - Typical DSC curves of glasses and their characteristic temperatures.
Source: adapted from BAIRD and TAYLOR (43)**.**

The thermal phenomena that occur in a glass formation are attributed to its composition, structure and the thermal history of the sample. Moreover, several phenomena are associated with T_g, such as the drastic change in viscosity, which goes from approximately 10^1 poises at the melting temperature to approximately 10^{13} poise in the glassy state (Figure I.3) (44). In addition to the cooling rate, another important process in the glass synthesis is the annealing after obtaining the sample. This procedure is performed at temperatures up to 30°C below T_g and assists in removing internal structural stresses caused by thermal shock. Thus, annealing directly influences the mechanical properties of the glasses, providing greater strength by reducing fractures and cracks in the samples (45).

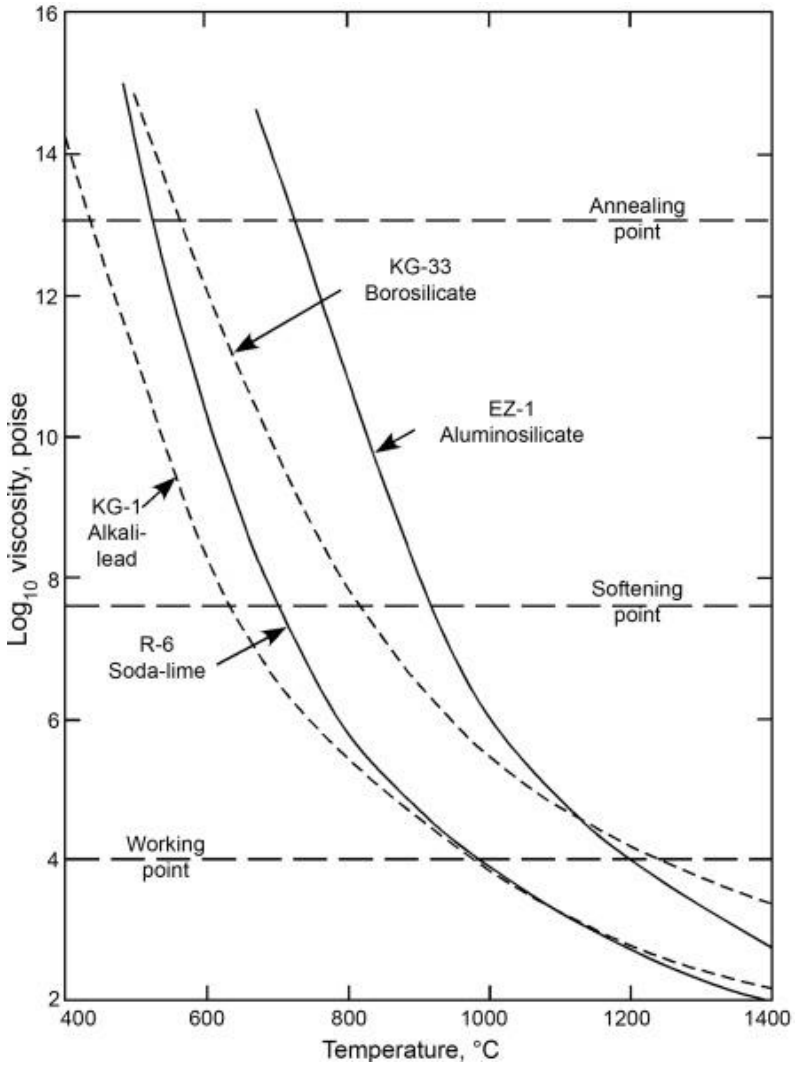

Figure I.3 - Viscosity–temperature curve for some commercial silicate glasses showing the intervals where the viscosity is standard of the different stages of getting a glass.
Source: reproduced from VARSHNEYA AND MAURO (37).

1.2. *Transparency window of glasses*

The transparency window of materials is limited by their vibrational and electronic absorption edges. A material is considered transparent when its molecules have fundamental oscillation frequencies at lower energies, absorbing predominantly in the infrared (IR) region, while transmitting light in the visible region. This characteristic transparency is observed in glasses, which exhibit multiple vibrational absorptions, also known as multiphonon absorption, occurring between 1 and 25 μm, depending on the composition of the glass (46). In addition to vibrational absorption, the transparency of glasses is also limited by the electronic absorptions, which occur at higher energy wavelengths in the UV-visible region. These absorptions are related to the electronic transitions of the atoms that make up the material.

Thus, the transparency window is defined as the range in the electromagnetic spectrum where the material is transparent. It is delimited by the two main factors: the band-gap frontier, which refers to electronic absorption in the UV-visible range, and the multiphonon frontier, which corresponds to vibrational absorption in the IR (46). These intrinsic absorptions are dependent on the glass composition (47). Figure I.4 shows the transmission spectra for some traditional glass families, highlighting their transparency windows and the influence of different compositions on these limits.

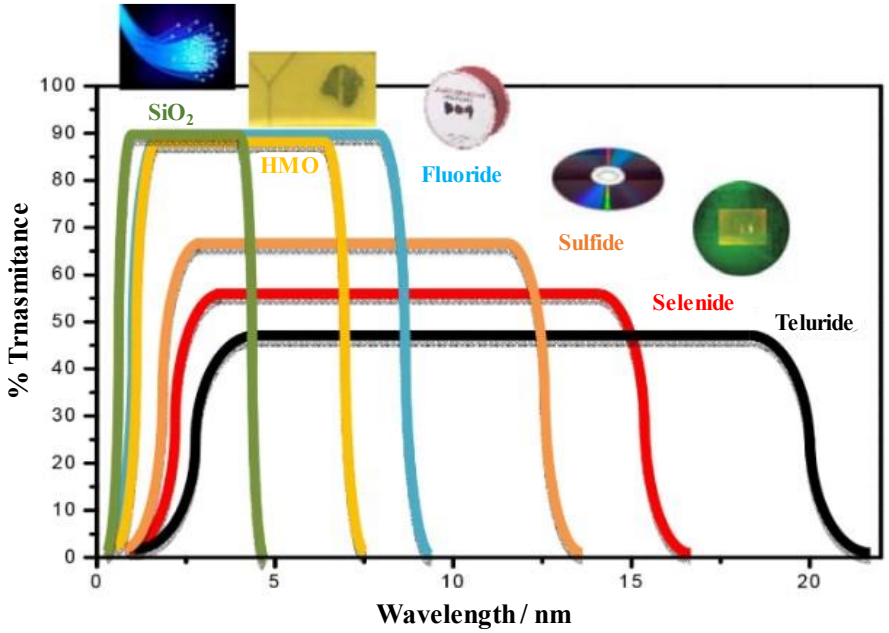

Figure I.4 - Illustration of transparency window of different glass families. The *insets* are examples of silicate, heavy-metal oxide, fluoride, sulfide, selenide and telluride glasses.
Source: adapted from NALIN et al. (47).

The bandgap frontier usually occurs in the UV-Visible region and corresponds to the electronic transitions of the glass matrix. The energy of short wavelengths corresponds to the energy gap between the conduction band and the valence band of the material. Thus, at wavelengths of equal or higher energy than the bandgap, the glass absorbs the radiation energy, and an electronic transition occurs between these bands (47).

In turn, the IR cut-off of glasses is primarily determined by the frequency of vibration of the chemical bonds, known as phonon energy (39). In fact, this absorption edge is due to the vibrations of the chemical bonds and their harmonics, that is, multiple energies of the fundamental vibration energies of these bonds. Since atoms vibrate cooperatively in response to the applied electric field, different vibrational modes will be seen due to the high disorder

and connectivity of the glasses. In this sense, glasses tend to absorb a wide spectral band in the IR region, configuring a vibrational absorption edge.

Aiming to extend the IR transmittance to longer wavelengths, larger cations and anions should be used (48). The maximum energy of the phonons is inversely proportional to the molar mass of the elements that constitute it, since the wavelength of a bond is expressed by the following formula:

$$\lambda = 2\pi . c \sqrt{\frac{\mu}{K}}$$

where **c** is the speed of light in vacuum, **μ** the reduced mass of bonds and **K** the bond strength constant. Therefore, the greater the mass of the components, the more the multiphonon absorption will be shifted to longer wavelengths. This is the main reason for chalcogenide and HMO glasses to have greater transparency in the mid-IR and, in some cases, far-IR.

1.3. Tellurite glasses

One of the most studied families of HMO glasses is the tellurite glasses. This glass were first explored in the 1970s, standing out as a promising material for acoustic-optical devices, such as light modulators. Tellurite glasses exhibit unique properties among oxide glasses, mainly due to their glass network, which is predominantly composed of tellurium (Te) and oxygen (O) atoms. The network features a multicoordination of tellurium atoms within oxygen polyhedra and the presence of a non-bonding electron pair, which contributes to their unusual linear and nonlinear optical properties (49).

From a structural perspective, the main difference between tellurite and silicate glasses lies in the arrangement of the structural units within their glass network. This distinct arrangement leads to lower characteristics temperatures in tellurite compared to silicate glasses. While silicate glasses are composed of highly condensed and connected tetrahedral units [SiO_4], tellurite glasses are formed by less symmetric polyhedrons [TeO_n] due to their non-bonding electronic pairs, allowing pyramidal e trigonal bipyramid geometries. Thus, tellurite glasses contain structural units similar to crystalline TeO_2, although these units are distorted in the glass network, forming three polyhedral structures of TeO_n (Figure I.5): [TeO_4], [TeO_{3+1}] and [TeO_3] (50).

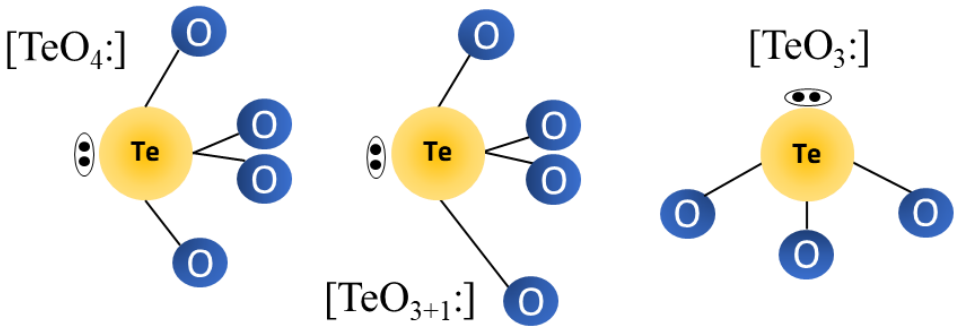

Figure I.5 - Schematic structures of (a) trigonal bipyramid TeO_4, (b) polyhedron TeO_{3+1} and (c) trigonal pyramid TeO_3.
Source: by the author.

In the TeO_4 unit, the Te atom is at the center of a trigonal bipyramid, and the Te sp^3d orbital is occupied by a lone pair of electrons. This unit is formed by two axial and 2 equatorial oxygen atoms. Moreover, the distance of the axial bond (Te-O_{ax} = 2.08 Å) is longer than the equatorial bond (Te-O_{eq} = 1.90 Å) and the third equatorial position is occupied by a lone pair of electrons (50).

Tellurium also has an intermediate coordination value between 3 and 4. The unit is defined as TeO_{3+1}, presenting an asymmetric polyhedron where one axial bond distance Te – O is smaller, while the other is more elongated. Then, the Te atom is bonded to 3 oxygens by the same distance as in TeO_4 units and to a fourth oxygen with a bonding distance greater than 2.30 Å (51).

Finally, tellurium can also be coordinated to only 3 oxygens in the glass matrix. This occurs when the fourth axial distance Te – O is longer than 2.58 Å, making the interaction between Te and O practically negligible. Thus, the TeO_3 unit is a trigonal pyramid structure with bond distances of 1.88 Å. In this structural unit, one of the four sp3 orbitals of Te is occupied by the lone electron pair (51).

The formation of distorted polyhedra as structural units is responsible for a less connected glass network in these matrices. Due to this structural characteristic, the multiphonon absorption edge it is extended to more than 4 μm, and low glass transition and melting temperatures are expected (52). Especially, the low phonon energy of tellurite glasses is an attractive factor for new mid-IR lasers and amplifiers, as well as for passive fibers and optical sensors. Simultaneously, the high electronic density of the tellurite units contributes to higher refractive indexes (linear and non-linear), as well as a UV–visible cutoff edge in the region of

0.35–0.40 μm (over mm length scale), which are also important for photonics applications in this spectral range (53).

The tellurite glass system most commonly utilized is based on a ternary composition of (75–80)TeO_2-(10–20)ZnO-(5–15)Na_2O (as known as TZN glasses) (52). The main properties of TZN glass with composition 75TeO_2-15ZnO-10Na_2O are high thermal stability against crystallization ($\Delta T > 100$ K), high linear refractive index (1.97–1.98), low phonon energy (700 cm^{-1}), in addition to a large transparency window, from 400 nm to 6 μm (for glasses with thickness of 1.4 mm) (54). Based on these suitable properties, optical fibers of TZN glasses have been applied in fiber lasers (55), as well as efficient supercontinuum generators (56).

Tellurite and other HMO matrices are known as "soft glasses", because of their interesting thermal properties, such as low glass transition and melt temperatures, depending on the composition (15). These glasses also present good stability against crystallization and chemical corrosion, allowing the use of these matrices in optical fiber applications (57). Moreover, the low melting temperatures (< 1000 °C) of tellurite glasses enable their melting in glovebox-based facilities, providing a dry atmosphere for dehydration and an oxidative environment to maintain tellurium in the Te^{4+} state (57).

Generally, HMO glasses present considerable content of hydroxyl (OH) groups in the matrix, even when the melting is conducted under dry O_2 atmosphere. As consequence, high losses in the mid-IR window of 2.5–5 μm, and non-radiative decay of RE^{3+} dopants are caused by OH content (59). Therefore, the main fabrication challenge for HMO glasses is to minimize the OH group content while preventing the formation of lower-valency heavy metals. Besides OH groups, the presence of metallic species, such as metallic tellurium, lead, and bismuth, can also lead to undesirable absorption in the glasses, posing challenges for various applications.

A widely used strategy to reduce OH group content is the addition of fluoride in tellurite glasses, which have recently received much attention in several works. In summary, the dehydroxylation is promoted by the reactions of zinc fluoride in the melt process, described as the following (60):

$$ZnF_2 + 2\ \text{Te-OH} \rightarrow ZnO + 2HF + \text{Te-O-Te}\ (1)\ \text{and}$$

$$ZnF_2 + H_2O \rightarrow ZnO + 2\ HF\ (2)$$

This strategy proved to be a good way to enhance the glass transparency window, from UV (~300 nm) to the mid-IR (4–6 μm), while also allowing the production of stable glasses and optical fibers containing high amounts of RE^{3+} (61-63). Despite that, a decrease in the mechanical and thermal stability is also expected, due to the predominant ionic character of the matrix. As an alternative, these difficulties can be minimized when a small amount of phosphates are introduced into a tellurite network, which tends to increase the network connectivity and provides more stability to the glass (64,65). Thus, structural studies of fluorotellurite and fluorophosphotellurite systems could be essential for the development of new glasses with appropriate mechanical, thermal and optical properties for application in photonics, mainly in optical fiber drawing.

1.4. Phosphate glasses

Phosphate glasses have emerged as a significant class of materials for optical applications due to their unique structural and physical properties (66). Compared to silicate glasses, phosphate glasses have lower characteristic temperatures and higher refractive indices, making them particularly attractive for a range of technological applications (67). A significant advantage of phosphate glasses is their high solubility for RE^{3+} ions, which is essential for optical and photonic applications such as lasers, amplifiers, and sensors (68,69).

Phosphate glasses present a relatively open glass 5network structure, typically composed of polyhedra of phosphorus-oxygen bonds, designated as [PO_4] units (65). The connectivity of these [PO_4] units varies depending on the glass composition and is expressed as Q^n where *n* represents the number of bridging oxygen (BO) atoms (Figure I.6) (65). Compared to silica glass, the localized excess charge from P^{5+} leads to less cross-linked structures in phosphate glasses (70). In the pure P_2O_5 glass system, the network is primarily composed of Q^3 units, where the phosphorous is coordinated by one non-bridging oxygen (NBO) and three BO (65). The introduction of alkali or alkaline earth oxides modifies the Q^n units, in glasses containing more than 50 mol% of P_2O_5 (ultraphosphate), the network consists of both Q^2 and Q^3 (71). With 50 mol% of P_2O_5 (metaphosphate), Q^2 units dominate, while at concentrations below 50 mol% (pyrophosphate), Q^2 units are converted to Q^1 (72). Additionally, in glasses containing less than 33 mol% of P_2O_5 (orthophosphate) the network mainly consists of Q^0 units, featuring four NBOs (72).

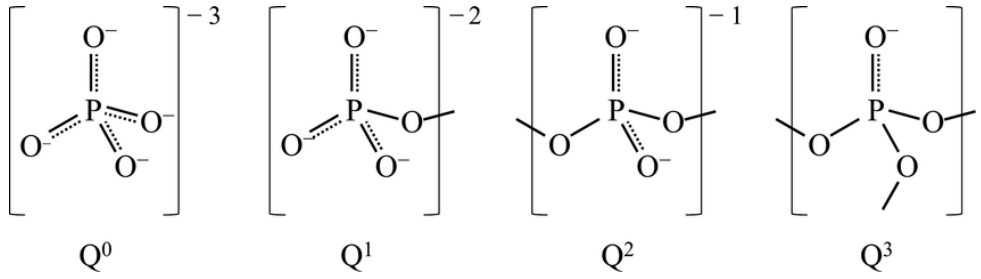

Figure I.6 – Schematic structures of Q^n of phosphate glasses.
Source: reproduced from ENDO et al. (73).

Phosphate glasses are notable for their low melting temperatures and high thermal expansion coefficients (74). However, vitreous phosphate glasses tend to exhibit high hygroscopicity due to their P–O–P bonds, which are easily hydrolyzed and less resistant to moisture (75,76). To address this issue, partial substitution of phosphorus with iron or aluminum increases their suitability for applications requiring enhanced durability and corrosion resistance (72,77).

The addition of Al_2O_3 strengthens the phosphate glass network by allowing Al^{3+} ions to cross-link the phosphate chains. [AlO_4] and [PO_4] tetrahedra form Al–O–P bonds, like the Si–O–Si bonds in SiO_2-based glass (70,78). The oxygen coordination of Al ions depends on the glass composition and is directly influenced by the O/P molar ratio (79).

Incorporating modifiers like Al_2O_3 not only improves thermal stability but also reduces the thermal expansion coefficient, which is essential for applications requiring dimensional stability (80). The incorporation of Al_2O_3 into the glass matrix enhances network connectivity, resulting in a more robust structure (81). This makes aluminum-phosphate glasses particularly valuable for applications requiring long-term stability in diverse environmental conditions, such as biomedical devices and high-performance optical systems (82-84).

Phosphate glasses also exhibit distinctive optical properties that set them apart from traditional silicate glasses. They typically have higher transparency in a wide spectral region, low refractive index, and the ability to incorporate larger amounts of RE^{3+} and transition metals (85,86). Additionally, phosphate glasses demonstrate excellent UV transmission, making them suitable for applications in photonics and sensing technologies. However, their typical low refractive index can be a limitation for certain applications. To address this, phosphate glasses are often combined with other glass-forming materials. For instance, germanium oxide (GeO_2) is commonly added to increase the refractive index of the glass (87).

Germanium-phosphate glasses are particularly remarkable for their enhancement of several properties. The addition of GeO_2 not only increases the refractive index but also improves the mechanical strength, making these glasses more suitable for high-performance optical applications (88,89). Their high ionic conductivity, combined with the capacity to incorporate significant amounts of RE^{3+} ions and metallic nanoparticles, makes germanium-phosphate glasses promising for efficient light emission and amplification, which is desirable in advanced photonic devices (89,90).

Finally, a key advantage of phosphate glasses is their suitability for optical fiber fabrication (84,91). Due to their lower viscosity and softening temperatures compared to silicate glasses, phosphate glasses offer a valuable alternative for producing optical fibers with varied designs (17,92,93). These fibers maintain the beneficial properties of bulk phosphate glasses, such as high solubility for RE^{3+} and excellent UV-visible transparency, making them versatile materials for advanced optical technologies (84,94).

1.5. Optically active glasses

Optically active glasses have been extensively studied due to their wide range of applications, such as light-emitting, telecommunication, and optical sensing (4,95-97). These materials, often doped with lanthanide ions, exhibit exceptional optical properties, making them indispensable in the development of modern solid state optical technology (98). The unique luminescence behavior of lanthanide ions arises from their electronic structure and glasses have been extensively used as host matrix for these dopants, due to the numerous advantages in terms of thermal stability, chemical resistance, and homogeneous dispersion (99).

The growing global demand for energy-efficient lighting has been one of the most relevant causes in promoting research into advanced materials designed to enhance light-emitting performance (8,100). Traditional incandescent and fluorescent lamps have been replaced by white light-emitting diodes (wLEDs), which are typically composed of $Y_3Al_5O_{12}:Ce^{3+}$ yellow phosphor and InGaN-based blue emitting LED, encapsulated in epoxy resin (101). However, this kind of wLEDs has its use limited in some advanced technologies due to the lack of sufficient red emission, poor color balance and significant re-absorption. (102). Additionally, these wLEDs often face other drawbacks, such as resin degradation by electrical current and photon scattering caused by the difference in refractive indices between

their components (103). In this sense, novel optically active glasses have emerged as a promising alternative to wLEDs, serving as hosts for phosphor materials or luminescent dopants for light-emitting materials (8,104-106).

Lanthanide-doped glasses tend to exhibit good thermal and chemical stability, a broad transparency range, ease of fabrication, and high dopant solubility, making them promising candidates for light-emitting devices (99,100). The shielding effect of the outer orbitals in lanthanide ions allows them to display stable and tunable luminescence, minimally affected by the chemical environment. As a result, using glasses as host materials is an effective strategy for producing stable luminescent materials (11,98). Moreover, lanthanide-doped glasses have been widely employed in advanced applications such as optical thermometry, photovoltaic cells, photocatalysis, and optical amplifiers (107-109).

The unique luminescence properties of lanthanide-doped glasses result from radiative transitions between the f-f energy levels of lanthanide ions. These emissions can cover a broad spectral range, from UV to IR, when excited by an appropriate light source (8). Three primary mechanisms are responsible for the luminescence processes in lanthanide ions: down-shifting (DS), quantum cutting (QC) or downconversion (DC), and upconversion (UC) (Figure I.7(a)). The DS process, a Stokes process, involves the absorption of high-energy photons and its re-emission as photons with lower energies (110). In contrast, QC can lead to quantum yields exceeding 100% by splitting a single high-energy photon into two or more lower-energy photons, as demonstrated in early works with Pr^{3+}-activated materials (111). Finally, UC, an anti-Stokes process, consists in the absorption of multiple low-energy photons followed by the emission of a higher-energy photon (112). UC can occur through various mechanisms, as illustrated in Figure I.7(b). Briefly, the most common types of UC process are excited state absorption (ESA), energy transfer up-conversion (ETU), photon avalanche (PA), cooperative energy transfer (CET).

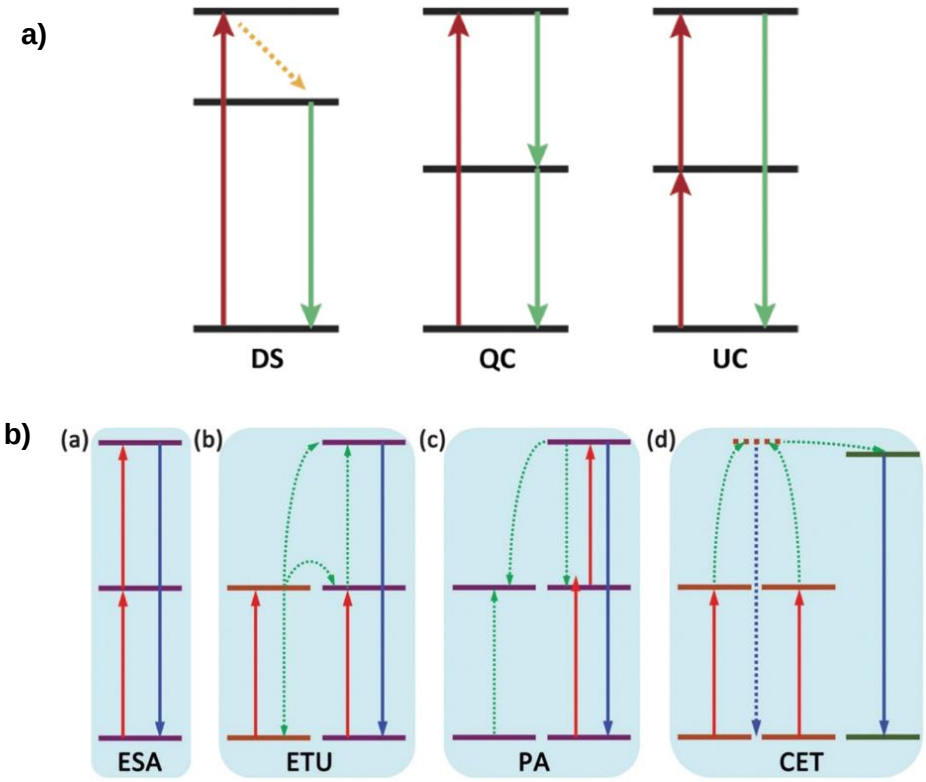

Figure I.7 - (a) Schematic representation of DS, QC and UC mechanisms; red arrows represent photon excitation and green arrows are radiative emission; the dashed line represents a non-radiative process.- (b) schemes of several UC process (ESA, ETU, PA, and CET); red and blue full arrows illustrate the excitation process and radiative emission, respectively, while green dashed arrows correspond to energy transfers.
Source: reproduced from EROL et al. (8).

UC luminescence in lanthanide ions is particularly appealing to researchers for two main reasons: it enables the generation of multiple visible photons using only a 980 nm diode laser, and the longer excitation wavelength helps prevent the degradation of the host material that can occur with short-wavelength UV excitation in DS processes (113). However, most lanthanide single-doped systems have shown low efficiency in IR-to-visible UC processes, particularly when excited in the near-IR region (114). The development of Yb^{3+}-sensitized materials has significantly improved UC efficiency by leveraging the high absorption cross-section of Yb^{3+}, which peaks around 980 nm, and its efficient energy transfer mechanism to the emitter ion. This advancement has led to substantial improvements in UC efficiency in co-doped glasses and optical fibers containing Yb^{3+} as sensitizer (115-117).

One of the most studied Yb^{3+}-sensitizer systems is the co-doping with Er^{3+}. Erbium-doped glasses are particularly appealing due to their emission at 1550 nm, a feature that makes Er^{3+}-doped fiber amplifiers (EDFAs) widely recognized and utilized in telecommunication systems (117). Additionally, when excited at 980 nm, Er^{3+}-doped glasses can also emit red and green light via UC process (118). The co-doping with Yb^{3+} further enhances both the IR and

UC emissions, as Yb^{3+} has a greater absorption cross-section at 980 nm compared to Er^{3+} (119,120). Numerous studies have explored various Er^{3+}/Yb^{3+} co-doped glass systems, particularly in phosphate and tellurite glasses, for applications in optical amplification and temperature sensing (121,122). Additionally, Tm^{3+}/Yb^{3+} co-doped glasses have also been investigated for their potential to generate blue UC emission from Tm^{3+} (123,124). In these systems, Yb^{3+} absorbs three 980 nm photons, followed by an ETU process that enhances the Tm^{3+}:$^3H_5 \rightarrow {}^3F_4$ radiative transition, producing emission around 480 nm (125). This blue emission can also occur by a two-photon ETU process in Tm^{3+}/Nd^{3+} co-doped glasses excited near 800 nm (126). The ability to generate blue light is particularly relevant, as materials emitting in the 450-500 nm wavelength range are considered promising for applications photonics and biophotonics (127,128).

In this regard, luminescent glasses have become highly valuable for modern photonic applications. The luminescent properties of lanthanide ions, combined with the thermal and chemical stability of glasses, as well as their transparency and simple fabrication process, make these materials attractive for a wide range of technologies. Particularly, optically active fibers offer the advantage of flexibility and light transmission over long distances, making them ideal for applications in telecommunications and remote sensing.

2. Fundamentals of optical fibers

Optical fiber research began in the late 1970s and played a revolutionary role in fields such as telecommunications and non-linear optical devices (129,130). The fibers operate by guiding the light by a mechanism called total internal reflection (TIR), which is only possible if the waveguide presents a difference in the refractive index between the medium in which the radiation will be conducted (higher index) and the surrounding medium (lowest index).

Conventional optical fibers can be described as cylindrical glass waveguides, consisting of an internal core, of refractive index $\mathbf{n_c}$, surrounded by a cladding with similar composition but with a slight lower refractive index, $\mathbf{n_s}$. Typically, the fibers are coated with polymers to improve the mechanical protection and to avoid environmental degradation, as shown in Figure I.8.

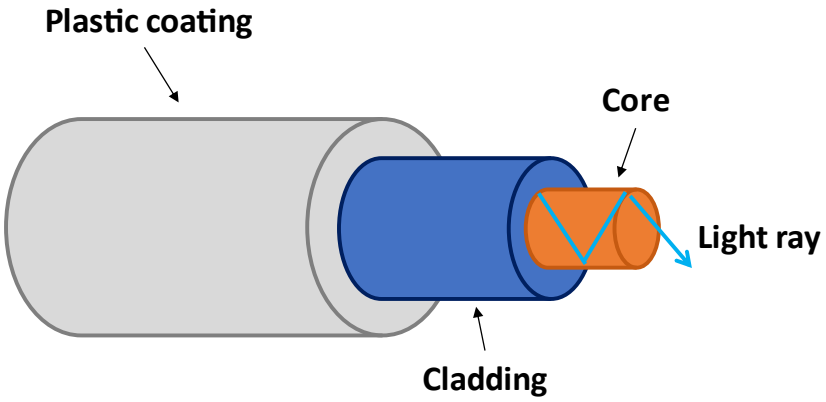

Figure I.8 - Representation of conventional core-cladding optical fiber.
Source: by the author.

When light travels from a medium with a higher refractive index to other with a lower refractive index, it results in a total reflection at the interface if the incidence angle exceeds a critical angle (θc) (130). This property, known as total internal reflection and represented in Figure I.9, is what allows light to propagate in the core of conventional optical fibers.

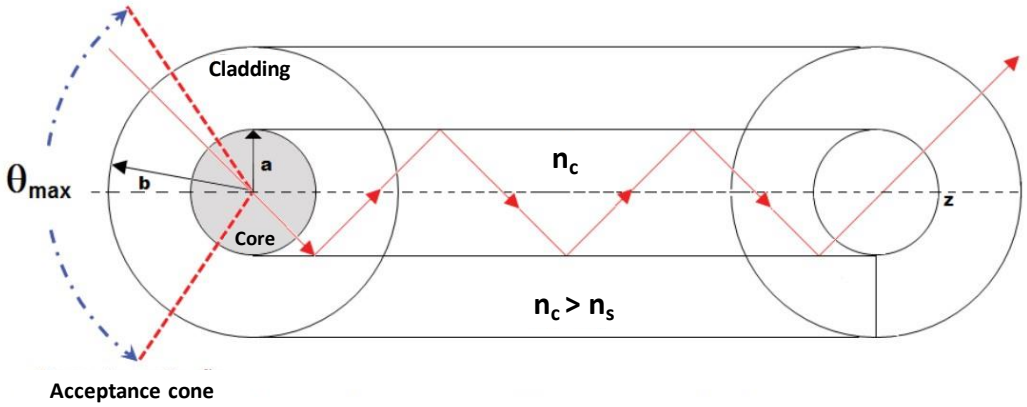

Figure I.9 - Representative scheme of the total internal reflection principle and the light propagation in an optical fiber.
Source: by the author.

The condition for total internal reflection in an optical fiber is determined by a maximum incidence angle at the interface between the core and the external medium. This angle defines the fiber's acceptance cone, with the sine of the angle being referred to as the numerical aperture (NA). The NA is a key parameter that determines the amount of light the fiber can guide through its core. A larger NA corresponds to a wider acceptance angle, which enhances the fiber's ability to guide light. The NA can be expressed as:

$$NA = \sqrt{n_c^2 - n_s^2}$$

2.1. Modes of propagation

The propagation of light within an optical fiber depends on the ratio of the core diameter to the overall diameter, allowing light to propagate along one or multiple paths, known as modes. Conventional optical fibers are categorized into three types: step-index multimode, graded-index multimode, and single-mode fibers. Step-index fibers feature a sharp change in refractive index at the core-cladding boundary, while graded-index fibers exhibit a gradual change in refractive index from the core to the cladding. Single-mode fibers, typically of the step-index type, have a small core diameter, usually around 8 – 12 μm (130). Figure I.10 illustrates these three types of fibers.

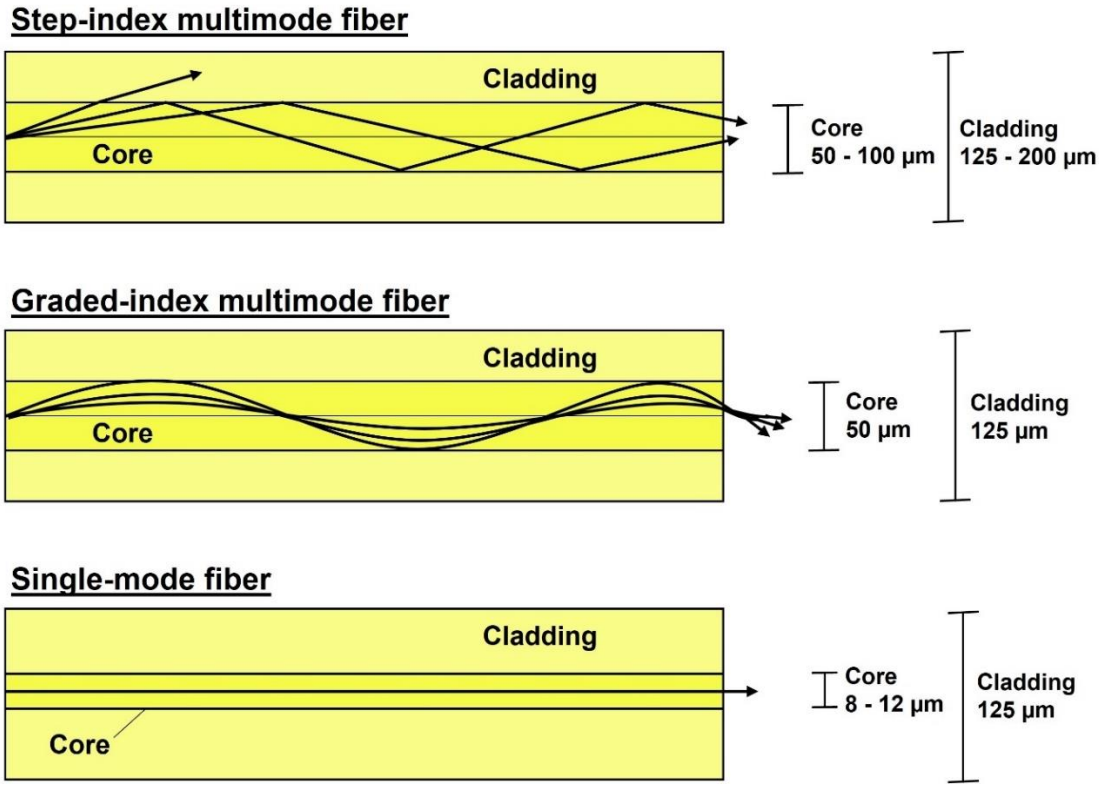

Figure I.10 - Representation of light propagation modes in optical fibers.
Source: by the author.

2.2. Attenuation and optical losses

Another important parameter of optical fiber guidance is the attenuation of the propagated signal, which can be caused by factors related to the material, such as component purity and compositional homogeneity, in addition to phenomena related to the interaction of light with matter.

As discussed in section 1.2., glasses have their transparency window limited by two intrinsic absorption bands: the electronic and vibrational edges. Consequently, wavelengths near these edges experience significant attenuation, leading to absorption within the optical fiber and impeding the efficient propagation of light. Furthermore, between these two bands extrinsic absorption bands are introduced by impurities such as hydroxyl groups, carbon, and transition metals. Hydroxyl groups, in particular, pose a significant challenge due to their strong absorption at several key wavelengths (131). A notable example is the absorption peak at 1.4 μm, which corresponds to the first overtone of O-H stretching vibrations and falls within the near-IR region, which is critical for fiber-optic communication. Transition metals and carbon impurities can introduce unwanted absorption in the visible and near-IR regions, further degrading the fiber's performance (131).

In addition to absorption losses, signal losses in an optical fiber can occur due to scattering phenomena, and the most frequent of which is known as Rayleigh scattering. This phenomenon occurs due to scattering centers much smaller than the wavelength of the radiation. Thus, the scattering degree depends on the size of the scattering centers and the wavelength of the light, with the scattered intensity being inversely proportional to the wavelength raised to a power of four: $I \propto {}^{1}/_{\lambda^4}$. Therefore, this phenomenon tends to present greater scattering intensity for smaller wavelengths, but it also depends on the atomic and molecular dipoles intrinsic to the material and which can be influenced by variations in the density and refractive index of the fiber (132). An example of the optical loss curve for a conventional silica fiber is depicted in Figure I.11.

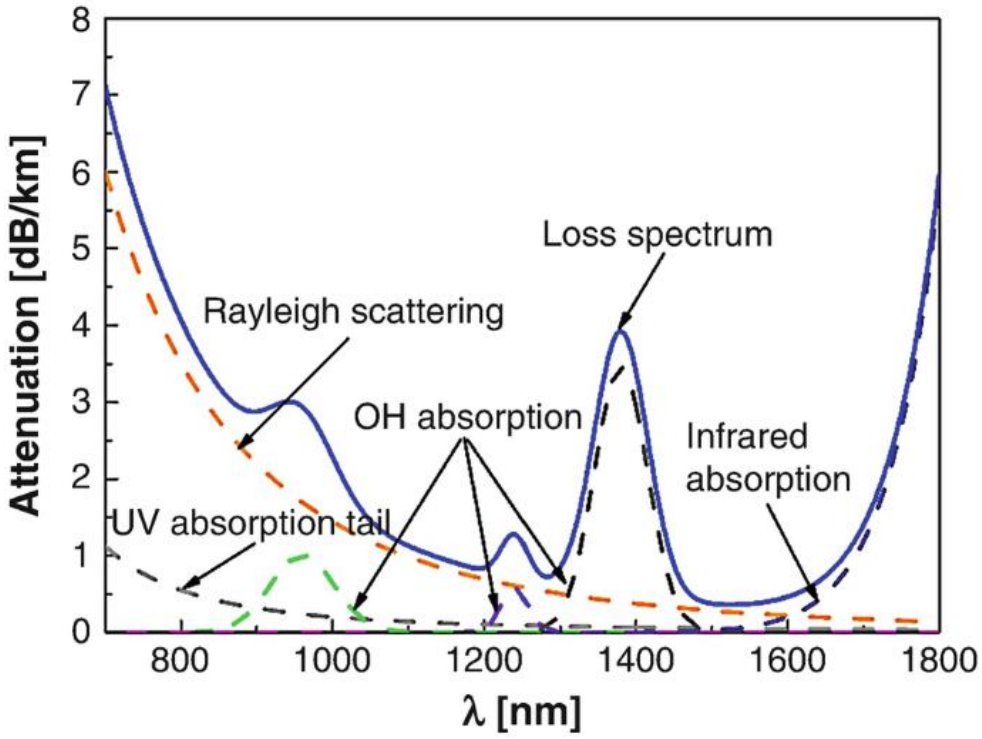

Figure I.11 - Optical loss curve for a silica optical fiber with several factors of attenuation.
Source: reproduced from DING et al. (132).

Finally, a last signal loss situation in optical guidance occurs when the fibers are bent or there are geometric defects at the core-cladding interface. In these situations, called curvature loss, the guidance condition changes, and some modes leave the total internal reflection condition and are refracted to the cladding, representing another optical loss factor (132).

Optical transmission loss is normally evaluated by optical attenuation measurements by the cut-back method (133). This method consists of measurements of the output intensity (I) of the coupled signal in different optical paths, keeping the input intensity constant (I_0). After the first intensity measurement I_1 relative to the length L_1, the fiber is cut n times, resulting in L_n sizes, each with an output I_n value. The fiber is always cut at the end opposite the light source coupling in order to not change the alignment. In this way, the fiber will have a length L_n smaller than L_1 and the fiber output intensity will be measured, with intensities I_n. The fiber attenuation, in dB/m, is determined by the following formula:

$$\alpha\left(\frac{dB}{m}\right) = \frac{10}{L_1 - L_n}\log\frac{I_n}{I_1}$$

2.3. Designs for optical fibers sensors

The sensing of gases or in solution analytes by optical fiber sensors is based on the interaction between the target species and the light conducted by the fiber. This interaction is often based on an intrinsic phenomenon in multimode optical fibers known as evanescence (134). In these fibers, electromagnetic waves propagate through the core, but part of the radiation is also directed toward the cladding. This portion of radiation that propagates around the core is called the evanescent field or light. If an optical fiber does not have a coating, the evanescent light, when leaving the core, is directed to a region outside the fiber, and can interact with species present in the surroundings.

In this sense, the use of fibers that favor the interaction between the evanescent field of the guided light and the analyte is suitable. In traditional core-cladding fibers, the evanescent field travels to the fiber cladding, but a small percentage of this radiation spreads to the surroundings. However, some optical fiber designs facilitate the propagation of the evanescent field to the external environment. Optical fibers of the TOF (Tapered Optical Fiber) type (Figure I.12(a)), for example, present a tapering in the sensing region, reducing the dimensions of both the cladding and core. Therefore, the smaller diameter of the fiber facilitates the extension of the evanescent field to the surroundings and its consequent interaction with the sample (135). TOF fibers are manufactured from a taper region that will be used to contact the analyte. The most common technique for causing this funneling is to stretch the optical fiber while it is heated with an oscillating flame torch. The diameter of the tapered region (p) varies with the elongation distance (z) and can be predicted by the expression:

$$P = p_0 \exp(-z/2L_0),$$

where p_0 is the initial fiber diameter and L_0 is the flame oscillation length.

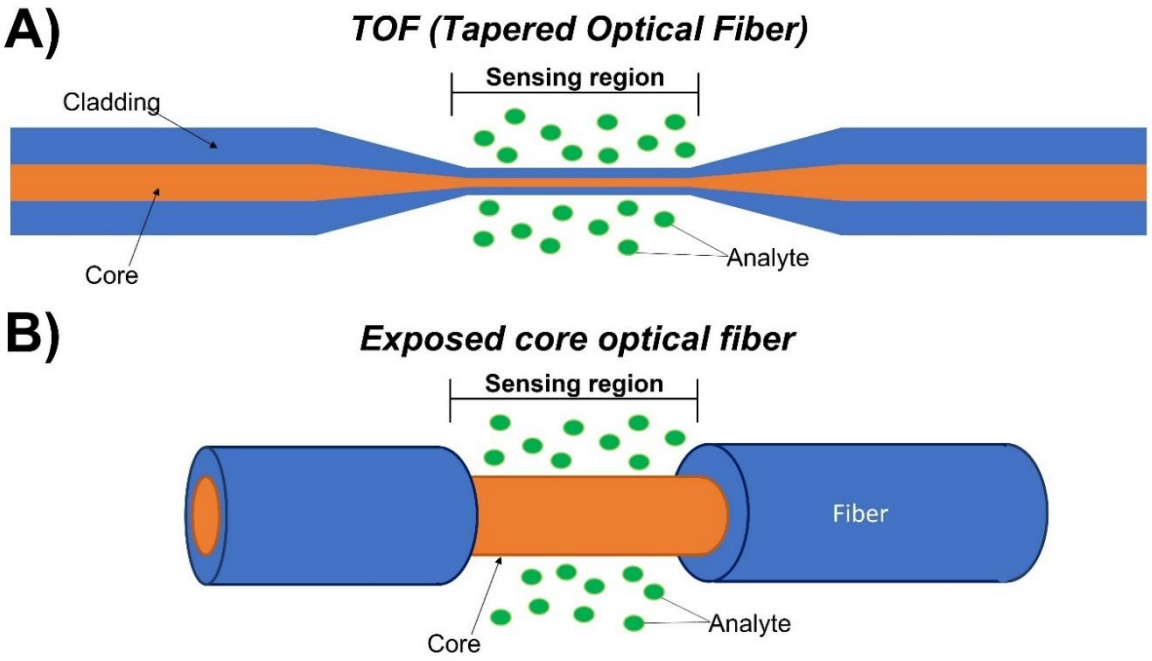

Figure I.12 - Examples of optical fiber designs for sensors: (a) TOF type fibers; (b) fibers with exposed core. Source: by the author.

In Figure I.12(b), the simple removal of the cladding covering the core in the sensing region induces the propagation of the evanescent field to the surroundings of the fiber. This fiber design increases the evanescent field interaction with the analytes, also enabling the functionalization of the fiber core with luminescent molecules, metallic films, nanoparticles, or even quantum dots, as demonstrated by Ding et al. (136), for the quantification of NO with QDs of CdS and CdTe, with issuance characteristic in the visible region, around 550 nm.

The exposure of the fiber core can be done by the controlled removal of the cladding in a specific region of the fiber in contact with the analyte. Generally, the removal is achieved through physical wear or chemical etching of the cladding. Chemical removal is often more convenient, using a solvent suitable for the composition of optical fiber. The most common agents for the glasses used in this project are acidic solutions, such as HF, HCl, H_2SO_4 solution or piranha solution (H_2O_2/H_2SO_4) (137). It is important to highlight that the fiber immersion time in the solution must be strictly controlled for the method's reproducibility and the verification and control of the wear must be done with the aid of an optical microscope (138).

3. Luminescent coordination polymers for optical sensing

Coordination polymers (CPs) are hybrid materials that combine inorganic and organic components, forming a coordination network extending in 1, 2, or 3 dimensions (139). CPs exhibit self-assembly through interactions involving metal ions or clusters and organic linkers via coordinate bonds, as well as secondary interactions such as hydrogen bonding, π–π stacking, and van der Waals forces (140). This variety of interactions allows CPs to adopt a wide range of structures, which can be tailored by selecting different metal ions and organic ligands (141). Although CPs do not necessarily exhibit a crystalline structure, they often share common features such as high surface area, permanent porosity, adsorption capacities, and tunable optical properties (139). As a result, the interest on CPs is based on their high potential for several applications, such as gas storage (142,143), heterogeneous catalysis (144,145), chemical sensing (146-148), drug delivery (149,150), and bioimaging (151,152).

In recent years, CPs containing lanthanide ions (Ln-CPs) have attracted great attention because of their potential as multifunctional luminescent materials (153). The luminescence of Ln-CPs typically arises through the so-called antenna effect, in which the organic ligand is excited by a photon absorption and the energy is transferred to the lanthanide ion (154). In some cases, guest molecules, such as solvent molecules trapped within the frameworks, can also contribute to the emission properties of CPs (148). Over the past decade, numerous Ln-CPs have been developed and employed in sensing application for detecting different chemical species, including metal ions (155,156), organic solvents (157,158), explosives (159), as well as for temperature sensing (160).

Metal-organic frameworks (MOFs) are a subset of CPs and consist of organic ligands coordinated to metallic cations, forming a network that extends in three dimensions (3D) and it can be crystalline or amorphous in nature (161). A representation can be seen in Figure I.13, showing the coordinated bonds between organic compounds and inorganic clusters or metallic cations, which form a regular structure that is tridimensional repeated (162). One of the most remarkable properties of MOFs is their high intrinsic porosity, which can reach up to 90% free volume. Additionally, they exhibit high specific areas, low density (around 0.8 $g.cm^{-3}$) and good thermal stability (400–500 ºC) (162).

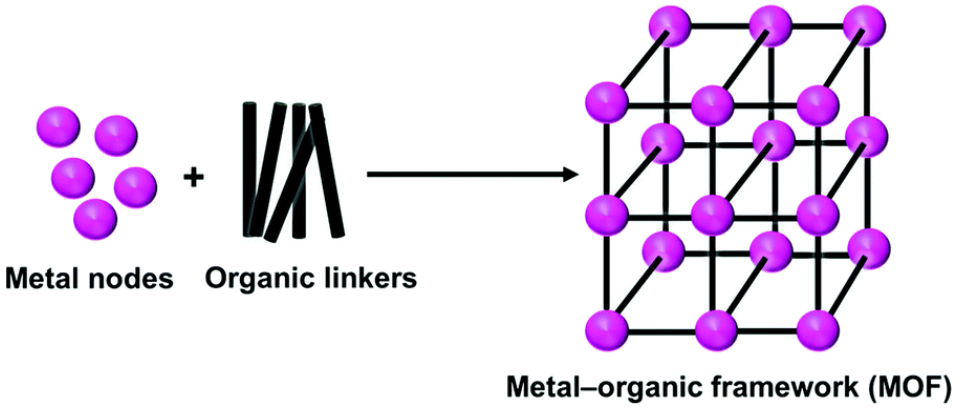

Figure I.13 – Scheme for representation of a MOF.
Source: reproduced from SARACI et al. (163).

MOFs synthesis is based on the reticular chemistry, an area responsible for the design of new ordered network materials with predicted structures (161). By examining the geometry and connections of the building blocks required to create a specific network structure, it becomes possible to replicate that structure across multiple building blocks. These blocks can be adjusted to maintain consistent geometry and connectivity, independent of their size (164). Then, the building blocks can be combined to form secondary building units (SBUs) that assemble into a three-dimensional (3D) structure (161).

As a rule, MOFs have a well-defined chemical structure and strong metal-ligand bond, giving them high crystallinity and permanent porosity. This last property facilitates the process of adsorption/release of guest molecules in the cavities of the material, without the structural collapse of the network. Due to this characteristic, MOFs were initially classified into four categories, as can be seen in Figure I.14 (165). Briefly, the first generation MOFs presented unstable network after the release of the host molecule, causing the structural collapse; in the second generation MOFs, the structure is more rigid and stable upon exit and resorption of the host molecule, maintaining its structural integrity; in turn, the networks of the third generation are dynamic and exhibit structural flexibility, changing reversibly with the presence of host molecules, but maintaining the topology, phase and porosity of the material; finally, the fourth generation MOFs can undergo post-synthetic modification without changing the topology of the network, aiming at the specific molecular recognition of a molecule of interest (165).

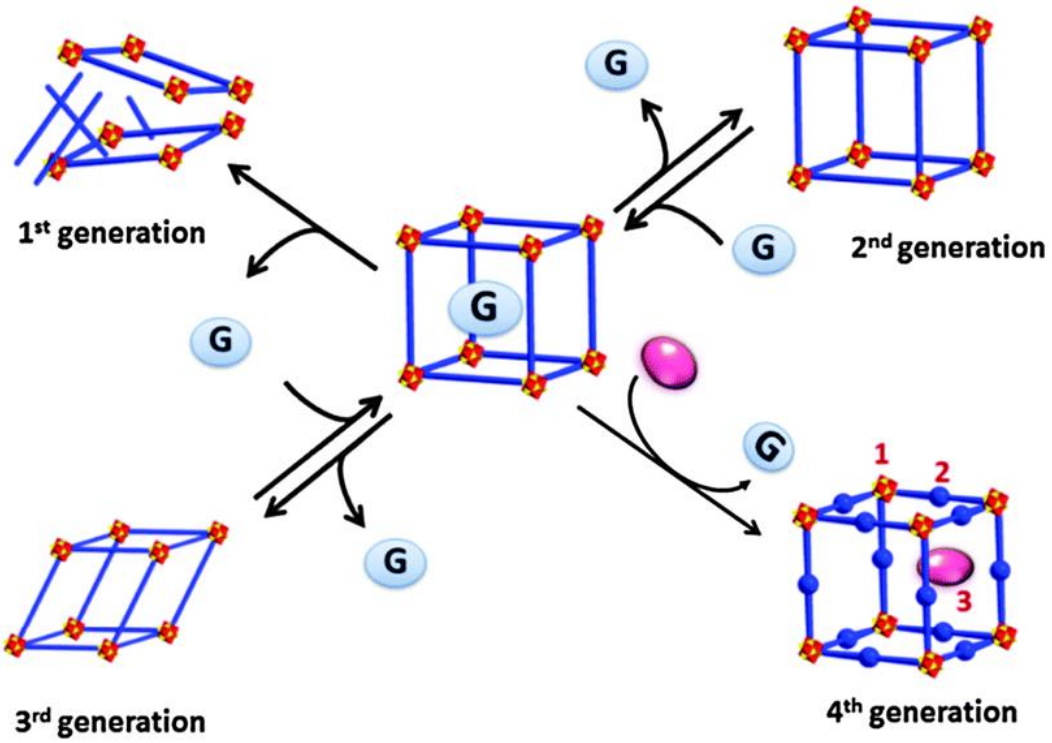

Figure I.14 - Classification of MOFs: 1st generation MOFs collapse when the guest molecules are removed; 2nd generation MOFs retain permanent porosity without guests; 3rd generation MOFs exhibit flexibility properties; and 4th generation MOFs are capable of withstanding post-synthetic modifications, including changes at (1) metal nodes, (2) organic ligands, and (3) vacant spaces.
Source: reproduced from LIU et al. (165).

Currently, the literature features numerous well-established methods for synthesizing MOFs, utilizing a variety of s, p, d, and f-block metals with diverse coordination numbers, geometries, and oxidation states. Nonetheless, there is still considerable potential for further exploration in this field. A particular subset of MOFs that holds interest both from a fundamental synthetic viewpoint and for applications are those synthesized from lanthanide ions, called Ln-MOFs (163).

3.1. Lanthanide metal-organic frameworks (Ln-MOFs)

Ln-MOFs typically form unusual topologies and diverse lattice structures and exhibit luminescence phenomenon. Unlike s-, p-, and d-block metal ions, f-block metal ions display high coordination numbers and multiple coordination modes, enabling the formation of structures that are not achievable with other types of metal ions. Additionally, lanthanide ions have an oxidation state of +3 (generally the more stable) and electronic configuration $[Xe]4f^n$. The 4f level is shielded by the outermost layers (5s and 5p), resulting in a low crystalline field influence. Due to these characteristics, the luminescence of lanthanide ions occurs by intra-

configurational f-f transitions, conferring unique spectroscopic characteristics, with fine and well-defined emission bands (166).

A notable class of organic ligands used to construct Ln-MOFs is multi-carboxylate ligands, valued for their strong coordination with metallic centers and photoluminescent properties (167,168). Specifically, benzenedicarboxylate (BDC) and benzenetricarboxylate (BTC) ligands have been widely explored in Eu^{3+}-based coordination polymers (CPs) (169-172). In these systems, the carboxylate groups can be fully or partially deprotonated, enabling them to coordinate with lanthanide ions. As a result, these ligands can link the metal centers in various orientations, generating multidimensional (2D and 3D) structures (167). Additionally, pyromellitic acid (1,2,4,5-benzenetetracarboxylic acid, H_4B4C) has also been employed in Ln-MOFs, primarily for its ability to efficiently transfer energy to RE^{3+} ions. Since the T_1 energy level of H_4B4C is near to the $^5D_0$ level of Eu^{3+}, this combination is particularly attractive for designing Ln-CPs with high quantum yields (173,174).

Based on the work by Liu et al. (175), the crystal structure of Ln-MOFs combining Eu^{3+} and BTC ligands (forming EuBTC MOF) is characterized as monoclinic, belonging to the space group Cc. The asymmetric unit of this compound features a central europium atom that exhibits nine coordination sites, being surrounded by six oxygen atoms from water molecules and three oxygen atoms from the carboxylate groups of the H_3BTC ligands, as shown in Figure I.15(a). This coordination results in a tricapped trigonal prismatic geometry (175). The ligands display different coordination modes: one carboxylate group acts as unidentate, another as bidentate, while each ligand also contains a free carboxylate group (Figure I.15(b)). The structural arrangement reveals parallel one-dimensional ribbon-like molecular motifs extending along the a-axis, with the phenyl groups of the ligands superimposing along the c-axis (Figure I.15(c)). Additionally, the structure is stabilized by noncovalent interactions, including hydrogen bonding and π-π stacking, which contribute to the formation of a three-dimensional network structure (Figure I.15(d)) (175). This detailed structural understanding of EuBTC is crucial for its potential applications in various fields, including chemical sensing and gas storage (171,172,174).

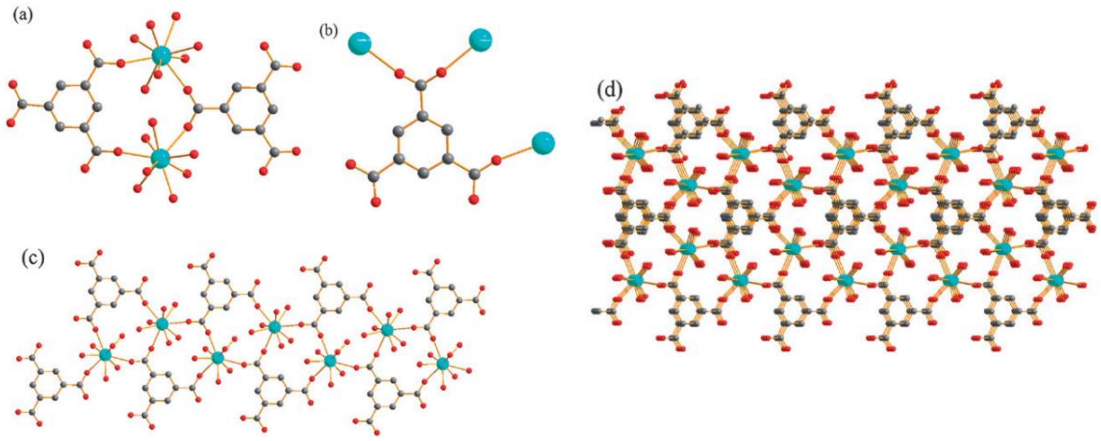

Figure I.15 - (a) The asymmetric unit of EuBTC; (b) coordination modes of the carboxylate groups; (c) 1D ribbonlike structure; (d) perspective view of the packing of the EuBTC. Atoms: Eu - blue, O - red, C – gray. Source: reproduced from LIU et al. (175).

For lantanide-B4C MOFs, the structures are characterized by a three-dimensional (3D) framework formed through complex coordination interactions (176,177). The europium centers (Eu^{3+}) adopt a distorted monocapped square anti-prism, where each Eu^{3+} is nine-coordinated (EuO_9) by oxygen atoms from pyromellitic acid ligands, as shown in Figure I.16(a) (178). These ligands exhibit multiple coordination modes, including tridentate-bridging-chelating and monodentate-chelating, connecting the europium centers into one-dimensional (1D) chains (Figures I.16(b) and I.16(c)) (179,176). These chains are further linked via oxocarboxylate bridges from B4C ligands, forming 2D layers (Figure I.16(d)) and the final 3D architecture is reinforced through strong hydrogen bonding between non-coordinated and coordinated oxygen atoms, completing the structure (176).

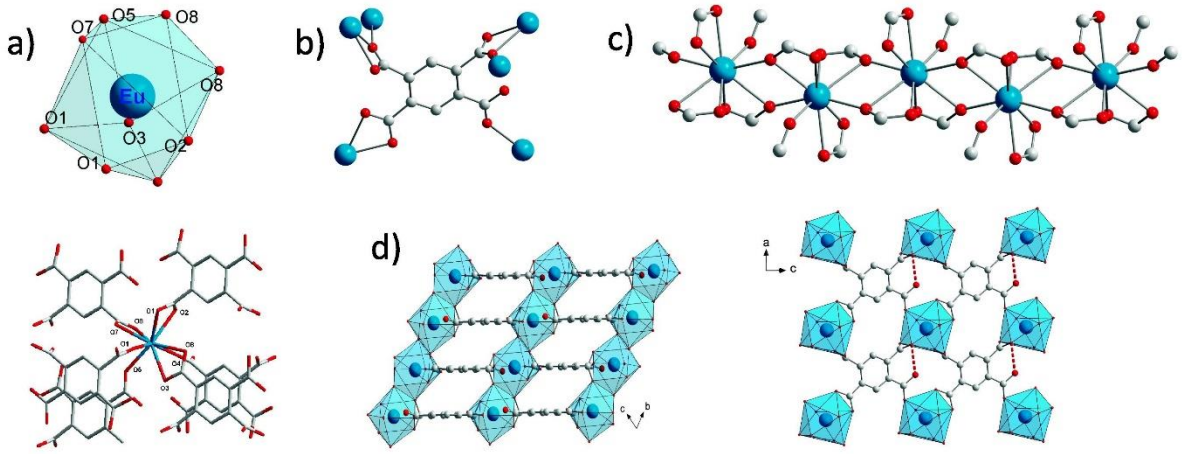

Figure I.16 – (a) Coordination sphere of Eu^{3+} in $[Eu(B4C)]_n$ (top) and asymmetric unit (bottom); (b) coordination mode of the B4C carboxylate; (c) chains formed by edge-connected EuO_9 polyhedra; and (d) $[Eu(B4C)]_n$ structure along the *a* axis and the *b* axis (EuO_9 polyhedra: blue, oxygen: red, carbon: grey; H-bonds: dotted red line). Source: adapted from AMIAUD et al. (178).

Given their unique properties, Ln-MOFs based on polycarboxylate ligands exhibit considerable potential for application in photoluminescent chemical sensing. In this work, the compositions EuBTC and EuB4C were synthesized as coatings on different glass substrates. These composites were exposed to various organic analytes, and their photoluminescent behavior was meticulously evaluated. The detailed results of this assessment will be discussed in Chapter VII.

3.2. Luminescence mechanisms and sensing activity

The luminescence in Ln-CPs generally originates from charge transfer processes, including metal-centered luminescence (MC), metal-to-ligand charge transfer (MLCT), ligand-to-metal charge transfer (LMCT), ligand-ligand charge transfer (LLCT) and metal-to-metal charge transfer (MMCT) (180). Direct photoexcitation of lanthanide ions is challenging due to their low transition probabilities and narrow absorption cross-section. This issue can be addressed by indirectly exciting the lanthanide ions through a coordinated organic ligand(181,182). This concept allows organic ligands, which do not exhibit forbidden transitions, to absorb light efficiently. If the energy levels of the excited ligand is near to those of the excited 4f states of the lanthanide, the energy transfer can occur from the ligand to the metal, leading to characteristic 4f-emissions (182).

This luminescence sensitization process, known as the antenna effect, is particularly relevant in Ln-CPs (183). In these materials, organic ligands can be excited from their ground state (S_0) to the first excited singlet state (S_1) upon absorbing light at an appropriate wavelength.

The excited molecule can then return to its ground state through either radiative or non-radiative processes. The transition from S_1 to the triplet excited state (T_1) is referred to as intersystem crossing (ISC) (180). Among these pathways, the radiative process leads to molecular luminescence, appearing as either fluorescence ($S_1 \rightarrow S_0$) or phosphorescence ($T_1 \rightarrow S_0$) (184). If the T_1 energy level of the ligand is well aligned with an energy level of the coordinated Ln^{3+} ion, energy can be efficiently transferred to the metal ion (Figure I.17(a)) (182). According to an empirical rule, the antenna effect occurs when the energy gap between the ligand's S_1 and T_1 states exceeds 5000 cm^{-1}, and the energy gap between the T_1 state and the $^5D_0$ state of the lanthanide ion is higher than 3000 cm^{-1} (185). For example, the ligand H_4B4C has an S_1 energy level at 39,841 cm^{-1} and a T_1 energy level at 20,790 cm^{-1}. Since the energy difference between H_4B4C T_1 state and the $^5D_0$ level of Eu^{3+} is 3290 cm^{-1}, H_4B4C is an effective sensitizer for Eu^{3+} (173). Additionally, luminescence can occur through mixed contributions, typically involving a combination of metal-centered (MC), ligand-centered (LC), and charge-transfer (CT) luminescence, with the latter being directly influenced by guest molecules (Figure I.17(b)) (186).

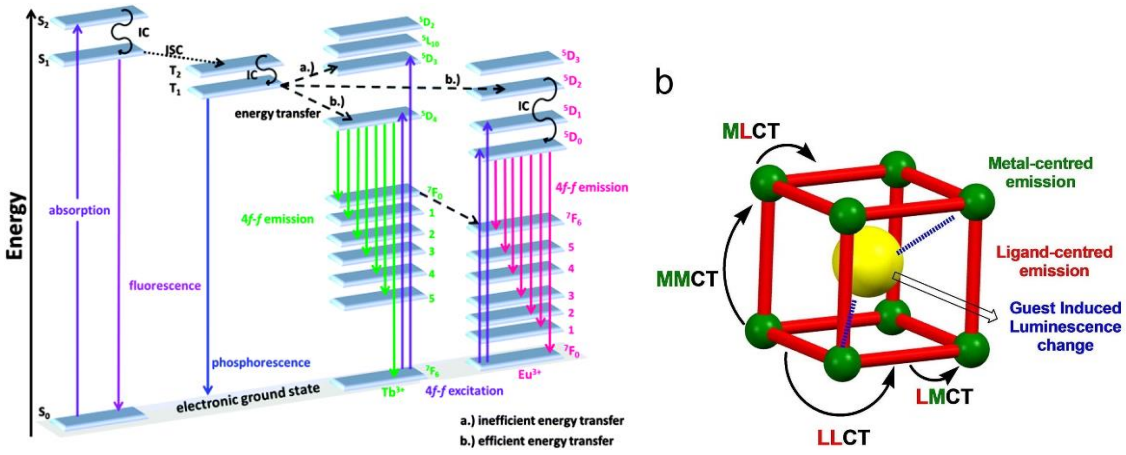

Figure I.17 – (a) Jablonski diagram for energy transfer in Ln-CPs; S = singlet states, T = triplet states; IC = internal conversion, ISC = intersystem crossing (both are non-radiative processes). (b) Energy transfer process in Ln-CPs with additional pathways for luminescence in the presence of guest molecules.
Source: (a) reproduced from STEEMERS et al. (185); (b) reproduced from LIU et al. (186).

In recent years, numerous studies have focused on the use of luminescent Ln-CPs as chemical sensors. The optical sensing is based on changes in the luminescence intensity or energy, which is disturbed when the analytes interact with the material, modifying the electron transfer from the excited state of the ligands to the emitting center. In the case of sensing of nitroaromatics, for example, their lower energy empty orbitals (LUMOs), in general, have lower energies than the conduction band of Ln-MOFs, facilitating electron transfer and, consequently, causing luminescence suppression (187). However, a variety of sensing mechanisms are

possible, often based on complexation between donor–acceptor species (186). The interaction with analytes can modulate the HOMO and LUMO energy levels of Ln-CPs, which may influence both the energy and intensity of the luminescence (188). Additionally, the analyte can serve as an efficient photon absorber, transferring the absorbed excitation energy to the luminescent sensing agent and thereby enhancing their emission (188). This process is particularly interesting for lanthanide-based sensors, as their spin-forbidden f–f transitions are difficult to excite directly (186).

Compared to traditional analytical techniques like chromatography, optical absorption, and electrochemistry, luminescence-based sensors offer several advantages, including simpler sample preparation, lower detection limits, the ability to detect signals visually, and suitability for real-time applications. Luminescent sensors based on Ln-CPs enable the detection of analytes that affect the antenna effect through measurable luminescence changes (189). Furthermore, the relatively easy functionalization on the surface of different materials and the high degree of permanent porosity in these compounds make them ideal for sensor devices, as they facilitate efficient interaction with target species. (32,33,190).

References

[1] ZHANG, H.; ZHANG, H. Special issue: rare earth luminescent materials. **Light:** science & applications, London, v. 11, n. 1, p. 260, 2022.

[2] RONDA, C. Challenges in application of luminescent materials, a tutorial overview (invited review). **Progress In Electromagnetics Research**, Cambridge, v. 147, p. 81–93, 2014.

[3] TANABE, S. Rare-earth-doped glasses for fiber amplifiers in broadband telecommunication. **Comptes Rendus Chimie**, Paris, v. 5, n. 12, p. 815–824, 2002.

[4] SUPE, A., SPOLITIS, S., ELSTS, E., MURNIEKS, R., DOKE, G., SENKANS, U., MATSENKO, S., GRUBE, J., BOBROVS, V. Recent developments in cladding-pumped doped fiber amplifiers for telecommunications systems. *In*: INTERNATIONAL CONFERENCE ON TRANSPARENT OPTICAL NETWORKS (ICTON), 2020. Bari. **Proceedings**…Piscataway: IEEE, 2020. p. 1-6.

[5] QIN, X., LIU, X., HUANG, W., BETTINELLI, M., LIU, X. Lanthanide-activated phosphors based on 4f-5d optical transitions: theoretical and experimental aspects. **Chemical Reviews**, Washington, v. 117, n. 5, p. 4488–4527, 2017.

[6] DONG, H, DU, S., ZHENG, X., LYU, G., SUN, L., LI, L., ZHANG, P., ZHANG, C., YAN, C. Lanthanide nanoparticles: from design toward bioimaging and therapy. **Chemical Reviews**, Washington, v. 115, n. 19, p. 10725–10815, 2015.

[7] CALDIÑO, U., BETTINELLI, M., FERRARI, M., PASQUINI, E., PELLI, S., SPEGHINI, A., RIGHINI, G.C. Rare earth doped glasses for displays and light generation. **Advances in Sciences and Technology**, Zurich, v. 90, p. 174-178, 2014.

[8] EROL, E., VAHEDIGHAREHCHOPOGH, N. KIBRISLI, O., ERSUNDU, M.Ç., ERSUNDU, A.E. Recent progress in lanthanide-doped luminescent glasses for solid-state lighting applications - a review. **Journal of Physics:** condensed matter, Bristol, v. 33, n. 48, p. 483001, 2021.

[9] JIMÉNEZ, J. A.; AMESIMENU, R.; THOMAS, M. Impact of Lanthanide (Nd^{3+}, Gd^{3+}, and Yb^{3+}) ionic field strength on the structure and thermal expansion of phosphate glasses. **The Journal of Physical Chemistry B**, Washington, v. 128, n. 12, p. 2995–3003, 2024.

[10] LI, W., SMET, P. F., MARTIN, L. I. D. J., PRITZEL, C., GÜNNE, J. S. Doping homogeneity in co-doped materials investigated at different length scales. **Physical Chemistry Chemical Physics**, London, v. 22, n. 2, p. 818–825, 2020.

[11] MINISCALCO, W. Optical and electronic properties of rare earth ions in glasses. *In*: DIGONNET, M. J. F. **Rare-earth-doped fiber lasers and amplifiers, revised and expanded.** New York: CRC Press**,** 2001.

[12] BABU, P.; JAYASANKAR, C. K. Optical spectroscopy of Eu^{3+} ions in lithium borate and lithium fluoroborate glasses. **Physica B:** condensed matter, Amsterdam, v. 279, n. 4, p. 262–281, 2000.

[13] ZAKIS, K. OLONKINS, S., UDALCOVS, A., LUKOSEVICS, I. PRIGUNOVS, D., GRUBE, J., BIKSE, L., SUOE, A, OZOLINS, O., SPOLITIS, S., BOBROVS, V. Cladding-Pumped Er/Yb-Co-Doped fiber amplifier for multi-channel operation. **Photonics**, Basel, v. 9, n. 7, p. 457, 2022.

[14] MONRO, T. M.; EBENDORFF-HEIDEPRIEM, H. Progress in microstructured optical fibers. **Annual Review of Materials Research**, San Mateo, v. 36, p. 467-495, 2006.

[15] JHA, A.; RICHARDS, B. D. O.; JOSE, G.; FERNANDEZ, T. T.; HILL, C. J.; LOUSTEAU, J. Review on structural, thermal, optical and spectroscopic properties of tellurium oxide based glasses for fibre optic and waveguide applications. **International Materials Reviews**, London, v. 57, n. 6, p. 357–382, 2012.

[16] GÖKÇE, M. Development of Eu^{3+} doped bismuth germanate glasses for red laser applications. **Journal of Non-Crystalline Solids**, Amsterdam, v. 505, p. 272–278, 2019.

[17] MUSSAVI RIZI, S. H, BOETTI, N.G., PUGLIESE, D., JANNER, D. Phosphate glass-based microstructured optical fibers with hole and core for biomedical applications. **Optical Materials**, Amsterdam, v. 131, p. 112644, 2022.

[18] PISARSKI, W. A., PISARKA, J., MACZKA, M., RYBA-ROMANOWSKI, W. Europium-doped lead fluoroborate glasses: Structural, thermal and optical investigations. **Journal of Molecular Structure**, Amsterdam, v. 792–793, p. 207–211, 2006.

[19] LAVAL, J. P., DUCLÉRE, J. R., COUDERC, V, ALLIX, M., GENEVOIS, C. Highly Transparent fluorotellurite glass-ceramics: structural investigations and luminescence properties. **Inorganic Chemistry**, Washington, v. 58, n. 24, p. 16387–16401, 2019.

[20] GALLEANI, G., SANTAGANELLI, S.H., LEDEMI, Y., MESSADDEQ, Y., JANKA, O., POTTGEN, R., ECKERT, H. Ultraviolet upconversion luminescence in a highly transparent triply-doped Gd^{3+}-Tm^{3+}-Yb^{3+} fluoride-phosphate glasses. **Journal of Physical Chemistry C**, Washington, v. 122, n. 4, p. 2275–2284, 2018.

[21] SHEN, L., REN, H., HUANG, M., WU, D., PEACOCK, A. C. A review of nonlinear applications in silicon optical fibers from telecom wavelengths into the mid-infrared spectral region. **Optics Communications**, Amsterdam, v. 463, p. 125437, 2020.

[22] BORZYCKI, K.; OSUCH, T. Hollow-core optical fibers for telecommunications and data transmission. **Applied Sciences**, Basel, v. 13, n. 19, p. 10699, 2023.

[23] ELSHERIF, M.; SALIH, A. E.; MUNOZ, M. G.; ALAM, F.; ALQATTAN, B. Optical fiber sensors: working principle, applications, and limitations. **Advanced Photonics Research**, Weinheim, v. 3, n. 11, 2022.

[24] YU, L; YE, L.; BAO, R.; ZHANG, X.; WANG, L.G. Sensitivity-enhanced Tm^{3+}/Yb^{3+} co-doped YAG single crystal optical fiber thermometry based on upconversion emissions. **Optics Communications**, Amsterdam, v. 410, p. 632–636, 2018.

[25] TANG, H.; ZHAO, L.; LIU, Z.; PENG, Q.; YU, X. A lanthanide-doped glass-ceramic fiber for stress sensing. **Cell Reports Physical Science**, Cambridge, v. 3, n. 10, p. 101093, 2022.

[26] CUI, S.; CHAHAL, R.; NAZABAL, V.; DOUALAN, J. L.; BUREAU, B. From selenium- to tellurium-based glass optical fibers for infrared spectroscopies. **Molecules**, Basel, v. 18, n. 5, p. 5373–5388, 2013.

[27] SMITH, D.; ŠPANĚL, P. The challenge of breath analysis for clinical diagnosis and therapeutic monitoring. **The Analyst**, London, v. 132, n. 5, p. 390–396, 2007.

[28] XU, H.; LIU, F.; CUI, Y.; CHEN, B.; QIAN, G. A luminescent nanoscale metal-organic framework for sensing of nitroaromatic explosives. **Chemical Communications**, London, v. 47, n. 11, p. 3153–3155, 2011.

[29] QIN, J.; MA, B.; LIU, X. F.; LU, H. L.; DONG, X. Y., ZANG, S. Q.; HOU, H. Aqueous- and vapor-phase detection of nitroaromatic explosives by a water-stable fluorescent microporous MOF directed by an ionic liquid. **Journal of Materials Chemistry A**, London, v. 3, n. 24, p. 12690–12697, 2015.

[30] CARLOS, L. D.; FERREIRA, R. A. S.; BERMUDEZ, V. Z.; RIBEIRO, S. J. L. Lanthanide-containing light-emitting organic-inorganic hybrids: a bet on the future. **Advanced Materials**, Weinheim, v. 21, n. 5, p. 509–534, 2009.

[31] UH, H.; PETOUD, S. Novel antennae for the sensitization of near infrared luminescent lanthanide cations. **Comptes Rendus Chimie**, Paris, v. 13, n. 6–7, p. 668–680, 2010.

[32] WALES, D. J.; GRAND, J.; MINTOVA, S.; BURROWS, A. D. Gas sensing using porous materials for automotive applications. **Chemical Society Reviews**, London, v. 44, n. 13, p. 4290–4321, 2015.

[33] WU, J.; ZHANG, W.; WANG, Y.; LI, B.; HAO, T.; ZHENG, Y. JIANG, L.; CHEN, K.; CHIANG, K.S. Nanoscale light–matter interactions in metal–organic frameworks cladding optical fibers. **Nanoscale**, London, v. 12, n. 18, p. 9991–10000, 2020.

[34] CUI, Y.; YUE, Y.; QIAN, G.; CHEN, B. Luminescent functional metal–organic frameworks. **Chemical Reviews**, Washington, v. 112, n. 2, p. 1126–1162, 2012.

[35] ZANOTTO, E. D.; MAURO, J. C. The glassy state of matter: Its definition and ultimate fate. **Journal of Non-Crystalline Solids**, Amsterdam, v. 471, p. 490–495, 2017.

[36] LIŠKA, M.; CHROMČÍKOVÁ, M. Thermal properties and related structural study of oxide glasses. *In*: SESTÁK, J.; MARES, J. J.; HUBÍK, P. **Glassy, amorphous and nano-crystalline materials**. Springer Nature, Berlin, p. 179–197, 2010.

[37] VARSHNEYA, A. K.; MAURO, J. C. Fundamentals of the glassy state. *In*: VARSHNEYA, A. K.; MAURO, J. C. **Fundamentals of inorganic glasses**. Elsevier, Amsterdam, p. 19–35, 2019.

[38] YOUNGMAN, R. E. Silicate glasses and their impact on humanity. **Reviews in Mineralogy and Geochemistry**, McLean, v. 87, n. 1, p. 1015–1038, 2022.

[39] EBENDORFF-HEIDEPRIEM, H.; WANG, P. Oxide glass and optical fiber fabrication. *In*: JACKSON, S.; BERNIER, M.; VALLÉE, R. **Mid-infrared fiber photonics**. Amsterdam: Elsevier, 2022. p. 111–176.

[40] DIETZEL, A. Glass structure and properties. **Glastechnische Berichte**, Frankfurt, v. 22, p. 1187, 1968.

[41] HRUBÝ, A. Evaluation of glass-forming tendency by means of DTA. **Czechoslovak Journal of Physics**, Berlin, v. 22, n. 11, p. 1187–1193, 1972.

[42] LENDVAYOVÁ, S.; MORICOVÁ, K.; JONA, E.; KRAXNER, J. Thermal properties of oxide glasses. **Journal of Thermal Analysis and Calorimetry**, Berlin, v. 108, n. 3, p. 901–904, 2012.

[43] BAIRD, J. A.; TAYLOR, L. S. Evaluation of amorphous solid dispersion properties using thermal analysis techniques. **Advanced Drug Delivery Reviews**, Amsterdam, v. 64, n. 5, p. 396–421, 2012.

[44] GARCIA-VALLES, M.; HAFEZ, H.S.; CRUZ-MATÍAS, I.; VERGÉS, E.; NOGUÉS, J.; MARTINEZ, S. Calculation of viscosity–temperature curves for glass obtained from four wastewater treatment plants in Egypt. **Journal of Thermal Analysis and Calorimetry**, Berlin, v. 111, n. 1, p. 107–114, 2013.

[45] SU, Y.; YIN, H.; HE, X.; ZHOU, Y. Influence of annealing on the structure of silica glass. **Journal of Wuhan University of Technology:** material science edition, Hubei, v. 28, n. 5, p. 902–906, 2013.

[46] CALVEZ, L. Chalcogenide glasses and glass-ceramics: transparent materials in the infrared for dual applications. **Comptes Rendus Physique**, Paris, v. 18, n. 5–6, p. 314–322, 2017.

[47] NALIN, M.; RIBEIRO, S. J. L.; MANZANI, D.; GONÇALVES, R. R.; MALTA, O.; YANNICK, L.; MESSADDEQ, S.; MESSADDEQ, Y. Glassy materials and light: part 1. **Química Nova**, São Paulo, v. 39, n. 3, p. 328-339, 2016.

[48] DUMBAUGH, W. H. Infrared transmitting germanate glasses**. Proceedings SPIE -** emerging optical materials, Bellingham, v. 297, 1982.

[49] WANG, J. S.; VOGEL, E. M.; SNITZER, E. Tellurite glass: a new candidate for fiber devices. **Optical Materials**, Amsterdam, v. 3, n. 3, p. 187–203, 1994.

[50] NEOV, S.; KOZHUHAROV, V.; GERASIMOVA, I.; KREZHOV, K.; SIDZHIMOV, B. A model for structural recombination in tellurite glasses. **Journal of Physics C:** solid state physics, Bristol, v. 12, n. 13, p. 2475–2485, 1979.

[51] SAKIDA, S.; HAYAKAWA, S.; YOKO, T. Part 2.125Te NMR study of M_2O–TeO_2 (M=Li, Na, K, Rb and Cs) glasses. **Journal of Non-Crystalline Solids**, Amsterdam, v. 243, n. 1, p. 13–25, 1999.

[52] SHEN, S.; JHA, A.; LIU, X.; NAFTALY, M. Tellurite glasses for broadband amplifiers and integrated optics. **Journal of the American Ceramic Society**, Washington, v. 85, n. 6, p. 1391–1395, 2002.

[53] WANG, J. S.; VOGEL, E. M.; SNITZER, E. Tellurite glass: a new candidate for fiber devices. **Optical Materials**, Amsterdam, v. 3, n. 3, p. 187–203, 1994.

[54] ANSARI, G. F.; BAIRAGI, S.; BARTWAL, K. S.; DHIMAN, S. K.; MAHAJAN, S. K. Effect of Zn concentration on characteristics of ternary zinc-tellurite glasses. **SSRN Electronic Journal**, Rochester, 2022.

[55] OHISHI, Y.; QIN, G.; LIAO, M.; YAN, X.; SUZUKI, T. Recent progress in tellurite fibers. *In*: OPTICAL FIBER COMMUNICATION CONFERENCE**,** San Diego, 2010. **Proceedings**…[*S. l.*]: Optica Publishing Group. 2010.

[56] FENG, X.; LOH, W. H.; FLANAGAN, J. C.; CARMELINGO, A. Single-mode tellurite glass holey fiber with extremely large mode area for infrared nonlinear applications. **Optics Express**, Rochester, v. 16, n. 18, p. 13651, 2008.

[57] EBENDORFF-HEIDEPRIEM, H.; MONRO, T. M. Analysis of glass flow during extrusion of optical fiber preforms. **Optical Materials Express**, Rochester, v. 2, n. 3, p. 304, 2012.

[58] OERMANN, M. R.; EBENDORFF-HEIDEPRIEM, H.; FOO, T. C.; MONRO, T. M. Index matching between passive and active tellurite glasses for use in microstructured fiber lasers: erbium doped lanthanum-tellurite glass. **Optics Express**, Rochester, v. 17, n. 18, p. 15578, 2009.

[59] RICHARDS, B. D. O.; TEDDY-FERNANDEZ, T.; JOSE, G.; BINKS, D.; JHA, A. Mid-IR (3–4 μm) fluorescence and ASE studies in Dy^{3+} doped tellurite and germanate glasses and a fs laser inscribed waveguide. **Laser Physics Letters**, Bristol, v. 10, n. 8, p. 085802, 2013.

[60] SAVELII, I.; DESEVEDAVY, F.; JULES, J. C.; GADRET, G.; FATOME, J.; KIBLER, B.; KAWASHIMA, H.; OHISHI, Y.; SMEKTALA, F. Management of OH absorption in tellurite optical fibers and related supercontinuum generation. **Optical Materials**, Amsterdam, v. 35, n. 8, p. 1595–1599, 2013.

[61] TAO, G.; EBENDORFF-HEIDEPRIEM, H.; ABOURADDY, A. F. Infrared fibers. **Advances in Optics and Photonics**, Rochester, v. 7, n. 2, p. 379, 2015.

[62] ZHAN, H.; SHI, T.; ZHANG, A.; ZHOU, Z.; SI, J.; LIN, A. Nonlinear characterization on mid-infrared fluorotellurite glass fiber. **Materials Letters**, Amsterdam, v. 120, p. 174–176, 2014.

[63] THOMAS, R. L.; NAMPOORI, V. P. N.; RADHAKRISHNAN, P.; THOMAS, S. Laser induced fluorescence in europium doped zinc tellurite glasses. **Optik**, Amsterdam, v. 124, n. 22, p. 5840–5842, 2013.

[64] MANZANI, D.; SOUZA-JUNIOR, J. B.; REYNA, A. S.; SILVA-NETO, M. L.; BAUTISTA, J. E. Q.; RIBEIRO, S. J. L.; ARAUJO, C. B. Phosphotellurite glass and glass-ceramics with

high TeO2 contents: thermal, structural and optical properties. **Dalton Transactions**, London, v. 48, n. 18, p. 6261–6272, 2019.

[65] BROW, R. K. Review: the structure of simple phosphate glasses. **Journal of Non-Crystalline Solids**, Amsterdam, v. 263-264, p. 1-28, 2000.

[66] SHARMIN, N.; RUDD, C. D. Structure, thermal properties, dissolution behaviour and biomedical applications of phosphate glasses and fibres: a review. **Journal of Materials Science**, v. 52, n. 15, p. 8733–8760, 2017.

[67] MUÑOZ, F. ROCHERULLÉ, J., AHMED, I., HU, L. Phosphate glasses. *In*: MUSGRAVES, J. D.; HU, J.; CALVEZ, L. **Springer handbook of glass**. Cham: Springer, 2019. p. 553–594.

[68] MANZANI, D.; ARAUJO, C. B.; BOUDEBS, G.; MESSADDEQ, Y.; RIBEIRO, S. J. L. The Role of Bi_2O_3 on the thermal, structural, and optical properties of tungsten-phosphate glasses. **The Journal of Physical Chemistry B**, Washington, v. 117, n. 1, p. 408–414, 2013.

[69] ELSAGHIER, H. M.; AZOOS, M. A.; ZIDA, N. A.; ABBAS, W.; OKASHA, A.; MARZOUK, S. Y. Spectroscopic and optical investigations on Er^{3+} ions doped alkali cadmium phosphate glasses for laser applications. **Journal of Non-Crystalline Solids**, Amsterdam, v. 588, p. 121616, 2022.

[70] BROW, R. K. Nature of alumina in phosphate glass: I, properties of sodium aluminophosphate glass. **Journal of the American Ceramic Society**, Hoboken, v. 76, n. 4, p. 913–918, 1993.

[71] OJOVAN, M. I.; LEE, W. E.; KALMYKOV, S. N. **An introduction to nuclear waste immobilisation**. Amsterdam: Elsevier, 2019.

[72] CHONG, S.; RILEY, B. J. Compositional effects on the chemical durabilities of aluminophosphate glasses: a review. **Journal of Non-Crystalline Solids:** x, Amsterdam v. 21, p. 100205, 2024.

[73] ENDO, J.; INABA, S.; HOMMA, O.; SUZUKI, Y. Structural features of $(Li,Na,K)PO_3$ mixed alkali metaphosphate glass for significant anisotropy. **Journal of the American Ceramic Society**, Hoboken, v. 105, n. 1, p. 217–224, 2022.

[74] KASER, S.; GUÉRINEAU, T.; STRUTYNSKI, C.; ZAKI, R.; DUSSAUZE, M.; DURAND, E.; MESSADDEQ, S.; DANTÓ, S.; MESSADDEQ, Y.; CARDINAL, T. Novel optical amorphous phosphate materials with a low melting temperature. **Materials Advances**, London, v. 3, n. 11, p. 4600–4607, 2022.

[75] SHI, X. Z.; GU, Y.; LIU, T. Y.; JIANG, Z. H.; LI, R.; ZENG, F. Effect of different P_2O_0/SnF_2 ratios on the structure and properties of phosphate glass. **Journal of Non-Crystalline Solids**, Amsterdam, v. 578, p. 121350, 2022.

[76] EHRT, D. Effect of OH-content on thermal and chemical properties of SnOP2O5 glasses. **Journal of Non-Crystalline Solids**, Amsterdam, v. 354, n. 2–9, p. 546–552, 2008.

[77] MA, L.; BROW, R. K.; SCHLESINGER, M. E. Dissolution behavior of Na2O–FeO–Fe2O3–P2O5 glasses. **Journal of Non-Crystalline Solids**, Amsterdam, v. 463, p. 90–101, 2017.

[78] BROW, R. K.; KIRKPATRICK, R. J.; TURNER, G. L. Nature of alumina in phosphate glass: II, structure of sodium alurninophosphate glass. **Journal of the American Ceramic Society**, Hoboken, v. 76, n. 4, p. 919–928, 1993.

[79] WEGNER, S.; VAN WÜLLEN, L.; TRICOT, G. The structure of aluminophosphate glasses revisited: application of modern solid state NMR strategies to determine structural motifs on intermediate length scales. **Journal of Non-Crystalline Solids**, Amsterdam, v. 354, n. 15–16, p. 1703–1714, 2008.

[80] CIECIŃSKA, M.; GOJ, P.; STOCH, A.; STOCH, P. Thermal properties of $60P_2O_5$–$(40-x)Al_2O_3$–xNa_2O glasses. **Journal of Thermal Analysis and Calorimetry**, Berlin, v. 139, n. 3, p. 1763–1769, 2020.

[81] BARIK, S. K. SENAPATI, A.; BALAKRISHNAN, S.; ANANTHASIVAN, K. Synthesis and characterization of rare-earth doped aluminium phosphate glasses. **Progress in Nuclear Energy**, Amsterdam, v. 152, p. 104372, 2022.

[82] FAZAL, S.; ZAMAN, F.; ALI, S.; IQBAL, Y.; CHANITHIMA, S. Investigation of europium-doped aluminium phosphate glass for red light generation. **Ceramics International**, Amsterdam, v. 48, n. 17, p. 24751–24757, 2022.

[83] ALAOUI, Y.; LAOURAYED, M.; BOUDALIA, M.; SEKKAT, Z.; WARAD, I.; GUENBOUR, A.; BELLAOUCHOU, A.; ZARROUK, A. Effect of alumina insertion on structural properties, thermal stability, and chemical durability of potassium calcium based-phosphate glasses. **Inorganic Chemistry Communications**, Amsterdam, v. 142, p. 109632, 2022.

[84] PANDAYIL, J.; BOETTI, N.; JANNER, D. Advancements in biomedical applications of calcium phosphate glass and glass-based devices - a review. **Journal of Functional Biomaterials**, Basel, v. 15, n. 3, p. 79, 2024.

[85] PISARSKA, J.; SOLTYS, M.; ZUR, L.; PISARSKI, W. A.; JAYASANKAR, C. K. Excitation and luminescence of rare earth-doped lead phosphate glasses. **Applied Physics B**, Berlin, v. 116, n. 4, p. 837–845, 2014.

[86] VENKATRAMU, V.; VIJAYA, R.; LÉON-LUIS, S. F.; BABU, P.; DHARESHWAR, L. J. Optical properties of Yb^{3+}-doped phosphate laser glasses. **Journal of Alloys and Compounds**, Amsterdam, v. 509, n. 16, p. 5084–5089, 2011.

[87] MOŠNER, P.; VOROKHTA, M.; LADISLAV KOUDELKA, L.; LIONEL MONTAGNE, L.; BERTRAND REVEL, B.; KRISTINA SKLEPIĆ, K.; MOGUŠ-MILANKOVIĆ, A. Effect of germanium oxide on the structure and properties of lithium borophosphate glasses. **Journal of Non-Crystalline Solids**, Amsterdam, v. 375, p. 1–6, 2013.

[88] YAN, S, YUE, Y.; WANG, Y.; DIAO, Y.; CHEN, D.; ZHANG, L. Effect of GeO_2 on structure and properties of Yb: phosphate glass. **Journal of Non-Crystalline Solids**, Amsterdam, v. 520, p. 119455, 2019.

[89] SADDEEK, Y. B. ISSA, S. A. M.; GUCLU, E. E. A.; KILICOGLU, O.; SUSOY, G.; TEKIN, H. O. Alkaline phosphate glasses and synergistic impact of germanium oxide (GeO_2) additive: mechanical and nuclear radiation shielding behaviors. **Ceramics International**, Amsterdam, v. 46, n. 10, p. 16781–16797, 2020.

[90] CAO, J.; ZHANG, Z.; LI, X.; PENG, M. Abnormal NIR photoemission from bismuth doped germanophosphate photonic glasses. **Journal of Materials Chemistry C**, London, v. 7, n. 11, p. 3218–3225, 2019.

[91] MANZANI, D. GUALBERTO, T., ALMEIDA, J. M. P.; MONTESSO, M.; MENDONÇA, C. R.; RIVERA, V. A. G.; NALIN, M.; RIBEIRO, S. J. L. Highly nonlinear $Pb_2P_2O_7$-Nb_2O_5 glasses for optical fiber production. **Journal of Non-Crystalline Solids**, Amsterdam, v. 443, p. 82–90, 2016.

[92] LOPEZ-ISCOA, P. OJHA, N.; PUGLIESE, D.; MISHRA, A.; GUMENYUK, R.; BOETTI, N. G.; JANNER, D.; TROLES, J.; BUREAU, B. Design, processing, and characterization of an optical core-bioactive clad phosphate fiber for biomedical applications. **Journal of the American Ceramic Society**, Hoboken, v. 102, n. 11, p. 6882–6892, 2019.

[93] MAHANI, R.; HELMY, A. KH.; FATHI, A. M. Electrical, optical, and electrochemical performances of phosphate-glasses-doped with ZnO and CuO and their composite with polyaniline. **Scientific Reports**, London, v. 14, n. 1, p. 1169, 2024.

[94] PODRAZKÝ, O.; PETERKA, P.; PUGLIESE, D.; BOETTI, N. G.; MILANESE, D. In vivo testing of a bioresorbable phosphate-based optical fiber. **Journal of Biophotonics**, Hoboken, v. 12, n. 7, 2019.

[95] SKRUODIENE, M. KEMERE, M. GRETA INKRATAITE, G.; LEIMANE, M.; RAMANAUSKAS, R.; SKAUDZIUS, R.; SARAKOVSKIS, A. Synthesis and investigation of novel optical active SiO_2 glasses with entrapped YAG:Ce synthesized via sol–gel method. **Gels**, Basel, v. 9, n. 6, p. 488, 2023.

[96] CALDERÓN, G. L.; RIVERA, V. A. G.; MESSADDEQ, Y.; MAREGA JÚNIOR, E. Thermometry and optical study of Er^{3+}-Yb^{3+} doped tellurite glasses as a suitable candidate for optical fibre. **Journal of Alloys and Compounds**, Amsterdam, v. 948, p. 169777, 2023.

[97] YU, Y.; SHAO, G.; DING, L.; ZHANG, H.; LIANG, X.; LIU, J.; XIANG, W. Ultra-stable Eu^{3+}-doped $CsPbCl_2Br_1$ perovskite quantum dots glass for optical temperature sensing. **Journal of Rare Earths**, Amsterdam, v. 39, n. 12, p. 1497–1505, 2021.

[98] YASAKA, P.; KAEWKHAO, J. Luminescence from lanthanides-doped glasses and applications: a review. *In*: INTERNATIONAL CONFERENCE ON INSTRUMENTATION, COMMUNICATIONS, INFORMATION TECHNOLOGY, AND BIOMEDICAL ENGINEERING (ICICI-BME), 4., 2015, Bandung. **Proceedings**… Piscataway: IEEE, 2015.

[99] KIBRISLI, O.; ERSUNDU, A. E.; ERSUNDU, M. Ç. Dy^{3+} doped tellurite glasses for solid-state lighting: an investigation through physical, thermal, structural and optical spectroscopy studies. **Journal of Non-Crystalline Solids**, Amsterdam, v. 513, p. 125–136, 2019.

[100]LIANG, X.; YANG, Y.; ZHU, C.; YUAN, S.; CHEN, G.; PRING, A.; XIA, F. Luminescence properties of Tb^{3+}–Sm^{3+} codoped glasses for white light emitting diodes. **Applied Physics Letters**, New York, v. 91, n. 9, p. 1–4, 2007.

[101]SHANG, M.; LI, C.; LIN, J. How to produce white light in a single-phase host? **Chemical Society Reviews**, London, v. 43, n. 5, p. 1372–1386, 2014.

[102]FAN, X.; SI, J.; XU, M.; LI, G.; TANG, J.; CAI, G. Photoluminescence and energy transfer of efficient and thermally stable white-emitting $Ca_9La(PO_4)_7$:Ce^{3+}, Tb^{3+}, Mn^{2+} phosphors. **Ceramics International**, Amsterdam, v. 47, n. 9, p. 12056–12065, 2021.

[103]RAHMAN, J. U.; KHAN, S.; JAIN, V.; RAJIV, A.; DASI, S.; FAWY, K. F.; JINDAL, P. K.; SIVARANJANI, R. Exploring inorganic phosphors: basics, types, fabrications and their luminescence properties for LED/WLED/displays. **Reviews in Inorganic Chemistry**, Berlin, 2024

[104]CHUNG, W. J.; NAM, Y. H. Review - a review on phosphor in glass as a high power LED color converter. **ECS Journal of Solid State Science and Technology**, Pennington, v. 9, n. 1, p. 016010, 2020.

[105]CHEN, D.; ZHONG, J.; YU, H.; DING, M.; LU, H.; JI, Z.; XIANG, W.; LIANG, X. Advances in transparent glass–ceramic phosphors for white light-emitting diodes - a review. **Journal of the European Ceramic Society**, Amsterdam, v. 35, n. 3, p. 859–869, 2015.

[106]LINGANNA, K.; RAO, CH. S.; JAYASANKAR, C. K. Optical properties and generation of white light in Dy^{3+}-doped lead phosphate glasses. **Journal of Quantitative Spectroscopy and Radiative Transfer**, Amsterdam, v. 118, p. 40–48, 2013.

[107]NEXHA, A.; CARVAJAL, J. J.; PUJOL, M. C.; DÍAZ, F.; AGUILÓ, M. Lanthanide doped luminescence nanothermometers in the biological windows: strategies and applications. **Nanoscale**, London, v. 13, n. 17, p. 7913–7987, 2021.

[108]YANG, W.; LI, X.; CHI, D.; ZHANG, H.; LIU, X. Lanthanide-doped upconversion materials: emerging applications for photovoltaics and photocatalysis. **Nanotechnology**, Bristol, v. 25, n. 48, p. 482001, 2014.

[109]WANG, W. C.; ZHOU, B.; XU, S. H.; YANG, Z. M.; ZHANG, Q. Y. Recent advances in soft optical glass fiber and fiber lasers. **Progress in Materials Science**, Amsterdam, v. 101, p. 90–171, 2019.

[110]ZHOU, J.; TENG, Y.; ZHOU, S.; QIU, J. Quantum cutting in luminescent glasses and glass ceramics. **International Journal of Applied Glass Science**, Hoboken, v. 3, n. 4, p. 299–308, 2012.

[111]PIPER, W. W.; DELUCA, J. A.; HAM, F. S. Cascade fluorescent decay in Pr^{3+}-doped fluorides: achievement of a quantum yield greater than unity for emission of visible light. **Journal of Luminescence**, Amsterdam, v. 8, n. 4, p. 344–348, 1974.

[112]AUZEL, F. History of upconversion discovery and its evolution. **Journal of Luminescence**, Amsterdam, v. 223, p. 116900, 2020.

[113]JOUBERT, M. F. Photon avalanche upconversion in rare earth laser materials. **Optical Materials**, Amsterdam, v. 11, n. 2–3, p. 181–203, 1999.

[114]GOUVEIA, E. A.; ARAUJO, M. T.; GOUVEIA-NETO, A. S. Thermal effects on light emission in Yb^{3+}-sensitized rare-earth doped optical glasses. **Brazilian Journal of Physics**, São Paulo, v. 31, n. 1, p. 89–101, 2001.

[115]TALEWAR, R. A.; MAHAMUDA, S.; SWAPNA, K.; VENKATESWARLU, M.; RAO, A. S. Sensitization of Er^{3+} NIR emission using Yb^{3+} ions in alkaline-earth chloro borate glasses for fiber laser and optical fiber amplifier applications. **Materials Research Bulletin**, Amsterdam, v. 136, p. 111144, 2021.

[116]DEVARAJULU, G.; KUMAR, B. K.; BABU, P. R.; DHANANJAYA, M.; BAK, N.; PASUPULETI, K. S.; RAJU, B. D. P.; KIM, M. Sensitization effect of Nd^{3+} ions on Yb^{3+}/Nd^{3+} co-doped oxyfluoride glasses and study of their optical, fluorescence, and upconversion abilities for visible laser and NIR amplifier applications. **Ceramics International**, Amsterdam, v. 48, n. 17, p. 24550–24559, 2022.

[117]YUAN, J.; ZHENG, G.; YE, Y.; CHEN, Y.; DENG, T.; XIAO, P.; YE, Y.; WANG, W. Enhanced 1.5 μm emission from Yb^{3+}/Er^{3+} codoped tungsten tellurite glasses for broadband near-infrared optical fiber amplifiers and tunable fiber lasers. **RSC Advances**, London, v. 11, n. 45, p. 27992–27999, 2021.

[118]YANG, J.; DAI, N.; DAI, S.; WEN, L.; HU, L.; JIANG, Z. Enhancement of upconversion luminescence in Er^{3+} doped tellurite glasses due to the introduction of $PbCl_2$. **Chemical Physics Letters**, Amsterdam, v. 376, n. 5–6, p. 671–675, 2003.

[119]DUBEY, A.; SONI, A. K.; KUMARI, A.; DEY, R.; RAI, V. K. Enhanced green upconversion emission in $NaYF_4$:$Er^{3+}/Yb^{3+}/Li^{+}$ phosphors for optical thermometry. **Journal of Alloys and Compounds**, Amsterdam, v. 693, p. 194–200, 2017.

[120]ZHAO, Z.; ZHANG, B.; GONG, Y.; REN, Y.; HUO, M.; WANG, Y. Concentration effect of Yb^{3+} ions on the spectroscopic properties of high-concentration Er^{3+}/Yb^{3+} co-doped phosphate glasses. **Journal of Molecular Structure**, Amsterdam, v. 1216, p. 128322, 2020.

[121]MANZANI, D.; FERRARI, J. L.; POLACHINI, F. C.; MESSADDEQ, Y.; RIBEIRO, S. J. L. 1.5 μm and visible up-conversion emissions in Er^{3+}/Yb^{3+} co-doped tellurite glasses and optical fibers for photonic applications. **Journal of Materials Chemistry**, London, v. 22, n. 32, p. 16540, 2012.

[122]BAO, R.; YU, L.; YE, L.; ZHANG, X.; WANG, L. G. Compact and sensitive Er^{3+}/Yb^{3+} co-doped YAG single crystal optical fiber thermometry based on up-conversion luminescence. **Sensors and Actuators A:** physical, Amsterdam, v. 269, p. 182–187, 2018.

[123]YANG, Y.; CHU, Y.; CHEN, Z.; MA, Y.; LIAO, L.; LI, H.; PENG, J.; DAI, N.; LI, J.; YANG, L. Blue upconversion luminescence for Yb^{3+}/Tm^{3+} co-doped borosilicate glasses. **Journal of Luminescence**, Amsterdam, v. 195, p. 247–251, 2018.

[124]PISARSKA, J.; LISIECKI, R.; RYBA-ROMANOWSKI, W.; DOMINIAK-DZIK, G.; PISARSKI, W. A. Up-converted luminescence in Yb–Tm co-doped lead fluoroborate glasses. **Journal of Alloys and Compounds**, Amsterdam, v. 451, n. 1–2, p. 226–228, 2008.

[125]WATEKAR, P. R.; JU, S.; BOO, S.; HAN, W. T. Linear and non-linear optical properties of Yb^{3+}/Tm^{3+} co-doped alumino-silicate glass prepared by sol–gel method. **Journal of Non-Crystalline Solids**, Amsterdam, v. 351, n. 30–32, p. 2446–2452, 2005.

[126]RAKOV, N.; MACIEL, G. S.; SUNDHEIMER, M. L.; MENEZES, L. S.; GOMES, A. S. L.; MESSADDEQ, Y.; CASSANJES, F. C.; POIRIER, G.; RIBEIRO, S. J. L. Blue upconversion enhancement by a factor of 200 in Tm^{3+}-doped tellurite glass by codoping with Nd^{3+} ions. **Journal of Applied Physics**, New York, v. 92, n. 10, p. 6337–6339, 2002.

[127]TINSLEY, J. N.; BANDARUPALLY, S.; PENTTINEN, J. P.; MANZOOR, S.; RANTA, S.; SALVI, L.; GUINA, M.; POLI, N. Watt-level blue light for precision spectroscopy, laser cooling and trapping of strontium and cadmium atoms. **Optics Express**, Washington, v. 29, n. 16, p. 25462, 2021.

[128]SOUSA, V.; GOMES, A. T. P. C.; FREITAS, A.; FAUSTINO, M. A. F.; NEVES, M. G. P. M. S.; ALMEIDA, A. Photodynamic inactivation of Candida albicans in blood plasma and whole blood. **Antibiotics**, Basel, v. 8, n. 4, p. 221, 2019.

[129]KAO, C. K. Optical fiber research present and future. **Applied Scientific Research**, v. 41, n. 3–4, p. 177–189, 1984.

[130]DAVIS, C.; MURPHY, T. Fiber-Optic Communications [In the Spotlight]. **IEEE Signal Processing Magazine**, v. 28, n. 4, p. 152–150, jul. 2011.

[131]JEWELL, J. M.; WILLIAMS, G. M.; JAGANATHAN, J.; AGGARWAL, I. D.; GREASON, P. Separation of intrinsic and extrinsic optical absorption in a fluoride glass. **Applied Physics Letters**, New York, v. 59, n. 1, p. 1–3, 1991.

[132]DING, M.; FAN, D.; WANG, W.; LUO, Y.; PENG, G. D. Basics of Optical Fiber Measurements. *In*: **Handbook of Optical Fibers**. Singapore: Springer Singapore, 2018. p. 1–39.

[133]DRIVER, R. D.; LESKOWITZ, G. M.; CURTISS, L. E. Applications of IR-transmitting optical fiber in the chemical industry. *In*: HARRINGTON, J. A.; KATZIR, A. (eds.). **Infrared fiber optics II**. Bellingham: SPIE, 1990. P. 233-245. (SPIE proceedings series, 1228).

[134]TAI, H.; YOSHINO, T.; TANAKA, H. Fiber-optic evanescent-wave methane-gas sensor using optical absorption for the 3.392-μm line of a He–Ne laser. **Optics Letters**, Washington, v. 12, n. 6, p. 437, 1987.

[135]WAECHTER, H.; LITMAN, J.; CHEUNG, A. H.; BARNES, J. A.; LOOCK, H. P. Chemical sensing using fiber cavity ring-down spectroscopy. **Sensors**, Basel, v. 10, n. 3, p. 1716–1742, 2010.

[136]DING, L.; RUAN, Y.; LI, T.; HUANG, J.; WARREN-SMITH, S. C.; EBENDORFF-HEIDEPRIEM, H.; MONRO, T. M. Nitric oxide optical fiber sensor based on exposed core fibers and CdTe/CdS quantum dots. **Sensors and Actuators B:** chemical, Amsterdam, v. 273, p. 9–17, 2018.

[137]DEL VILLAR, I.; ZAMARREÑO, C. R.; HERNAEZ, M.; ARREGUI, F. J.; MATIAS, I. R. Resonances in coated long period fiber gratings and cladding removed multimode optical fibers: a comparative study. **Optics Express**, Washington, v. 18, n. 19, p. 20183, 2010.

[138]PRAKASHAN, V. P.; GEORGE, G.; SANU, M. S.; SAJNA, M. S.; SARITHA, A. C.; SUDARSANAKUMAR, C.; BIJU, P. R.; JOSEPH, C.; UNNIKRISHNAN, N. V. Investigations on SPR induced Cu@Ag core shell doped SiO_2-TiO_2-ZrO_2 fiber optic sensor for mercury detection. **Applied Surface Science**, Amsterdam, v. 507, p. 144957, 2020.

[139]BATTEN, S. R.; CHAMPNESS, N. R.; CHEN, X. M.; GARCIA-MARTINEZ, J.; KITAGAWA, S.; ÖHRSTRÖM, L.; O'KEEFFE, M.; SUH, M. P.; REEDIJK, J. Terminology of metal–organic frameworks and coordination polymers (IUPAC Recommendations 2013). **Pure and Applied Chemistry**, Berlin, v. 85, n. 8, p. 1715–1724, 2013.

[140]LIU, J.-Q.; LUO, Z.-D.; PAN, Y.; SINGH, A. K.; TRIVEDI, M.; KUMAR, A. Recent developments in luminescent coordination polymers: designing strategies, sensing application and theoretical evidences. **Coordination Chemistry Reviews**, Amsterdam, v. 406, p. 213145, 2020.

[141]O'KEEFFE, M.; YAGHI, O. M. Deconstructing the crystal structures of metal–organic frameworks and related materials into their underlying nets. **Chemical Reviews**, Washington, v. 112, n. 2, p. 675–702, 2012.

[142]XUE, D.-X.; BELMABKHOUT, Y.; SHEKHAH, O.; JIANG, H.; ADIL, K.; CAIRNS, A. J.; EDDAOUDI, M. Tunable rare earth fcu-MOF platform: access to adsorption kinetics driven gas/vapor separations via pore size contraction. **Journal of the American Chemical Society**, Washington, v. 137, n. 15, p. 5034–5040, 2015.

[143]MURRAY, L. J.; DINCĂ, M.; LONG, J. R. Hydrogen storage in metal–organic frameworks. **Chemical Society Reviews**, London, v. 38, n. 5, p. 1294, 2009.

[144]YANG, D.; GATES, B. C. Catalysis by metal organic frameworks: perspective and suggestions for future research. **ACS Catalysis**, Washington, v. 9, n. 3, p. 1779–1798, 2019.

[145]OTAKE, K.; CUI, Y.; BURU, C. T.; LI, Z.; HUPP, J. T.; FARHA, O. K. Single-atom-based vanadium oxide catalysts supported on metal–organic frameworks: selective alcohol oxidation and structure–activity relationship. **Journal of the American Chemical Society**, Washington, v. 140, n. 28, p. 8652–8656, 2018.

[146]KRENO, L. E.; LEONG, K.; FARHA, O. K.; ALLENDORF, M.; VAN DUYNE, R. P.; HUPP, J. T. Metal–organic framework materials as chemical sensors. **Chemical Reviews**, Washington, v. 112, n. 2, p. 1105–1125, 2012.

[147]TU, D.; ZHENG, W.; LIU, Y.; ZHU, H.; CHEN, X. Luminescent biodetection based on lanthanide-doped inorganic nanoprobes. **Coordination Chemistry Reviews**, Amsterdam, v. 273–274, p. 13–29, 2014.

[148]ZHANG, X.; WANG, W.; HU, Z.; WANG, G.; UVDAL, K. Coordination polymers for energy transfer: preparations, properties, sensing applications, and perspectives. **Coordination Chemistry Reviews**, Amsterdam, v. 284, p. 206–235, 2015.

[149]ORELLANA-TAVRA, C.; MARSHALL, R. J.; BAXTER, E. F.; ABÁNADES LÁZARO, I.; TAO, A.; CHEETHAM, A. K.; FORGAN, R. S.; FAIREN-JIMENEZ, D. Drug delivery and controlled release from biocompatible metal–organic frameworks using mechanical amorphization. **Journal of Materials Chemistry B**, London, v. 4, n. 47, p. 7697–7707, 2016.

[150]BEGUM, S.; HASSAN, Z.; BRÄSE, S.; WÖLL, C.; TSOTSALAS, M. Metal–organic framework-templated biomaterials: recent progress in synthesis, functionalization, and applications. **Accounts of Chemical Research**, Washington, v. 52, n. 6, p. 1598–1610, 2019.

[151]CUI, Y.; LI, B.; HE, H.; ZHOU, W.; CHEN, B.; QIAN, G. Metal–organic frameworks as platforms for functional materials. **Accounts of Chemical Research**, Washington, v. 49, n. 3, p. 483–493, 2016.

[152]TU, D.; ZHENG, W.; HUANG, P.; CHEN, X. Europium-activated luminescent nanoprobes: from fundamentals to bioapplications. **Coordination Chemistry Reviews**, Amsterdam, v. 378, p. 104–120, 2019.

[153]GORAI, T.; SCHMITT, W.; GUNNLAUGSSON, T. Highlights of the development and application of luminescent lanthanide based coordination polymers, MOFs and functional nanomaterials. **Dalton Transactions**, London, v. 50, n. 3, p. 770–784, 2021.

[154]SUGIMOTO, S.; OHTSU, H.; TSUGE, K. Luminescent mixed-ligand iodido copper(I) coordination polymers having antenna effect. **Journal of Photochemistry and Photobiology A:** chemistry, Amsterdam, v. 353, p. 602–611, 2018.

[155]LIAN, C.; CHEN, Y.; LI, S.; HAO, M.; GAO, F.; YANG, L. Synthesis and characterization of lanthanide-based coordination polymers for highly selective and sensitive luminescent sensor for Pb^{2+} over mixed metal ions. **Journal of Alloys and Compounds**, Amsterdam, v. 702, p. 303–308, 2017.

[156]HUANG, L.; YU, K.; ZHOU, W.; TENG, Q.; WANG, Z.; DAI, Z. Quantitative principal component analysis of multiple metal ions with lanthanide coordination polymer networks. **Sensors and Actuators B:** chemical, Amsterdam, v. 346, p. 130469, 2021.

[157]WANG, Y.-M.; XU, Y.; YANG, Z. R.; ZHANG, X.; HU, Y.; YANG, R. Multi-functional lanthanide coordination polymers for multi-modal detection of nitroaromatics and trace water in organic solvents. **Journal of Colloid and Interface Science**, Amsterdam, v. 598, p. 474–482, 2021.

[158]WANG, H.; QIN, J.; HUANG, C.; HAN, Y.; XU, W.; HOU, H. Mono/bimetallic water-stable lanthanide coordination polymers as luminescent probes for detecting cations, anions and

organic solvent molecules. **Dalton Transactions**, London, v. 45, n. 32, p. 12710–12716, 2016.

[159]BHAT, S. A.; YELAMAGGAD, C. V. The fluorometric detection of explosives: an application of photoluminiscent coordination polymers. **ACS Applied Polymer Materials**, Washington, v. 4, n. 10, p. 7126–7134, 2022.

[160]SONG, X.-Q.; ZHANG, M.; WANG, C.; SHAMSHOOMA, A. A. A.; MENG, H. H.; XI, W. Mixed lanthanide coordination polymers for temperature sensing and enhanced Nd^{3+} NIR luminescence. **Journal of Luminescence**, Amsterdam, v. 201, p. 410–418, 2018.

[161]YAGHI, O. M. Reticular chemistry in all dimensions. **ACS Central Science**, Washington, v. 5, n. 8, p. 1295–1300, 2019.

[162]KONDO, M.; YOSHITOMI, T.; MATSUZAKA, H.; KITAGAWA, S.; SEKI, K. Three-dimensional framework with channeling cavities for small molecules: $\{M_2(4, 4'\text{-bpy})_3(NO_3)_4 \cdot xH_2O\}_n$ (M = Co, Ni, Zn). **Angewandte Chemie International Edition in English**, Weinheim, v. 36, n. 16, p. 1725–1727, 1997.

[163]SARACI, F.; QUEZADA-NOVOA, V.; DONNARUMMA, P. R.; HOWARTH, A. J. Rare-earth metal–organic frameworks: from structure to applications. **Chemical Society Reviews**, London, v. 49, n. 22, p. 7949–7977, 2020.

[164]O'KEEFFE, M.; PESKOV, M. A.; RAMSDEN, S. J.; YAGHI, O. M. The Reticular Chemistry Structure Resource (RCSR) database of, and symbols for, crystal nets. **Accounts of Chemical Research**, Washington, v. 41, n. 12, p. 1782–1789, 2008.

[165]LIU, J.; CHEN, L.; CUI, H.; ZHANG, J.; ZHANG, L.; SU, C. Y. Applications of metal–organic frameworks in heterogeneous supramolecular catalysis. **Chemical Society Reviews**, London, v. 43, n. 16, p. 6011–6061, 2014.

[166]FORDHAM, S.; WANG, X.; BOSCH, M.; ZHOU, H. C. Lanthanide metal-organic frameworks: syntheses, properties, and potential applications. In: CHENG, P. (ed.). **Lanthanide metal-organic frameworks**. Berlin: Springer, 2014. p. 1–27.

[167]GHASEMPOUR, H.; WANG, K. Y.; POWELL, J. A.; ZAREKARIZI, F.; LV, X. L.; MORSALI, A.; ZHOU, H. C. Metal–organic frameworks based on multicarboxylate linkers. **Coordination Chemistry Reviews**, Amsterdam, v. 426, p. 213542, 2021.

[168]YANG, D.; CHEN, Y.; SU, Z.; ZHANG, X.; ZHANG, W.; SRINIVAS, K. Organic carboxylate-based MOFs and derivatives for electrocatalytic water oxidation. **Coordination Chemistry Reviews**, Amsterdam, v. 428, p. 213619, 2021.

[169]PANYARAT, K.; SURINWONG, S.; PRIOR, T. J.; KONNO, T.; RUJIWATRA, A. Crystal structures and gas adsorption behavior of new lanthanide-benzene-1,4-dicarboxylate frameworks. **Microporous and Mesoporous Materials**, Amsterdam, v. 251, p. 155–164, 2017.

[170]FENG, H.-J.; XU, L.; LIU, B.; JIAO, H. Europium metal–organic frameworks as recyclable and selective turn-off fluorescent sensors for aniline detection. **Dalton Transactions**, London, v. 45, n. 43, p. 17392–17400, 2016.

[171]ZHANG, X.; KANG, X.; CUI, W.; ZHANG, Q.; ZHENG, Z.; CUI, X. Floral and lamellar europium(III)-based metal–organic frameworks as high sensitivity luminescence sensors for acetone. **New Journal of Chemistry**, London, v. 43, n. 21, p. 8363–8369, 2019.

[172]SUN, J.; ZHANG, P.; YAN, K.; PAN, A.; CHEN, F.; HONG, J.; ZHAO, C.; CHEN, X.; XIONG, W. Europium/1,3,5-benzenetricarboxylic acid metal–organic framework nanorods decorated with CdSe quantum dots as coatings for noncontact ratiometric optical temperature sensing. **ACS Applied Nano Materials**, Washington, v. 6, n. 13, p. 12087–12094, 2023.

[173]WU, S.; LIN, Y.; LIU, J.; SHI, W.; YANG, G.; CHENG, P. Rapid detection of the biomarkers for carcinoid tumors by a water stable luminescent lanthanide metal–organic framework sensor. **Advanced Functional Materials**, Weinheim, v. 28, n. 17, 2018.

[174]YU, L.; CHEN, H.; YUE, J.; CHEN, X.; SUN, M.; HOU, J.; ALAMRY, K. A.; MARWANI, H. M.; WANG, X.; WANG, S. Europium metal-organic framework for selective and sensitive detection of doxycycline based on fluorescence enhancement. **Talanta**, Amsterdam, v. 207, p. 120297, 2020.

[175]LIU, K.; YOU, H.; ZHENG, Y.; JIA, G.; ZHANG, L.; HUANG, Y.; YANG, M.; SONG, Y.; ZHANG, H. Facile shape-controlled synthesis of luminescent europium benzene-1,3,5-tricarboxylate architectures at room temperature. **CrystEngComm**, Cambridge, v. 11, n. 12, p. 2622, 2009.

[176]ACAR, Y. Photoluminescence properties of Gd(III) and Ce(III) lanthanide based metal organic frameworks. **Anadolu University Journal of Science and Technology A -** applied sciences and engineering, Eskisehir, v. 17, n. AFG5 special issue, p. 754, 2016.

[177]AMIAUD, T.; JUBERA, V.; SERIER-BRAULT, H. A new highly sensitive cryogenic luminescent MOF thermometer built with pyromellitic acid. **Journal of Materials Chemistry C**, London, v. 11, n. 32, p. 10951–10956, 2023.

[178]AMIAUD, T.; STEPANT, N.; DESSAPT, R.; SERIER-BRAULT, H. Microwave-assisted synthesis of anhydrous lanthanide-based coordination polymers built upon benzene-1,2,4,5-tetracarboxylic acid. **Polyhedron**, Amsterdam, v. 204, p. 115261, 2021.

[179]LAHOUD, M. G.; FREM, R. C. G.; MARQUES, L. F.; ARROYOS, G.; BRANDÃO, P.; FERREIRA, R. A. S.; CARLOS, L. D. A novel near monochromatic red emissive europium(III) metal-organic framework based on 1,2,4,5-benzenetetracarboxylate: from synthesis to photoluminescence studies. **Journal of Solid State Chemistry**, Amsterdam, v. 253, p. 176–183, 2017.

[180]ZHANG, R.; ZHU, L.; YUE, B. Luminescent properties and recent progress in applications of lanthanide metal-organic frameworks. **Chinese Chemical Letters**, Beijing, v. 34, n. 2, p. 108009, 2023.

[181] BINNEMANS, K. Lanthanide-based luminescent hybrid materials. **Chemical Reviews**, Washington, v. 109, n. 9, p. 4283–4374, 2009.

[182] MEYER, L. V.; SCHÖNFELD, F.; MÜLLER-BUSCHBAUM, K. Lanthanide based tuning of luminescence in MOFs and dense frameworks – from mono- and multimetal systems to sensors and films. **Chemical Communications**, London, v. 50, n. 60, p. 8093, 2014.

[183] GONZÁLEZ, J.; SEVILLA, P.; GABARRÓ-RIERA, G.; JOVER, J.; ECHEVERRÍA, J.; FUERTES, S.; ARAUZO, A.; BARTOLOMÉ, E.; SAÑUDO, E. C. A Multifunctional dysprosium-carboxylato 2D metal–organic framework. **Angewandte Chemie International Edition**, Weinheim, v. 60, n. 21, p. 12001–12006, 2021.

[184] ZHAO, Y.; LI, D. Lanthanide-functionalized metal–organic frameworks as ratiometric luminescent sensors. **Journal of Materials Chemistry C**, London, v. 8, n. 37, p. 12739–12754, 2020.

[185] STEEMERS, F. J.; VERBOOM, W.; REINHOUDT, D. N.; VAN DER TOL, E. B.; VERHOEVEN, J. W. New Sensitizer-modified calix4arenes enabling near-UV excitation of complexed luminescent lanthanide ions. **Journal of the American Chemical Society**, Washington, v. 117, n. 37, p. 9408–9414, 1995.

[186] LIU, J.-Q.; LUO, Z. D.; PAN, Y.; SINGH, A. K.; TRIVEDI, M.; KUMAR, A. Recent developments in luminescent coordination polymers: designing strategies, sensing application and theoretical evidences. **Coordination Chemistry Reviews**, Amsterdam, v. 406, p. 213145, 2020.

[187] PRAMANIK, S.; ZHENG, C.; ZHANG, X.; EMGE, T. J.; LI, J. New microporous metal−organic framework demonstrating unique selectivity for detection of high explosives and aromatic compounds. **Journal of the American Chemical Society**, Washington, v. 133, n. 12, p. 4153–4155, 2011.

[188] YANG, X.; CHEN, X.; HOU, G. H.; GUAN, R. F.; SHAO, R.; XIE, M. H. A Multiresponsive metal–organic framework: direct chemiluminescence, photoluminescence, and dual tunable sensing applications. **Advanced Functional Materials**, Weinheim, v. 26, n. 3, p. 393–398, 2016.

[189] ZHAO, S.-N.; WANG, G.; POELMAN, D.; DE VOORT, P. Luminescent lanthanide MOFs: a unique platform for chemical sensing. **Materials**, Basel, v. 11, n. 4, p. 572, 2018.

[190] WADE, C. R.; LI, M.; DINCĂ, M. Facile deposition of multicolored electrochromic metal-organic framework thin films. **Angewandte Chemie International Edition**, Weinheim, v. 52, n. 50, p. 13377–13381, 2013.

CHAPTER II:

Research project and scientific goals

1. Proposal and objectives

The research project aims to develop innovative optically active materials and optical fiber-based sensors for detection of environmentally, industrially, and medically relevant analytes. By utilizing oxide glass matrices, such as tellurite and phosphate glasses, the project seeks to exploit the unique optical properties of these materials, including their broad transmission windows (from UV to mid-IR), low characteristic temperatures, high refractive indices, and their capability to dissolve rare earth ions effectively.

A key aspect of the project is the systematic characterization of the glass matrices using techniques such as X-ray diffraction (XRD), differential scanning calorimetry (DSC), Fourier-transform infrared spectroscopy (FT-IR), absorption spectroscopy, Raman spectroscopy, solid-state nuclear magnetic resonance (NMR), and refractive index measurements. These techniques provide comprehensive insights into the optical, thermal, and structural properties of the glasses, enabling the evaluation of their suitability for optical fiber drawing, which is critical for their potential use in various technological applications.

The fabrication process begins with characterized glass materials, which are processed in a fiber-pulling tower to create core-shell fibers with diameters ranging from 125 μm to 1 mm. A key performance metric in this stage is optical loss characterization, which evaluates the fiber's ability to guide light across different wavelengths. This process will also explore optically active fibers, which are crucial for applications like optical amplifiers and sensors.

In the development of new chemical sensors, the project focuses on modifying and functionalizing the surfaces of the glass and fibers with luminescent coordination polymers (CPs), particularly lanthanide-based metal-organic frameworks (Ln-MOFs). This functionalization allows enhanced interaction between the chemosensor and analytes within the sensor region, leading to improved chemical sensing through luminescence measurements.

The main goal of this project is to develop new remote optical sensors by investigating the luminescent properties of optically active glass materials and composites. This objective will be achieved by focusing on the following specific aims:

1. Conducting a systematic study of oxide glass matrices, mainly those based on tellurite and phosphate glasses, combined with other network modifiers, such as Na_2O, ZnO, ZnF_2, GeO_2, and Al_2O_3, to evaluate their suitability for optical fiber production. These studies will focus on the thermal, optical, and structural properties of the glasses, aiming

to produce fibers with effective light guidance in the visible and near-IR regions. Additionally, optically active glasses from these matrices will be studied to assess dopant solubility and luminescence efficiency.

2. Fabricating optical fibers with different diameters and compositions to optimize light guidance in the visible and near-IR regions.

3. Modifying the surfaces of the glasses and fibers' tips to promote the *in situ* growth of Ln-CPs, followed by analysis of their structural, morphological, and luminescent properties. The luminescence behavior is monitored upon exposure to various organic analytes to evaluate their potential for chemical sensing via the "antenna effect."

4. Developing methods for detecting, monitoring, and quantifying relevant analytes using glass@Ln-CPs composites and fiber-based optical sensors. The analytes of interest include carbonyl compounds such as acetone and 2-pentanone, which are commonly considered biomarkers for several diseases.

By achieving these objectives, the project will contribute to the advancement of fiber-optic technology and luminescent sensing applications, positioning these devices for widespread use in remote sensing and optical detection systems. This project has the potential to drive significant advancements in the field of photonic materials, contributing to the scientific and technological progress of glass science and optical sensors. By integrating advanced glass matrices with luminescent coordination polymers (Ln-CPs), the research seeks to expand the frontiers of optical fiber technology, creating a new class of highly sensitive, selective, and remote sensors.

2. Work Plan and Execution Schedule

The execution schedule of the research project, for a period of 48 months, is presented according to the work timeline in the Table II.1.

Table II.1 - Schedule of activities conducted during the PhD. Periods highlighted in yellow correspond to work performed at LaMIV/IQSC-USP, in blue at ICB/uB, and in purple at GSOLFA/UCM.

Main activities	Semesters							
	1	**2**	**3**	**4**	**5**	**6**	**7**	**8**
Literature review update	X	X	X	X	X	X	X	X
Synthesis and characterization of glasses	X	X	X	X	X			
In situ growth of Ln-CPs on glass substrates		X	X	X	X	X	X	
Synthesis of preforms for optical fibers					X	X		
Production and characterization of optical fibers					X	X		
Coating of Ln-CPs on fiber tips and luminescence measurements					X	X	X	
Sensing tests on bulk samples				X			X	
Sensing tests on coated optical fibers							X	
Writing of scientific articles		X	X	X		X	X	
Writing of doctoral thesis				X				X

The work was conducted across three different laboratories in different countries. The initial two years of the project were carried out at the Laboratory of Inorganic and Glass Materials (LaMIV) at IQSC-USP. During this period, the focus was on studying various glass matrices, performing general characterizations, and producing optically active glasses. The next phase took place at the Laboratory Interdisciplinary Carnot de Bourgogne (ICB), at uB, where the previously studied glass compositions were used to manufacture single-index optical fibers. This 12-month period concentrated on the optical characterization of the fibers, including studies on optically active fibers and the application of luminescent coatings at the tips of these waveguides. Subsequently, the final phase involved a research internship at the Chemical Optosensors and Applied Photochemistry Group (GSOLFA) at Universidad Complutense de Madrid, under the supervision of Prof. Guillermo Orellana. This stage focused on applying the developed composite materials as chemical sensors for small organic molecules. After completing the experimental work over seven semesters, the final months were dedicated to preparing the thesis manuscript.

3. Dissemination of results

The results obtained throughout this PhD project have been organized into five distinct manuscripts. Of these, four have already been published in scientific journals, and the final

manuscript is in the last stages of preparation for submission. These manuscripts form the basis of the following five chapters of this thesis and can be grouped and interrelated as follows:

a. Systematic studies on TeO_2-based glasses

This section focuses on the synthesis and comprehensive characterization of new glass matrices containing TeO_2 as the major component. Two distinct studies, presented in Chapters III and IV, systematically analyze the structural, thermal, and optical properties of different subclasses of tellurite glasses. The goal of these studies is to evaluate the suitability of these glass systems for use as substrates for luminescent films and optical fiber applications. A brief summary of each chapter is provided below:

- **Chapter III:** *Synthesis and structural characterization of a new fluorophosphotellurite glass system* - Ternary systems composed of fluorophosphotellurite glasses were synthesized by combining TeO_2, $NaPO_3$, and NaF to form two different series of compositions. The samples were analyzed using advanced techniques such as solid-state NMR and Raman spectroscopy, which enabled the proposal of a structural model for this glass system. Additionally, thermal and optical characterizations provided a comprehensive understanding of how the properties varied with composition. This allowed for the identification of compositions with high potential for photonics applications.

- **Chapter IV:** *Exploring the influence of ZnF_2 on zinc-tellurite glass: unveiling changes in oh content, structure, and optical properties* - This chapter explores zinc-tellurite glasses modified by adding ZnF_2 to achieve a wider transparency window, extending from UV to mid-IR. The various compositions were characterized in terms of their structural, thermal, and optical properties, with the addition of small amounts of Eu^{3+} as a structural probe. As a result, stable zinc-tellurite glasses were obtained, showing an absorption edge shifted to shorter wavelengths and a significant reduction in hydroxyl content in the matrix. In addition, these matrices presented high potential for fiber drawing and optical fibers were produced and optically characterized, as presented at the supplementary section of this chapter.

b. Optically active phosphate glasses

Chapters V and VI explore optically active glasses containing RE^{3+}, materials of great interest for various multifunctional applications. Different families of phosphate glasses were used as host materials for luminescent dopants. These glasses had previously been reported in the literature, and the impact of dopants on the structure and properties of the original undoped matrices was also evaluated. Additionally, optically active optical fibers were produced and analyzed for their optical and luminescent properties, aligned with the specific objectives described in Section 1 of this chapter. These two chapters can be summarized as follows:

- **Chapter V:** *Effect of silver nanoparticles on the visible upconversion emission of Er^{3+}/Yb^{3+} co-doped $SbPO_4$-GeO_2 glasses* – This chapter investigates the influence of silver nanoparticles (Ag-NPs) on the visible upconversion emission in Er^{3+}/Yb^{3+}-co-doped $SbPO_4$-GeO_2 glasses. Controlled heat treatment was employed to obtain and regulate the size of the nanoparticles, and their effect on Er^{3+} emission was analyzed, revealing a significant enhancement in luminescence. Complementary characterizations provided insights into how the glass properties changed with the addition of dopants. The study highlights that these optically active germanium-phosphate glasses have great potential for applications in data storage and solid-state light-emitting devices.

- **Chapter VI:** *Blue upconversion emission of $Nd^{3+}/Tm^{3+}/Yb^{3+}$ triply doped aluminophosphate optical fibers* - This chapter focuses on the development of optically active optical fibers, capitalizing on the intrinsic properties of aluminophosphate glasses. These glasses exhibit good transparency in the UV-visible region, high RE^{3+} solubility, and excellent fiber-drawing capability. Various doped glass bulks were synthesized, and their photoluminescence behavior was evaluated. Subsequently, triply doped optical fibers were produced, and blue upconversion was measured through the fiber, demonstrating the strong potential of these materials for fiber-based photonic applications.

c. Luminescent composites for chemical sensing

To achieve the scientific goals outlined in the project, this section shifts its focus to the development and application of luminescent composites for chemical sensing, specifically using lanthanide coordination polymers (Ln-CPs) as active sensing materials. This chapter presents a study on the *in situ* growth of Ln-CPs on oxide glasses and optical fibers from the

previous chapters, selecting those with appropriate optical properties and evaluating their substrate adhesion. Given the thermal stability of the studied matrices, zinc-tellurite and aluminum-phosphate glasses, as reported in Chapters VI and VII, were chosen as substrates for the *in situ* growth of Ln-CPs, as well as their respective optical fibers. Thus, Chapter VII introduces the synthesis of new glass@Ln-CP composites aimed at enhancing the performance of optical sensors in the detection of chemical analytes, highlighting their potential for advanced chemical sensing applications.

- **Chapter VII:** *In situ Growth of Lanthanide Coordination Polymers on Oxide Glass and Optical Fibers: A Promising Material for Chemical Sensing* - In this chapter, the synthesis and coating process of Ln-CPs directly onto tellurite and phosphate glass substrates are detailed. By employing polycarboxylic acids as ligands in the CPs, luminescent films with strong adhesion to the glass surfaces were achieved. The optical fibers coated with these Ln-CPs displayed remarkable potential for use in remote sensing applications. The sensitivity of these coatings was particularly notable when exposed to carbonyl organic compounds, where a significant luminescent response was observed even at low concentrations, demonstrating their efficacy in chemical sensing.

CHAPTER III:

Synthesis and structural characterization of a new fluorophosphotellurite glass system

Reprinted with permission from R. G. Capelo, J. M. Gerdes, U. Rehfuß, L. D. Silva, M. R. Hansen, L. van Wüllen, H. Eckert and D. Manzani, **Structural characterization of a new fluorophosphotellurite glass system**, *Dalton Trans.*, 2023, 52, 2227. doi.org/10.1039/D2DT03292A.

Abstract

While phosphotellurite glasses have superior properties over SiO_2–based glasses for many applications in optoelectronics and photonics devices, their high hydroxyl content limits their use in the mid–infrared range. This drawback can be overcome by fluoride addition to the formulation. In this work, we report the preparation, optical, and structural characterization of new glasses in the ternary system yTeO$_2$ – (1–y[xNaF – (1–x)NaPO$_3$)] (y = 0.6, 0.8; $0 \leq x \leq 1$) obtained by the traditional melting–quenching method. Differential scanning calorimetry (DSC) reveals high thermal stability against crystallization, with T_x–T_g varying from 80 to 130 °C, depending on fluoride/phosphate ratios. Raman spectroscopy suggests that the network connectivity increases with increasing phosphate concentration. ^{125}Te, ^{23}Na, ^{31}P, and ^{19}F NMR spectroscopy provides detailed structural information about Te–O–P, Te–F, Te–O–Te, P–O–P, and P–F linkages and the charge compensation mechanism for the sodium ions. The present study is the first comprehensive structural characterization of a fluorophosphotellurite glass system.

Volume 52
Number 8
28 February 2023
Pages 2185-2534

Dalton Transactions

An international journal of inorganic chemistry

rsc.li/dalton

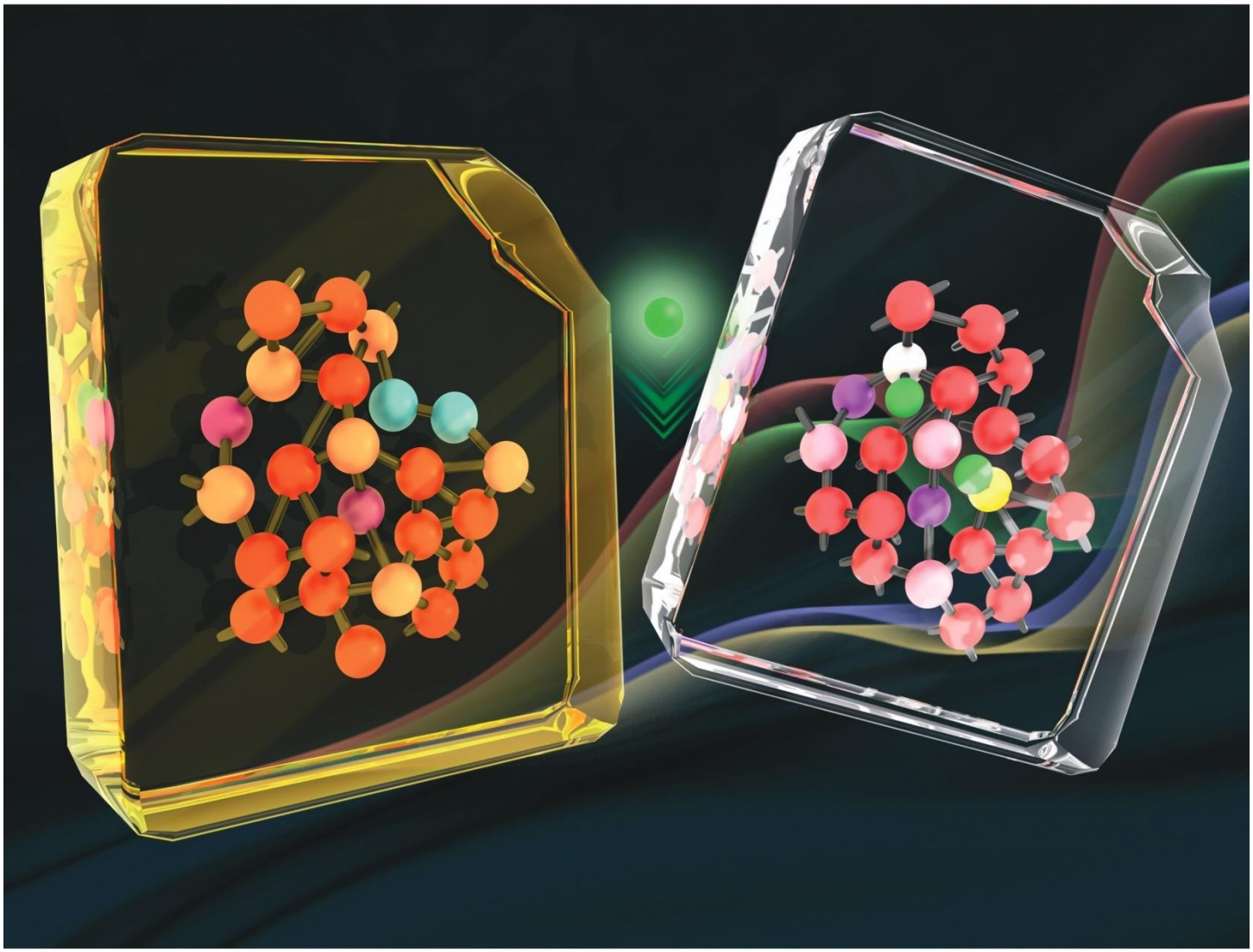

ISSN 1477-9226

ROYAL SOCIETY OF CHEMISTRY

PAPER

Michael Ryan Hansen, Leo van Wüllen, Hellmut Eckert, Danilo Manzani *et al.*
Structural characterization of a new fluorophosphotellurite glass system

Dalton Transactions

ROYAL SOCIETY OF CHEMISTRY

PAPER

Cite this: *Dalton Trans.*, 2023, **52**, 2227

Structural characterization of a new fluorophosphotellurite glass system†

Renato Grigolon Capelo,‡[a] Josef Maximilian Gerdes,‡[b] Ulrich Rehfuß,‡[c] Lais Dantas Silva,[e] Michael Ryan Hansen,*[b] Leo van Wüllen,*[c] Hellmut Eckert*[b,d] and Danilo Manzani*[a]

Received 11th October 2022,
Accepted 12th December 2022

DOI: 10.1039/d2dt03292a

rsc.li/dalton

While phosphotellurite glasses have superior properties over SiO_2-based glasses for many applications in optoelectronics and photonic devices, their high hydroxyl content limits their use in the mid-infrared range. This drawback can be overcome by fluoride addition to the formulation. In this work, we report the preparation, optical, and structural characterization of new glasses in the ternary system TeO_2–xNaF–$NaPO_3$ having the compositions $0.8TeO_2$–$0.2[x\text{NaF}–(1-x)NaPO_3]$ and $0.6TeO_2$–$0.4[x\text{NaF}–(1-x)NaPO_3]$ ($0 \leq x \leq 1$) obtained by the traditional melt-quenching method and labeled as T8NNx and T6NNx, respectively. Differential scanning calorimetry (DSC) reveals high thermal stability against crystallization, with $T_x - T_g$ varying from 80 to 130 °C, depending on fluoride/phosphate ratios. Raman spectroscopy suggests that the network connectivity increases with increasing phosphate concentration. ^{125}Te, ^{23}Na, ^{31}P, and ^{19}F NMR spectroscopy provides detailed structural information about Te–O–P, Te–F, Te–O–Te, P–O–P, and P–F linkages and the charge compensation mechanism for the sodium ions. The present study is the first comprehensive structural characterization of a fluorophosphotellurite glass system.

1. Introduction

Tellurium oxide (TeO_2) – based glasses have received considerable attention in photonics due to their wide transmission range (~350 nm to 6 μm), good thermal stability against crystallization, appreciable solubility of lanthanide ions, good mechanical strength and corrosion resistance, relatively low phonon energy among oxide glasses (~800 cm^{-1}), and high linear and nonlinear refractive indexes.[1–7] Therefore, tellurite glasses are attractive candidates for optoelectronics and photonic devices, such as optical fiber amplifiers, thermal lenses, optical sensing, luminescent displays and devices, and energy conversion.[8–12]

TeO_2 is generally considered a conditional glass former: while it can be obtained in its amorphous form by very fast melt quenching, the addition of a glass modifier or intermediate oxide is required for the formation of stable glasses. Still, glasses based on TeO_2 as a single network former component have poor thermal, mechanical, and crystallization stabilities. However, these properties can be considerably improved if additional network formers are included in the glass formulation. Beyond this benefit, the combination of several network formers usually offers the possibility of fine-tuning physical property combinations to specific technological demands. In this regard, phosphotellurite glasses have recently emerged as very promising infrared laser host materials,[13–21] even though the improvement in stability and mechanical properties is bought at an expense of decreases in emission lifetimes and intensities. Another significant drawback of phosphotellurite glasses obtained by the conventional melt-quenching method is their relatively high content of hydroxyl groups, requiring additional measures for obtaining "dry" glasses. As previously shown the addition of small amounts of metal fluoride to the batch is a simple way of avoiding hydroxyl group formation.[22,23] In addition, incorporating larger amounts of fluoride precursors could also enhance the optical properties of the resulting fluorophosphotellurite glasses, including wider transmission windows

[a]*Department of Chemistry and Molecular Physics, São Carlos Institute of Chemistry – IQSC, University of São Paulo – USP, São Carlos, SP, Brazil. E-mail: dmanzani@usp.br; Tel: +55 16 99289–5252*
[b]*Institut of Physical Chemistry, WWU Münster, Germany. E-mail: mhansen@uni–muenster.de*
[c]*Physics Institute, University of Augsburg, Germany. E-mail: Leo.van.wuellen@physik.uni-augsburg.de*
[d]*São Carlos Institute of Physics – IFSC, University of São Paulo – USP, São Carlos, SP, Brazil. E-mail: eckert@ifsc.usp.br; Tel: +55 16 997542003*
[e]*Center of Research, Technology, and Education in Vitreous Materials (CeRTEV), Department of Materials Engineering (DEMa), Federal University of São Carlos (UFSCar), 13565-905 São Carlos, SP, Brazil*

†Electronic supplementary information (ESI) available: Additional experimental characterization by differential scanning calorimetry, tentative deconvolution of Raman spectra, tentative deconvolutions of solid-state NMR spectra. See DOI: https://doi.org/10.1039/d2dt03292a

‡Equally contributing authors.

ranging from UV (~300 nm) to the mid-IR range (4–7 μm), higher rare-earth solubility, and lower phonon energies. In this way, enhanced optical performance of fluorotellurite glasses[24–35] can be combined in an ideal way with the improved mechanical and chemical stability of the glasses, resulting from the presence of the phosphate network former. However, as relatively few studies have been published on fluorophosphotellurite glasses[22,36–38] this remains a wide-open field of investigation.

In this paper, we report the glass formation, structural, thermal, and optical properties of two series of glasses in the ternary TeO_2–$NaPO_3$–NaF system. To develop and improve our understanding of the composition–structure–property relations in these glasses, we report their characterization by differential scanning calorimetry (DSC), Raman spectroscopy, UV-vis and mid-IR absorption, and solid-state nuclear magnetic resonance (NMR). NMR in particular has been quite instrumental in supplying detailed structural information about the short- and medium range order in glasses, based on an analysis of internal magnetic and electric interactions of the nuclei with their local environments.[39] A substantial body of work already exists, both on fluorophosphate[40] and phosphotellurite[41–43] glasses, whereas to date, the structural characterization of ternary fluorophosphotellurite glasses has been rather limited.[44] In this work, we will expand on these studies, by investigating the effect of the fluoride/phosphate ratio on the macroscopic and structural properties in this system.

2. Experimental

2.1 Sample preparation and characterization

Fluorophosphotellurite glass samples were obtained in two sets of compositional series with respect to TeO_2 content: series T8NN10x, corresponding to $0.8TeO_2$–$0.2[x\text{NaF}–(1-x)NaPO_3]$ (samples T8NN0 to T8NN10) and series T6NN10x corresponding to $0.6TeO_2$–$0.4[x\text{NaF}–(1-x)NaPO_3]$ (samples T6NN0 to T6NN10) compositions with $0 \leq x \leq 1$, as summarized in Table 1. The commercially available raw materials TeO_2 (Prichem, 99.99%), $NaPO_3$ (Aldrich, 96%), and NaF (Aldrich, >99%) were used. Bulk glass samples of about 5 g mass were obtained by the traditional melt-quenching method at ambient atmosphere in a covered gold crucible. Depending on the composition, samples were melted between 720 to 800 °C for 40 min in a muffle furnace to ensure complete elimination of adsorbed gases and good homogenization. The liquids were cast into a stainless-steel mold preheated at 20 °C below the glass transition temperature, T_g, and annealed at the same temperature for 2 h before they were slowly cooled to room temperature. The bulk glass pieces were cut and polished for optical characterizations.

Differential scanning calorimetry (DSC) was conducted on powdered samples (particle size < 20 μm) using a NETZSCH DSC 449 F3 Jupiter thermal analyzer to identify the glass transition onset temperature, T_g, the onset and peak crystallization temperatures, T_x and T_P, and the liquidus temperature, T_L, using platinum crucibles in air atmosphere. Each composition was heated from room temperature up to the corresponding liquidus or melting temperatures using a heating rate of 10 °C min^{-1}.

Optical absorption spectra were recorded in a Cary 500 (Varian) Double-beam spectrophotometer from 300 to 800 nm, and in a Perkin–Elmer FTIR Spectrum 2000 instrument in the wavelength region of 1 to 7 μm on polished glass pieces of 1.7 mm thickness. Raman spectra were recorded at room temperature from 50 to 1500 cm^{-1} using a LabRAM HR micro-Raman Horiba Jobin Yvon spectrometer equipped with a HeNe laser (632.8 nm) delivering 17 mW power.

2.2 Solid-state NMR

Solid-state ^{125}Te NMR experiments were performed at room temperature on static samples in a Bruker AVANCE-III 300 MHz spectrometer (operating frequency 94.3 MHz), using the wideband uniform rate smooth truncation (WURST) pulse

Table 1 Glass sample labels, molar compositions, characteristics temperatures (T_g, T_x, T_P, T_L), glass stability against crystallization parameters (K_{LL}, K_H, K_W and ΔT) data obtained for the T6NN and T8NN powder glass samples series. Estimated errors for the characteristic temperatures are ±2 °C

	Molar composition (mol%)			Characteristic temperatures (°C)					Glass stability parameters			
Samples label	TeO_2	$NaPO_3$	NaF	T_g	T_x	T_{P1}	T_{P2}	T_L	K_{LL}	K_H	K_W	ΔT (°C)
T8NN0	80	20	0	322	387	404	452	650	0.435	0.245	0.089	65
T8NN1		18	2	314	383	398	447	658	0.432	0.251	0.091	69
T8NN2		16	4	308	383	401	443	658	0.434	0.272	0.099	75
T8NN3		14	6	301	367	380	407	663	0.424	0.223	0.084	66
T8NN4		12	8	295	356	366	450	667	0.417	0.194	0.076	61
T8NN5		10	10	288	373	390	—	665	0.431	0.292	0.109	85
T8NN10		0	20	240	289	293	311	621	0.399	0.145	0.059	49
T6NN0	60	40	0	318	455	460	—	663	0.476	0.654	0.152	137
T6NN1		36	4	313	407	442	—	657	0.449	0.375	0.138	94
T6NN2		32	8	301	391	412	432	640	0.447	0.363	0.122	90
T6NN3		28	12	290	377	390	410	612	0.449	0.371	0.114	87
T6NN4		24	16	278	361	374	390	596	0.447	0.357	0.111	83
T6NN5		20	20	274	371	383	397	596	0.455	0.432	0.126	97
T6NN10		0	40	—	289	298	307	542	—	—	—	—

sequence,[45–47] combined with the Carr–Purcell–Meiboom–Gill (CPMG)[48,49] echo train acquisition scheme. The advantage of the WURST-CPMG over the traditional CPMG pulse sequence is that the excitation bandwidth of the WURST pulses is broad enough so that the full spectrum can be excited (and refocused) in a single experiment, without the need of changing the carrier frequency, as it is conventionally done in CPMG experiments. WURST-20 excitation and refocusing pulses of 100 μs were used for an excitation bandwidth of 1 MHz, corresponding to R = 10 kHz μs^{-1} [50] with a recycle delay of 60 s. The spikelet separation was set to 4.5 kHz and 300 CPMG loops were accumulated in each scan. The WURST-CPMG spectra were obtained in two different ways: (i) by fast Fourier transformation of the whole echo train, resulting in spikelet patterns and (ii) by fast Fourier transformation of the sum of the individual echoes, resulting in an envelope spectrum. The advantage of the second method is that the signal-to-noise ratio is greatly improved. Chemical shifts are reported relative to $Te(CH_3)_2$ at 0 ppm, referenced with $Te(OH)_6$ solution (1 M) as secondary reference at 713 ppm.

Solid state ^{31}P NMR studies were carried out at 121.5 MHz on a Bruker Avance III spectrometer equipped with a 4 mm probe which was operated at spinning frequencies up to 10.0 kHz. MAS-NMR spectra were recorded using 90° pulses of 4.1 μs length and a relaxation delay of 60 s using a saturation comb. In addition, double-quantum (DQ) filtered spectra were measured using the 1-D refocused INADEQUATE sequence.[51,52] This experiment results in the selective detection of only those ^{31}P nuclei that are involved in at least one P–O–P linkage and therefore give rise to the excitation of a double quantum coherence through indirect ^{31}P–^{31}P spin–spin coupling. In contrast, the signals of the other network former units not involved in P–O–P linkages, such as P^0 and $P^n_{m\mathrm{Te}}$ (where $m = n$) are suppressed by this pulse sequence. Experimental conditions were spinning frequency 10.0 kHz, π/2 pulse length 4.1 μs, and relaxation delay 60 s. The mixing time for DQ coherence creation was 8.3 ms, corresponding to a value of the indirect spin–spin coupling constant $^2J(^{31}\mathrm{P}–^{31}\mathrm{P})$ of 30 Hz, which is a typical value for P–O–P linkages in phosphate glasses. Chemical shifts were referenced against an external 85% H_3PO_4 standard. ^{31}P NMR line shape analysis and deconvolutions were done using the DMFIT[53] and ssNake[54] routines. ^{23}Na MAS-NMR spectra were carried out at 79.4 MHz on a Bruker Avance III spectrometer equipped with a 4 mm probe, which was operated at a spinning speed of 10.0 kHz. MAS NMR spectra were recorded using short pulses of 0.8 μs length and a relaxation delay of 3.5 s. Chemical shifts are referenced to an aqueous 1 M NaCl solution.

^{19}F MAS NMR spectra were recorded on a Bruker DSX 200 spectrometer (Larmor frequency for ^{19}F of 188.33 MHz) in 2.5 mm rotors spinning at 25.0 kHz, using a rotor-synchronized Hahn-Echo sequence with 2 rotor cycles for the echo formation to remove the probe background signal. Different evolution times were tested. The values used in the experiments do not influence the relative intensities of the resolved spectral components, indicating similar spin–spin relaxation times. 90° pulses of 2.33 μs length and relaxation delays of 5 s were used. Chemical shifts are reported relative to $CFCl_3$ using solid AlF_3 as a secondary reference (−172 ppm). $^{19}\mathrm{F}\{^{31}\mathrm{P}\}$ rotational echo double resonance (REDOR) measurements were carried out on a Varian VNMR spectrometer system at 11.7 T in 1.6 mm rotors spinning at 30.0 kHz, using the standard pulse sequence of Gullion and Schaefer.[55] In these experiments, the π pulse length was 6.3 μs.

The static ^{19}F NMR free-induction decays (FID) for quantification of the fluorine content were recorded on a Benchtop Bruker Minispec mq20 system operating at 18.82 MHz using 10 mm sample tubes filled with 0.5–1 g sample mass. 90° pulses of 2.66 μs length were used and recycle delays between 2–35 s were optimized for each sample based on saturation recovery experiments.

3. Results and discussion

3.1 Physical properties

The glasses from both series were obtained as optically homogeneous bulk samples, except for the T6NN10 samples, which easily crystallized under the same quenching conditions. All samples, particularly those of the T8 series are yellowish in color. Comparing the UV-vis absorption spectra of fluoride-free T6NN0 and T8NN0 samples a small shift of the absorption edge is observed towards shorter wavelengths in the sample with the lower concentration of tellurium oxide. As observed in Fig. 1, the same trend is seen for the whole set of F-containing samples as well. Replacement of phosphate by fluoride does not significantly impact the location of the absorption edge but tends to decrease transparency in the interval of ~350 nm to ~400 nm. Photos of the studied glass samples are presented in Fig. S1.† From the photos no obvious anomaly is apparent. Using the obtained absorption spectra, the band gap energy between valence and conduction bands was calculated with eqn (1) considering the glass system presents a direct allowed transition.[56]

$$\alpha(h\nu) = B(h\nu - E_g)^{1/2} \quad (1)$$

In eqn (1), $\alpha(h\nu)$ is the absorption coefficient determined in Fig. 1, B is a constant which defines as the band tailing, E_g is the band gap energy in eV, and $h\nu$ is the incident photon energy. The E_g of the T6 and T8 glass samples were estimated by extrapolating linear fits (Tauc's plots) onto the abscissa ($[(\alpha h\nu)^2 = 0$) (Fig. S2†). As expected, the same behavior was observed in the series T6 and T8, in which the band gap energy varied from 3.44 eV (T8NN0) to 3.49 eV (T8NN5), and from 3.59 (T6NN0) to 3.63 eV (T6NN5), respectively, with respect to NaF addition. This behavior indicates a slight increase of the glass network ionic character upon replacement of the $NaPO_3$ component by NaF.

The addition of fluoride into oxide melts is a powerful chemical strategy to remove OH from the glass network, making the glasses more suitable for applications in the infrared spectral range, where OH absorption may interfere. Fig. 2

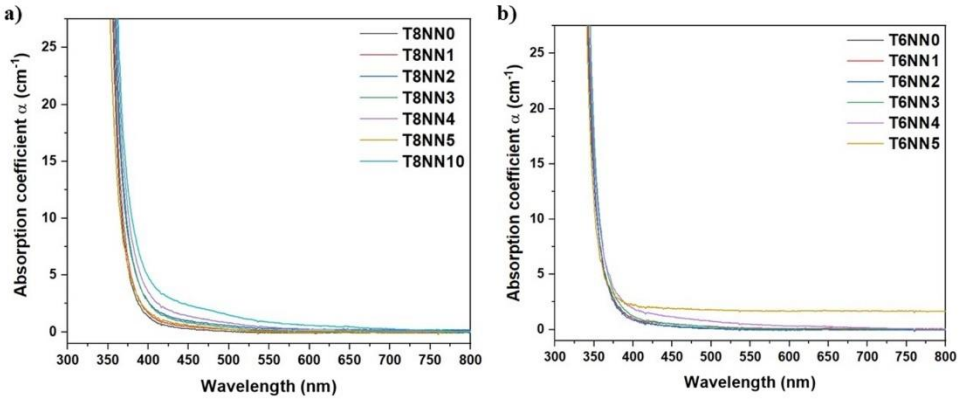

Fig. 1 UV-vis absorption spectra of glass samples in the series T8 (a) and T6 (b).

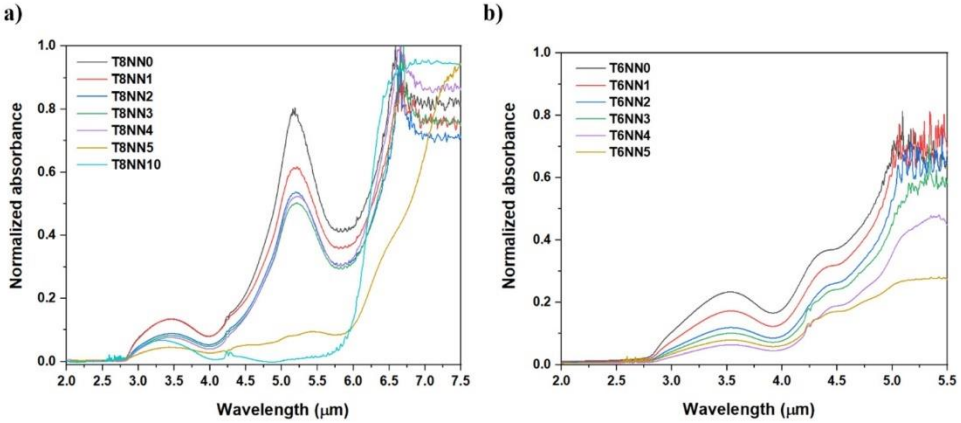

Fig. 2 Mid-infrared absorption spectra of glasses from (a) the T8 series and (b) the T6 series as a function of replacement of $NaPO_3$ by NaF.

shows the normalized mid-infrared absorption spectra of the samples from set T8 and T6. The spectra of the T8 series are composed of two bands at 3.4 and 5.2 μm (Fig. 2(a)), while in the T6 series bands at 3.4 and 4.4 μm are observed (Fig. 2(b)). The OH absorption bands depend on the OH bond strength in the glass: the absorption band at ~3.4 μm is assigned to weakly bound and free OH groups in the glass matrix whereas the absorption peaks at ~4.4 and ~5.2 μm are assigned to OH groups strongly connected with tellurite units, forming terminal Te–OH bonds.[57]

Fig. 2 also reveals that with increasing NaF for $NaPO_3$ substitution the OH absorption band intensities are clearly reduced. The probable melt reaction of the fluorine that promotes the dehydroxylation of the melt can be written as $OH^- + F^- \rightarrow HF + O^{2-}$.[42] The higher TeO_2 content samples from the T8 series show a broad multiphonon absorption edge extended up to ~6.0 μm but disrupted due to the presence of absorption bands assigned to the stretching vibrations of the OH groups. The T8NN10 sample showed a typical multiphonon absorption edge of tellurite and fluoride glasses without the vibration band at ~5.2 μm. Substitution of $NaPO_3$ by NaF slightly shifts this multiphonon edge towards higher wavelengths and greatly reduces the intensity of the OH bands at 3.4 and 5.2 μm. For T8NN5, a large edge shift is observed in comparison to T8NN4, and a very low-OH fluorophosphotellurite glass is obtained with the widest transmittance window extending to ~7.0 μm. In the phosphate-richer samples of the T6 series the transparency window in the mid-IR is limited to ~5.0 μm due to the higher intensity of the OH absorption band. Nevertheless, as observed for the T8 series, the multiphonon edge is shifted towards higher frequencies and the OH absorption bands at 3.4 μm and 4.4 μm are decreased as also reported in the literature.[23] The dehydroxylation promoted by the addition of NaF in both sets of samples is accompanied by fluorine loss which was investigated by ^{19}F NMR and corresponds to an average loss of 5–10% as discussed below.

Fig. S3† presents the DSC curves. Some samples show two separate crystallization events. Values of T_g, T_x, T_{P1}, T_{P2}, and T_L are summarized in Table 1. Table 1 also lists the various glass

stability parameters defined by Hruby, K_H,[58] Weinberg, K_W,[59] and Lu and Liu, K_{LL}.[60]

$$K_H = \frac{(T_x - T_g)}{(T_L - T_x)},\ K_W = \frac{(T_x - T_g)}{T_x - T_g},\ \text{and}\ K_{LL} = \frac{T_x}{(T_g + T_L)}$$

No such values could be listed for the T6NN10 sample, owing to its high crystallization tendency.

Table 1 reveals no difference between T_g values of the fluoride-free samples T8NN0 and T6NN0. On the other hand, Fig. 3 shows that successive substitution of the $NaPO_3$ component by NaF leads to a monotonic decrease of T_g, from 314 °C to 288 °C, and from 313 °C to 274 °C for the series T8 and T6, respectively. In principle, composition-related trends in the value of the glass transition temperature reflect changes in the network connectivity and/or rigidity. A possible structural explanation may invoke the depolymerization of the network, *i.e.* the breakage of P–O–P, P–O–Te, and Te–O–Te linkages with the formation of Te–F and P–F terminal bonds. Finally, Table 1 shows that an increase of phosphate content tends to enhance ΔT and glass stability for both series, even though in the case of the T8NN5 sample, a non-monotonic behavior is observed, and deeper investigations are necessary to understand this trend deviation. The lowest ΔT and glass stability parameters for the T8NN10 sample can be attributed to a highly depolymerized fluorotellurite glass network due to the formation of Te–F terminal linkages. This issue will be addressed below based on the NMR results.

In order to improve the understanding of the mixed glass network modification by the replacement of $NaPO_3$ with NaF, Raman spectra of both sets of glass samples and the raw materials were recorded as shown in Fig. 4. In general, in tellurite glasses the glass network is mainly formed by three distinct types of [TeO_n] polyhedra, whose quantitative distribution depends on the network modifier content.[61–67] Glasses with high TeO_2 contents are mainly composed of highly connected pseudo-trigonal bipyramidal [TeO_4] units. The addition of glass modifier compounds usually leads to the conversion of [TeO_4] to [TeO_{3+1}] units, in which one of the axial Te–O linkages is elongated. At high content of modifiers, a less connected network is formed predominated by [TeO_3] units.[21,61–67] In turn, the phosphate glass network may be composed of up to four different types of [PO_n] polyhedra. In mixed network former systems, these are denominated by the $P^n{}_m x$ terminology, where n is the number of bridging O atoms connecting to other network formers while m denotes the number of these linkages connecting the

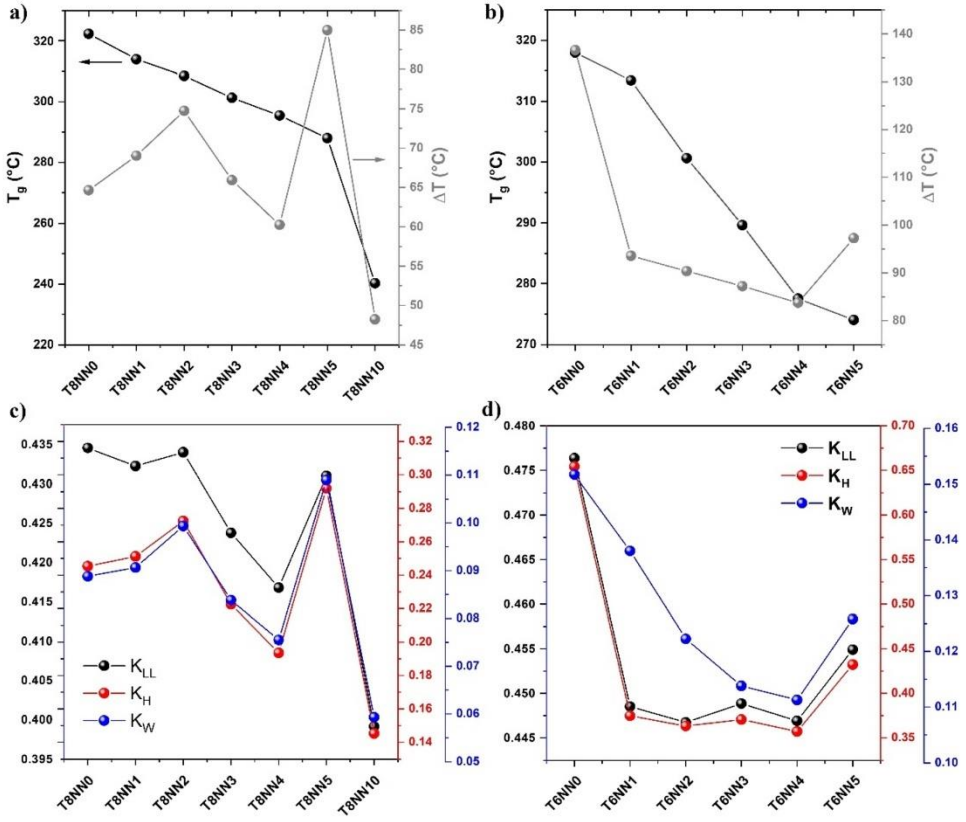

Fig. 3 Glass transition temperature (T_g) and the thermal stability parameter ΔT behavior of the T8 series (a) and the T6 series (b) of samples, and the behavior of the glass stability parameters K_{LL}, K_H, and K_W for glass samples from series T8 (c) and T6 (d).

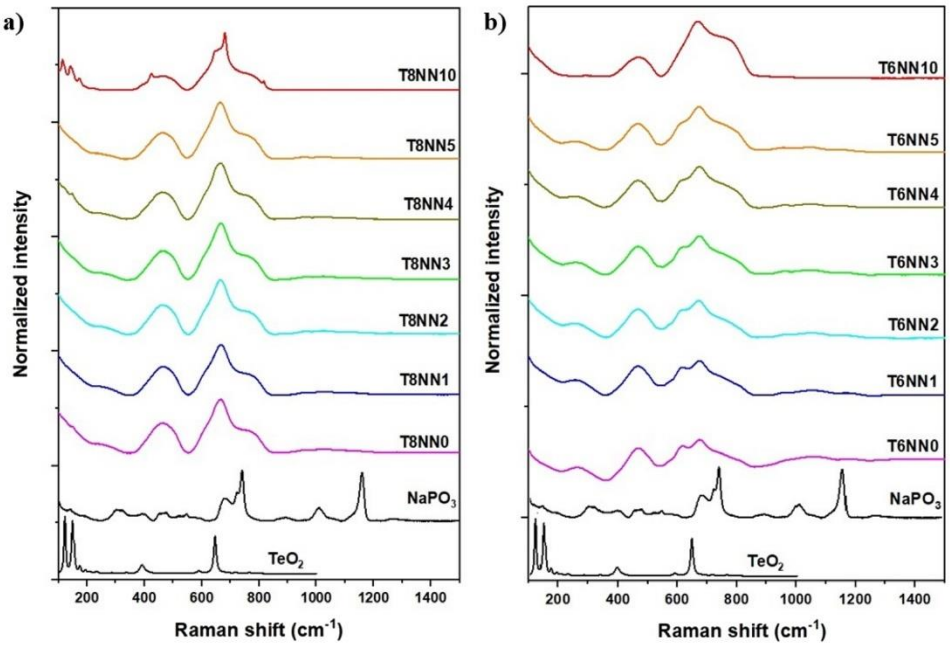

Fig. 4 Raman spectra of reference materials and glasses of (a) the T8 and (b) the T6 series.

phosphate polyhedron with the specific network former species X;[68] this reference also states the relationship to the Q^n terminology used for single-network former phosphate glasses.[69]

Fig. 4 also includes Raman spectra of the model compounds TeO_2 and $NaPO_3$. The structure of crystalline α-TeO_2 is based on linear chains of $TeO_{4/2}$ units arranged in a trigonal bipyramidal crystal system (paratellurite). The Raman spectra of paratellurite present four intense bands at 119, 147, 430, and 670 cm^{-1}, assigned to the symmetric and asymmetric Te–O stretching in a three-dimensional network. Sodium metaphosphate is constituted by linear chains of metaphosphate $[P(O)_2O_{2/2}]^-$ (P^2_{2P}) units and the two most intense bands at ~710 and 1160 cm^{-1} are assigned to the symmetric stretching vibrations of P–O–P linkages, and the symmetric stretching vibration of the terminal P–O bonds belonging to the various Q^2 (P^2_{2P}) units. The two weak bands centered at ~1010 and ~1270 cm^{-1} are related to the symmetric P–O stretching mode in Q^1 tetrahedra (chain end members and hydrolysis reaction products), and to the asymmetric P–O stretching of Q^2 units, respectively.[69]

The Raman spectra observed in the glasses are composed of broadened, superimposed components, which makes it difficult to follow the structural modifications caused by the substitution of $NaPO_3$ by NaF. Fig. S4† shows some tentative deconvolutions of the spectra, suggesting four principal contributions within the spectral region from 550 to 900 cm^{-1}. The maximum near 660 cm^{-1} is attributed to a combination band involving vibrations of neutral TeO_4 and TeO_{3+1} units,[27] whereas scattering intensity near and above 750 cm^{-1} can be assigned to anionic TeO_{3+1}, and TeO_3 units. The latter contribution to the overall scattering intensity appears to be higher in the samples from the T6 series than in those from the T8 series, suggesting that the T6 glasses present a higher degree of modification of the network former component TeO_2. For either series, successive replacement of the $NaPO_3$ by the NaF component has no effect on the relative intensity of the 750 cm^{-1} band suggesting no significant changes in average coordination number of the Te species and/or the number of non-bridging O atoms. Comparison of the spectra of the T6 and the T8 series further suggests a feature near 620 cm^{-1} which may be attributable to the stretching vibrations of bridging oxygen atoms belonging to P–O–Te linkages, as this band is more visible in the glasses with higher phosphorus concentrations. A second component from P–O–P stretching would be expected as well, even though the NMR results discussed below suggest that this contribution is minor. Inspection of the phosphate free samples T8NN10 and T6NN10, and comparison with crystalline TeO_2 suggests further that part the scattering intensity in this region also originates from stretching motions of Te-based network former units, presumably of the TeO_4 type.

Fig. 5 shows vertically expanded partial spectra in the 900–1250 cm^{-1} region, and a tentative deconvolution is included in Fig. S4.† Three separate bands are visible, which can be assigned to the O–P–O stretching modes in Q^0 (P^2_{2Te}) units (960 cm^{-1}), in Q^1 (P^2_{1Te1P}) units (1050 cm^{-1}), and in Q^2 (P^2_{2P}) units (1160 cm^{-1}), respectively; a similar distinction is possible for the T8 glasses. We note that our assignment implies that all the phosphate species are considered mono-

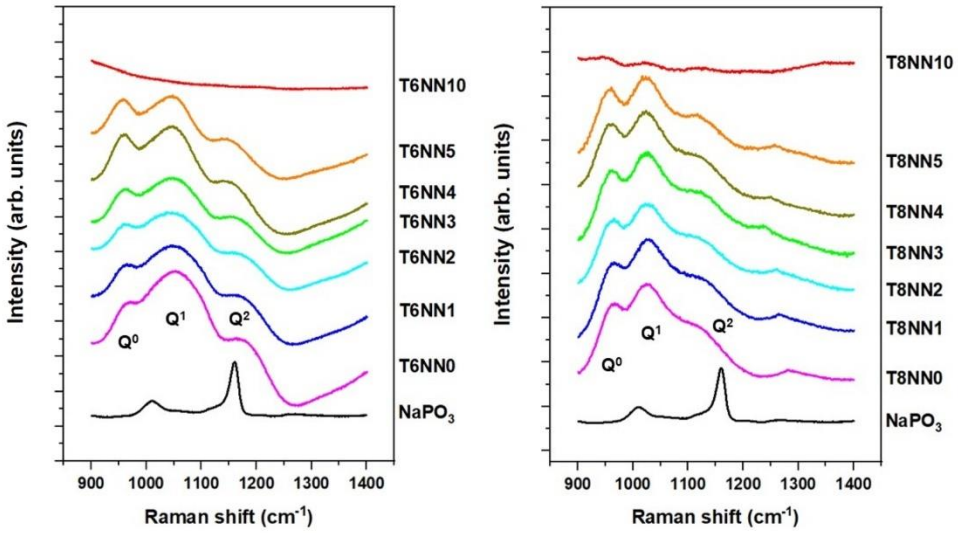

Fig. 5 Raman spectra observed in the 900–1250 cm^{-1} spectral region and suggested peak assignments.

anionic as in $NaPO_3$ and the main spectroscopic differentiation arises from the number of P–O–P *vs.* P–O–Te linkages present. Owing to different scattering cross-sections of these units involved, quantification is not possible. Nevertheless, we can note interesting trends in relative band intensities: the bands at 1160 cm^{-1} have a lower relative intensity for glasses of the T8 series, suggesting fewer Q^2 (P^2_{2P}) units than present in the T6 glasses. This is expected from the lower phosphate content of the former. Secondly, we can note that with increasing NaF content x there is a tendency of the number of P–O–P linkages to decrease and the fraction of Q^0 (P^2_{2Te}) units to become more prominent. This latter effect can be studied more quantitatively using ^{31}P solid state NMR as discussed in the next section.

3.3. Solid-state ^{31}P NMR

Fig. 6 shows the ^{31}P MAS-NMR spectra obtained without and with homonuclear double-quantum filtering. The latter experiment utilizes J-based double quantum coherences to selectively detect only those ^{31}P nuclei that are involved in P–O–P linking. It is evident that the ^{31}P NMR chemical shifts of those nuclei that are involved in P–O–P linkages give rise to a component at lower frequencies than the main resonance. Using the parameters of this line shape in the T6 series and the isotropic shift measured for this species in the T8 series as constraints for the complete ^{31}P MAS-NMR line shape analysis we arrive at the peak deconvolutions shown in Fig. 7 and listed in Table 2. As expected, the contribution of the component involved in P–O–P linkages (*i.e.*, of $P^2_{1Te,1P}$ and of P^2_{2P}) increases from the T8 series to the T6 series for all the samples ($0 \leq x \leq 0.5$). Furthermore, there is a tendency that the ratio of $P^2_{1Te,1P}/P^2_{2Te}$ units decreases with increasing NaF content, confirming the trend seen in the Raman spectra. This result is expected, as the P/Te ratio decreases with increasing x, decreasing the statistical probability of P–O–P linkage formation.

Note that the information from the Raman spectra and that from solid-state NMR complement each other: while not quantitative, Raman spectroscopy offers a superior differentiation regarding next-nearest neighbor connectivity in the network, while DQ-filtered NMR and constrained peak fitting allow the quantification of the P^2_{2Te} species. On the other hand, separate resonances arising from $P^2_{1Te,1P}$ and P^2_{2P} units cannot be resolved (unlike the situation in the Raman spectra). Still, Table 2 indicates a distinct chemical shift trend towards lower values with increasing phosphate content (decreasing x) suggesting an increasing contribution of the P^2_{2P} units in this direction for both the T6 and the T8 series as expected.

3.4 ^{23}Na MAS-NMR

Fig. 8 sumarizes the ^{23}Na MAS-NMR spectra. They show central transition line shapes dominated by nuclear electric quadrupolar interactions, which can be described by second-order perturbation theory. The asymmetrically broadened line shapes arise from a wide distribution of local electric field gradients, which is typical for the intrinsic disorder in the glassy state. Mathematically this line shape can be simulated by the Czjzek model,[70] which is implemented in the DMfit program *via* the *CZ*-simple module. Table 3 summarizes the average isotropic chemical shifts and nuclear electric quadrupole coupling constants extracted from these fits. The isotropic chemical shifts show a monotonic dependence on F content, shifting from −2.7 ppm in T6NN0 to 1.1 ppm in T6NN10; very similar increments are observed in the T8 series. The chemical shifts measured in these glasses are quite different from the values between +5 and +10 ppm in sodium tellurite glasses.[71] For sample T6NN10, the presence of an additional narrow signal at 6.7 ppm may indicate the precipitation of NaF (δ_{iso} =

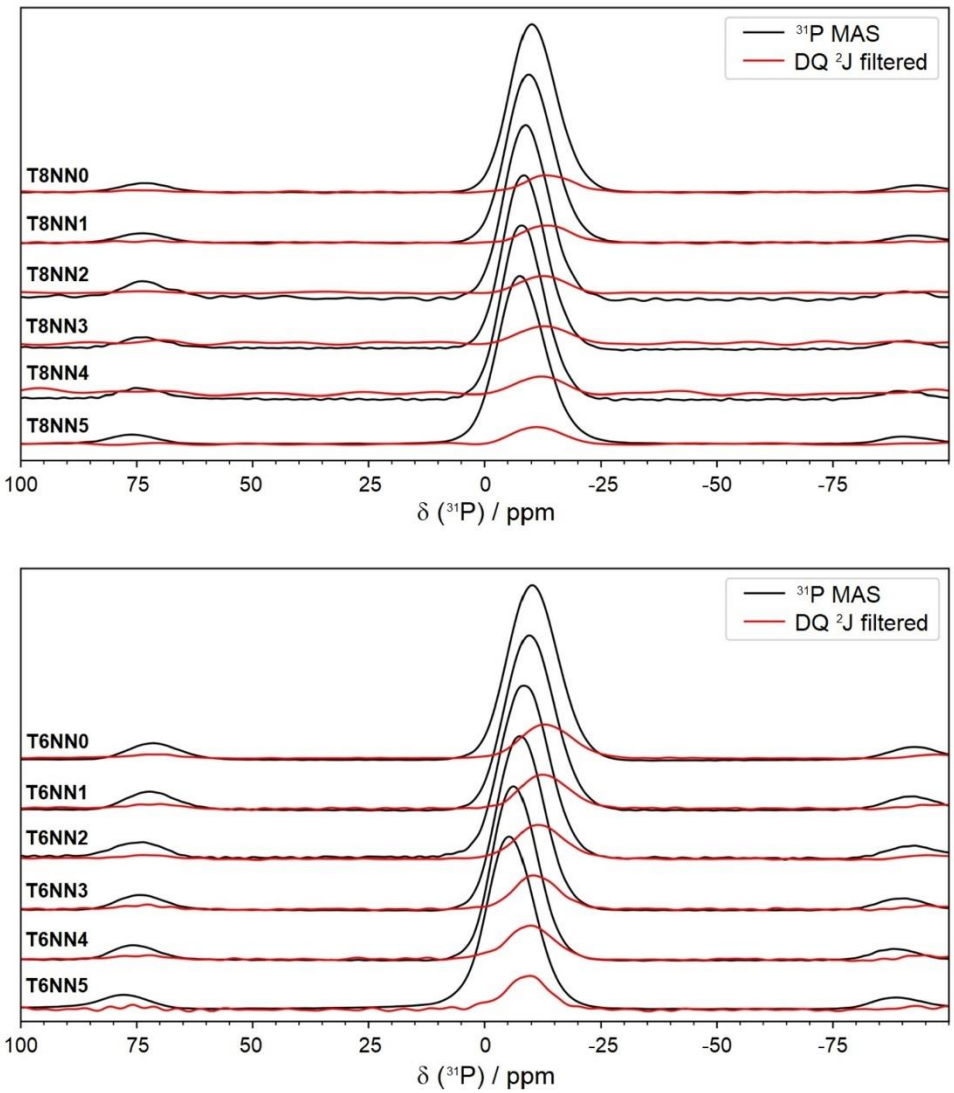

Fig. 6 Regular (black) and DQ-filtered (red) ^{31}P MAS-NMR spectra of the samples under study.

7.2 ppm),[72] consistent with ^{19}F NMR results reported below. All these results illustrate that the sodium cations interact dominantly with phosphate and fluoride species. In agreement with the Raman data the ^{23}Na MAS-NMR data do not give any evidence that the substitution of the $NaPO_3$ by the NaF component creates any additional tellurium species bound to non-bridging-oxygen atoms.

3.5 ^{19}F NMR and ^{19}F{^{31}P} REDOR

Fig. 9 shows experimental FID intensities (I_{exp}) measured at a low magnetic field (ν_L = 18.82 MHz) of the T6 and T8 glasses compared to theoretical values for various external references. The theoretically expected ^{19}F NMR intensities (I_{theo}) are calculated based on the nominal mass content in the T6 and T8 series; the inset in Fig. 9 shows the ratio I_{exp}/I_{theo} as a function of NaF content, x. While lower fluorine concentrations tend to be overestimated due to the background signal of the probe head, for the other glasses the intensities expected from the batch contents are reproduced within a deviation of about 5–10%. Different reference samples were used to estimate the systematic error from the different FID decay rates due to homonuclear dipole–dipole interactions of different strengths in the reference compounds NaF, Na_2PO_3F, and Teflon. This error is estimated to about 5% of the total signal intensity. Thus, the maximum loss of fluorine is estimated to be not larger than 10% in the samples with medium to high fluorine content. In glasses with low F concentrations the quantification is obstructed by the background signal.

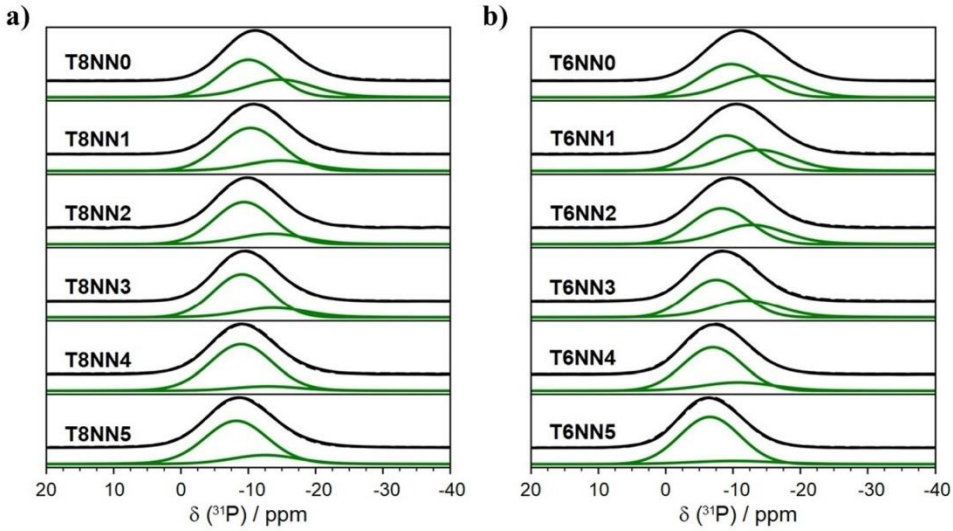

Fig. 7 Deconvolution of the ^{31}P MAS-NMR spectra of the T8 series in (a) and the T6 series in (b), constrained by the line shapes of the DQ-filtered MAS-NMR spectra of the samples under study. Fit components are shown in green.

Table 2 Deconvolution results from ^{31}P MAS NMR of the T8 and T6 glass series (Fig. 7). Estimated errors are ±0.5 ppm for the peak positions (δ_{iso}) and ±2% for the area percentages

	$P^2_{1Te,1P}$ & P^2_{2P}		P^2_{2Te}	
Sample	δ_{iso}/ppm	Area/%	δ_{iso}/ppm	Area/%
T6NN0	−13.3	44	−8.7	56
T6NN1	−12.9	42	−8.1	58
T6NN2	−11.8	41	−7.3	59
T6NN3	−11.1	38	−6.5	62
T6NN4	−9.9	21	−6	79
T6NN5	−9.2	10	−5.6	90
T8NN0	−13.8	41	−9	59
T8NN1	−13.4	25	−9	75
T8NN2	−12.6	24	−8.4	76
T8NN3	−12.7	24	−8	76
T8NN4	−11.9	11	−7.9	89
T8NN5	−11.5	21	−7.2	79

Fig. 10 shows the high field ^{19}F MAS-NMR data. The spectra show a very broad resonance with a maximum near −60 ppm. The line shapes are distinctly asymmetric, suggesting the presence of multiple components. In general, the ^{19}F chemical shifts measured in this system are much more positive than those measured in other types of fluorophosphate glasses containing group-12 and 13 elements.[68,73–75] On the other hand, some of such previously measured fluorophosphate glasses had also shown weak signals in the −70 ppm region, which could be assigned to P-bonded fluorine species based on ^{19}F{^{31}P} REDOR data and the comparison with crystalline Na_2PO_3F.[68,73–75] For the present glasses Fig. 11 illustrates an analogous comparison of ^{19}F{^{31}P} REDOR data for some representative glasses. Also included are two-spin simulations based on some effective ^{19}F–^{31}P internuclear distances. While for Na_2PO_3F the simulation of the REDOR curve produces a P–F distance of 1.69 Å (dipolar coupling constant of 9500 Hz) in reasonable agreement with the crystallographic distance (1.64–1.66 Å), the dipolar dephasing is much weaker in the glasses, corresponding to effective distances near 2.7 to 3.8 Å if a two-spin interaction is assumed. Based on these values we can conclude that P–F bonds do not occur in these glasses to any appreciable extent. We therefore attribute the principal resonance signal with a maximum near −60 to −70 ppm to Te–bonded F species. This assignment is supported by the literature value of δ_{iso} (^{19}F) = −27 ppm in a toluene solution of TeF_4.[76] The signal shape observed in the glasses indicates, however, a wide chemical shift distribution. While we have given a tentative deconvolution into three components in Fig. S5 and Table S3,† there are many ways in which these spectra can be simulated. For this reason, the data in Fig. 10 are shown without any simulation effort and only the center of gravity of the resonance is reported in Table 4, which shows no clear trend. We speculate that the fluoride species, in addition to being Te-bonded, experience a broad range of local environments with different spatial proximities to sodium ions affecting their chemical shifts. These additional interactions may result in low-frequency signal displacements of different magnitudes, producing the wide chemical shift distribution that is experimentally observed. This hypothesis could, in principle, be tested by ^{19}F{^{23}Na} REDOR or REAPDOR experiments. From such experiments, to be reported later, we expect to observe a strong correlation of the ^{19}F isotropic chemical shifts with the strength of the ^{19}F–^{23}Na magnetic dipole–dipole couplings. Furthermore, those experiments would be useful for developing some constraints for spectral deconvolutions. Finally, glasses from both series with the highest F contents show a sharp component near −220 ppm, signifying partial

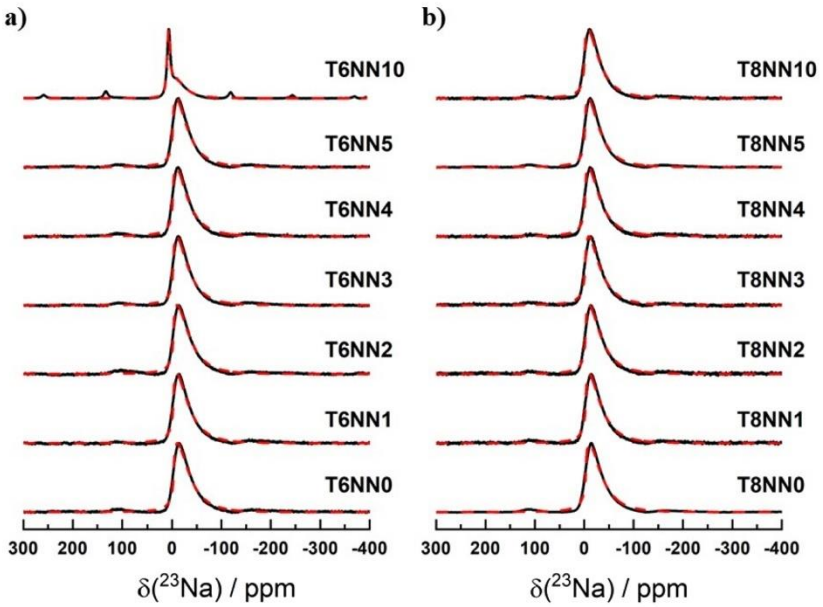

Fig. 8 ^{23}Na MAS-NMR spectra of the (a) T6 and (b) T8 series of glasses under study. Dashed curves illustrate the fits to a Czjzek model, leading to the line shape parameters summarized in Table 3. Spinning sidebands are labelled by asterisks.

Table 3 ^{23}Na MAS NMR line shape parameters in the glasses under study

Sample label	$\langle\delta_{iso}\rangle$/ppm (±0.5)	$\langle\lvert C_Q\rvert\rangle$/MHz (±0.1)
T6NN0	−2.7	2.4
T6NN1	−2	2.3
T6NN2	−2	2.4
T6NN3	−1.7	2.3
T6NN4	−1	2.4
T6NN5	−0.9	2.4
T6NN10	1.1	2.2
T8NN0	−2.8	2.3
T8NN1	−2.4	2.3
T8NN2	−2.1	2.3
T8NN3	−1.7	2.4
T8NN4	−1.3	2.3
T8NN5	−1	2.4
T8NN10	0	2.3

crystallization of NaF which likely can be attributed to a limit of fluorine incorporation. For ground samples that did not show this resonance initially, exposure to the ambient atmosphere the NaF signal emerged over time (days to months). Thus, we conclude that NaF crystallization is promoted by the interaction of the powders with atmospheric humidity.

3.6 Static ^{125}Te NMR

^{125}Te NMR spectra, obtained in the static mode by the WCPMG method, are shown in Fig. 12. The data are typical of the effect of the chemical shift anisotropy, characterized by a distribution of principal components. The spectra are rather similar but distinctly dependent on the fluoride content, which is consistent with the formation of Te–F linkages. As

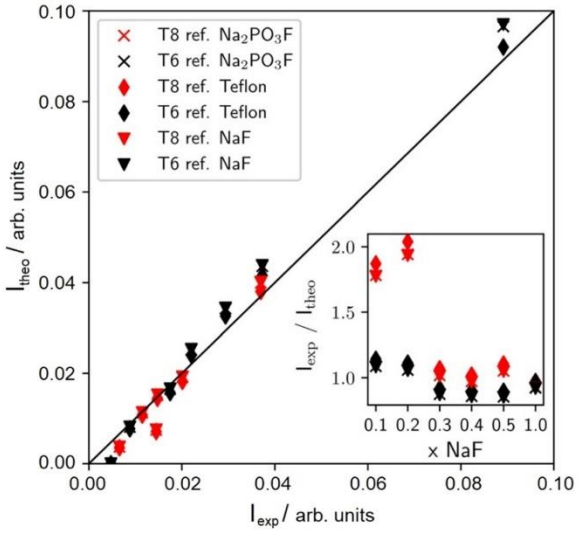

Fig. 9 ^{19}F FID intensities measured at a low magnetic field (0.47 T) compared to theoretical values calculated from reference compounds, see text for details. Statistical errors are represented by the symbol sizes, possible systematic errors are discussed in the text. The solid black line denotes the identity. The inset in the lower right-hand corner shows the ratio I_{exp}/I_{theo} as a function of NaF content, x.

indicated by Table 4 in both series the average isotropic chemical shift as deduced from the center of gravity tends to increase monotonically with increasing F/P ratio. The spectra of the phosphate-free samples T8NN10 and T6NN10 show pro-

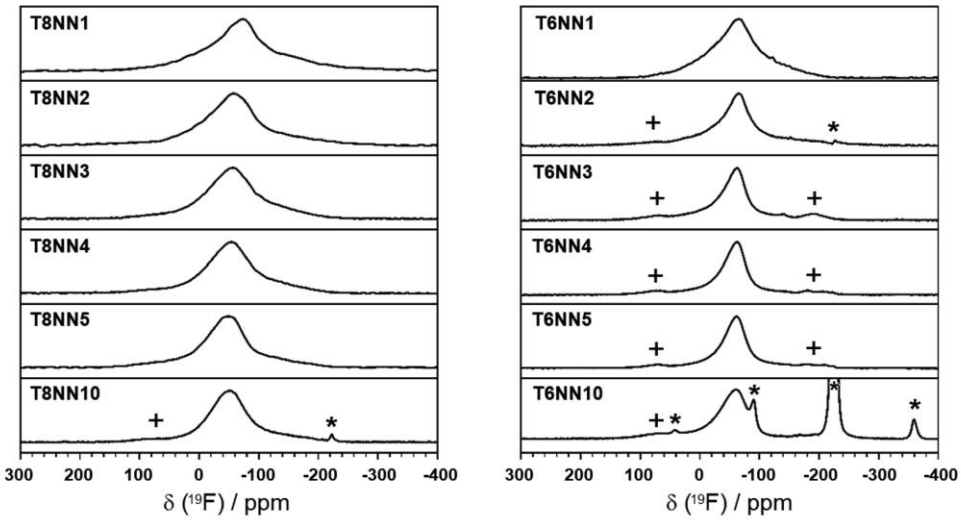

Fig. 10 ^{19}F MAS NMR spectra (obtained by rotor-synchronized Hahn-Echo acquisition) of the samples under study. A crystalline NaF impurity (due to crystallization) and its associated spinning sidebands are labeled by asterisks, visible spinning sidebands attributed to the glassy state are marked with the symbol +.

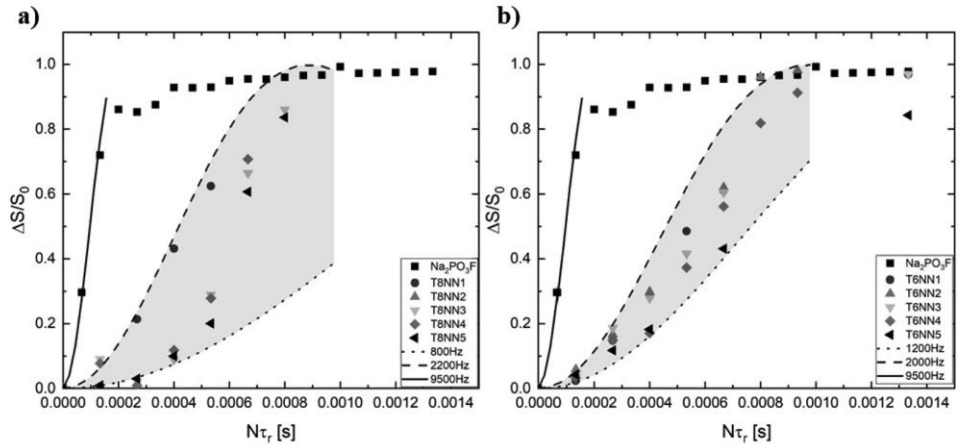

Fig. 11 ^{19}F{^{31}P} REDOR data of representative glass samples and crystalline Na_2PO_3F. (a) T8 series, (b) T6 series. Solid, dashed and dotted curves are two-spin simulations based on scenarios with different dipolar interaction strengths. The data confirm the absence of P–F bonding.

nounced spectral intensity near 1800–2000 ppm suggesting that this feature could arise from F-bonded tellurium species. No influence of ^{19}F decoupling on the lineshapes, could be noted. Fig. S6 and Table S4† show tentative simulations in terms of single set of chemical shift tensor values convoluted with Gaussian broadening functions to account for a distribution of tensor values; however, these only provide a rough approximation to the line shape. Most likely there are multiple species arising from different Te–O *vs.* Te–F bonding configurations characterized by distinct isotropic chemical shifts. To resolve such species, ultra-fast MAS experiments will be required (~100 kHz at moderately low magnetic field strengths), supported by spectral editing experiments exploiting direct or indirect ^{125}Te–^{19}F spin–spin interactions. Such experiments are currently under consideration in our laboratories.

4. Discussion

Based on the results outlined above, a preliminary structural model can be formulated, as summarized schematically by Fig. 13. In the F-free glasses the principal building units are the Q^2 and the Te_4[4] units, which can be randomly linked *via* Te–O–P linkages. In this manner three distinct P^2 environments are formed, which contribute to the ^{31}P MAS-NMR line

Table 4 Center of gravity δ_{CG} of the ^{19}F and ^{125}Te resonances attributed to the glassy state for the samples under study

Samples	δ_{CG} of ^{19}F/ppm (±1)	δ_{CG} of ^{125}Te/ppm (±10)
T6NN0	—	1558
T6NN1	−60	1541
T6NN2	−59	1546
T6NN3	−56	1552
T6NN4	−55	1557
T6NN5	−58	1565
T6NN10	−43	1599
T8NN0	—	1513
T8NN1	−59	1525
T8NN2	−55	1531
T8NN3	−55	1542
T8NN4	−53	1539
T8NN5	−45	1554
T8NN10	−52	1608

shape, namely P^2_{2P}, $P^2_{1Te,1P}$, and P^2_{2Te} units. As the latter are not detected by the double quantum filtering method, suitable fitting constraints to the MAS-NMR line shape can be developed. The final deconvolution, summarized in Fig. 7 corresponds to the expectations of a random linkage model: P^2_{2Te} units dominate and their contribution to the overall P inventory is larger in the T8 series than in the T6 series, as expected from the composition. At the moment, the contributions from $P^2_{1Te,1P}$ and P^2_{2P} units cannot be individually resolved; in principle this would be possible by measuring double-quantum coherence buildup rates or DQ-DRENAR experiments, which are sensitive to the strength of the homonuclear ^{31}P–^{31}P magnetic dipole–dipole-interactions. Furthermore, in the fluoride-containing glasses, owing to their decreasing P content with

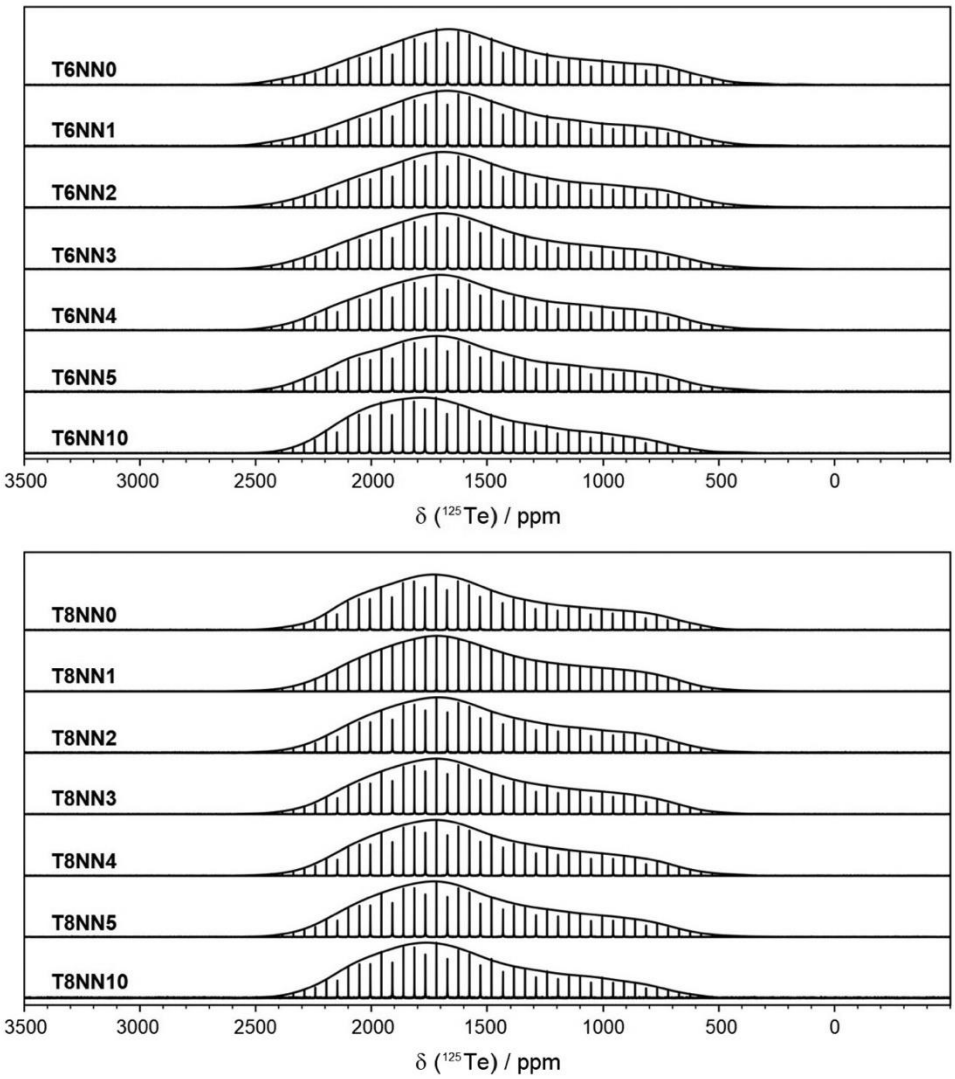

Fig. 12 Static ^{125}Te NMR spectra of the samples under study. Envelope representations are stacked on top of the respective spikelet spektrum obtained from the CPMG acquisition mode.

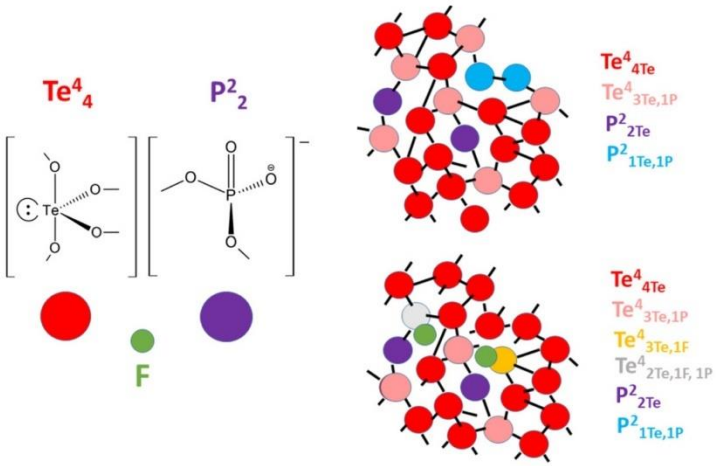

Fig. 13 Structural scheme of $yTeO_2$–$(1-y)[xNaF$–$(1-x)NaPO_3]$ glasses exemplarily depicted for the compositions $80TeO_2$–$20NaPO_3$ (y = 0.2, x = 0, top) and $80TeO_2$–$10NaPO_3$–10NaF (y = 0.2, x = 0.5, bottom). Network former units with different local environments and connectivity are denoted with different colors.

increasing x, the P^2_{2Te} units become more dominant in both the T8 and the T6 series as the NaF/$NaPO_3$ ratio is increased, see Fig. 7. The structural effect of NaF for $NaPO_3$ substitution can be summarized by the following models involving depolymerization of Te–O–Te, Te–O–P, and P–O–P linkages by the hypothetical melt reactions:

$$_{3/2}\mathrm{OTe{-}O{-}TeO_{3/2}} + \mathrm{NaF} \rightarrow {}_{3/2}\ \mathrm{OTe{-}O^-\,Na^+} + \mathrm{F{-}TeO_{3/2}} \quad (1)$$

$$\mathrm{Na^+\,{}^-(O)_2(O)_{1/2}\,P-O-TeO_{3/2}} + \mathrm{NaF} \rightarrow \mathrm{Na^+\,{}^-(O)_2(O)_{1/2}P-O^-\,Na^+} + \mathrm{F-TeO_{3/2}} \quad (2)$$

$$\mathrm{Na^+\,{}^-(O)_2(O)_{1/2}\,P-O-TeO_{3/2}} + \mathrm{NaF} \rightarrow \mathrm{{}^-(O)_2(O)_{1/2}P-F} + \mathrm{Na^+\,O^-} - \mathrm{TeO_{3/2}} \quad (3)$$

$$\mathrm{Na^+\,{}^-(O)_2(O)_{1/2}P-O-}P(\mathrm{O_{1/2}})\,\mathrm{O^-\,Na^+} + \mathrm{NaF} \rightarrow \mathrm{Na^+\,{}^-(O)_2(O)_{1/2}P-F} + \mathrm{Na^+\,{}^-O-}P(\mathrm{O_{1/2}})\mathrm{O^-\,Na^+} \quad (4)$$

In this model, reaction (1) involves breakage of a Te–O–Te linkage forming a Te–F bond and a non-bridging O atom linked to Te. Reaction (2) involves breakage of a Te–O–P linkage with formation of a Te–F bond and a non-bridging O-atom linked to Phosphorus, which would then become a P^1 unit. In reaction (3) the P–O–Te linkage would be broken with formation of a P–F bond and an additional non-bridging oxygen atom linked to tellurium, while reaction (4) implies breakage of a P–O–P linkage forming a P–F bond and a P^1 unit. The solid-state NMR results suggest that reactions (1) and (2) dominate, while the noticeable absence of P–F bonding detected by the $^{19}F\{^{31}P\}$ REDOR experiments shown in Fig. 11 suggest that reactions (3) and (4) play only a minor role. Fig. 13 shows a structural scheme exemplarily depicted for the glass compositions $80TeO_2$–$20NaPO_3$ and $80TeO_2$–$10NaPO_3$–10NaF. Network former units with different local environments and connectivity are denoted with different colors. Based on this preliminary working hypothesis the development of a comprehensive structural model will involve the quantification of these different network former units and a clarification of the structural role of the sodium ions.

At the present stage, the experimental evidence for Te–F bonding is only indirect and qualitative and is mainly based on the ^{19}F isotropic chemical shifts. In principle further spectroscopic evidence for Te–F bonding can be obtained by $^{125}Te/^{19}F$ double resonance experiments, which are, however, rather challenging. Measurements with direct ^{125}Te detection such as $^{125}Te\{^{19}F\}$ REDOR experiments are complicated by the large width of the ^{125}Te NMR signals and long spin–lattice relaxation times. In this regard an indirect detection method involving heteronuclear ^{125}Te–^{19}F double quantum coherences by the HQMC method, as first demonstrated under MAS conditions in various inorganic solids featuring nuclei with low natural abundances[77] appears more promising, particularly considering the large $^1J(^{125}Te$–$^{19}F)$ coupling constants found in the literature.[76] Such experiments are currently under consideration in our laboratories and will be subject of a forthcoming study.

5. Conclusions

To summarize, we have prepared new fluorophosphotellurite glasses in the ternary system TeO_2–NaF–$NaPO_3$ having the compositions $0.8TeO_2$–$0.2[x$NaF–$(1-x)NaPO_3]$ and $0.6TeO_2$–$0.4[x$NaF–$(1-x)NaPO_3]$ ($0 \le x \le 1$) and characterized their physical, optical and vibrational properties. Detailed structural information regarding the network-forming units and their

connectivity has been obtained from Raman spectroscopy and multinuclear solid-state NMR, using a variety of interaction-selective spectral editing approaches. The fluoride-free glasses can be understood, to a first approximation, in terms of a network comprised of randomly connected $TeO_{4/2}$ and $P(O_{2/2})(O_2)^-$ (metaphosphate-P^2 type) units with P–O–P, P–O–Te, and Te–O–Te linkages. On the other hand, replacement of the $NaPO_3$ by the NaF component results in partial network depolymerization reducing P–O–P connectivity without the formation of P–F bonds. Both ^{125}Te and ^{19}F NMR suggest the formation of new tellurium species characterized by Te–F bonding. The further spectroscopic characterization of these units and additional experiments clarifying the structural role of the sodium ions in these glasses by more advanced NMR studies are in progress, aiming at the development of a comprehensive structural model to be presented in a future contribution.

Conflicts of interest

The authors declare no competing financial interest.

Acknowledgements

Funding by DFG Grants No WU 237/8–1, EC168/20–1, and HA8201/3–1 is gratefully acknowledged. The authors also thank The São Paulo Research Foundation (FAPESP) for support *via* process 2013/07793–6. R. C. thanks FAPESP for a doctoral fellowship, process 2020/122801.

References

1 A. Jha, B. D. O. Richards, G. Jose, T. Toney Fernandez, C. J. Hill, J. Lousteau and P. Joshi, Review on structural, thermal, optical and spectroscopic properties of tellurium oxide-based glasses for fibre optic and waveguide applications, *Int. Mater. Rev.*, 2012, **57**, 357–382.

2 A. Jha, B. Richards, J. Gin, T. Teddy-Fernandez, P. Joshi, X. Jiang and J. Lousteau, Rare–earth ion doped TeO_2 and GeO_2 glasses as laser materials, *Prog. Mater. Sci.*, 2012, **57**, 1426–1491.

3 R. El Mallawany, *Tellurite Glasses Handbook*, CRC Press, Boca Raton, 2nd edn, 2016.

4 Y. Dimitriev, Glass Formation and Structural Models of Tellurite Glasses, *Chim. Chron.*, 1994, **23**, 361–366.

5 J. S. Wang, E. M. Vogel and E. Snitzer, Tellurite Glass: A New Candidate for Fiber Devices, *Opt. Mater.*, 1994, **3**, 187–203.

6 V. A. G. Rivera and D. Manzani, *Technological Advances in Tellurite Glasses: Properties, Processing, and Applications*, Springer Ser. Mater. Sci., Springers, 2017.

7 L. C. Barbosa, C. O. Filho and E. F. Chillcce, *Tellurite glasses for optical amplifiers*, Springer Ser. Mater. Sci., 2017, vol. 254, pp. 131–153.

8 M. Seshadri, L. C. Barbosa and M. Radha, Study on Structural, Optical and Gain Properties of 1.2 and 2.0 μm Emission Transitions in Ho^{3+}Doped Tellurite Glasses, *J. Non-Cryst. Solids*, 2014, **406**, 62–72.

9 D. Manzani, J. F. D. S. Petruci, K. Nigoghossian, A. A. Cardoso and S. J. L. Ribeiro, A portable luminescent thermometer based on green up–conversion emission of Er^{3+}/Yb^{3+}co-doped tellurite glass, *Sci. Rep.*, 2017, **7**, 41596.

10 C. Dunn, F. Kong, G. Gu, T. W. Hawkins, M. Jones, J. Parsons, A. Runnion, M. T. Kalichevsky-Dong, R. Salem, D. Liu, *et al.*, Solid tellurite optical fiber based on stack–and–draw method for mid–infrared supercontinuum generation, *Fibers*, 2017, **5**, 37–48.

11 R. G. Capelo, J. M. P. Almeida, D. F. Franco, G. Y. Poirier, C. R. Mendonça, M. Nalin and D. Manzani, *J. Mater. Res. Technol.*, 2021, **13**, 1296–1304.

12 W. C. Wang, W. J. Zhang, L. X. Li, Y. Liu, D. D. Chen, Q. Qian and Q. Y. Zhang, Spectroscopic and structural characterization of barium tellurite glass fibers for mid–infrared ultra–broad tunable fiber lasers, *Opt. Mater. Express*, 2016, **6**, 2095–2107.

13 M. Irrannejad, G. Jose, A. Jha and D. P. Stevenson, A Parametric study of Er^{3+} ions doped phosphor–tellurite glass thin films by pulsed laser deposition, *Opt. Mater.*, 2010, **33**, 215–219.

14 I. Apakova, O. Yanush, O. Derkacheva, V. Goncharuk, I. Maslennikova, I. Polyakova, A. Anan'ev, L. Maksimov and T. Markova, *J. Non-Cryst. Solids*, 2011, **357**, 2675–2683.

15 J. M. M. de Souza, K. O. Lima, J. L. Ferrari, L. J. Q. Maia, R. R. Gonçalves, R. F. Falci and D. Manzani, *Dalton Trans.*, 2022, **51**, 4087–4096.

16 Z. Duan, H. T. Tong, M. Liao, T. Cheng, M. Erwan, T. Suzuki and Y. Ohishi, New Phospho–Tellurite Glasses with Optimization of Transition Temperature and Refractive Index for Hybrid Microstructured Optical Fibers, *Opt. Mater.*, 2013, **35**, 2473–2479.

17 P. Nandi, A. Srinivasan and G. Jose, Structural Dependent Thermal and Optical Properties of Rare Earth Doped Glass with Mixed Glass Formers, *Opt. Mater.*, 2009, **31**, 653–659.

18 P. Nandi and G. Jose, Ytterbium–Doped P_2O_5–TeO_2 Glass for Laser Applications, *IEEE J. Quantum Electron.*, 2006, **13**, 101–103.

19 M. J. Weber, J. D. Myers and D. H. Blackburn, Optical Properties of Nd^{3+} in Tellurite and Phosphortellurite Glasses, *J. Appl. Phys.*, 1981, **52**, 2944–2949.

20 M. de Oliveira Jr., R. J. Amjad, A. S. S. de Camargo and H. Eckert, Network Former Mixing Effects in Heavy Metal Oxide Glasses: Structural Characterization of Lead Zinc Phosphotellurite Glasses Using NMR and EPR Spectroscopies, *J. Phys. Chem. C*, 2018, **122**, 23698–23711.

21 D. Manzani, J. B. Souza Junior, A. S. Reyna, M. L. Silva Neto, J. E. Q. Bautista, S. J. L. Ribeiro and C. B. de Araújo, Phosphotellurite glass and glass–ceramics with high TeO_2 contents: thermal, structural and optical properties, *Dalton Trans.*, 2019, **48**, 6261–6272.

22 J. Massera, A. Haldeman, J. Jackson, C. Rivero-Baleine, L. Petit and K. Richardson, Processing of tellurite–based glass with low OH content, *J. Am. Ceram. Soc.*, 2014, **94**, 130–136.

23 H. Ebendorff-Heidepriem, K. Kuan, M. R. Oermann, K. Knight and T. M. Monro, Extruded tellurite glass and fibers with low OH content for mid–infrared applications, *Opt. Mater. Express*, 2012, **2**, 432–442.

24 M. Lesniak, J. Zmojda, M. Kochanowicz, P. Miluski, A. Baranowska, G. Mach, M. Kuwik, J. Pisarska, W. A. Pisarski and D. Dorosz, Spectroscopic Properties of Erbium–Doped Oxyfluoride Phospho–Tellurite Glass and Transparent Glass–Ceramic Containing BaF_2 Nanocrystals, *Materials*, 2019, **12**, 3429.

25 M. D. O'Donnell, C. A. Miller, D. Furniss, V. K. Tikhomirov and A. B. Seddon, Fluorotellurite glasses with improved mid–infrared transmission, *J. Non-Cryst. Solids*, 2003, **331**, 48–57.

26 J. J. Zhang, J. B. Qiu and Y. Kawamoto, New oxyfluorotellurite glass: thermal analysis and structural analysis by means of Raman scattering, *Mater. Lett.*, 2002, **55**, 77–82.

27 M. D. O'Donnell, K. Richardson, R. Stolen, A. B. Seddon, D. Furniss, V. K. Tikhomirov, C. Rivero, M. Ramme, R. Stegeman, G. Stegeman, M. Couzi and T. Cardinal, Tellurite and Fluorotellurite Glasses for Fiberoptic Raman Amplifiers: Glass Characterization, Optical Properties, Raman Gain, Preliminary Fiberization, and Fiber Characterization, *J. Am. Ceram. Soc.*, 2007, **90**, 1448–1457.

28 G. Liao, Q. Chen, J. Xing, H. Gebavi, D. Milanese, M. Fokine and M. Ferraris, Preparation and characterization of new fluorotellurite glasses for photonics application, *J. Non-Cryst. Solids*, 2009, **355**, 447–452.

29 F. Huang, X. Liu, Y. Ma, S. Kang, L. Hu and D. Chen, Origin of near to middle infrared luminescence and energy transfer process of Er^{3+}/Yb^{3+} co–doped fluorotellurite glasses under different excitations, *Sci. Rep.*, 2015, **5**, 8233.

30 J. P. Laval, J. R. Duclere, V. Couderc, M. Allix, C. Genevois, V. Sarou-Kanlan, F. Fayon, P. E. Coulon, S. Chenu, M. Colas, J. Corenette and P. Thomas, Highly transparent flurotellurite glass–ceramics: Structural investigations and luminescence properties, *Inorg. Chem.*, 2019, **58**, 16387–16401.

31 E. K. Barimah, Y. Chen and R. Tenwick, Effect of Yb^{3+} on the Structural and Visible to Near–Infrared Wavelength Photoluminescence Properties in Sm^{3+}–Yb^{3+}–Codoped Barium Fluorotellurite Glasses, *J. Non-Cryst. Solids*, 2017, **472**(15), 39–45.

32 R. Tenwick, M. Al-Murish, G. Sherma and A. Jha, Effect of Yb^{3+} on the Structural and Visible to Near-Infrared Wavelength Photoluminescence Properties in Sm^{3+}–Yb^{3+}–Codoped Barium Fluorotellurite Glasses, *Materials*, 2022, **15**, 3314.

33 H. Lei, L. Zeng, F. Lin, Z. Qin, G. Li and J. Tang, Yb^{3+}/Er^{3+}incorporated fluorotellurite glasses with varying TeO_2 content for optical temperature sensing based on upconverted FIR technique, *J. Lumin.*, 2021, **229**, 117677.

34 P. Vani, G. Vinitha and N. Manikandan, Effect of dopants on the nonlinear optical properties of fluorotellurite glasses for optical limiting application, *Phys. Scr.*, 2021, **96**, 125804.

35 J. S. Barbosa, J. G. Batista, S. Danto, E. Fargin, T. Cardinal, G. Poirier and F. C. Cassanjes, Transparent Glasses and Glass–Ceramics in the Ternary System TeO_2–Nb_2O_5–PbF_2, *Materials*, 2021, **14**, 317.

36 M. Jayasimhadri, L. R. Moorthy, S. A. Saleem and R. V. S. S. N. Ravikumar, Spectroscopic characteristics of Sm^{3+} doped alkali fluorophosphate glasses, *Spectrochim. Acta, Part A*, 2006, **64**, 939–944.

37 L. R. Moorthy, M. Jayasimhadri, A. Radhapathy and R. V. S. S. N. Ravikumar, Lasing properties of Pr^{3+}–doped tellurofluorophosphate glasses, *Mater. Chem. Phys.*, 2005, **93**, 455–460.

38 M. Jayasimhadri, L. R. Moorthy, K. Kojima, K. Yamamoto, N. Wada and N. Wada, Optical properties of Dy^{3+} ions in alkalitelluro fluorophosphate glasses for laser materials, *J. Phys. D: Appl. Phys.*, 2006, **39**, 635–641.

39 H. Eckert, Spying with spins on messy materials, 60 years of glass structural elucidation by NMR spectroscopy, *Int. J. Appl. Glass Sci.*, 2018, **9**, 167–187.

40 D. Möncke and H. Eckert, Review on the structural analysis of fluoride phosphate and fluorophosphate glasses, *J. Non-Cryst. Solids X*, 2019, **3**, 100026.

41 M. T. Rinke, L. Zhang and H. Eckert, Structural integration of tellurium oxide into mixed–network former glasses: Connectivity distribution in the system $NaPO_3$–TeO_2, *ChemPhysChem*, 2007, **8**, 1988–1998.

42 D. Larink, M. T. Rinke and H. Eckert, Mixed Network Former Effects in Tellurite Glass Systems: Structure/Property Correlations in the System $(Na_2O)_{1/3}[(2TeO_2)_x, (P_2O_5)_{1-x}]_{2/3}$, *J. Phys. Chem. C*, 2015, **119**, 17539–17551.

43 P. Mosner, K. Vosejpkova, L. Koudelka, L. Montagne and B. Revel, Structure and properties of glasses in ZnO–P_2O_5–TeO_2 system, *J. Non-Cryst. Solids*, 2011, **357**, 2648–2652.

44 L. N. Alexiko, V. Y. Kavun, V. I. Kharchenko, A. B. Slobodyuk, I. G. Maslennikova and V. K. Goncharuk, Influence of the lead difluoride on ion mobility and thermal behavior of glasses in the TeO_2–PbO–P_2O_5–PbF_2 system according to NMR and DTA data, *J. Non-Cryst. Solids*, 2014, **401**, 119–123.

45 E. Kupce, R. Freeman and R. Adiabatic, Pulses for Wideband Inversion and Broadband Decoupling, *J. Magn. Reson., Ser. A*, 1995, **115**, 273–276.

46 L. A. O'Dell and R. W. Schurko, QCPMG Using Adiabatic Pulses for Faster Acquisition of Ultra–Wideline NMR Spectra, *Chem. Phys. Lett.*, 2008, **464**, 97–102.

47 A. W. MacGregor, L. A. O'Dell and R. W. Schurko, New Methods for the Acquisition of Ultra–Wideline Solid–State NMR Spectra of Spin–1/2 Nuclides, *J. Magn. Reson.*, 2011, **208**, 103–113.

48 H. Y. Carr and E. M. Purcell, Effects of Diffusion on Free Precession in Nuclear Magnetic Resonance Experiments, *Phys. Rev.*, 1954, **94**, 630–638.

49 S. Meiboom and D. Gill, Modified Spin–Echo Method for Measuring Nuclear Relaxation Times, *Rev. Sci. Instrum.*, 1958, **29**, 688–691.
50 J. Koppe and M. R. H. Hansen, Minimizing Lineshape Distortions in Static Ultra-wideline Nuclear Magnetic Resonance of Half-Integer Spin Quadrupolar Nuclei, *J. Phys. Chem. A*, 2020, **124**, 4314–4321.
51 A. Lesage, M. Bardet and L. Emsley, Through,–Bond Carbon–Carbon Connectivities in Disordered Solids by NMR, *J. Am. Chem. Soc.*, 1999, **121**, 10987–10993.
52 S. Cadars, J. Sein, L. Duma, A. Lesage, T. N. Pham, J. H. Baltisberger, S. P. Brown and L. Emsley, The Refocused INADEQUATE Experiment in Multiple Spin–systems: Interpreting Observed Correlation Peaks and Optimizing Lineshapes, *J. Magn. Reson.*, 2007, **188**, 24–34.
53 S. G. J. van Meerten, W. M. J. Franssen and A. P. M. Kentgens, ssNake: A cross–platform open–source NMR data processing and fitting application, *J. Magn. Reson.*, 2019, **301**, 56–66.
54 D. Massiot, F. Fayon, M. Capron, I. King, S. L. Calve, B. Alonso, J. O. Durand, B. Bujoli, Z. Gan, G. Hoatson and G. Modelling, One– and Two–Dimensional Solid–State NMR Spectra, *Magn. Reson. Chem.*, 2002, **40**, 70–76.
55 T. Gullion and J. Schaefer, Rotational–echo double–resonance NMR, *J. Magn. Reson.*, 1989, **81**, 196–200.
56 M. Luo, X. Sha, B. Chen, X. Zhang, H. Yu, X. Li, J. Zhang, S. Xu, Y. Cao, Y. Wang, X. Wang, Y. Zhang, D. Gao and L. Wang, Optical transition properties, internal quantum efficiencies, and temperature sensing of Er^{3+} doped $BaGd_2O_4$ phosphor with low maximum phonon energy, *J. Am. Ceram. Soc.*, 2022, **105**, 3353–3363.
57 I. Savelii, J. C. Jules, G. Gadret, B. Kibler, J. Fatome, M. El-Amraoui, N. Manikandan, X. Zheng, F. Désévédavy, J. M. Dudley, J. Troles, L. Brilland, G. Renversez and F. Smektala, Suspended core tellurite glass optical fibers for infrared supercontinuum generation, *Opt. Mater.*, 2011, **33**, 1661–1666.
58 A. Hrubý, Evaluation of glass–forming tendency by means of DTA, *Czech. J. Phys.*, 1972, **22**, 1187–1193.
59 M. C. Weinberg, Assessment of glass stability criteria, *Phys. Chem. Glasses*, 1994, **35**, 119–123.
60 Z. P. Lu and C. T. Liu, A new glass–forming ability criterion for bulk metallic glasses, *Acta Mater.*, 2002, **50**, 3501–3512.
61 Q. J. Rong, A. Osaka, T. Nanba, J. Takada and Y. Miwa, *J. Mater. Sci.*, 1992, **27**, 3793–3798.
62 J. Heo, D. Lam, G. Sigel, E. Mendoza and D. Hensley, Spectroscopic analysis of the structure and properties of alkali tellurite glasses, *J. Am. Ceram. Soc.*, 1992, **75**, 277–281.
63 T. Sekiya, N. Mochida, A. Ohtsuka and M. Tonokawa, Raman spectra of $MO_{1/2}TeO_2$ (M=Li, Na, K, Rb, Cs) glasses, *J. Non-Cryst. Solids*, 1992, **144**, 128–144.
64 H. Bradtmüller, A. C. M. Rodrigues and H. Eckert, Network former mixing (NFM) effects in alkali germanotellurite glasses, *J. Alloys Compd.*, 2021, **873**, 159835.
65 N. S. Tagiara, K. I. Chatzipanagis, H. Bradtmüller, A. C. M. Rodrigues, D. Möncke and E. I. Kamitsos, Network former mixing (NFM) effects in alkali germanotellurite glasses. A vibrational spectroscopic study, *J. Alloys Compd.*, 2021, **882**, 160782.
66 H. Li, Y. Su and S. K. Sundaram, Raman spectroscopic study of Nd–doped $10Na_2O$–$90TeO_2$ glasses, *J. Non-Cryst. Solids*, 2001, **293–295**, 402–409.
67 D. Manzani, J. B. S. Junior, A. S. Reyna, M. L. S. Neto, J. E. Q. Bautista, S. J. L. Ribeiro and C. B. de Araújo, Phosphotellurite glass and glass–ceramics with high TeO_2 contents: thermal, structural and optical properties, *Dalton Trans.*, 2019, **48**, 6261–6272.
68 G. Galleani, H. Bradtmüller, H. Fares, S. H. Santagneli, M. Nalin and H. Eckert, BiF_3 Incorporation in Na/Ba Mixed Network Modifier Fluoride–Phosphate Glasses: Structural Studies by Solid–State NMR and Raman Spectroscopies, *J. Phys. Chem. C*, 2020, **124**, 25578–25587.
69 R. K. Brow, Review: the structure of simple phosphate glasses, *J. Non-Cryst. Solids*, 2000, **263–264**, 1–28.
70 J. B. d'Espinose de Lacaillere, C. Fretigny and D. Massiot, MAS NMR spectra of quadrupolar nuclei in disordered solids: the Czjzek model, *J. Magn. Reson.*, 2008, **192**, 244–251.
71 H. Eckert, Short and Medium Range Order in Ion Conducting Glasses Studied by Modern Solid State NMR Techniques, *Z. Phys. Chem.*, 2010, **224**, 1591–1653.
72 P. J. Dirken, J. B. H. Jansen and R. D. Schuiling, Influence of octahedral polymerization on ^{23}Na and ^{27}Al MAS NMR in alkali fluoroaluminates, *Am. Mineral.*, 1992, **77**, 718–724.
73 M. de Oliveira, T. Uesbeck, T. S. Gonçalves, C. J. Magon, P. S. Pizani, A. S. S. de Camargo and H. Eckert, Network Structure and Rare–Earth Ion Local Environments in Fluoride Phosphate Photonic Glasses Studied by Solid–State NMR and Electron Paramagnetic Resonance Spectroscopies, *J. Phys. Chem. C*, 2015, **119**, 24574–24587.
74 M. de Oliveira, T. S. Gonçalves, C. Ferrari, C. J. Magon, P. S. Pizani, A. S. S. de Camargo and H. Eckert, Structure–Property Relations in Fluorophosphate Glasses: An Integrated Spectroscopic Strategy, *J. Phys. Chem. C*, 2017, **121**, 2968–2986.
75 H. Bradtmüller, L. Zhang, C. C. de Araujo, H. Eckert, D. Möncke, D. Ehrt and D. Structural, Studies of $NaPO_3$–AlF_3 Glasses by High–Resolution Double–Resonance NMR Spectroscopy, *J. Phys. Chem. C*, 2018, **122**, 21579–21588.
76 E. L. Muetterties and W. D. Phillips, Structure and exchange processes in some inorganic fluorides by nuclear magnetic resonance, *J. Am. Chem. Soc.*, 1959, **81**, 1084–1088.
77 D. Franke, C. Hudalla and H. Eckert, Heteronuclear X–Y Double Quantum MAS–NMR in Crystalline Inorganic Solids. Applications for Indirect Detection and Spectral Editing of Rare–Spin Resonances, *Solid State Nucl. Magn. Reson.*, 1992, **1**, 33–40.

Electronic Supplementary Material (ESI) for Dalton Transactions.

Structural characterization of a new fluorophosphotellurite glass system

Renato Grigolon Capelo[1#], Josef Maximilian Gerdes[2#], Ulrich Rehfuß[3#], Lais Dantas Silva[5], Michael Ryan Hansen[2*], Leo van Wüllen[3*], Hellmut Eckert[2,4*], Danilo Manzani[1*]

[1]São Carlos Institute of Chemistry – IQSC, University of São Paulo – USP, São Carlos, SP, Brazil
[2]Institut of Physical Chemistry, WWU Münster, Germany
[3]Physics Institute, University of Augsburg, Germany
[4]São Carlos Institute of Physics – IFSC, University of São Paulo – USP, São Carlos, SP, Brazil
[5] Center of Research, Technology, and Education in Vitreous Materials (CeRTEV), Department of Materials Engineering (DEMa), Federal University of São Carlos (UFSCar), 13565-905, São Carlos, SP, Brazil.

# Equally contributing authors

Supplemental Materials

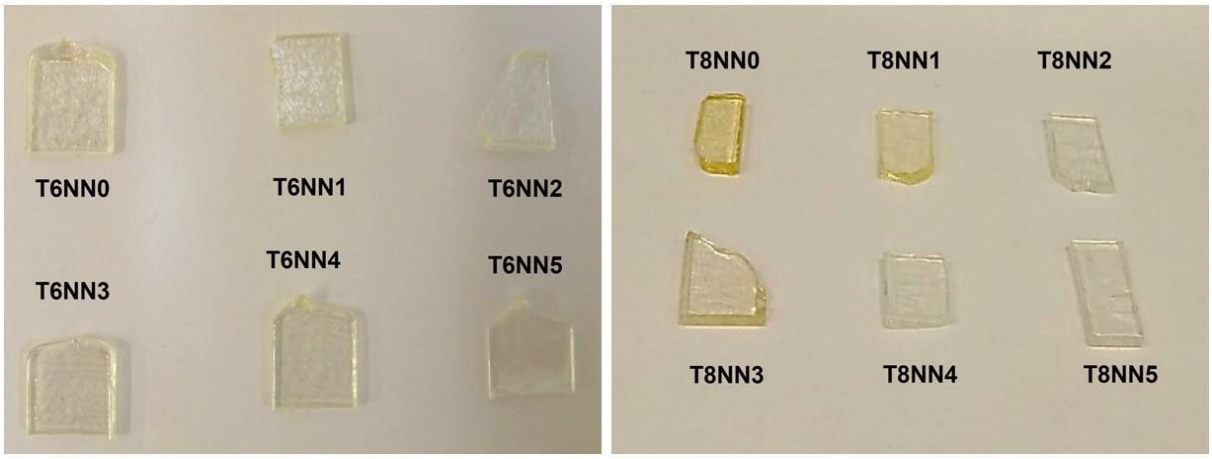

Figure S1. Photographs of the T6 and T8 set of glass samples.

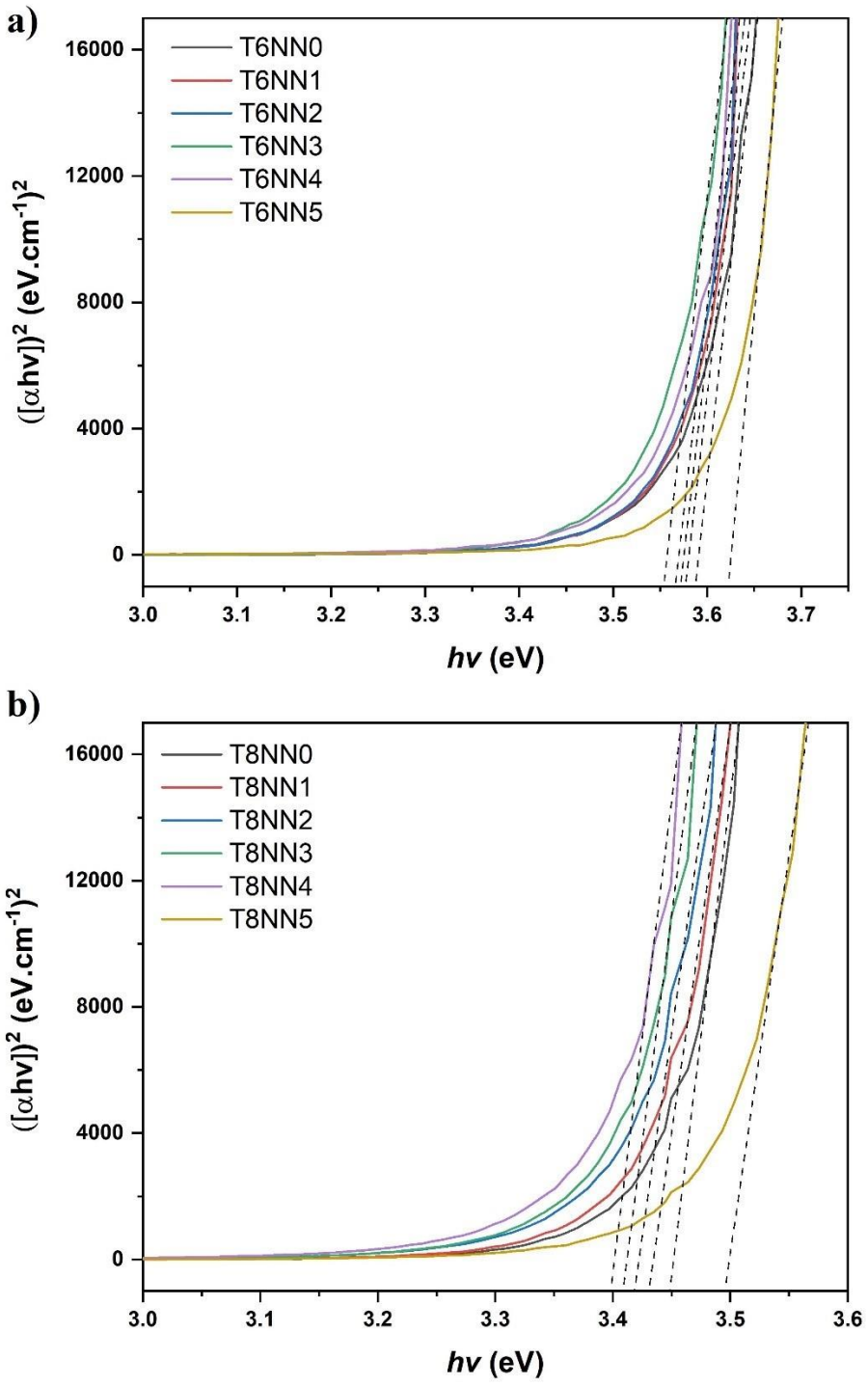

Figure S2. Curves $[\alpha(hv)]^2$ vs. hv obtained from the absorption spectra of (a) T6, and (b) T8 set of glass samples.

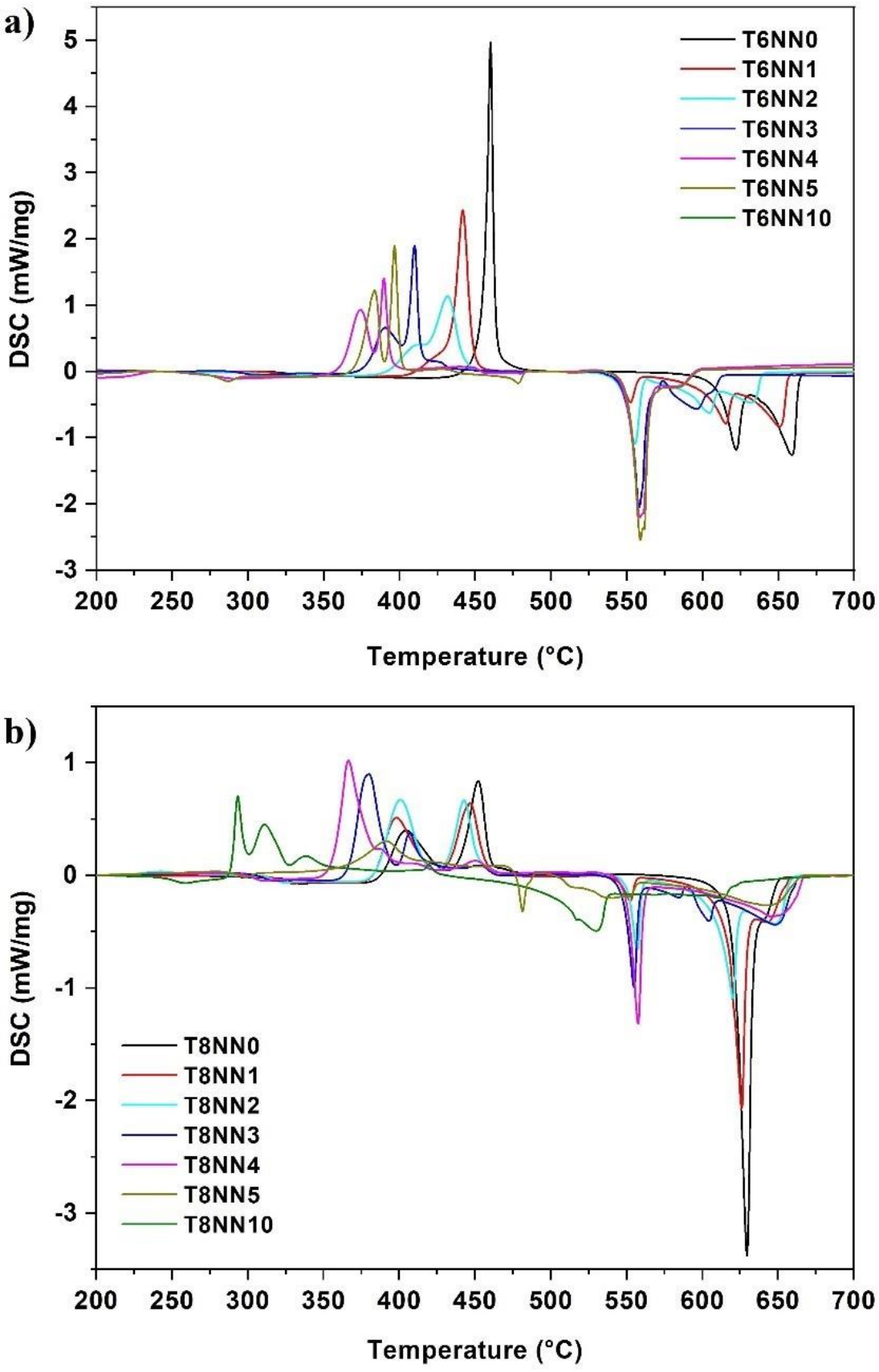

Figure S3. DSC curves for (a) series T6; and (b) series T8 of fluorophosphotellurite powder samples.

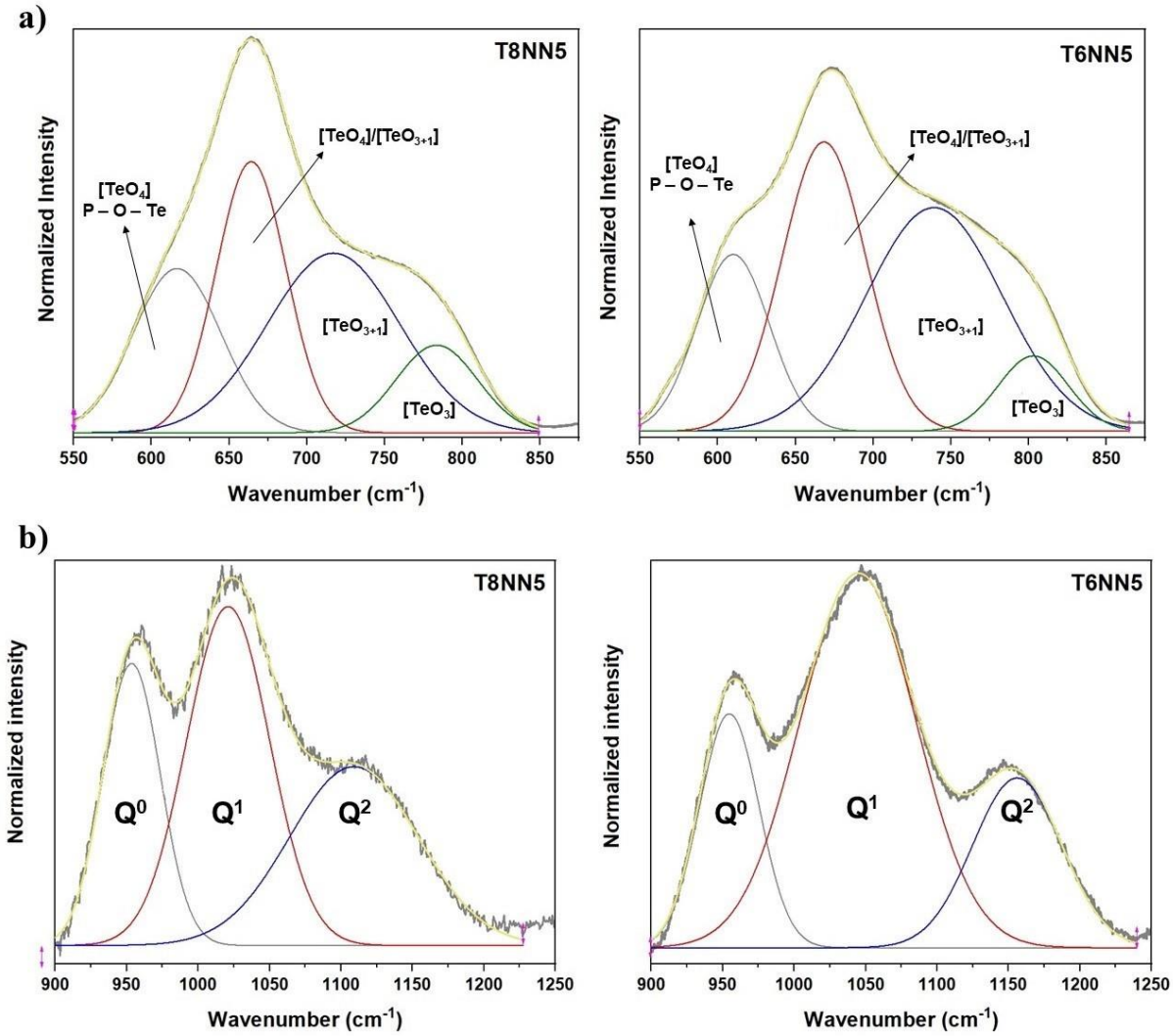

Figure S4. Representative Raman deconvoluted bands between (a) 550 to 900 cm^{-1} (tellurite bands), and (b) 900 to 1250 cm-1 (phosphate bands) for the T8NN5 and T6NN5 samples.

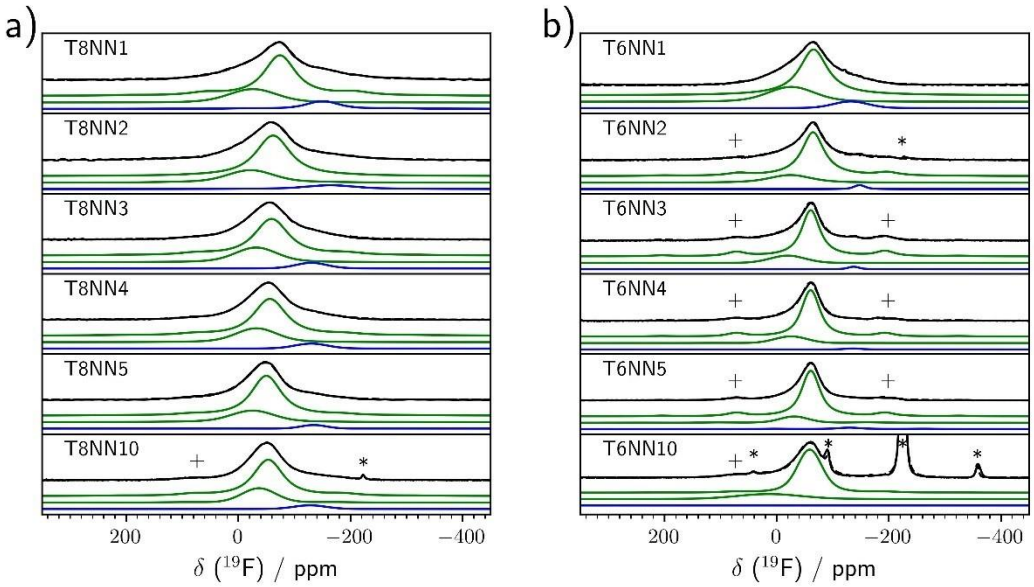

Figure S5. ^{19}F MAS NMR spectra of the samples under study, recorded with a rotor-synchronized Hahn-echo sequence at a rotation frequency of 25 kHz. Experimental spectra are shown on top with each fit component from tentative deconvolutions stacked below in green and blue. Visible spinning side bands are marked with a + symbol, impurities of NaF with their respective spinning sidebands are marked with asterisks.

Table S3. Isotropic chemical shifts and fractional area in percent of the integral as obtained from the tentative fits to the ^{19}F MAS NMR spectra to three distinct components.

	Component 1		**Component 2**		**Component 3**	
Sample	**δ / ppm**	**Area / %**	**δ / ppm**	**Area / %**	**δ / ppm**	**Area / %**
T6NN1	-25.1	27	-65.0	65	-131.2	8
T6NN2	-23.5	19	-63.9	79	-147	2
T6NN3	-18.7	14	-59.8	84	-136.3	2
T6NN4	-24.6	14	-59.7	85	-135.1	1
T6NN5	-30.3	14	-59.9	82	-129	4
T6NN10	14.6	21	-58.1	79		
T8NN1	-25.2	23	-73.4	66	-149.7	11
T8NN2	-21.0	24	-61.2	67	-163	9
T8NN3	-30.8	24	-58.4	69	-129.3	7
T8NN4	-31.4	24	-55.5	69	-129.1	7
T8NN5	-24.5	24	-49.2	72	-133.7	4
T8NN10	-36.1	24	-52.5	71	-126.8	5

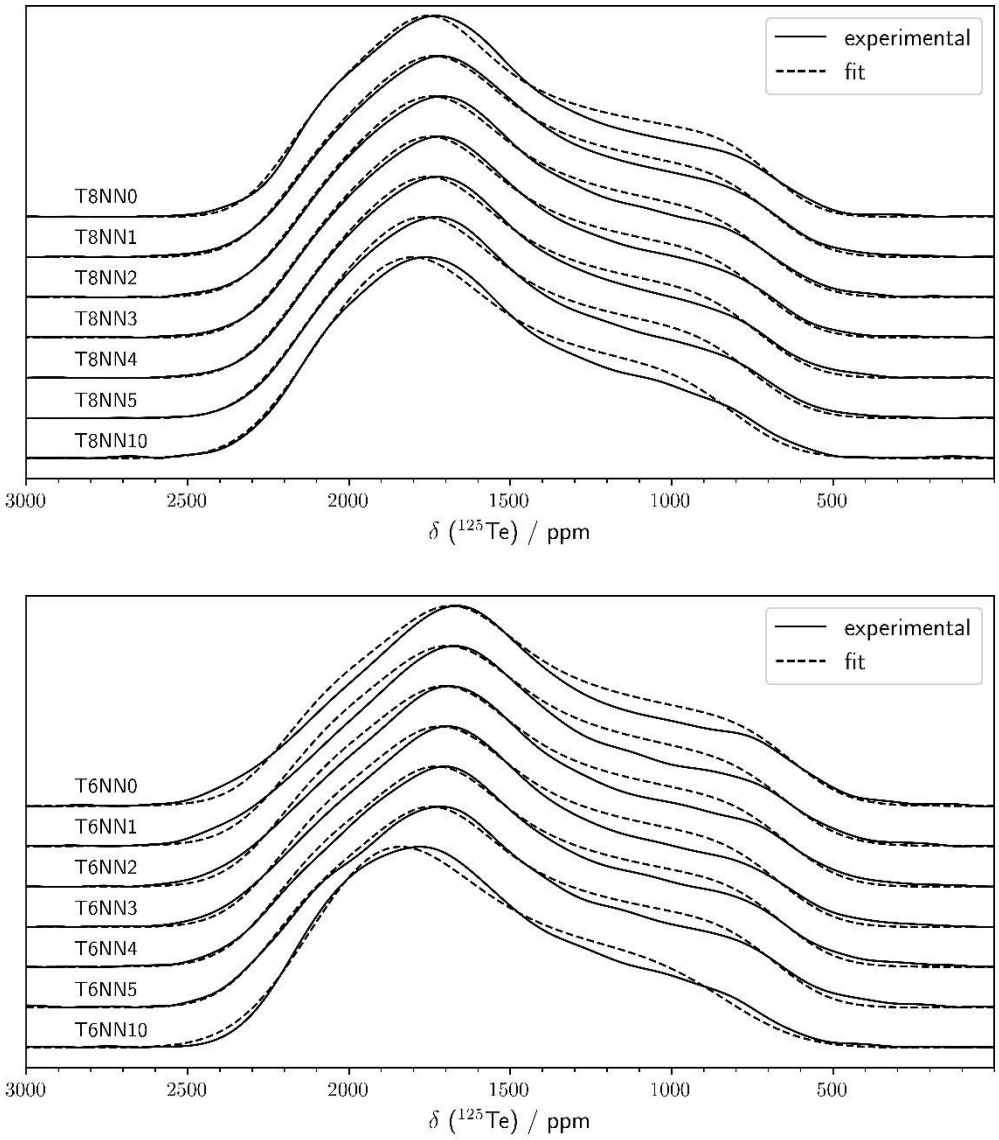

Figure S6. Static ^{125}Te NMR spectra of the samples under study. Dashed curves illustrate tentative fits assuming single Te-sites with the chemical shift tensor values listed in Table S4.

Table S4. Tentative ^{125}Te NMR lineshape fitting parameters for the glasses under study. Tensor elements are listed in the Haeberlen convention as well as principal axis values. The respective linebroadening paramter (lb) accounts for Gaussian type broadening of the resonance.

Sample	**δ_{iso} /ppm**	**δ_{aniso} /ppm**	**η**	**δ_{11} /ppm**	**δ_{22} /ppm**	**δ_{33} /ppm**	**lb /kHz**
T8NN0	1536	-854	0.52	2185	1740	682	27.2
T8NN1	1527	-848	0.54	2180	1722	679	30.6
T8NN2	1532	-839	0.53	2172	1729	693	30.9
T8NN3	1538	-834	0.54	2180	1729	704	30.3
T8NN4	1544	-828	0.53	2177	1739	716	30.9
T8NN5	1554	-820	0.51	2173	1755	734	32.1
T8NN10	1585	-790	0.48	2170	1790	795	33.4
T6NN0	1494	-878	0.59	2192	1674	616	29.4
T6NN1	1506	-870	0.59	2197	1684	636	30.7
T6NN2	1513	-880	0.59	2193	1693	633	31.1
T6NN3	1526	-871	0.59	2218	1704	655	31
T6NN4	1530	-884	0.58	2228	1716	646	29.5
T6NN5	1545	-879	0.57	2235	1734	666	30.7
T6NN10	1604	-795	0.36	2145	1858	809	40.1

CHAPTER IV:

Exploring the influence of ZnF_2 on zinc-tellurite glass: unveiling changes in OH content, structure, and optical properties

Reprinted with permission from R. G. Capelo, R. S. Baltieri, M Oliveira Jr and D. Manzani, **Exploring the Influence of ZnF_2 on Zinc-Tellurite Glass: Unveiling Changes in OH Content, Structure, and Optical Properties.** *ACS Omega*, 2023, 8, 38, 35266–35274. https://doi.org/10.1021/acsomega.3c05010.

Abstract

Tellurite glasses have garnered considerable interest as optical host materials due to their advantageous properties, including low processing temperature, high resistance to corrosion and crystallization, and excellent solubility for rare earth ions. However, their applicability in the infrared (IR) region is limited by the absorption of species with distinct vibrations. The incorporation of fluorides has emerged as a promising approach to reduce hydroxyl (OH) absorption during the precursor melting process. In this study, we investigated the influence of ZnF_2 on a glass matrix composed of TeO_2-ZnO-Na_2O, resulting in notable changes in the glass structure and optical properties, with Eu^{3+} serving as an environmental optical probe. The samples underwent comprehensive structural, thermal, and optical characterization. Structural analyses encompassed ^{19}F and ^{125}Te nuclear magnetic resonance (NMR), with the latter being complemented by mathematical simulations, and these findings were consistent with observations from Raman scattering. The main findings indicate an enhancement in thermal stability, modifications in the Te–O connectivity, and a reduction in emission intensity attributed to the effects of ligand polarizability and symmetry changes around Eu^{3+}. Additionally, the fluorotellurite matrices exhibited a shift in the absorption edge toward higher energies, accompanied by a decrease in mid-IR absorptions, thereby expanding the transparency window. As a result, these glass matrices hold substantial potential for applications across various regions of the electromagnetic spectrum, including optical fiber drawing and the development of solid-state emitting materials.

ACS OMEGA

Open Access

http://pubs.acs.org/journal/acsodf

Article

Exploring the Influence of ZnF_2 on Zinc-Tellurite Glass: Unveiling Changes in OH Content, Structure, and Optical Properties

Renato Grigolon Capelo,[§] Ricardo Santos Baltieri,[§] Marcos de Oliveira, Jr., and Danilo Manzani*

Cite This: *ACS Omega* 2023, 8, 35266−35274

Read Online

ACCESS | Metrics & More | Article Recommendations | Supporting Information

ABSTRACT: Tellurite glasses have garnered considerable interest as optical host materials due to their advantageous properties, including low processing temperature, high resistance to corrosion and crystallization, and excellent solubility for rare earth ions. However, their applicability in the infrared (IR) region is limited by the absorption of species with distinct vibrations. The incorporation of fluorides has emerged as a promising approach to reduce hydroxyl (OH) absorption during the precursor melting process. In this study, we investigated the influence of ZnF_2 on a glass matrix composed of TeO_2-ZnO-Na_2O, resulting in notable changes in the glass structure and optical properties, with Eu^{3+} serving as an environmental optical probe. The samples underwent comprehensive structural, thermal, and optical characterization. Structural analyses encompassed ^{19}F and ^{125}Te nuclear magnetic resonance (NMR), with the latter being complemented by mathematical simulations, and these findings were consistent with observations from Raman scattering. The main findings indicate an enhancement in thermal stability, modifications in the Te−O connectivity, and a reduction in emission intensity attributed to the effects of ligand polarizability and symmetry changes around Eu^{3+}. Additionally, the fluorotellurite matrices exhibited a shift in the absorption edge toward higher energies, accompanied by a decrease in mid-IR absorptions, thereby expanding the transparency window. As a result, these glass matrices hold substantial potential for applications across various regions of the electromagnetic spectrum, including optical fiber drawing and the development of solid-state emitting materials.

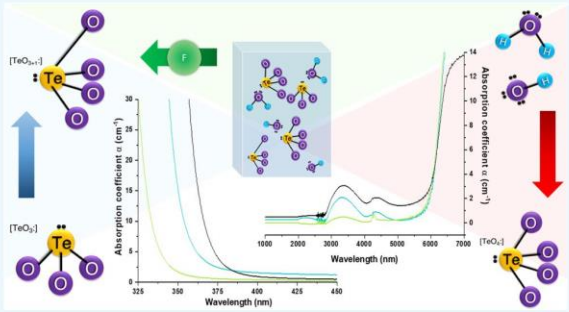

1. INTRODUCTION

Tellurite glasses, based on TeO_2, have been widely used as an alternative to traditional SiO_2-based glasses in various photonics applications.[1−3] Their unique structural and optical properties make them excellent host materials for optical fiber amplifiers, optical sensors, biosensors, energy converters, emitter devices, and several other applications.[4−7] Tellurite glasses generally present high stability against crystallization and corrosion, low phonon energy, and low melt and glass transition temperatures compared to other traditional glass matrices.[6,8] Moreover, according to their composition, this glass class also shows a highly linear and nonlinear refractive index, a broad optical window, and high solubility for photoluminescent rare earth ions (RE^{3+}).[9,10]

In general, TeO_2 is combined with alkali-based, alkaline earth, and transition metal oxides to form stable glasses.[11] For instance, in recent years, several studies on TeO_2-ZnO-Na_2O ternary glasses (TZN) have been performed for fiber optics drawing due to their interesting nonlinear properties and suitable glass stability.[12−14] However, the transparency window in the infrared region is commonly limited to 3 μm for these glasses due to the OH-group content and their strong absorption, which limits their use in some applications.[5] In this context, the addition of fluoride ions in tellurite glasses has received significant attention in research due to their potential to reduce the OH^- content by reacting with Te−OH bonds and water within the matrix.[2,12] Although it is expected to decrease thermal and mechanical stability, this approach proves effective to increase the glass transparency range from UV (~300 nm) to the mid-IR (4−6 μm), as well as enabling the production of stable glasses and optical fibers with high concentrations of RE^{3+}.[7,15−19]

Désévédavy and co-authors[2] have conducted a comprehensive examination of dehydration processes and their impact on the quality of optical fiber transmission. Undesirable OH absorption, which can originate from either H_2O or terminal groups, can have two primary sources: (1) the raw materials and (2) the glass synthesis process. Manufacturers rarely provide information concerning the former source of OH content, as it greatly depends on their specific synthesis

Received: July 12, 2023
Accepted: August 25, 2023
Published: September 13, 2023

methods. Nevertheless, this issue can be addressed through heat treatment of the oxides. However, as demonstrated by Dorofeev and co-authors,[20] the use of low O_2 pressure during this TeO_2 treatment may lead to tellurium reduction, necessitating specific conditions for consideration. In order to achieve better results, some research groups have chosen to prepare their own chemicals.[21] The second source of OH content arises during the fusion process and can result from reactions occurring within the melt or the furnace atmosphere. Specific reactions during the melting process can be induced by the addition of solid chemicals, such as alkali fluorides. Alternatively, control of the furnace atmosphere with reactive agents like F_2 and Cl_2 gases can also achieve the desired outcome, albeit requiring a more complex system. While the addition of alkali fluorides offers a simpler approach, it can significantly alter the structure of the glass matrix, a topic that is seldom discussed.

In summary, various methods have been explored to enhance the mid-infrared (mid-IR) quality of tellurite glasses, ranging from the addition of solid chemicals during the initial stages to controlling the atmosphere during preliminary heat treatment and glass melting in the synthesis process. Contamination from metals with 3d electrons is typically not visually apparent in tellurite glasses, as the electronic absorption edge of tellurite occurs at longer wavelengths than the electronic absorption of these metals.

Furthermore, the choice of crucibles[2] plays a significant role in the color of tellurite glasses when working with this type of glass. Common crucibles like platinum or corundum (Al_2O_3), can have a significant impact on the optical and structural properties. Although Pt or Al do not facilitate redox reactions with TeO_2, even during the melting of precursors, some authors have demonstrated that Pt can dissolve in the process, resulting in a yellowish coloration in the glass, unlike the completely transparent appearance achieved with Au crucibles. Considering the conditions required to achieve high mid-IR quality in tellurite-based glasses using desiccant chemicals like alkali fluorides, this study aims to investigate the observed changes in structural behavior when employing zinc fluoride (ZnF_2). Au crucibles were utilized to obtain fully transparent bulk glasses, and subsequently, a more detailed exploration of rare earth (RE) element doping is conducted.

Europium (Eu^{3+}) stands out as one of the most captivating and extensively researched RE^{3+}, primarily due to its myriad applications in lasers and optical communication. Additionally, its luminescence properties exhibit remarkable sensitivity to environmental factors, rendering it an invaluable spectroscopic probe.[22−25] The $^5D_0 \rightarrow {}^7F_2$ emission, referred to as hypersensitive, is strictly forbidden in sites with inversion centers;[26] therefore, any distortion caused by the environment around the ion increases the emission intensity. As an electric dipole transition, the hypersensitive emission of Eu^{3+} relies on the establishment of a vector within the ion, necessitating interaction with ligands. The magnitude of this vector decreases as the ion gets closer to a center of symmetry, leading to a reduction in emission intensity.[27] In contrast, for the emission involving $^7F_1$, which is a magnetic dipole transition, it is generally unaffected by the environment and can be used to calibrate all other emissions based on the total integrated intensity of the band. As several authors have enlightened,[26,28] factors beyond symmetry also influence the emission of most RE^{3+}, especially Eu^{3+}, such as polarizability and shape of ligands, which must be considered before drawing any conclusion. The ratio of $^5D_0 \rightarrow {}^7F_2$ to $^5D_0 \rightarrow {}^7F_2$ integrated intensity peak (electric to magnetic intensity ratio, EMIR) can be very helpful in understanding changes in Eu^{3+} emissions. In most oxide glasses, EMIR values typically fall within the range of 3−7, while for fluorides, they are generally in the range of 0.9−1.3.[29]

By these means, this study investigated how the addition of fluorine in tellurite glasses alters their optical properties and structural characteristics, with Eu^{3+} serving as a luminescent probe. In order to obtain additional information on structural behavior, we conducted Raman spectroscopy, ^{19}F nuclear magnetic resonance, and differential scanning calorimetry.

2. EXPERIMENTAL SECTION

2.1. Materials. Tellurium dioxide (TeO_2, Prichem, 99.99%), zinc oxide (ZnO, Alfa Aesar, 99%), anhydrous zinc fluoride (ZnF_2, Sigma-Aldrich, 99%), sodium carbonate (Na_2CO_3, Sigma-Aldrich, 99.5%), and europium oxide (Eu_2O_3, Lumtec, 99.9%) were used as received from the companies.

2.2. Glass Synthesis and Characterization. Undoped and Eu^{3+}-doped samples were prepared using the conventional melt-quenching method with compositions of TeO_2−ZnO−ZnF_2−Na_2O and TeO_2−ZnO−ZnF_2−Na_2O:Eu_2O_3, labeled as indicated in Table 1. Each batch was heated in a furnace at 750 °C for 20 min, then poured into a preheated brass mold, annealed for 120 min at 250 °C, and finally cooled at a rate of 10 °C/min down to room temperature. The samples were cut and polished for the measurements. For the samples containing 20 and 30% of ZnF_2, the concentrations of TeO_2 and Na_2O were also reduced. Additionally, samples doped with 0.5 mol % of Eu_2O_3 for TZN and TZNFx (x = 5, 10, 15, and 20 mol %) were prepared.

Table 1. Sample Labels and Molar Concentrations

	molar compositions (mol %)				
sample labels	TeO_2	ZnO	ZnF_2	Na_2O	Eu_2O_3
TZN	75	15	0	10	
TZNF5	75	10	5	10	
TZNF10	75	5	10	10	
TZNF15	75	0	15	10	
TZNF20	70	0	20	10	
TZNF30	62	0	30	8	
TZN-Eu	75	15	0	10	0.5
TZNF5-Eu	75	10	5	10	0.5
TZNF10-Eu	75	5	10	10	0.5
TZNF15-Eu	75	0	15	10	0.5
TZNF20-Eu	70	0	20	10	0.5

2.3. Differential Scanning Calorimetry. The DSC curves of the glass samples were recorded in a calorimeter DSC 404 F3 Pegasus, Netzsch, to identify the characteristic glass transition temperature (T_g, ±2 K), the onset temperature of crystallization (T_x, ±2 K), and thermal stability parameter ($\Delta T = T_x - T_g$, ±4 K) of the obtained glasses. Each bulk glass sample (~10 mg) was placed in an alumina crucible and heated from 100 to 550 °C at a heating rate of 10 K min^{-1} under a nitrogen atmosphere (20 mL min^{-1}).

2.4. Absorption Spectroscopy. The absorption spectra of the glass samples in both the UV−Visible and near-infrared (NIR) regions were measured at room temperature using a dual-beam spectrometer (Varian Cary 500) over the 300−900

https://doi.org/10.1021/acsomega.3c05010
ACS Omega 2023, 8, 35266−35274

nm range with a spectral resolution of 1.0 nm. To calculate the indirect optical band gap values, experimental absorbance data were utilized, and the samples had a thickness of approximately 1.7 mm.

2.5. Raman Spectroscopy. The Raman spectra were recorded over the 50−1500 cm^{-1} range with a spectral resolution of 1 cm^{-1} using a LabRAM HR micro-Raman (Horiba Jobin Yvon) equipped with a continuous HeNe laser emitting at 632.8 nm and delivering a power of 17 mW at room temperature.

2.6. Solid-State NMR. ^{19}F MAS and ^{125}Te static NMR spectra were recorded in an Agilent DD2 spectrometer operating at 5.64 T (corresponding to ^{1}H Larmor frequency of 240 MHz). ^{19}F spectra were acquired using 1.6 mm rotors spinning at 38 kHz with a DEPTH pulse sequence for background suppression,[30] a 90° pulse-length of 1.5 μs, relaxation delays of 300 s, and up to 160 scans for noise average. ^{19}F chemical shifts are reported relative to $CFCl_3$ using solid AlF_3 as a secondary reference (−172 ppm). Static ^{125}Te NMR spectra were obtained using the wideband-uniform rate-smooth truncation (WURST) scheme,[31,32] combined with the Carr−Purcell−Meiboom−Gill (CPMG) pulse sequence. Identical WURST-80 excitation and refocusing pulses were used, with pulse lengths set to 50.0 μs and the excitation bandwidth set to 500 kHz, recycle delay of 50 s, spikelet separation of 1 and 5 kHz (for crystalline α-TeO_2 and the glasses, respectively), and 128 Meiboom−Gill loops. The WURST-CPMG spectra presented here were obtained by fast Fourier transformation of the sum of the individual CPMG-echoes, resulting in an envelope spectrum. The advantage of this second method is that the signal-to-noise ratio is greatly improved. ^{125}Te Chemical shifts are reported relative to $Te(CH_3)_2$ using the isotropic shift of α-TeO_2 (1469 ppm) as secondary standard.[33]

2.7. Photoluminescence Spectra. The emission spectra of the Eu^{3+}-doped glass samples within the visible spectral range (550−750 nm) were acquired in a Horiba Fluorolog-3 spectrofluorometer using the front face acquisition mode. A 350 W Xenon arc lamp served as the excitation source, emitting at 394 nm. Detection was performed using a photodiode detector, PPD-850. To ensure accuracy, the emission spectra were corrected for the detection and optical spectral response of the spectrofluorometer.

3. RESULTS AND DISCUSSION

The glasses used in this study were optically homogeneous bulk samples with a colorless appearance, as depicted in the inset of Figure 1. A noticeable shift of the absorption edge toward higher energies was observed in samples containing ZnF_2 compared to the fluoride-free TZN sample. Figure 1 shows that the TZN sample exhibited an absorption edge at around 375 nm, corresponding to a band gap energy of 3.4 eV. Even with a lower ZnF_2 content (5 mol %), the sample exhibited a blue shift of more than 10 nm (or 0.13 eV), resulting in enhanced transparency. This trend continued as the fluoride concentration increased, ultimately reaching 330 nm (with a band gap energy of 3.8 eV) for the TZNF30 sample. Detailed band gap energy values are presented in Figure S1 and Table S1 in the Supporting Information (SI).

In addition to shifting the electronic absorption edge and enhancing transparency in the UV region, the incorporation of fluorides into oxide glasses proves to be an effective strategy for reducing the OH content within the glass network, thereby

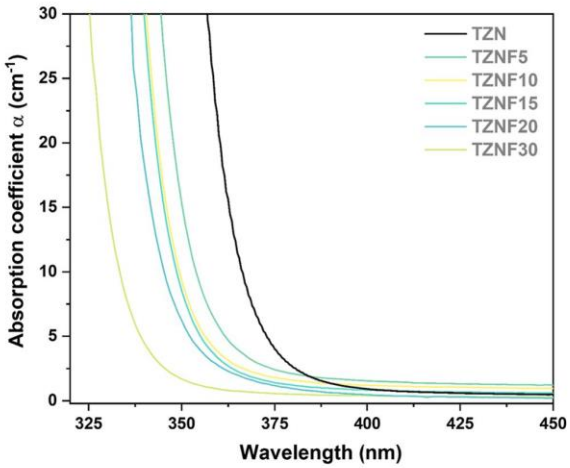

Figure 1. UV−vis absorption spectra carried out from 325 to 450 nm.

making them more suitable for infrared (IR) applications. Figure 2 illustrates the transparency window of the glass

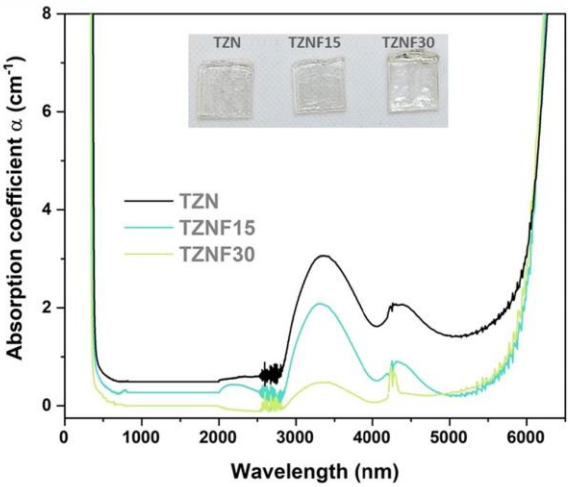

Figure 2. TZN, TZNF15, and TZNF30 transparency windows were obtained from the UV to mid-IR range. Inset: photograph of the synthesized glass samples.

samples from UV to the mid-infrared range. Within the mid-IR region, two prominent bands at 3.4 and 4.4 μm are associated with free OH groups and H_2O content, respectively.[40] It is evident that these bands significantly diminish as the concentration of ZnF_2 increases. The dehydroxylation process is facilitated by the reactions of ZnF_2 during the melting process, which can be described by the following equations.[41]

$$ZnF_2 + 2[\text{Te-OH}] \rightarrow ZnO + 2HF + [\text{Te−O−Te}] \quad (1)$$

and

$$2ZnF_2 + H_2O \rightarrow ZnO + 2HF \quad (2)$$

Therefore, while the extension of the multiphonon absorption edge is not considerably enhanced in this series, samples with higher ZnF_2 content exhibit a significant reduction in the OH band at 3.4 and 4.4 μm. This behavior not only confirms the

https://doi.org/10.1021/acsomega.3c05010
ACS Omega 2023, 8, 35266−35274

effectiveness of fluoride addition as an efficient strategy for producing oxide glasses with low OH content but also highlights the promising potential of these matrices as host materials for mid-IR lasers and optical amplifiers. Moreover, when combined with the favorable characteristics of tellurite glasses, including good thermal stability and high RE^{3+} solubility, these fluoride-modified glasses become even more suitable for such applications.[42−44]

The DSC curves were recorded for TZN, TZNF5, TZNF15, TZNF20, and TZNF30 samples and are presented in Figure 3.

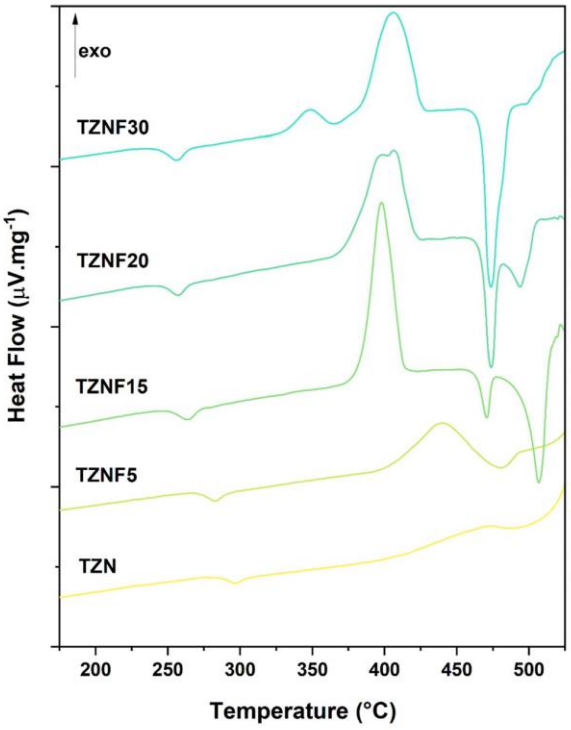

Figure 3. DSC curves for the samples TZN, TZNF5, TZNF15, TZNF20, and TZNF30.

The characteristic temperatures, including the glass transition (T_g) and the onset of crystallization (T_x), were estimated in accordance with the method described by ref 34 with an associated error of ±2 °C. A decrease in the characteristic temperatures can be observed as the fluoride content amount increases, which is attributed to the glass network depolymerization and softening.[18] The addition of ZnF_2 increases the ionic character of the matrix by replacing covalent bonds and making the glass structure less connected, lowering the T_g values.[35] An increase in the thermal stability against crystallization ($\Delta T = T_x - T_g$) for the samples with 5, 15, and 20 mol % of ZnF_2 in comparison to the TZN sample is also observed, as can be seen in Table 2. This behavior is important to evaluate the suitability of the matrices for optical fiber fabrication, as a larger ΔT is desirable to expand the working temperature range without inducing crystallization.[36] Once a glass with $\Delta T \geq 100$ °C is considered stable to be drawing as a fiber, it can be inferred that our tellurite and fluorotellurite glasses are thermically suitable for optical fiber production, with the exception of the TZNF30 sample, which

Table 2. Characteristic Temperatures (T_g, T_x, T_{p1}, and T_{p2}) and Thermal Stability against Crystallization ($\Delta T = T_x - T_g$) Obtained from DSC Measures

samples	T_g (°C)	T_x (°C)	T_{p1} (°C)	T_{p2} (°C)	ΔT (°C)
TZN	285	404	472		119
TZNF5	271	400	439		129
TZNF15	250	377	397		127
TZNF20	247	369	397	406	122
TZNF30	243	330	347	406	87

presents a higher tendency for devitrification and a thermal stability of 87 °C.

Particularly for the TZNF20 sample, a broad crystallization peak consisting of two distinct components is observed. It appears that these components become more separated as the ZnF_2 content increases to 30 mol % in the TZNF30 sample. In the DSC curve of TZNF30, two distinct crystallization peaks are observed, occurring at T_{p1} = 347 °C (TZNF30-T_{p1}) and T_{p2} = 406 °C (TZNF30-T_{p2}). To gain insights into this crystallization behavior, two bulk pieces of the TZNF30 sample were subjected to heat treatment at T_{p1} and T_{p2} for 30 min, followed by XRD analysis to identify the crystallized phases. XRD results for both portions of the sample (Figure S2) indicate the predominant formation of γ-TeO_2 at T_{p1} and α-TeO_2 at T_{p2}, along with some degree of mixing of the phase $Zn_2Te_3O_8$ in both portions. While these results may not have immediate practical implications, they contribute valuable insights into the structural and thermal behavior of this glass system, suggesting that the addition of ZnF_2 enhances the tendency for the formation of crystalline TeO_2 through network depolymerization.

Raman spectroscopy provides additional insight into the structural changes induced by the addition of ZnF_2. Typically, tellurite glasses exhibit characteristic bands in the range of 400−900 cm^{-1}. More specifically, Raman modes between 400 and 500 cm^{-1} are associated with bonds in Te−O−Te bridging configurations, while the bands in the higher frequency region correspond to tellurite structural units and the presence of non-bridging oxygen (NBO).[31] In this study, the focus is on the range of 550−900 cm^{-1}, referred to as the T region, which allows us to describe the structural behavior of the glass network in relation to fluoride content. In Figure 4, the Raman spectra of all samples are presented, exhibiting distinguishable variations in band intensities. To facilitate understanding, the T region (550−900 cm^{-1}) was deconvoluted into four Gaussian peaks, yielding a high correlation coefficient (R2) of ≥ 0.995 across all samples, as shown in Figure S3a−d. The identified vibrational modes labeled T1, T2, T3, and T4 correspond to specific structural units within the tellurite matrix. The T1 band, centered at 610 cm^{-1}, is assigned to the antisymmetric stretching of the [TeO_4] units, forming a continuous network.[36,37] At 660 cm^{-1}, the T2 band is associated with the antisymmetric vibrations of Te−O−Te bonds, involving two nonequivalent Te−O bonds.[36] Additionally, this band is influenced by the presence of [TeO_{3+1}] units, which exhibit a structural deformation with one elongated Te−O bond.[38] Hence, these bands can serve as indicators of network connectivity in the glass structure. Finally, the bands observed around 715 and 775 cm^{-1}, labeled as T3 and T4, respectively, can be attributed to the stretching modes of non-bridging oxygen (NBO) in the TeO_3 and TeO_{3+1} units. These

https://doi.org/10.1021/acsomega.3c05010
ACS Omega 2023, 8, 35266−35274

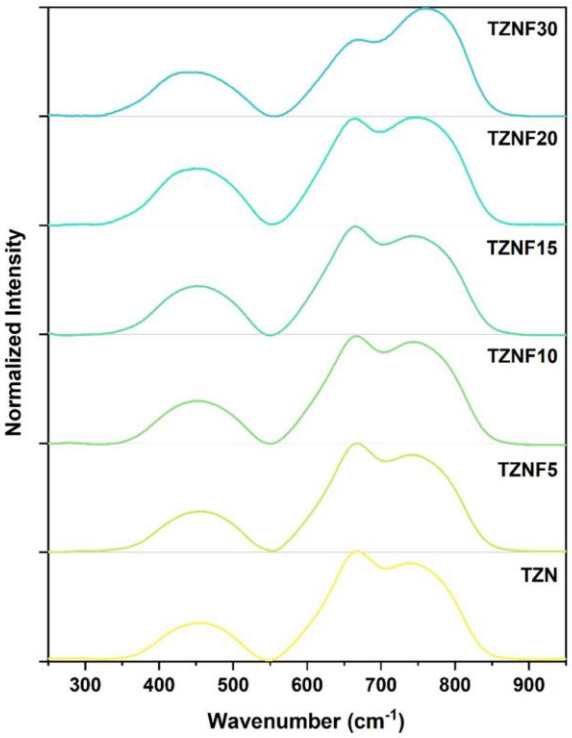

Figure 4. Raman spectra for all undoped glass systems.

bands have been linked to lower coordination [TeO_3] units, indicating depolymerization of the glass network.[18]

The integrated areas of each deconvoluted Raman band were normalized to the total intensity and are presented in Figure 5. To provide a semi-quantitative description of the influence of fluoride content on the glass network, the T1 and T2 bands were combined, as were the T3 and T4 bands. Table S2 presents the attribution, position, and relative area of each Raman band. This approach was employed to better characterize the network connectivity, where higher intensities of T1 and T2 indicate a more connected glass structure, while increased T3 and T4 intensities suggest a more open structural arrangement. As depicted in Figure 5, the incorporation of ZnF_2 into the glass composition leads to higher percentage values of T3 and T4 intensities, indicating an increased content of NBOs and the prevalence of [TeO_3] units in the glass network.[39] Specifically, this increase is most pronounced for the TZNF10 and TZNF30 samples, highlighting significant differences in their structural and optical properties when the fluoride content exceeds 10 mol %. FTIR measurements (Figure S4) were also conducted on the powdered samples; however, no additional insights into the structural behavior could be provided as a complement to the Raman analysis.[40−42]

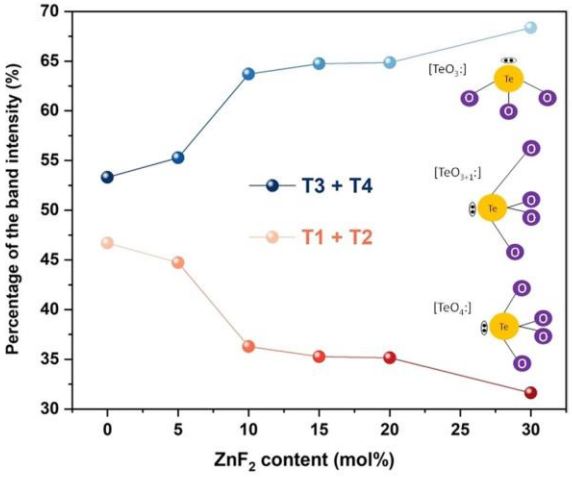

Figure 5. Percentage of characteristic tellurite Raman band intensities grouped as T1 + T2 and T3 + T4.

3.1. ^{19}F and ^{125}Te Solid-State NMR Spectroscopy.

Figure 6 displays the high-field ^{19}F MAS−NMR data, revealing

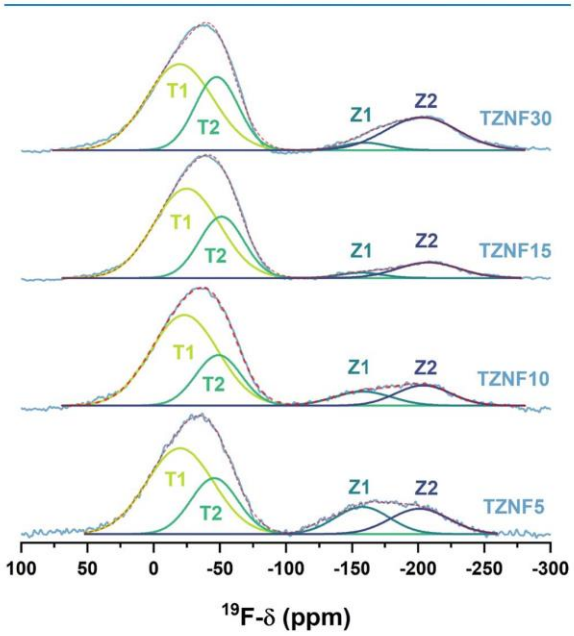

Figure 6. ^{19}F MAS−NMR spectra of the fluorotellurite samples with each fit component from tentative deconvolutions in black and gray.

two broad resonance bands at approximately −40 ppm and −170 ppm. The asymmetric line shapes suggest the presence of multiple components. Subsequent deconvolution of each broad peak was performed, and the results are summarized in Table 3. The first band is divided into two components centered around −23 ppm (T1) and −49 ppm (T2), respectively, with the former being more prominent. These chemical shift values are consistent with literature values for Te-bonded F species, previously assigned to δ_{iso} (^{19}F) = −27 ppm in a toluene solution of TeF_4 and δ_{iso} (^{19}F) = −45 ppm for TeF_5Cl.[43,44] Components Z1 and Z2, on the other hand, indicate the involvement of fluorine atoms in an alkaline medium and the presence of Zn−F interactions.[45−47] Component Z2 can be attributed to a mixed ZnF_2/NaF environment, with a chemical shift around −204 ppm consistent with the reference value for ZnF_2 and in proximity to the characteristic shift of NaF (−220 ppm).[48,49] The

https://doi.org/10.1021/acsomega.3c05010
ACS Omega 2023, 8, 35266−35274

Table 3. Isotropic Chemical Shifts and Fractional Area in Percent of the Integral, as Obtained from the Tentative Fits to the ^{19}F MAS−NMR Spectra to Four Distinct Components

	component 1		component 2		component 3		component 4	
sample	δ ^{19}F (±0.5 ppm)	area (±0.5%)	δ ^{19}F (±0.5 ppm)	area (±0.5%)	δ ^{19}F (±0.5 ppm)	area (±0.5%)	δ ^{19}F (±0.5 ppm)	area (±0.5%)
TZNF5	−21.4	50.7	−51.8	23.2	−156.3	13.1	202.6	13.0
TZNF10	−23.8	59.0	−47.9	22.2	−157.0	7.9	204.6	10.8
TZNF15	−25.5	60.0	−48.7	27.9	−157.8	2.3	208.9	9.8
TZNF30	−20.2	49.4	−46.0	27.3	−158.3	2.9	204.4	20.4

calculated area of each deconvoluted component suggests a trend of increasing Te−F interactions with the fluorine content, attributable to the high TeO_2 molar concentration (75 mol %). Additionally, for the TZNF30 sample, an increase in the area of component Z2 is observed, which aligns with the higher amount of ZnF_2. These ^{19}F NMR data support the results obtained from Raman spectroscopy and contribute to a better understanding of the glass structure in this system by highlighting the replacement of NBOs through the creation of terminal Te−F bonds.

Qualitative information about Te structural units can be provided by ^{125}Te NMR. Due to the low abundance (~7%) and high chemical shift anisotropy, combined with the intrinsic disorder of glasses, high-resolution ^{125}Te NMR is usually not practical in glass systems. Therefore, we have obtained static WURST-CPMG ^{125}Te NMR spectra for selected compositions, which are shown in Figure 7. As indicated by Raman

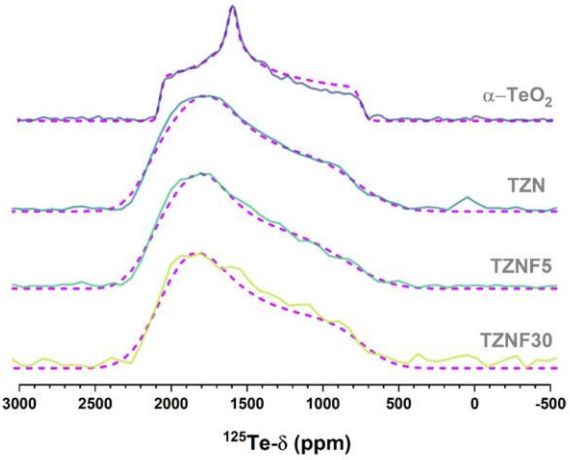

Figure 7. WURST-CPMG ^{125}Te NMR spectra for glass samples TZN, TZNF5, and TZNF30 (black solid curves). The plot shows Fourier-transformed spectra from the sum of the individual echoes in the CPMG FID. Red dashed curves are simulations considering distributions of static CSA powder patterns. 125Te Chemical shifts are referenced to $Te(CH_3)_2$.

data, the glass structure is formed by a mixture of distinct types of $[TeO_n]$ units. As a result, the NMR spectra are characterized by the superposition of resonances from distinct species. The resonance of each species, in its turn, is characterized by broad and anisotropic powder patterns resulting from distributions of chemical shift anisotropy parameters. Due to this strong overlap, the ^{125}Te spectra in Figure 7 do not provide site-selective information. To have qualitative information about the ^{125}Te spectra, we have performed simulations considering a statistical distribution of powder patterns with uncorrelated Gaussian distributions of the three principal values of the chemical shift tensor. This approach was employed recently by us for the study of heavy-metal oxide tellurium-phosphate glasses.[50] The best-fit simulations are shown in Figure 7. These simulations need to be treated as a simple mathematical tool to explore the characteristics of the average ^{125}Te NMR line shapes, and the simulation parameters are displayed in Table 4. The observed isotropic shifts agree with those previously observed for fluorophosphotellurite glasses containing similar concentrations of network modifier species.[49] The simulations show very minor variations in ^{125}Te NMR line shapes as a function of fluorine concentration. Remarkably, the width of the distribution in δ_{zz} becomes narrower for increasing ZnF_2 concentration. We can understand this narrower distribution of chemical shift parameters as the preferential formation of a certain type of Te structural unity. This agrees with the Raman results, which show that there is a tendency for the preferential formation of anionic TeO_3-like units with increasing F content.

3.2. Eu^{3+} as a Structural Probe for Structural Elucidation. To further elucidate the structural changes induced by the addition of ZnF_2, TZN and TZNF samples doped with Eu^{3+} were prepared, utilizing europium emission as a luminescent probe. Figure 8 illustrates the luminescence spectra of Eu^{3+} incorporated in the tellurite glass samples. To enhance the visualization of changes in the intensity of the $^5D_0 \rightarrow {}^7F_2$ hypersensitive transition, known to be dependent on the symmetry degree around Eu^{3+}, the spectra were normalized to the emission intensity of the $^5D_0 \rightarrow {}^7F_1$ transition. The observed decrease in band intensity for the $J = 2$ emission with increasing fluoride content clearly indicates that the presence of fluoride induces changes in the Eu^{3+} environment. Hypersensitive emission relies on the interaction with the dipole vector of ligands in the first coordination sphere and the distortion of the symmetric center. These changes suggest that Eu^{3+} preferentially binds with fluoride, a poorly polarizable ligand, even at low concentrations. Additionally, the addition of fluoride may bring the Eu^{3+} site closer to a centrosymmetric environment, resulting in a decrease in emission intensity, as demonstrated by the calculated EMIR (Europium Maximum Intensity Ratio). Furthermore, the analysis of the ratio between the integrated intensity of the non-normalized $J = 2$ and 1 transitions confirms the initial observation. The obtained values were 3.0, 2.8, 2.4, and 1.8 for TZN-Eu, TZNF5-Eu, TZNF10-Eu, and TZNF15-Eu, respectively, as shown in the inset of Figure 8. While the ratio of TZN falls within the expected range for oxide glasses, the addition of fluoride decreases the ratio to a minimum of 1.8, which is very close to that of fluoride glass matrices.[29] Consequently, the values of EMIR indicate that the $^5D_0 \rightarrow {}^7F_2$ transition is always dominant in these matrices, and the lower the fluoride content, the closer the site approaches a centrosymmetric environment expected for Eu^{3+}.

https://doi.org/10.1021/acsomega.3c05010
ACS Omega 2023, 8, 35266−35274

Table 4. Parameters Obtained from the Simulation of ^{125}Te Spectra Considering the Sum of Chemical Shift Anisotropy Powder Patterns with an Uncorrelated Normal Distribution of Principal Tensor Values[a]

samples	$\delta_{CG}(\pm 5)$	$\delta_{xx}(\pm 10)$	$\delta_{yy}(\pm 20)$	$\delta_{zz}(\pm 10)$	$\Delta\delta_{xx}(\pm 50)$	$\Delta\delta_{yy}(\pm 50)$	$\Delta\delta_{zz}(\pm 50)$	$\Delta(\pm 10)$
TZN	1540	2150	1760	745	100	300	600	200
TZNF5	1589	2150	1800	850	50	200	500	210
TZNF30	1522	2100	1820	730	50	200	200	250
α-TeO_2	1469	2070	1596	742				35

[a] δ_{ii} is the average value for the chemical shift principal values and $\Delta\delta_{ii}$ is the width of the distribution for each parameter. An isotropic line broadening parameter was also used (Δ) in the simulations. The center of gravity of the experimental spectrum, δ_{CG}, is also shown. All values are given in ppm, relative to $Te(CH_3)_2$.

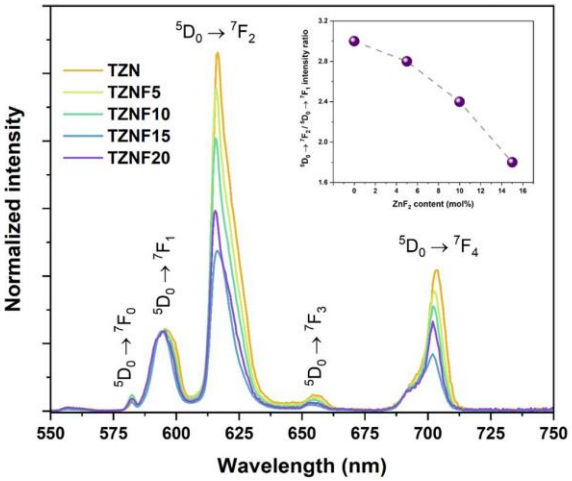

Figure 8. Photoluminescence spectra of fluorotellurite samples doped with Eu^{3+}.

Furthermore, it might be expected that the emissions of TZNF15-Eu and TZNF20-Eu would exhibit an inversion in intensity as the fluoride content increases. However, it should be noted that TZNF20-Eu demonstrates a significant decrease in TeO_2 content compared to the TZNF15-Eu sample. Therefore, a direct comparison of the two emissions must consider the structural changes that may have occurred between them. The results suggest that, despite the higher fluoride concentration, modifications induced in the matric structure have led to the Eu^{3+} occupying sites with enhanced emission symmetry. As discussed, the emission is influenced not only by the polarizability of fluoride but also by the symmetry of the europium ion's site, which is likely closer to a group with an inversion center for TZNF5-Eu, TZNF10-Eu, and TZNF15-Eu. The Ω_2 and Ω_4 parameters were calculated using Judd–Ofelt from Emission Spectra (JOES) software[51] and are presented in Table 5. This software simplifies the JO parameter calculations by inputting the Eu^{3+} emission spectra and indicating the emission range for each specific electronic transition. The refractive index values (n = 1.96) used for the calculations were obtained from matrices with similar compositions reported in the literature, such as $75TeO_2$-$15ZnO$-$10Na_2O$, which is identical to the TZN in this study, and $70TeO_2$-$10ZnO$-$20ZnF_2$, to account for the presence of ZnF_2.[18,52]

The Ω_2 parameter has been associated with the covalence of the glass matrix and the symmetry around Eu^{3+}, while the Ω_4 parameter has been linked to the rigidity and viscosity of the glassy network.[27,53] However, it should be noted that further research is needed to fully understand the Ω_4 parameter. In Table 5, both experimental parameters Ω_2 and Ω_4 exhibit a decrease as the fluoride concentration increases. This trend aligns with the findings from EMIR calculations and reinforces the notion that the addition of fluoride to the matrix modifies europium emission by altering properties such as network connectivity and the character of ionic/covalent bonds. The decrease in Ω_4, indicative of a less rigid matrix, is consistent with the observed decrease in T_g. It is important to mention that caution is advised when interpreting small changes in the experimental parameters Ω_2 and Ω_4, as there may be an error margin of up to 20%. Nevertheless, these results are in line with the conclusions drawn from other characterization techniques, including DSC, Raman, and NMR data.

Table 5. Calculated Judd–Ofelt Parameters Ω_2 and Ω_4 and Comparison with the Literature

	n	Ω_2 [10^{-20} cm^2]	Ω_4 [10^{-20} cm^2]	references
TZN-Eu	1.96	5.496	4.043	this work
TZNF5-Eu	1.96	4.846	3.323	this work
TZNF10-Eu	1.96	4.201	2.922	this work
TZNF15-Eu	1.96	3.177	2.350	this work
TZNF20-Eu	1.96	3.357	2.570	this work
TeO_2–Li_2CO_3	2.40	11.06	4.58	27
TeO_2–Li_2O-K_2O-ZnF_2	1.99	3.77	2.10	53
P_2O_5–MgO–$ZnSO_4$	1.75	14.40	1.26	54
SiO_2 (nanofiber)	1.45	3.27	2.80	55
$(Y_{0.7}Gd_{0.3})_2O_3$	1.65	1.30	1.20	56

4. CONCLUSIONS

The structural and optical properties of tellurite and fluorotellurite glasses were thoroughly examined in this study. The results demonstrate that the incorporation of fluoride induces significant changes in tellurite glasses, leading to a less covalently connected matrix, particularly affecting the [TeO_3] domains and enhancing the thermal stability against crystallization. Moreover, the Raman results obtained in this study are consistent with those obtained from the solid-state nuclear magnetic resonance (NMR) of ^{125}Te and ^{19}F. The addition of fluoride expands the transparency range of fluorotellurite glasses, both in the ultraviolet and infrared regions, resulting in a notable shift in the electronic edge and a significant reduction in OH band absorption. Furthermore, the investigation of luminescence behavior using Eu^{3+} as a spectroscopic probe reveals a strong interaction between fluoride and the emitting ion. This interaction also influences the glass matrix, affecting the coordination environment and modifying the emission through changes in ligand polarizability and symmetry. Despite a decrease in emission intensity with

https://doi.org/10.1021/acsomega.3c05010
ACS Omega 2023, 8, 35266−35274

increasing fluoride concentration, the emission intensity remains higher than in matrices containing solely fluorides, with the dominant process being the $^5D_0 \rightarrow {}^7F_2$ transition. Hence, these findings suggest that substituting ZnO with ZnF_2 in this glass system enhances its optical transmission while preserving thermal stability. Such properties are advantageous for applications involving luminescent glasses and the fabrication of optical fibers with low OH content.

■ ASSOCIATED CONTENT

Supporting Information

The Supporting Information is available free of charge at https://pubs.acs.org/doi/10.1021/acsomega.3c05010.

Band gap energy of all undoped glass samples calculated by the Tauc Plot method; complementary measurements of XRD and FTIR and deconvolution of Raman spectra for the TZN, TZNF10, TZNF20, and TZNF30 samples (PDF)

■ AUTHOR INFORMATION

Corresponding Author

Danilo Manzani − *São Carlos Institute of Chemistry—IQSC, University of São Paulo—USP, São Carlos 13560-970 SP, Brazil;* orcid.org/0000-0001-7280-5404; Email: dmanzani@usp.br

Authors

Renato Grigolon Capelo − *São Carlos Institute of Chemistry—IQSC, University of São Paulo—USP, São Carlos 13560-970 SP, Brazil*

Ricardo Santos Baltieri − *São Carlos Institute of Chemistry—IQSC, University of São Paulo—USP, São Carlos 13560-970 SP, Brazil;* orcid.org/0000-0003-3854-5850

Marcos de Oliveira, Jr. − *São Carlos Institute of Physics—IFSC, University of São Paulo—USP, São Carlos 13560-970 SP, Brazil;* orcid.org/0000-0001-6538-2204

Complete contact information is available at: https://pubs.acs.org/10.1021/acsomega.3c05010

Author Contributions

[§]R.G.C. and R.S.B. equally contributing authors.

Notes

The authors declare no competing financial interest.

■ ACKNOWLEDGMENTS

The authors acknowledge the financial support provided by the Brazilian research grants from São Paulo Research Foundation—FAPESP (2020/11038-2, 2020/12280-1, 2022/02974-1, and 2021/08111-2), CAPES (88887.495341/2020-00), and CNPq (405048/2021-1 and 311069/2020-7). R.G.C. acknowledges the funding received from Campus France 116708R.

■ REFERENCES

(1) Mori, A. Tellurite-based fibers and their applications to optical communication networks. *J. Ceram. Soc. Jpn.* **2008**, *116*, 1040−1051.

(2) Désévédavy, F.; Strutynski, C.; Lemière, A.; Mathey, P.; Gadret, G.; Jules, J.; Kibler, B.; Smektala, F. Review of tellurite glasses purification issues for mid-IR optical fiber applications. *J. Am. Ceram. Soc.* **2020**, *103*, 4017−4034.

(3) Saini, T. S.; Sinha, R. K. Mid-infrared supercontinuum generation in soft-glass specialty optical fibers: A review. *Prog Quantum Electron.* **2021**, *78*, No. 100342.

(4) Manzani, D.; Petruci, J. F. D. S.; Nigoghossian, K.; Cardoso, A. A.; Ribeiro, S. J. L. A portable luminescent thermometer based on green up-conversion emission of Er3+/Yb3+ co-doped tellurite glass. *Sci. Rep.* **2017**, *7*, No. 41596.

(5) Lin, A.; Zhang, A.; Bushong, E. J.; Toulouse, J. Solid-core tellurite glass fiber for infrared and nonlinear applications. *Opt. Express* **2009**, *17*, 16716.

(6) Jha, A.; Richards, B. D. O.; Jose, G.; Toney Fernandez, T.; Hill, C. J.; Lousteau, J.; Joshi, P. Review on structural, thermal, optical and spectroscopic properties of tellurium oxide based glasses for fibre optic and waveguide applications. *Int. Mater. Rev.* **2012**, *57*, 357−382.

(7) Ebendorff-Heidepriem, H.; Kuan, K.; Oermann, M. R.; Knight, K.; Monro, T. M. Extruded tellurite glass and fibers with low OH content for mid-infrared applications. *Opt. Mater. Express* **2012**, *2*, 432.

(8) Noguera, O.; Merle-Méjean, T.; Mirgorodsky, A. P.; Smirnov, M. B.; Thomas, P.; Champarnaud-Mesjard, J.-C. Vibrational and structural properties of glass and crystalline phases of TeO2. *J. Non-Cryst. Solids* **2003**, *330*, 50−60.

(9) El-Mallawany, R. A. H. *Tellurite Glasses Handbook: Physical Properties and Data*, 2nd ed.; CRC Press, 2016.

(10) Wang, W. C.; Zhang, W. J.; Li, L. X.; Liu, Y.; Chen, D. D.; Qian, Q.; Zhang, Q. Y. Spectroscopic and structural characterization of barium tellurite glass fibers for mid-infrared ultra-broad tunable fiber lasers. *Opt. Mater. Express* **2016**, *6*, 2095−2107.

(11) Mirdda, J. N.; Mukhopadhyay, S.; Sahu, K. R.; Goswami, M. N. Enhancement of Optical Emission and Dielectric Properties of Eu3+-Doped Na2O−ZnO−TeO2 Glass Material. *Glass Phys. Chem.* **2020**, *46*, 218−227.

(12) Savelii, I.; Desevedavy, F.; Jules, J.-C.; Gadret, G.; Fatome, J.; Kibler, B.; Kawashima, H.; Ohishi, Y.; Smektala, F. Management of OH absorption in tellurite optical fibers and related supercontinuum generation. *Opt. Mater.* **2013**, *35*, 1595−1599.

(13) Feng, X.; Shi, J.; Segura, M.; White, N. M.; Kannan, P.; Loh, W. H.; Calvez, L.; Zhang, X.; Brilland, L. Halo-tellurite glass fiber with low OH content for 2-5μm mid-infrared nonlinear applications. *Opt. Express* **2013**, *21*, 18949.

(14) Lin, A.; Ryasnyanskiy, A.; Toulouse, J. Fabrication and characterization of a water-free mid-infrared fluorotellurite glass. *Opt Lett.* **2011**, *36*, 740.

(15) Tao, G.; Ebendorff-Heidepriem, H.; Stolyarov, A. M.; Danto, S.; Badding, J. V.; Fink, Y.; Ballato, J.; Abouraddy, A. F. Infrared fibers. *Adv. Opt. Photonics* **2015**, *7*, 379.

(16) Zhan, H.; Shi, T.; Zhang, A.; Zhou, Z.; Si, J.; Lin, A. Nonlinear characterization on mid-infrared fluorotellurite glass fiber. *Mater. Lett.* **2014**, *120*, 174−176.

(17) Thomas, R. L.; Nampoori, V. P. N.; Radhakrishnan, P.; Thomas, S. Laser induced fluorescence in europium doped zinc tellurite glasses. *Optik* **2013**, *124*, 5840−5842.

(18) O'Donnell, M. D.; Richardson, K.; Stolen, R.; Seddon, A. B.; Furniss, D.; Tikhomirov, V. K.; Rivero, C.; Ramme, M.; Stegeman, R.; Stegeman, G.; Couzi, M.; Cardinal, T. Tellurite and Fluorotellurite Glasses for Fiberoptic Raman Amplifiers: Glass Characterization, Optical Properties, Raman Gain, Preliminary Fiberization, and Fiber Characterization. *J. Am. Ceram. Soc.* **2007**, *90*, 1448−1457.

(19) Saad, M. In *Fluoride Glass Fiber: State of the Art*, Proceedings Volume 7316, Fiber Optic Sensors and Applications VI, 2009.

(20) Dorofeev, V. V.; Moiseev, A. N.; Churbanov, M. F.; Snopatin, G. E.; Chilyasov, A. V.; Kraev, I. A.; Lobanov, A. S.; Kotereva, T. V.; Ketkova, L. A.; Pushkin, A. A.; Gerasimenko, V. V.; Plotnichenko, V. G.; Kosolapov, A. F.; Dianov, E. M. High-purity TeO2−WO3−(La2O3,Bi2O3) glasses for fiber-optics. *Opt. Mater.* **2011**, *33*, 1911−1915.

(21) Mori, A.; Kobayashi, K.; Yamada, M.; Kanamori, T.; Oikawa, K.; Nishida, Y.; Ohishi, Y. Low noise broadband tellurite-based Er3+-doped fibre amplifiers. *Electron. Lett.* **1998**, *34*, 887.

(22) Melgoza-Ramírez, M. L.; Ramírez-Bon, R. Europium ions as a spectroscopic probe in the study of PMMA-SiO2 hybrid micro-

structure with variable coupling agent. *J. Sol-Gel Sci. Technol.* **2021**, 46−56.
(23) Reisfeld, R.; Zigansky, E.; Gaft, M. Europium probe for estimation of site symmetry in glass films, glasses and crystals. *Molecular Physics* **2004**, *102*, 1319−1330.
(24) Kolesnikov, I. E.; Povolotskiy, A. V.; Mamonova, D. V.; Kolesnikov, E.Yu.; Kurochkin, A. V.; Lähderanta, E.; Mikhailov, M. D. Asymmetry ratio as a parameter of Eu 3+ local environment in phosphors. *J. Rare Earths* **2018**, *36*, 474−481.
(25) Cascales, C.; Balda, R.; Fernández, J.; Arriandiaga, M. A.; Fdez-Navarro, J. M. Fluorescence line narrowing spectroscopy of Eu3+ in TeO2−TiO2−Nb2O5 glass. *Opt. Mater.* **2009**, *31*, 1092−1095.
(26) Binnemans, K. Interpretation of europium(III) spectra. *Coord. Chem. Rev.* **2015**, *295*, 1−45.
(27) Kumar, A.; Rai, D. K.; Rai, S. B. Optical studies of Eu3+ ions doped in tellurite glass. *Spectrochim. Acta, Part A* **2002**, *58*, 2115−2125.
(28) Tanner, P. A. Some misconceptions concerning the electronic spectra of tri-positive europium and cerium. *Chem. Soc. Rev.* **2013**, *42*, 5090.
(29) Babu, P.; Jayasankar, C. K. Optical spectroscopy of Eu3+ ions in lithium borate and lithium fluoroborate glasses. *Phys. B* **2000**, *279*, 262−281.
(30) Cory, D. G.; Ritchey, W. M. Suppression of signals from the probe in bloch decay spectra. *J. Magn. Reson.* **1969**, *80*, 128−132.
(31) Schurko, R. W. Ultra-Wideline Solid-State NMR Spectroscopy. *Acc. Chem. Res.* **2013**, *46*, 1985−1995.
(32) O'Dell, L. A. The WURST kind of pulses in solid-state NMR. *Solid State Nucl. Magn. Reson.* **2013**, *55*−*56*, 28−41.
(33) Garaga, M. N.; Werner-Zwanziger, U.; Zwanziger, J. W. ^{125}Te NMR Probes of Tellurium Oxide Crystals: Shielding-Structure Correlations. *Inorg. Chem.* **2018**, *57*, 892−898.
(34) Varshneya, A. K.; Mauro, J. C. *Fundamentals of Inorganic Glasses*; Elsevier, 2019.
(35) Miguel, A.; Morea, R.; Gonzalo, J.; Arriandiaga, M. A.; Fernandez, J.; Balda, R. Near-infrared emission and upconversion in Er3+-doped TeO2−ZnO−ZnF2 glasses. *J Lumin.* **2013**, *140*, 38−44.
(36) Manning, S.; Ebendorff-Heidepriem, H.; Monro, T. M. Ternary tellurite glasses for the fabrication of nonlinear optical fibres. *Opt. Mater. Express* **2012**, *2*, 140.
(37) Heo, J.; Lam, D.; Sigel, G. H.; Mendoza, E. A.; Hensley, D. A. Spectroscopic Analysis of the Structure and Properties of Alkali Tellurite Glasses. *J. Am. Ceram. Soc.* **1992**, *75*, 277−281.
(38) Sekiya, T.; Mochida, N.; Ohtsuka, A.; Tonokawa, M. Raman spectra of MO1/2TeO2 (M = Li, Na, K, Rb, Cs and Tl) glasses. *J. Non-Cryst. Solids* **1992**, *144*, 128−144.
(39) Ahmmad, S. K.; Samee, M. A.; Taqiullah, S. M.; Rahman, S. FT-IR and Raman spectroscopic studies of ZnF_2 −ZnO−As_2 O_3 −TeO_2 glasses. *J. Taibah Univ. Sci.* **2016**, *10*, 329−339.
(40) Heo, J.; Lam, D.; Sigel, G. H.; Mendoza, E. A.; Hensley, D. A. Spectroscopic Analysis of the Structure and Properties of Alkali Tellurite Glasses. *J. Am. Ceram. Soc.* **1992**, *75*, 277−281.
(41) El Agammy, E. F.; Doweidar, H.; El-Egili, K.; Ramadan, R. Structure of PbF2−TeO2 glasses and glass-ceramics. *J. Mater. Res. Technol.* **2020**, *9*, 4016−4024.
(42) El Agammy, E. F.; Doweidar, H.; El-Egili, K.; Ramadan, R.; Jaremko, M.; Emwas, A.-H. Structure of NaF−TeO2 glasses and glass-ceramics. *Ceram. Int.* **2020**, *46*, 18551−18561.
(43) Muetterties, E. L.; Phillips, W. D. Structure and Exchange Processes in Some Inorganic Fluorides by Nuclear Magnetic Resonance[1]. *J. Am. Chem. Soc.* **1959**, *81*, 1084−1088.
(44) Lawlor, L. J.; Martin, A.; Murchie, M. P.; Passmore, J.; Sanders, J. C. P. ^{125}Te and ^{19}F NMR spectroscopic study of the hydrolysis of pentafluorotellurium chloride: evidence for *trans* - and *cis* -$HOTeF_4$ Cl and *cis*, *mer* -$(HO)_2$ TeF_3 Cl. *Can. J. Chem.* **1989**, *67*, 1501−1505.
(45) Chan, J. C. C.; Eckert, H. High-resolution 27Al−19F solid-state double resonance NMR studies of AlF3−BaF2−CaF2 glasses. *J. Non-Cryst. Solids* **2001**, *284*, 16−21.
(46) de Oliveira, M.; Uesbeck, T.; Gonçalves, T. S.; Magon, C. J.; Pizani, P. S.; de Camargo, A. S. S.; Eckert, H. Network Structure and Rare-Earth Ion Local Environments in Fluoride Phosphate Photonic Glasses Studied by Solid-State NMR and Electron Paramagnetic Resonance Spectroscopies. *J. Phys. Chem. C* **2015**, *119*, 24574−24587.
(47) Kilic, G.; Issever, U. G.; Ilik, E. Synthesis, characterization and crystalline phase studies of TeO2−Ta2O5−ZnO/ZnF2 oxyfluoride semiconducting glasses. *J. Non-Cryst. Solids* **2020**, *527*, No. 119747.
(48) Zheng, A.; Liu, S.-B.; Deng, F. ^{19}F Chemical Shift of Crystalline Metal Fluorides: Theoretical Predictions Based on Periodic Structure Models. *J. Phys. Chem. C* **2009**, *113*, 15018−15023.
(49) Capelo, R. G.; Gerdes, J. M.; Rehfuß, U.; Silva, L. D.; Hansen, M. R.; van Wüllen, L.; Eckert, H.; Manzani, D. Structural characterization of a new fluorophosphotellurite glass system. *Dalton Trans.* **2023**, *52*, 2227−2242.
(50) de Oliveira, M.; Amjad, R. J.; de Camargo, A. S. S.; Eckert, H. Network Former Mixing Effects in Heavy Metal Oxide Glasses: Structural Characterization of Lead Zinc Phosphotellurite Glasses Using NMR and EPR Spectroscopies. *J. Phys. Chem. C* **2018**, *122*, 23698−23711.
(51) Ćirić, A.; Stojadinović, S.; Sekulić, M.; Dramićanin, M. D. JOES: An application software for Judd-Ofelt analysis from Eu3+ emission spectra. *J. Lumin.* **2019**, *205*, 351−356.
(52) Ruan, Y.; Ji, H.; Johnson, B. C.; Ohshima, T.; Greentree, A. D.; Gibson, B. C.; Monro, T. M.; Ebendorff-Heidepriem, H. Nano-diamond in tellurite glass Part II: practical nanodiamond-doped fibers. *Opt. Mater. Express* **2015**, *5*, 73.
(53) Joseph, X.; George, R.; Thomas, S.; Gopinath, M.; Sajna, M. S.; Unnikrishnan, N. V. Spectroscopic investigations on Eu3+ ions in Li−K−Zn fluorotellurite glasses. *Opt. Mater.* **2014**, *37*, 552−560.
(54) Danmallam, I. M.; Ghoshal, S. K.; Ariffin, R.; Jupri, S. A.; Sharma, S.; Bulus, I. Judd-Ofelt evaluation of europium ion transition enhancement in phosphate glass. *Optik* **2019**, *196*, No. 163197.
(55) Chen, J.; Song, Y.; Sheng, Y.; Chang, M.; Xie, X.; Abualrejal, M. M. A.; Guan, H.; Shi, Z.; Zou, H. Luminescence properties and Judd−Ofelt analysis of SiO 2:Ln 3+ (Eu, Tb) hollow nanofibers fabricated by co-axial electrospinning method. *J. Alloys Compd.* **2017**, *716*, 144−155.
(56) Vujčić, I.; Glais, E.; Vuković, K.; Sekulić, M.; Mašić, S.; Chanéac, C.; Dramićanin, M. D.; Viana, B. Radiation effects, photoluminescence and radioluminescence of Eu-doped (Y0.7Gd0.3)2O3 nanoparticles with various sizes. *Opt. Mater.* **2018**, *86*, 582−589.

https://doi.org/10.1021/acsomega.3c05010
ACS Omega 2023, 8, 35266−35274

SUPPORTING INFORMATION

Exploring the influence of ZnF_2 on zinc-tellurite glass: Unveiling changes in OH content, structure, and optical properties

Renato Grigolon Capelo[1#], Ricardo Santos Baltieri[1#], Marcos de Oliveira Jr. [2], Danilo Manzani[1]*

[1] *São Carlos Institute of Chemistry - IQSC, University of São Paulo - USP, São Carlos, SP, Brazil*
[1] *São Carlos Institute of Physics – IFSC, University of São Paulo – USP, São Carlos, SP, Brazil*

# Equally contributing authors

*Corresponding author: dmanzani@usp.br

Supplementary figures

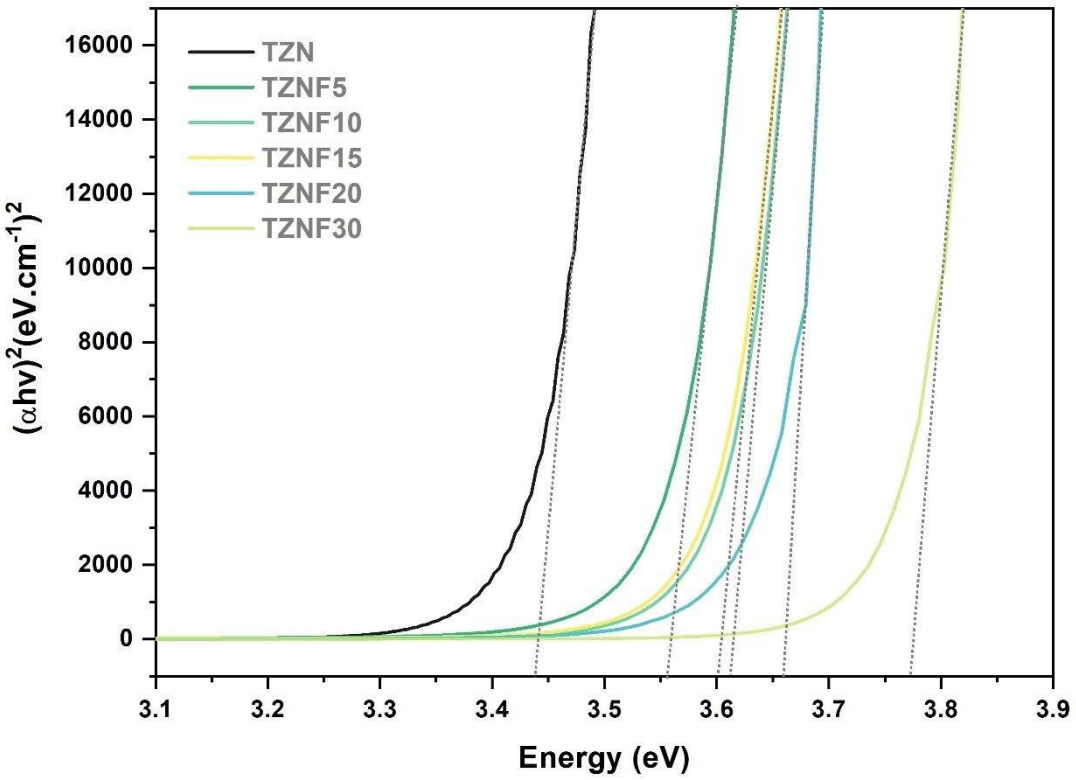

Figure S1. Bandgap energy curves calculated by Plot Tauc method.

Table S1. Bandgap energy values calculated for all undoped glass samples.

Samples	Bandgap Energy (eV)
TZN	3.43
TZNF5	3.56
TZNF10	3.60
TZNF15	3.61
TZNF20	3.65
TZNF30	3.76

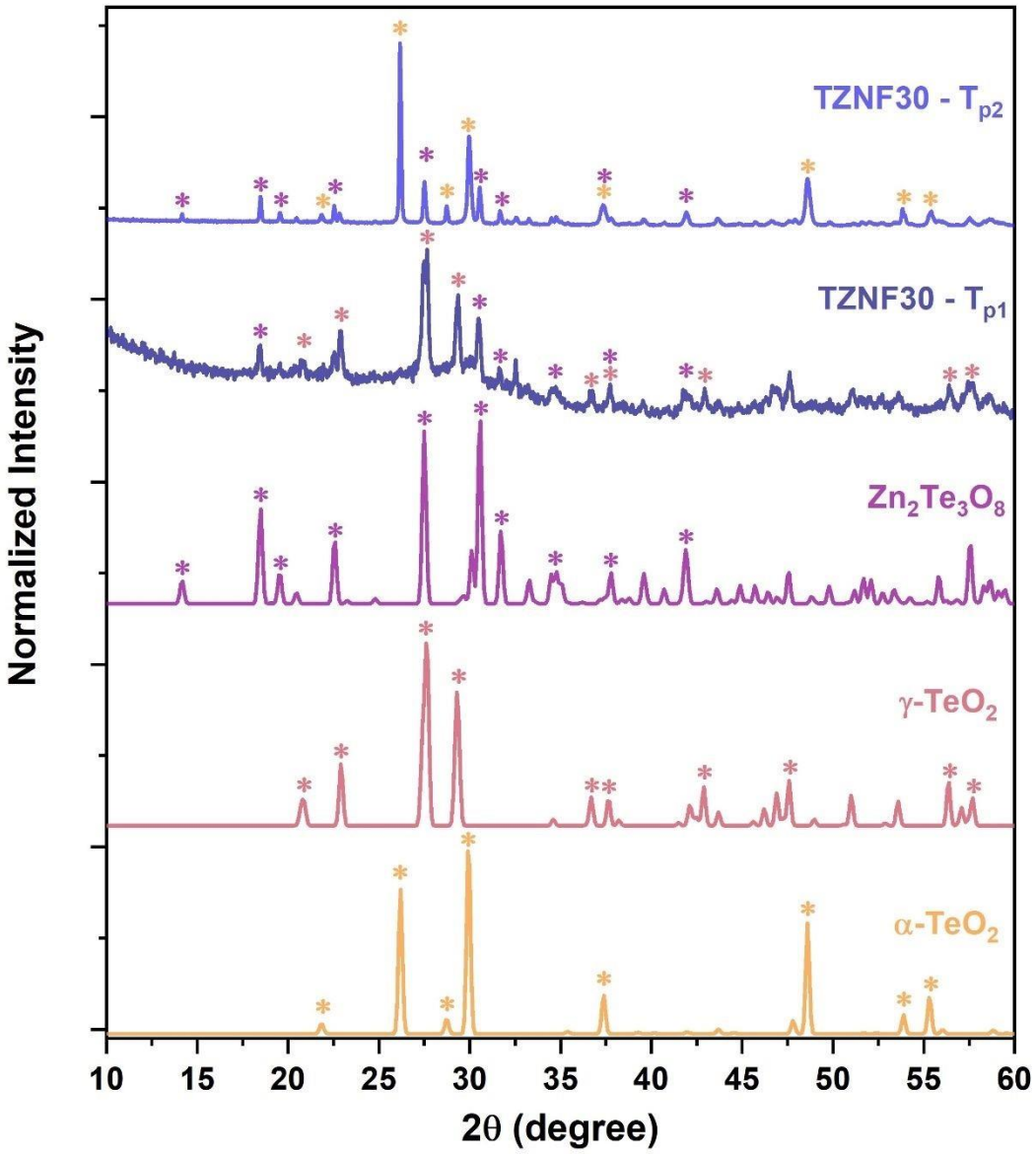

Figure S2. XRD diffractograms of TZNF30 sample treated at Tp1 = 347 °C and Tp2 = 406 °C and the diffraction patterns of α-TeO_2, γ--TeO_2, and $Zn_2Te_3O_8$ phases.

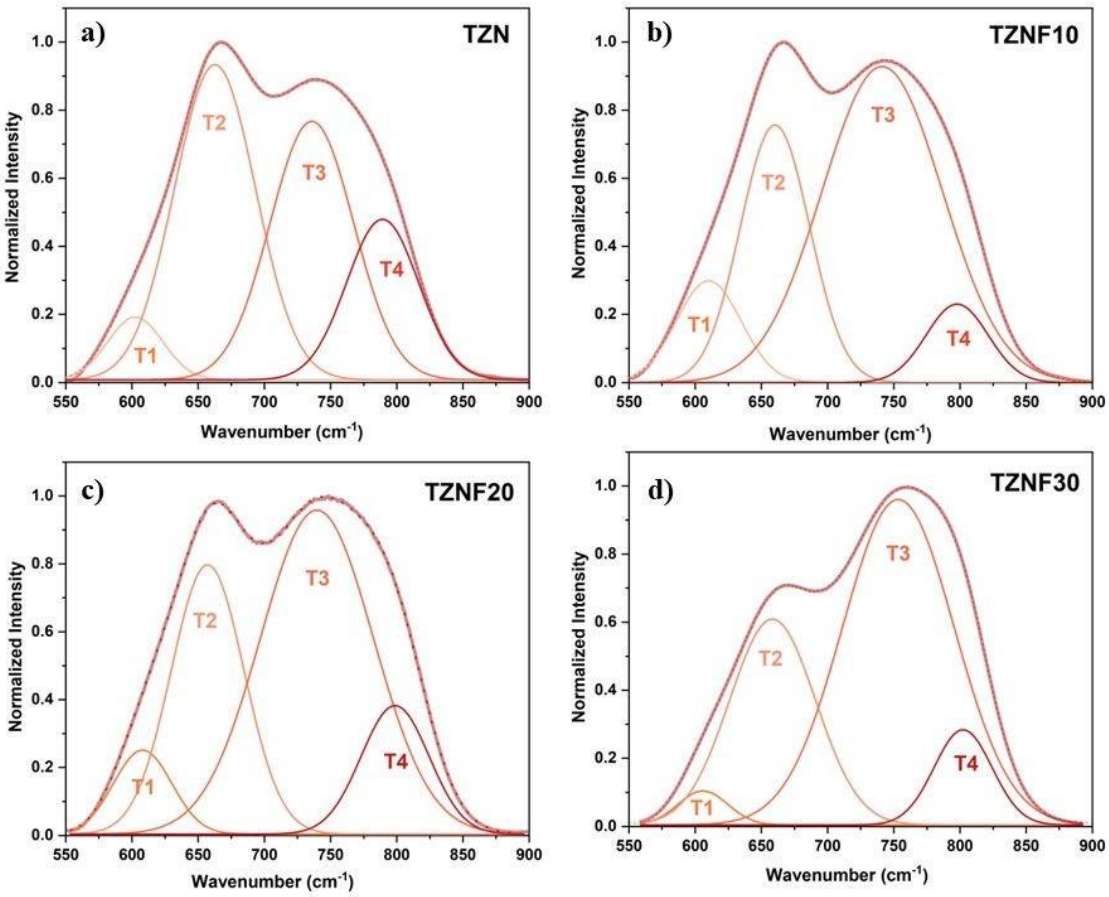

Figure S3. Representative Raman deconvoluted bands between 550 to 900 cm^{-1} (tellurite bands) for the (a) TZN, (b) TZNF10, (c) TZNF20, and (d) TZNF30 samples.

Table S2. Raman deconvoluted bands area in percent of the integral as obtained from the deconvolution of each Raman spectra.

Sample	Area (±0.5%)			
	T1 (610 cm^{-1})	T2 (660 cm^{-1})	T3 (715 cm^{-1})	T4 (755 cm^{-1})
TZN	5.6	41.1	34.7	18.6
TZNF5	6.7	38.0	35.6	19.6
TZNF10	9.8	26.5	56.5	7.2
TZNF15	9.5	25.7	57.6	7.1
TZNF20	7.0	28.2	52.3	12.5
TZNF30	2.7	28.9	59.3	9.1

CHAPTER V:

Effect of silver nanoparticles on the visible upconversion emission of Er^{3+}/Yb^{3+} co-doped $SbPO_4$-GeO_2 glasses

Reprinted with permission from R. G. Capelo, T. I. Rubio, G. L. Calderón, D. A. Moraes, E. Marega Jr, M. Nalin and D. Manzani, **Effect of silver nanoparticles on the visible upconversion emission of Er^{3+}/Yb^{3+} co-doped $SbPO_4$-GeO_2 glasses.** *Optical Materials*, 2023, 135, 113234. https://doi.org/10.1016/j.optmat.2022.113234.

Abstract

Rare earth-doped glasses are largely studied for developing new and efficient photonic devices. The influence of localized electric fields from the LSPR of metallic nanoparticles (MNP) on the rare-earth luminescent properties is a matter of study. This work describes the effect of Ag-MNP on the visible-upconversion emission of Er^{3+}/Yb^{3+}-co-doped $SbPO_4$-GeO_2 glass. Ag-MNP was obtained with an average size of ~5 nm and a LSPR absorption band at 520 nm. A significant enhancement of the red emission (~650 nm) of Er^{3+} as a function of Ag-MNPs content was observed. It showed silver nanocluster emission through excitation at infrared via energy transfer from Er^{3+} to the Ag nanoclusters. Photoluminescence spectroscopy revealed that longer heat treatment times increase the red emission and enhance the rapid depopulation of $^4F_{9/2}$ level, reducing the lifetime by 57% due to the LSPR of Ag-MNPs in the vicinity of the Er^{3+} and Yb^{3+}.

Optical Materials 135 (2023) 113234

Contents lists available at ScienceDirect

Optical Materials

journal homepage: www.elsevier.com/locate/optmat

Research Article

Effect of silver nanoparticles on the visible upconversion emission of Er^{3+}/Yb^{3+} co-doped $SbPO_4$-GeO_2 glasses

Renato Grigolon Capelo [a,1], Thiago Israel Rubio [a,1], Gaston Lozano Calderón [b,1], Daniel Angeli de Moraes [a], Euclydes Marega Junior [b], Marcelo Nalin [c], Danilo Manzani [a,*]

[a] São Carlos Institute of Chemistry - IQSC, University of São Paulo - USP, São Carlos, SP, Brazil
[b] São Carlos Institute of Physics - IFSC, University of São Paulo - USP, São Carlos, SP, Brazil
[c] Institute of Chemistry, São Paulo State University – UNESP, Araraquara, SP, Brazil

ARTICLE INFO

Keywords:
Antimony-phosphogermanate glass
Upconversion emission
Metallic nanoparticle
Localized-surface plasmon resonance

ABSTRACT

Rare earth-doped glasses are largely studied for developing new and efficient photonic devices. The influence of localized electric fields from the LSPR of metallic nanoparticles (MNP) on the rare-earth luminescent properties is a matter of study. This work describes the effect of Ag-MNP on the visible-upconversion emission of Er^{3+}/Yb^{3+}-co-doped $SbPO_4$-GeO_2 glass. Ag-MNP was obtained with an average size of ~5 nm and a LSPR absorption band at 520 nm. A significant enhancement of the red emission (~650 nm) of Er^{3+} as a function of Ag-MNPs content was observed. It showed silver nanocluster emission through excitation at infrared via energy transfer from Er^{3+} to the Ag nanoclusters. Photoluminescence spectroscopy revealed that longer heat treatment times increase the red emission and enhance the rapid depopulation of $^4F_{9/2}$ level, reducing the lifetime by 57% due to the LSPR of Ag-MNPs in the vicinity of the Er^{3+} and Yb^{3+}.

1. Introduction

Among the luminescent rare-earth ions (RE^{3+}), Er^{3+} plays an important role owing to their emission centered at 1550 nm, particularly important for optical amplification in integrated telecom systems [1]. Moreover, under 980 nm excitation, depending on their concentration, Er^{3+}-doped glasses also present visible emissions in green and red regions mainly through energy transfer upconversion (ETU) and excited-state absorption (ESA) mechanisms. These processes can be enhanced by co-doping with Yb^{3+}, which has a larger absorption cross-section at infrared and may effectively transfer energy to Er^{3+} beyond itself [2,3]. These emissions provide important applications in many areas, from high-density optical storage, optoelectronic devices for medical, photovoltaics, energy conversion, and optical amplifiers waveguides applications [4–7]. Furthermore, the addition of metallic nanoparticles (MNPs) may affect the upconversion (UC) luminescence by the presence of localized surface plasmon resonance (LSPR) and metal electronic bands. The LSPR consists of an optical phenomenon that occurs by the collective oscillation of the surface free electrons of the MNP contained in the conduction band, generating a localized electromagnetic field that enables the particles to act as a "nano-antenna", which perturbates the radiative and non-radiative decay rates of some RE^{3+} mostly mediated by local field effects (LFE), reflecting on their luminescence properties [8–11].

Silver MNPs have attracted considerable attention due to their tunable LSPR absorption from UV to the visible region, which usually can vary between 350 and 600 nm depending on the nanoparticle size and shape [12]. The coupling of f-f absorptions of RE^{3+} and LSPR bands from MNP can be resonant in energy leading to distortions in the energy transfer mechanisms involved in the UC luminescence processes [13]. Recently, Er^{3+}/Yb^{3+}-codoped glasses containing metallic silver nanoparticles (Ag-MNPs) have been studied regarding their luminescence properties and the enhancement of the UC emission intensities associated with LFE of the LSPR [14,15]. However, large amounts of Ag-MNP may reduce the luminescence intensities due to the light absorption by the MNPS and the energy transfer from RE^{3+} excited states to the metal electronic band [16]. Since the luminescence behavior is a function of the MNP concentration, size, and shape, new glass systems doped with RE^{3+} containing metallic nanoparticles have been the subject of several studies aimed at the development of improved materials for photonics

* Corresponding author. University of São Paulo, São Carlos Institute of Chemistry – IQSC. Department of Chemistry and Molecular Physics, São Carlos, SP, Brazil.
E-mail address: dmanzani@usp.br (D. Manzani).
[1] These authors equally contributed with this work.

https://doi.org/10.1016/j.optmat.2022.113234
Received 24 October 2022; Received in revised form 9 November 2022; Accepted 12 November 2022
Available online 28 November 2022
0925-3467/

[17–20].

Previous studies were carried out with the aim of broadening infrared emissions of Er^{3+} doped oxide glass in phosphate [21], boron-germanate [22], and tellurite [23], mainly for optical amplification. However, the interest in the UC emissions at the visible range is a growing field and has been extensively exploited for applications in energy conversion, photovoltaics, and solid-state lasers [24]. While silica-based glasses have good thermal stability, the drawbacks regard high phonon energy and low RE^{3+} solubility [25]. The choice of the glass composition is crucial for the development of RE^{3+} doped advanced photonic materials containing MNP since each composition presents a specific network that reflects on their viscosity and ions mobilities for a homogeneous MNP precipitation [26].

Phosphate glasses are enabling materials for laser technologies, sensing, and optical transmission based on their large transparency window from visible to near-infrared, low melting point, and high thermal stability against crystallization [27,28]. Specifically, antimony-phosphate glass has been used as photonic material due to its high linear and nonlinear refractive indexes [29], large transparency window from UV (350 nm) to NIR (4 μm) [30], low glass transition (T_g) and softening temperatures, which allow the design of optical fibers. On the other hand, glasses containing high concentrations of antimony are not good hosts for RE^{3+} and are usually present in combination with other oxides, such as GeO_2, which helps to increase the RE^{3+} solubility [31,32]. Meanwhile, germanate glasses have been increasingly studied due to their great properties regarding thermal stability, appreciating RE^{3+} solubility, wide infrared transparency up to 5 μm, and chemical durability [31], which make them an attractive alternative for infrared optical fiber production [33]. Thus, the combination of antimony-phosphate and germanate-based glasses is an interesting alternative for optical and luminescent materials containing RE^{3+} due to the resulted in low phonon energy, visible transparency, and thermally stable glass matrix [34].

In this sense, the aim of this work lies to study the effect of Ag-MNP on the UC photoluminescence properties of an Er^{3+}/Yb^{3+} co-doped $SbPO_4$-GeO_2 binary glass system. Due to the low RE^{3+} solubility in antimony-phosphate-based glasses, new strategies must be devised to overcome this limitation and improve the luminescence efficiency even at low concentrations of Er^{3+}/Yb^{3+} by precipitating Ag-MNP into the glass matrix, as proposed here. The glass samples containing Ag-MNP were investigated through transmission electron microscopy (TEM), UV–Vis–NIR absorption, and photoluminescence (excitation, emission, and lifetime) to understand the effect of Ag-MNP on the Er^{3+}/Yb^{3+} UC mechanisms.

2. Experimental part

The glass sample was synthesized by the conventional melt-quenching method. The starting materials were germanium oxide, GeO_2 (Alfa Aesar 99.999% pure), antimony orthophosphate, $SbPO_4$ (prepared as described in Ref. [29]), and AgCl (Aldrich, 99%), while RE^{3+} were supplied using ytterbium oxide, Yb_2O_3 (Lumintech, 99.9% pure) and erbium oxide, Er_2O_3 (Lumintech, 99.99% pure). The raw materials were stoichiometrically weighted with the molar composition of $98.5[40SbPO_4\text{-}60GeO_2]$:1AgCl:$0.2Yb_2O_3$:$0.3Er_2O_3$, grounded in an agate mortar and loaded into a Pt/Au crucible. The batch was melted at 1100 °C for 40 min under air, ensuring complete elimination of adsorbed gases and good homogenization. Then, the melt was cast in a preheated stainless-steel mold at 20 °C below T_g and annealed at this temperature for 2 h before slowly cooling to room temperature to minimize residual internal stress. The obtained samples were optically polished and cut into 6 pieces. Each one was submitted to heat treatment (HT) above the glass transition temperature at 442 °C for different times of 1, 2, 4, 8, and 24 h to promote the formation of Ag-MNP. The samples were labeled as SG0 (without HT), SG1, SG2, SG4, SG8 and SG24. The Er^{3+}/Yb^{3+} co-doped sample without Ag was also synthesized with a molar composition of $99.5[40SbPO_4\text{-}60GeO_2]$:$0.2Yb_2O_3$/$0.3Er_2O_3$ and labeled as S4G6.

Characteristic temperatures (T_g for glass transition and T_x for the onset of crystallization) of the SG0 sample were obtained using differential scanning calorimetry (DSC) at 300 and 800 °C under N_2 at a heating rate of 10 °C/min, using a NETZSCH equipment DSC 404 F3. To investigate the size and distribution of Ag-MNPs, a transmission electron microscopy (TEM) - Jeol-JEM-2100 operating at an accelerating voltage of 200 kV was used for the powdered samples redispersed in acetone and dropped and dried on the copper grid before analysis. UV–Vis–NIR absorption spectra were recorded in the wavelength range of 300–1600 nm on the optically polished glass pieces using a Perkin Elmer spectrophotometer model Lambda 1050. Photoluminescence spectroscopy was performed by using a Horiba iHR320 Photoluminescence Microspectrometer, in which the laser spot diameter operating at 980 nm was maintained at 10 μm for all measurements. The emission and excited-state lifetime measurements were recorded by a Horiba Jobyn Yvon spectrofluorimeter model Fluorolog FL1057, with a CW laser operating at 980 nm and a pulsed Xe lamp. The signals were measured by a photodiode detector model PPD-850 in the visible, and by a Hamamatsu photomultiplier in the infrared.

3. Results and discussion

In order to define the HT temperature and time conditions, the glass transition (T_g) and the onset crystallization (T_x) temperatures were obtained via DSC analysis for S4G6 and SG0 samples as shown in Fig. 1. The addition of 1 mol% of AgCl led to a slight decrease in glass transition temperature from 412 °C (S4G6) to 402 °C (SG0), and the shifting of the crystallization peak to lower temperature, from 588 °C to 500 °C, resulting in a decrease in thermal stability against crystallization, $\Delta T = (T_x - T_g)$, from ~200 °C for S4G6, as previously reported in Ref. [34], to ~ 100 °C for SG0 sample. As observed, AgCl increases the crystallization tendency by acting as a nucleation agent through the probable formation of nanoclusters of Ag_m^{x+} or Ag^0 [35,36].

Based on the SG0 thermogram, a few attempts of HT conditions were tried and the optimal temperature to allow control of the HT process was defined at T_g + 40 °C, i.e., at 442 °C. Above this HT temperature, the glass rapidly crystallizes instead to allow the control of nucleation and growth of only silver nanoparticles on an appropriate time scale.

SG0 sample was obtained as a transparent and optically homogeneous bulk to the naked eye and became purplish-colored after heat

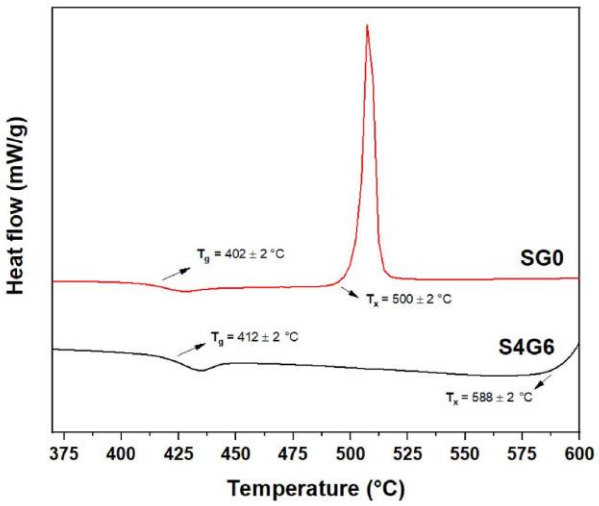

Fig. 1. DSC curves for S4G6 and SG0 samples.

treatment, as shown in the inset of Fig. 2(a). These changes in color are attributed to the LSPR band associated with the increases in particle size of metallic Ag^0 nanoparticles [35,37]. As observed, the Ag^0 LSPR band increase in intensity as a function of HT time, reducing the transparency in the visible due to the purplish color of the samples (see inset pictures in Fig. 2). The spontaneous redox reaction: $Sb^{3+} + 2Ag^{+} \rightarrow Sb^{5+} + 2Ag^0/E^0 = 1.02$ V, $\Delta G = -197$ kJ, acts as a driving force in the initial step of nanoparticles formation, enabling follow the nucleation, formation of nanoclusters, and growth of the MNPs [38]. The absence of the LSPR band for the SG0 sample is a consequence of only ionic silver being dissolved into the glass matrix, which may agglomerate as silver cations of m ions Ag_m^{x+} as further discussed [35,39]. Following the increase of HT time, the broad LSPR band centered at ~520 nm increases in intensity due to the increasing amount of Ag-MNP formed in the vitreous matrix [40]. In addition to the LSPR band, the absorption curves clearly evidenced the insertion of Er^{3+} and Yb^{3+} in the glass due to the presence of f-f absorptions from Er^{3+} ground state $^4I_{15/2}$ to their excited states $^4G_{9/2}$ (364 nm), $^4G_{11/2}$ (377 nm), $^4F_{7/2}$ (487 nm), $^2H_{11/2}$ (520 nm), $^4S_{3/2}$ (544 nm), $^4F_{9/2}$ (650 nm), as shown in Fig. 2(a) and from their ground state to the $^4I_{11/2}$ (980 nm) level in the near-infrared range (Fig. 2(b)), overlapped with the absorption from Yb^{3+} ground state $^2F_{7/2}$ to their excited level $^2F_{5/2}$ (~975 nm) [41]. It is worth saying that co-doping with Yb^{3+} is a well-known route used to enhance the visible photoluminescence of Er^{3+} through efficient UC mechanisms involving the absorption of two infrared photons and emission of a single visible one by erbium ion due to the larger absorption cross-section of Yb^{3+} [42].

To evaluate the effect of Ag-MNPs on the luminescent properties, UC spectroscopy was performed. The spectra obtained for the samples under excitation of 980 nm (100 mW) in the range of 400–700 nm are plotted in Fig. 3(a). As observed, the red emission intensity centered at 650 nm increases with the increment of the heat treatment time. This increment may be attributed to the enhancement of the local electric field (LEF) induced by the Ag-MNPs that increase in size and quantity proportionally to heat treatment time. The LSPR generated in the vicinity of the Er^{3+} enhances the red emission yield, assigned to the transition $^4F_{9/2} \rightarrow {}^4I_{15/2}$, by several orders [43]. This emission is predominant for all samples compared to the green emissions centered at 525 and 545 nm assigned to the $^2H_{11/2} \rightarrow {}^4I_{15/2}$ and $^4S_{3/2} \rightarrow {}^4I_{15/2}$ transitions, respectively. The low green emission can be understood by the energy transfer of the excited state electrons at $^2H_{11/2}$ and $^4S_{3/2}$ levels of Er^{3+} to the Ag-MNP band due to the resonant energy of the LSPR absorption and those excited levels of Er^{3+}. For a better understanding and makes the discussion clearer, the region between 500 and 640 nm from Fig. 3(a) was expanded and is shown in Fig. 3(b). This progressive energy transfer that results in the increase of red emission intensity is followed by the decrease of the broad and low-intensity emission band centered at 580 nm, which was already assigned to the presence of charged silver nanocluster species by Fares and coauthors, and discussed below for our case [35]. As the HT time increases, the charged silver nanoclusters decrease in concentration to form metallic silver nanoparticles, resulting in a decrease of ionic clusters-silver emission, as described when Fig. 5 is discussed, and an increase of Er^{3+} red emission through depopulation of the $^2H_{11/2}$ and $^4S_{3/2}$ states by the nanoparticles LEF [44,45].

The formation of Ag-MNP under HT was supported by TEM analysis as shown in Fig. 4 for SG1 (Fig. 4(a) and (b)) and SG8 (Fig. 4(c) and (d)) samples. It is clearly seen that for both SG1 and SG8 samples, Ag-MNP have a quite large variation in diameter appearing as a set of quasi-spherical dark spots homogeneously distributed across the glass matrix. The average diameter of 2.5 ± 0.8 nm and 4.7 ± 1.5 nm, were obtained from a log distribution with a R^2 of 0.92 and 0.99, respectively, as shown in Fig. 4(c) and (d). The quantity and size of the MNPs in SG8 are greater than in SG1 due to the longer HT time which increases. This fact is expected since the mobility of ions and clusters tend to be smaller within the glass network when compared to the diffusion of similar species in colloidal media. In the glass, the increase of the HT time increases the effectiveness in the nucleation and growth of Ag-MNPs [38].

Fig. 5 depicts the photoluminescence excitation (PLE) and emission spectra of the SG0 and HT samples. The excitation spectra (Fig. 5(a)) exhibit one broad band centered at 280 nm assigned to the electronic transition of small Ag nanoclusters [46,47], which progressively decreases in intensity in the function of HT time when the emission centered at 580 nm was monitored. Like the PLE, the emission band observed in the spectra of Fig. 5(b) under excitation at 280 nm, also decreases in intensity after HT time increase. Combining the results and photoluminescence spectra of SG0 and HT samples, we can relate the quenching of Ag nanocluster emission with the increase of Ag-MNP amount as a function of HT, as indicated by the evolution of the Ag-MNP size by the TEM. As expected, the HT aggregates the Ag nanoclusters in larger non-luminescent Ag-MNP. The formation of Ag-MNP led to cease of the nanocluster's emission, which is assigned to the small size compared to the Fermi wavelength in Ag^+, Ag_2^{2+}, and Ag_m^{x+} molecular species, responsible for the observed emission band [48,49]. From our best knowledge, it is the first time that an Ag emission is observed through excitation at 980 nm, as shown in Fig. 3(b), via an effective energy transfer from Er^{3+} ($^2H_{11/2}$ and $^4S_{3/2}$ excited energy levels) to the molecular-like Ag nanoclusters conduction bands.

Since the SG24 glass exhibits the most intense emission, the UC spectra of this sample at different excitation power are plotted in Fig. 6 (a). Additionally, even at large excitation power values, the green emissions present very low intensity and are weakly detected. For a better understanding of the UC process, the integrated area of the $^4S_{3/2} \rightarrow {}^4I_{15/2}$ and $^4F_{9/2} \rightarrow {}^4I_{15/2}$ bands as a function of the excitation power, in a log-log scale, are shown in Fig. 6(b). These two bands were chosen

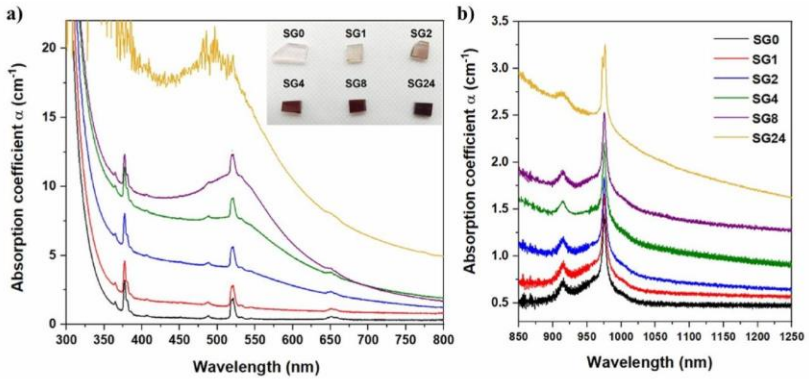

Fig. 2. Absorption spectra in the (a) UV–Visible, and (b) near-infrared ranges of SG0, SG1, SG2, SG4, SG8 and SG24 samples. Inset: digital picture of the samples.

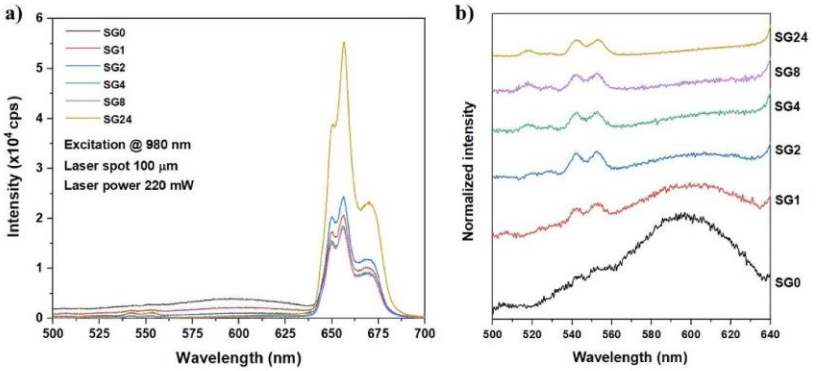

Fig. 3. (a) UC spectra of the SG glasses under 980 nm with an excitation power of 220 mW, and (b) UC emission in the range of 500–640 nm.

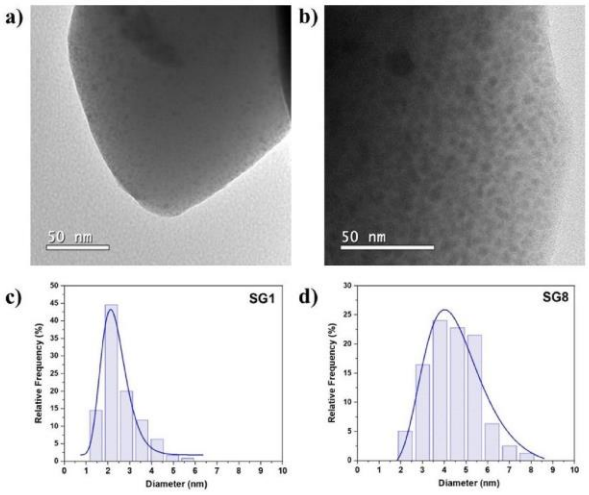

Fig. 4. TEM images of SG1 (a) and SG8 (b) samples and their relative frequency distribution of nanoparticle diameters (c and d, respectively).

because their intensity values are large enough for analysis. The UC emission intensity depends on the incident excitation power as $I \propto I_{exc}^{n}$, where n is the number of infrared photons involved in the population inversion process for a UC emission band. Therefore, a linear fitting ($R^2 > 0.99$) was performed and revealed that the value of the slopes, i.e., n, for the bands centered at 544 and 656 nm are 1.78 and 1.54, respectively, and as n must be an integer, we can conclude that there are two 980 nm photons involved in these transitions. Whereas the Er^{3+}: $^2H_{11/2}$ and $^4S_{3/2}$ levels are close in energy, we can assume that two 980 nm photons are involved in the $^2H_{11/2} \rightarrow {}^4I_{15/2}$ transition.

Fig. 7 shows the simplified energy level diagram of the UC process in these glasses with Ag-MNPs based on the quadratic dependence on pumping power. Under 980 nm excitation, Er^{3+} excited states $^2H_{11/2}$, $^4S_{3/2}$, and $^4F_{9/2}$, responsible for the green (525 nm and 545 nm), and red (650 nm) emissions, are populated through different paths added to the contributions by direct absorption of Er^{3+}. The larger absorption cross-section of Yb^{3+} at 980 nm compared to Er^{3+} makes the ETU mechanisms preferable to populate the $^2H_{11/2}$ and $^4S_{3/2}$ levels by energy transfer from excited states Yb^{3+} ($^2F_{5/2}$ level) to the Er^{3+} ($^4I_{11/2}$ level), emitting at 525 and 545 nm, respectively, after the absorption of two infrared photons, when radiatively decays to the Er^{3+} ground state ($^4I_{15/2}$ level). The red emission arising from the $^4F_{9/2} \rightarrow {}^4I_{15/2}$ transition is obtained by two possible paths: (i) the $^4I_{11/2}$ level is populated via ET from the Yb^{3+}: $^2F_{5/2} \rightarrow {}^2F_{7/2}$ emission or direct excitation with a 980 nm photon, excited via excited-state absorption (ESA) to the Er^{3+}: $^4F_{7/2}$, and then

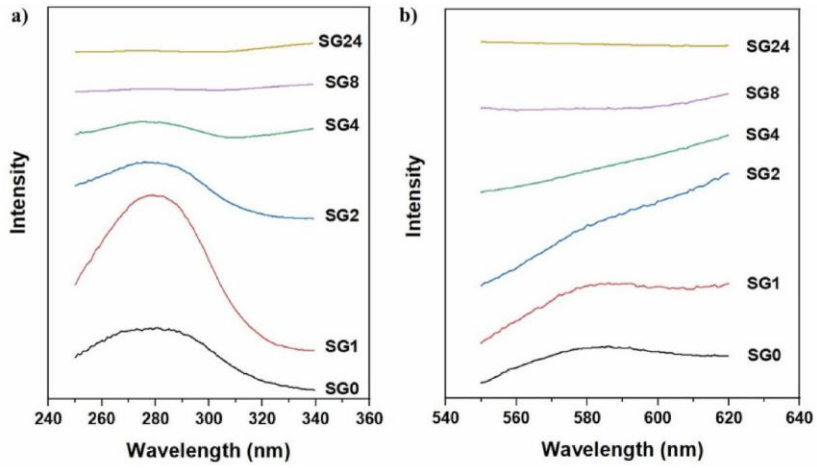

Fig. 5. Photoluminescence spectra of SG0 and heat-treated samples: (a) excitation spectra monitoring the emission at 580 nm from 250 to 340 nm, and (b) emission spectra under 280 nm excitation with a Xe lamp in the range of 550–620 nm.

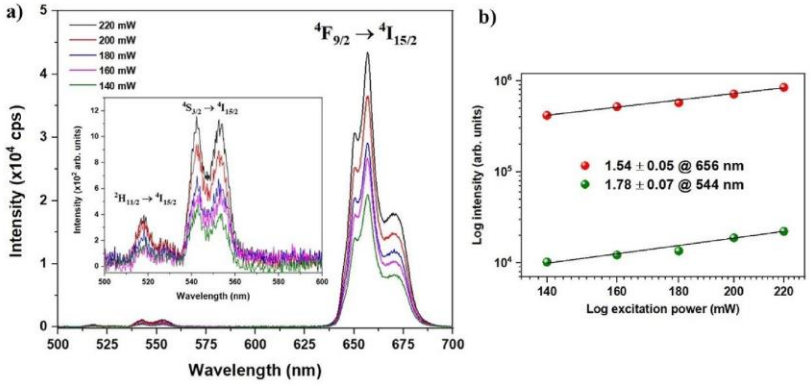

Fig. 6. (a) Visible emission spectra of SG24 sample in function of power excitation from 140 to 220 mW. Inset: emission in the range of 500–600 nm. (b) The log-log plot of the integrated emission intensity as a function of the excitation power.

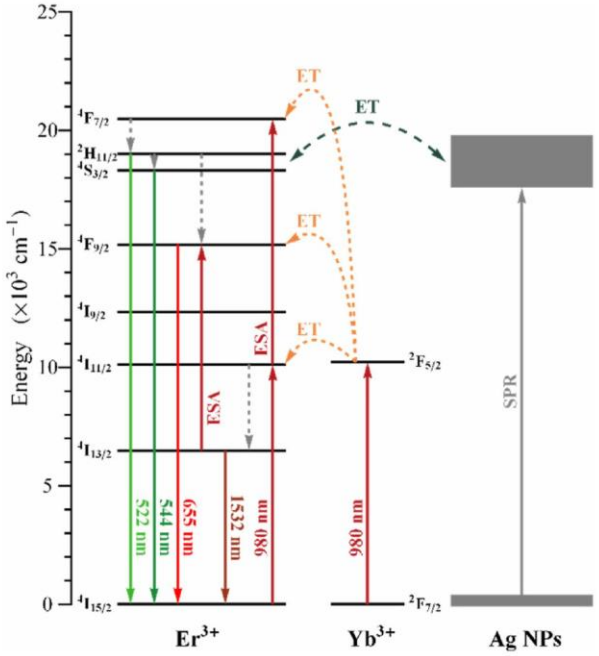

Fig. 7. Simplified energy level diagram with the possible transition pathways for the Er^{3+}/Yb^{3+} co-doped $SbPO_4$-GeO_2 glasses with Ag-MNP. Vertical dashed lines indicate non-radiative decays.

non-radiatively relax through consecutive phonon-assisted decays towards the emissive $^4F_{9/2}$ energy level, and (ii) through ETU where $^4I_{11/2}$ level is populated via ground state absorption, and from this level decays non-radiatively to the $^4I_{13/2}$ level, followed by absorption of a second 980 nm infrared photon, responsible to excite the electrons to the $^4F_{9/2}$ level, emitting red light when decays to $^4I_{15/2}$ state of Er^{3+}. Since the $^2H_{11/2} \rightarrow {}^4I_{15/2}$ and $^2S_{3/2} \rightarrow {}^4I_{15/2}$ transitions in Er^{3+} are in resonance with the LSPR, there is an ET process toward Ag-MNP responsible for the reabsorption of green emitted radiation from Er^{3+}.

The depopulation of the Er^{3+} exciting levels led to the enhancement of red emission intensity in the function of an increase in size and amount of the Ag MNP, the lifetime decays were measured. Fig. 8(a) presents the normalized lifetime curves on the logarithmic scale of the $^4F_{9/2} \rightarrow {}^4I_{15/2}$ transition. These curves were fitted by using a double exponential decay function and the lifetime was computed using the standard expression reported elsewhere [50]. The lifetime behavior as a function of the HT time is shown in Fig. 8(b) indicating an enhancement of the rapid depopulation rate which may be attributed to LEF effects of Ag MNPs [51], accompanied by an increment of the integrated area. These effects are greatly observed for HT times greater than 2 h, being the maximum value corresponding to the sample SG0 with a lifetime of ≈37.8 μs, which reduces to the minimum value for the sample SG24 with a lifetime of ≈16.2 μs.

Several research have been explored the study of Er^{3+} infrared emission ($^4I_{13/2} \rightarrow {}^4I_{15/2}$ transition at 1550 nm) enhancement in the presence of metallic nanoparticles in glass matrixes [52–54]. In our case, under 980 nm with P = 15 mW, there is no variation in the line shape and luminescence intensity with the increment of the HT time, as can be seen in Fig. 9. However, the SG24 sample exhibits a change in the line shape, increment in the full width at half maximum (FWHM), and a slight emission enhancement, due to the modification in the LEF induced by the presence of Ag MNPs, modifying the Stark levels of the Er^{3+}: $^4I_{13/2}$ excited state [55,56].

4. Conclusions

In conclusion, silver nanoparticles were successfully precipitated through the HT process in a glass system based on $SbPO_4$-GeO_2 co-doped with Er^{3+} and Yb^{3+}. The influence of heat treatment time on the formation of Ag-MNP was investigated by TEM and the presence of LSPR absorption band centered at 520 nm which supports the presence of Ag-MNPs in our vitreous matrix. Under excitation at 980 nm, there is a significant enhancement of Er^{3+} up-conversion emission at 656 nm ($^4F_{9/2} \rightarrow {}^4I_{15/2}$) with the increment of the heat treatment, and a relative decrease in emission intensity at 522 and 544 nm ($^2H_{11/2} \rightarrow {}^4I_{15/2}$ and $^4S_{3/2} \rightarrow {}^4I_{15/2}$, respectively) due to the absorption of the Ag-MNPs and a non-radiative decay to the $^4F_{9/2}$ excited state. The increase of HT time decreases the emission of molecular Ag nanoclusters, responsible for the low-intense and broad emission centered at 580 nm. It was demonstrated an Ag emission through excitation at the infrared (980 nm) via energy transfer from Er^{3+} to the molecular-like Ag nanoclusters conduction bands. By photoluminescence spectroscopy at different excitation power, was determined that the value of the slopes for the 656 nm emission is 1.54, indicating that there are two 980 nm photons involved in this transition. Furthermore, the lifetime measurements suggest that a rapid depopulation rate is enhanced with the HT time, which can be attributed to the enhancement of LEF of Ag-MNPs. Thus, due to the intense red emission by excitation at IR, substantial thermal stability, and large transparency window, this new Ag-doped antimony-germanium-phosphate glass has great potential for many applications in

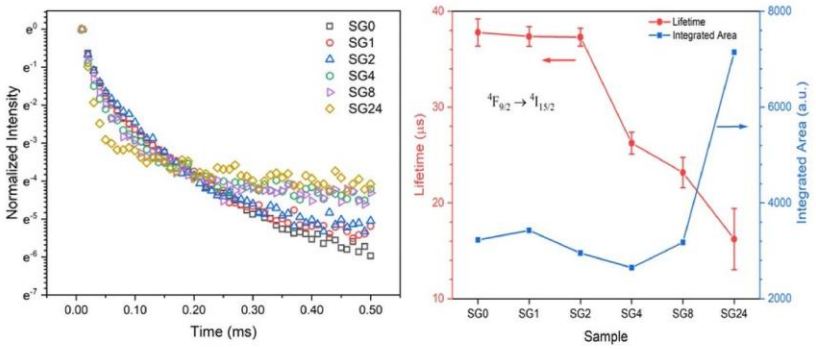

Fig. 8. a) Normalized lifetime curves in log scale; and b) lifetime and integrated area for $^4F_{9/2} \rightarrow {}^4I_{15/2}$ transition in the SG samples.

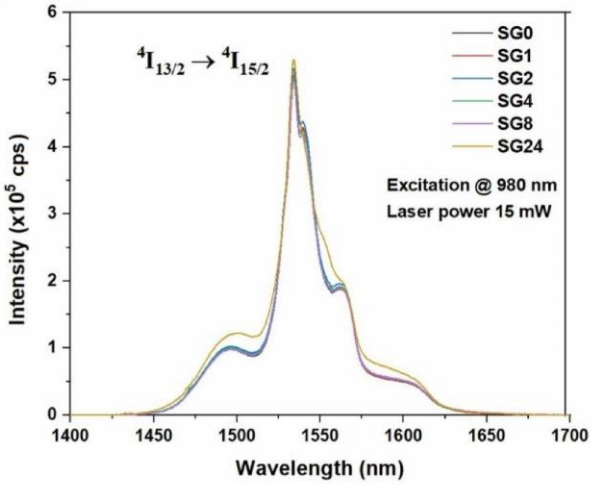

Fig. 9. Infrared emission at 1532 nm of the SG glasses under excitation at 980 nm. Inset: FWHM in function of the heat treatment time.

photonics as high-capacity data storage devices, photodynamic therapy, and solid-state light-emitting material.

CRediT authorship contribution statement

Renato Grigolon Capelo: Conceptualization, Methodology, Investigation, Writing – review & editing, Writing – original draft. **Thiago Israel Rubio:** Conceptualization, Methodology, Investigation, Writing – review & editing, Writing – original draft. **Gaston Lozano Calderón:** Conceptualization, Methodology, Investigation, Writing – review & editing, Writing – original draft. **Daniel Angeli de Moraes:** Investigation, Formal analysis, Writing – review & editing. **Euclydes Marega Junior:** Resources, Writing – original draft. **Marcelo Nalin:** Resources, Writing – original draft, Writing – review & editing, Funding acquisition. **Danilo Manzani:** Supervision, Conceptualization, Resources, Writing – review & editing, Funding acquisition.

Declaration of competing interest

The authors declare that they have no known competing financial interests or personal relationships that could have appeared to influence the work reported in this paper.

Data availability

No data was used for the research described in the article.

Acknowledgments

DM and MN dedicate this work in honor of the memory of their friend and researcher Dr. Murilo Montesso. The authors acknowledge grants from São Paulo Research Foundation – FAPESP (2020/12280–1, 2019/16230–1, 2018/16126–7, 2013/07793–6, 2020/04835–3) for financial support.

References

[1] E.J. Tarbox, R.I. Laming, P.R. Morkel, "Absorption and emission cross section of Er3+ doped silica fibers,", IEEE J. Quant. Electron. (1991) https://doi.org/10.1109/3.83335.

[2] F. Weng, D. Chen, Y. Wang, Y. Yu, P. Huang, H. Lin, "Energy transfer and up-conversion luminescence in Er3+/Yb3+ co-doped transparent glass ceramic containing YF3 nano-crystals,", Ceram. Int. (2009) https://doi.org/10.1016/j.ceramint.2009.02.026.

[3] V.M. Lojpur, P.S. Ahrenkiel, M.D. Dramićanin, "Color-tunable up-conversion emission in Y2O3:Yb3+, Er3+ nanoparticles prepared by polymer complex solution method,", Nanoscale Res. Lett. (2013) https://doi.org/10.1186/1556-276X-8-131.

[4] Y. Wu, et al., "Silver nanoparticles enhanced upconversion luminescence in Er 3+/Yb 3+ codoped bismuth-germanate glasses,", J. Phys. Chem. C (2011) https://doi.org/10.1021/jp207035c.

[5] A. Shalav, B.S. Richards, T. Trupke, K.W. Krämer, H.U. Güdel, "Application of NaYF4: Er3+ up-converting phosphors for enhanced near-infrared silicon solar cell response,", Appl. Phys. Lett. (2005) https://doi.org/10.1063/1.1844592.

[6] N. Jaba, A. Kanoun, H. Mejri, A. Selmi, S. Alaya, H. Maaref, "Infrared to visible up-conversion study for erbium-doped zinc tellurite glasses,", J. Phys. Condens. Matter (2000) https://doi.org/10.1088/0953-8984/12/20/307.

[7] L. Aarts, B.M. van der Ende, A. Meijerink, "Downconversion for solar cells in NaYF4:Er,Yb,", J. Appl. Phys. (2009) https://doi.org/10.1063/1.3177257.

[8] O.L. Malta, P.A. Santa-Cruz, G.F. de Sá, F. Auzel, "Fluorescence enhancement induced by the presence of small silver particles in Eu3+ doped materials,", J. Lumin. (1985) https://doi.org/10.1016/0022-2313(85)90003-1.

[9] R.J. Amjad, et al., "Annealing time dependent up-conversion luminescence enhancement in magnesium-tellurite glass,", J. Lumin. (2013) https://doi.org/10.1016/j.jlumin.2012.11.028.

[10] A. Resta, R. Felici, M. Kumar, M. Pedio, "Ni and Cu Octaethyl Porphyrins Ordered Monolayer on Au(111) Surfaces,", 2010, https://doi.org/10.1016/j.jnoncrysol.2010.05.051.

[11] N.N. Yusof, S.K. Ghoshal, S.A. Jupri, M.N. Azlan, "Synergistic effects of Nd3+ and Ag nanoparticles doping on spectroscopic attributes of phosphate glass,", Opt. Mater. 110 (Dec. 2020), 110403 https://doi.org/10.1016/j.optmat.2020.110403.

[12] A. Zada, et al., "Surface plasmonic-assisted photocatalysis and optoelectronic devices with noble metal nanocrystals: design, synthesis, and applications,", Adv. Funct. Mater. 30 (7) (Feb. 2020), 1906744 https://doi.org/10.1002/adfm.201906744.

[13] M. Eichelbaum, K. Rademann, "Plasmonic enhancement or energy transfer? on the luminescence of gold-, silver-, and lanthanide-doped silicate glasses and its potential for light-emitting devices,", Adv. Funct. Mater. (2009) https://doi.org/10.1002/adfm.200801892.

[14] D. Rajesh, M. Reza Dousti, R.J. Amjad, A.S.S. de Camargo, "Enhancement of down- and upconversion intensities in Er3+/Yb3+ co-doped oxyfluoro tellurite glasses induced by Ag species and nanoparticles,", J. Lumin. (2017) https://doi.org/10.1016/j.jlumin.2017.06.059.

[15] I. Soltani, S. Hraiech, K. Horchani-Naifer, M. Férid, "Effects of silver nanoparticles on the enhancement of up conversion and infrared emission in Er3+/Yb3+ co-doped phosphate glasses,", Opt. Mater. (2018) https://doi.org/10.1016/j.optmat.2018.01.036.

[16] J. Qiu, Q. Jiao, D. Zhou, Z. Yang, "Recent progress on upconversion luminescence enhancement in rare-earth doped transparent glass-ceramics,", J. Rare Earths 34 (4) (Apr. 2016) 341–367, https://doi.org/10.1016/S1002-0721(16)60034-0.

[17] I. Fuks-Janczarek, R. Miedzinski, L.R.P. Kassab, C.D.S. Bordon, "Effect of annealing time on the linear and nonlinear optical properties of PbOGeOGaO glasses doped with Er and Yb, Au ions,", Opt. Mater. 102 (Apr. 2020), 109794, https://doi.org/10.1016/j.optmat.2020.109794.

[18] M.M. Martins, L.R.P. Kassab, D.M. da Silva, C.B. de Araújo, "Tm3+ doped Bi2O3-GeO2 glasses with silver nanoparticles for optical amplifiers in the short-wave-infrared-region,", J. Alloys Compd. 772 (Jan. 2019) 58–63, https://doi.org/10.1016/j.jallcom.2018.08.146.

[19] D.S. da Silva, L.P. Naranjo, L.R.P. Kassab, C.B. de Araújo, "Photoluminescence from germanate glasses containing silicon nanocrystals and erbium ions,", Appl. Phys. B 106 (4) (Mar. 2012) 1015–1018, https://doi.org/10.1007/s00340-011-4798-3.

[20] S. Stanek, et al., "The influence of silver-ion doping using ion implantation on the luminescence properties of Er–Yb silicate glasses,", Nucl. Instrum. Methods Phys. Res. Sect. B Beam Interact. Mater. Atoms 371 (Mar. 2016) 350–354, https://doi.org/10.1016/j.nimb.2015.09.078.

[21] A.F. Obaton, C. Labbé, P. le Boulanger, B. Elouadi, G. Boulon, "Excited state absorption in Yb3+ -Er3+ -codoped phosphate glasses (ZnO-Al2O3-La2O3-P2O 5) around the 4I13/2→4I15/2 emission spectral range,", Spectrochim. Acta Mol. Biomol. Spectrosc. (1999) https://doi.org/10.1016/S1386-1425(98)00192-9.

[22] G.E. Malashkevich, et al., "Luminescence of borogermanate glasses activated by Er3+ and Yb3+ ions,", J. Non-Cryst. Solids (2011) https://doi.org/10.1016/j.jnoncrysol.2010.09.007.

[23] D. Manzani, J.L. Ferrari, F.C. Polachini, Y. Messaddeq, S.J.L. Ribeiro, "1.5 μm and visible up-conversion emissions in Er 3+/Yb 3+ co-doped tellurite glasses and optical fibers for photonic applications,", J. Mater. Chem. (2012) https://doi.org/10.1039/c2jm33057a.

[24] M.K. Halimah, et al., "Effect of erbium nanoparticles on structural and spectroscopic properties of bio-silica borotellurite glasses containing silver oxide,", Mater. Chem. Phys. 236 (Oct. 2019), 121795 https://doi.org/10.1016/j.matchemphys.2019.121795.

[25] M. Li, G. Bai, Y. Guo, L. Hu, J. Zhang, "Investigation on Tm 3+-doped silicate glass for 1.8 μm emission,", J. Lumin. (2012) https://doi.org/10.1016/j.jlumin.2012.02.022.

[26] K.-C. Feng, et al., "Ag-diffusion inhibition mechanism in SiO2-added glass-ceramics for 5G antenna applications,", Ceram. Int. 46 (15) (Oct. 2020) 24083–24090, https://doi.org/10.1016/j.ceramint.2020.06.186.

[27] E. Mura, J. Lousteau, D. Milanese, S. Abrate, V.M. Sglavo, "Phosphate glasses for optical fibers: synthesis, characterization and mechanical properties,", J. Non-Cryst. Solids (2013) https://doi.org/10.1016/j.jnoncrysol.2012.11.029.

[28] D. Manzani, C.B. de Araújo, G. Boudebs, Y. Messaddeq, S.J.L. Ribeiro, "The role of Bi_2O_3 on the thermal, structural, and optical properties of Tungsten-phosphate glasses,", J. Phys. Chem. B 117 (1) (Jan. 2013) 408–414, https://doi.org/10.1021/jp3097296.

[29] M. Nalin, M. Poulain, M. Poulain, S.J.L. Ribeiro, Y. Messaddeq, "Antimony oxide based glasses,", J. Non-Cryst. Solids (2001) https://doi.org/10.1016/S0022-3093(01)00388-X.

[30] M. Nalin, et al., "Structural organization and thermal properties of the Sb2O 3-SbPO4 glass system,", J. Mater. Chem. (2004) https://doi.org/10.1039/b406075j.

[31] H. Takahashi, I. Sugimoto, "A germanium-oxide glass optical fiber prepared by A VAD method,", J. Lightwave Technol. (1984) https://doi.org/10.1109/JLT.1984.1073663.

[32] D. Manzani, M. Montesso, C.F. Mathias, K.V. Krishanaiah, S.J.L. Ribeiro, M. Nalin, "Visible up-conversion and near-infrared luminescence of Er3+/Yb3+ co-doped SbPO4-GeO2 glasses,", Opt. Mater. (2016) https://doi.org/10.1016/j.optmat.2016.04.019.

[33] H.T. Munasinghe, et al., "Lead-germanate glasses and fibers: a practical alternative to tellurite for nonlinear fiber applications,", Opt. Mater. Express (2013) https://doi.org/10.1364/ome.3.001488.

[34] M. Montesso, et al., "Synthesis and structural characterization of a new SbPO4-GeO2 glass system,", J. Non-Cryst. Solids (2018) https://doi.org/10.1016/j.jnoncrysol.2018.07.005.

[35] H. Fares, et al., "Highly luminescent silver nanocluster-doped fluorophosphate glasses for microfabrication of 3D waveguides,", RSC Adv. 7 (88) (2017) 55935–55944, https://doi.org/10.1039/C7RA11792B.

[36] M. Reza Dousti, M.R. Sahar, S.K. Ghoshal, R.J. Amjad, A.R. Samavati, "Effect of AgCl on spectroscopic properties of erbium doped zinc tellurite glass,", J. Mol. Struct. 1035 (Mar. 2013) 6–12, https://doi.org/10.1016/j.molstruc.2012.09.023.

[37] S. Sareen, V. Mutreja, S. Singh, B. Pal, "Highly dispersed Au, Ag and Cu nanoparticles in mesoporous SBA-15 for highly selective catalytic reduction of nitroaromatics,", RSC Adv. 5 (1) (2015) 184–190, https://doi.org/10.1039/C4RA10050F.

[38] Y. Al−Hadeethi, M.I. Sayyed, A.Z. Barasheed, M. Ahmed, G. Jagannath, "Nanosecond nonlinear optical, optical limiting and structural properties of Eu3+ activated antimony sodium borate glasses embedded with silver nanoparticles: effect of heat treatment,", Opt. Mater. 125 (Mar. 2022), 112106 https://doi.org/10.1016/j.optmat.2022.112106.

[39] L.R.P. Kassab, F.A. Bomfim, J.R. Martinelli, N.U. Wetter, J.J. Neto, C.B. de Araújo, "Energy transfer and frequency upconversion in Yb3+-Er 3+-doped PbO-GeO2 glass containing silver nanoparticles,", Appl. Phys. B Laser Opt. 94 (2) (Feb. 2009) 239–242, https://doi.org/10.1007/s00340-008-3249-2.

[40] Y. Fang, et al., "Experimental study of growth of silver nanoparticles embedded in Bi2O3-SiO2-B2O3 glass,", J. Alloys Compd. 809 (Nov. 2019), 151725 https://doi.org/10.1016/j.jallcom.2019.151725.

[41] Y. Ledemi, M. el Amraoui, J.L. Ferrari, P.-L. Fortin, S.J.L. Ribeiro, Y. Messaddeq, Infrared to visible up-conversion emission in Er^{3+}/Yb^{3+} codoped Fluoro-phosphate glass-ceramics, J. Am. Ceram. Soc. 96 (3) (Mar. 2013) 825–832, https://doi.org/10.1111/jace.12109.

[42] S.F. Li, Q.Y. Zhang, Y.P. Lee, "Absorption and photoluminescence properties of Er-doped and Er/Yb codoped soda-silicate laser glasses,", J. Appl. Phys. 96 (9) (Nov. 2004) 4746–4750, https://doi.org/10.1063/1.1792388.

[43] Y. Qi, et al., "Silver nanoparticles enhanced 1.53μm band fluorescence of Er3+/Yb3+ codoped tellurite glasses,", J. Lumin. 153 (Sep. 2014) 401–407, https://doi.org/10.1016/j.jlumin.2014.03.069.

[44] T. Li, C. Guo, L. Li, "Up-conversion luminescence of Erˆ3+-Ybˆ3+ co-doped CaIn_2O_4,", Opt Express 21 (15) (Jul. 2013), 18281 https://doi.org/10.1364/OE.21.018281.

[45] K. Linganna, R. Narro-García, P. Manasa, H. Desirena, E. de la Rosa, C. K. Jayasankar, "Effect of BaF 2 addition on luminescence properties of Er 3+/Yb 3+ co-doped phosphate glasses,", J. Rare Earths 36 (1) (Jan. 2018) 58–63, https://doi.org/10.1016/j.jre.2017.06.008.

[46] H. Lin, D. Chen, Y. Yu, R. Zhang, Y. Wang, "Molecular-like Ag clusters sensitized near-infrared down-conversion luminescence in oxyfluoride glasses for broadband spectral modification,", Appl. Phys. Lett. 103 (9) (Aug. 2013), 091902 https://doi.org/10.1063/1.4819951.

[47] H. Fares, T. Castro, J.R. Orives, D.F. Franco, M. Nalin, "White light and multicolor emission tuning in Ag nanocluster doped fluorophosphate glasses,", RSC Adv. 7 (70) (2017) 44356–44365, https://doi.org/10.1039/C7RA08778K.

[48] V.K. Tikhomirov, V.D. Rodríguez, A. Kuznetsov, D. Kirilenko, G. van Tendeloo, V. v. Moshchalkov, "Preparation and luminescence of bulk oxyfluoride glasses doped with Ag nanoclusters,", Opt Express 18 (21) (Oct. 2010), 22032 https://doi.org/10.1364/OE.18.022032.

[49] H. Fares, et al., Highly luminescent silver nanocluster-doped fluorophosphate glasses for microfabrication of 3D waveguides, RSC Adv. 7 (88) (2017) 55935–55944, https://doi.org/10.1039/C7RA11792B.

[50] M. Haouari, F. ben Slimen, A. Maaoui, N. Gaumer, "Structural and spectroscopic properties of Eu3+ doped tellurite glass containing silver nanoparticles,", J. Alloys Compd. 743 (Apr. 2018) 586–596, https://doi.org/10.1016/j.jallcom.2018.01.192.

[51] M. Reza Dousti, R.J. Amjad, "Effect of silver nanoparticles on the upconversion and near-infrared emissions of Er 3+ :Yb 3+ co-doped zinc tellurite glasses,", Measurement 105 (Jul. 2017) 114–119, https://doi.org/10.1016/j.measurement.2017.04.007.

[52] T.M. Machado, R.F. Falci, I.L. Silva, V. Anjos, M.J.V. Bell, M.A.P. Silva, "Erbium 1.55μm luminescence enhancement due to copper nanoparticles plasmonic activity in tellurite glasses,", Mater. Chem. Phys. 224 (Feb. 2019) 73–78, https://doi.org/10.1016/j.matchemphys.2018.11.059.

[53] L.R.P. Kassab, D.S. da Silva, C.B. de Araújo, "Influence of metallic nanoparticles on electric-dipole and magnetic-dipole transitions of Eu3+ doped germanate glasses,", J. Appl. Phys. 107 (11) (Jun. 2010), 113506 https://doi.org/10.1063/1.3431347.

[54] V.A.G. Rivera, et al., "Efficient plasmonic coupling between Er3+:(Ag/Au) in tellurite glasses,", J. Non-Cryst. Solids 358 (2) (Jan. 2012) 399–405, https://doi.org/10.1016/j.jnoncrysol.2011.10.008.

[55] I. Soltani, S. Hraiech, K. Horchani-Naifer, M. Férid, "Effects of silver nanoparticles on the enhancement of up conversion and infrared emission in Er3+/Yb3+ co-doped phosphate glasses,", Opt. Mater. 77 (Mar. 2018) 161–169, https://doi.org/10.1016/j.optmat.2018.01.036.

[56] V.A.G. Rivera, et al., "Localized surface plasmon resonance interaction with Erˆ3+-doped tellurite glass,", Opt Express 18 (24) (Nov. 2010), 25321 https://doi.org/10.1364/OE.18.025321.

CHAPTER VI:

Blue upconversion emission of $Nd^{3+}/Tm^{3+}/Yb^{3+}$ triply doped aluminophosphate optical fibers

Reprinted with permission from R. G. Capelo, C. Strutynski, G. Gadret, F. Désévédavy, F. Smektala and D. Manzani, **Blue upconversion emission of $Nd^{3+}/Tm^{3+}/Yb^{3+}$ triply doped aluminophosphate optical fibers.** *ACS Applied Optical Materials*, 2024, 2, 12 2501-2508. https://doi.org/10.1021/acsaom.4c00348.

Abstract

Glasses containing rare-earth ions (RE^{3+}) for upconversion (UC) luminescence have been widely explored in several photonic applications. Materials containing Tm^{3+} present an intense blue emission when excited in the near-infrared range, allowing them to be used as solid-state lasers and other emitter devices. Tm^{3+} are generally combined with other RE^{3+} to improve the UC efficiency; however, increasing the number of dopants can be an issue for their solubility in the glass matrix and for fiber drawing. In this work, alkali–aluminum–phosphate glasses, a host matrix with high RE^{3+} solubility and fiber-drawing ability, were produced containing different amounts of Tm^{3+}, Nd^{3+}, and Yb^{3+}, as well as the respective tridoped optical fibers. Glass samples containing RE^{3+} were excited at 808 and 980 nm to evaluate the mechanism involved in the luminescence process. In addition, triply doped optical fibers were excited at 788 and 980 nm, and a bright blue luminescence was observed at both wavelengths. Thus, due to the intense UC emission measured on RE^{3+} triply doped optical fibers with low optical loss, the developed material presents great potential for fiber-based photonic applications.

ACS APPLIED OPTICAL MATERIALS

pubs.acs.org/acsaom
Article

Blue Upconversion Emission of $Nd^{3+}/Tm^{3+}/Yb^{3+}$ Triply Doped Aluminophosphate Optical Fibers

Renato Grigolon Capelo,* Clément Strutynski, Gregory Gadret, Frédéric Désévédavy, Frédéric Smektala, and Danilo Manzani*

Cite This: ACS Appl. Opt. Mater. 2024, 2, 2501−2508
Read Online
ACCESS | Metrics & More | Article Recommendations | Supporting Information

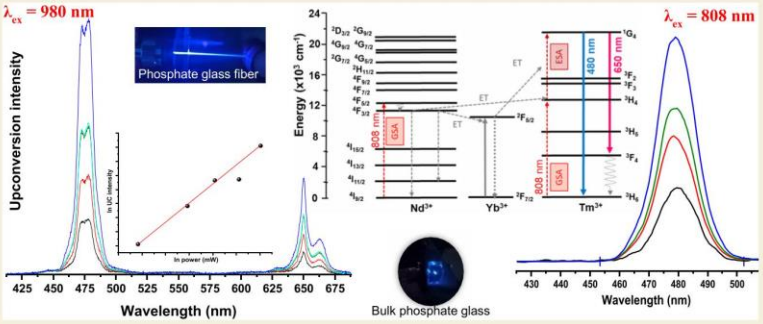

ABSTRACT: Glasses containing rare-earth ions (RE^{3+}) for upconversion (UC) luminescence have been widely explored in several photonic applications. Materials containing Tm^{3+} present an intense blue emission when excited in the near-infrared range, allowing them to be used as solid-state lasers and other emitter devices. Tm^{3+} are generally combined with other RE^{3+} to improve the UC efficiency; however, increasing the number of dopants can be an issue for their solubility in the glass matrix and for fiber drawing. In this work, alkali−aluminum−phosphate glasses, a host matrix with high RE^{3+} solubility and fiber-drawing ability, were produced containing different amounts of Tm^{3+}, Nd^{3+}, and Yb^{3+}, as well as the respective tridoped optical fibers. Glass samples containing RE^{3+} were excited at 808 and 980 nm to evaluate the mechanism involved in the luminescence process. In addition, triply doped optical fibers were excited at 788 and 980 nm, and a bright blue luminescence was observed at both wavelengths. Thus, due to the intense UC emission measured on RE^{3+} triply doped optical fibers with low optical loss, the developed material presents great potential for fiber-based photonic applications.

KEYWORDS: *blue upconversion, rare-earth luminescence, aluminophosphate glasses, optically active optical fibers, photonics*

1. INTRODUCTION

Near-infrared (NIR) to visible (Vis) UC luminescence from RE^{3+}-doped glasses has garnered much attention due to their diverse range of applications, such as solid-state lasers, optical data storage, biomedical diagnostics and treatments, thermal sensors, multicolor displays, among others.[1−6] Tm^{3+} is commonly used as an activator for UC emission, owing to their $^1G_4 \rightarrow {}^3H_6$ transition, which yields strong blue luminescence.[7,8] However, due to Tm^{3+}'s narrow absorption cross section, these ions are generally combined with other RE^{3+} to enhance the efficiency of the radiative process.[9,10] In this sense, one potential method for sensitizing the Tm^{3+} UC process involves the use of Nd^{3+}, which possesses many energy levels close to that of Tm^{3+}, allowing energy transfer (ET) between them. Moreover, the most common sensitizer for UC in RE-doped materials is Yb^{3+}, mainly due to its intrinsic high absorption cross section at 980 nm. Yb^{3+} also serves as a bridge ion in several ET processes, including the transfer from Nd^{3+} to Tm^{3+}.[11,12]

The sensitization process involves multi-ion interactions, where sensitizer species are excited and transfer energy to the emitter ion. In the case of Tm^{3+} blue emission, systems codoped with Yb^{3+} have been extensively investigated under a 980 nm excitation.[13,14] However, in various applications, there is interest in promoting visible emission by employing a different excitation source to avoid overlap with the vibrational overtone of the O−H bonds of the water molecules, located around 970 nm.[15] The high absorption coefficient from the

Received: August 7, 2024
Revised: November 18, 2024
Accepted: November 19, 2024
Published: November 25, 2024

https://doi.org/10.1021/acsaom.4c00348
ACS Appl. Opt. Mater. 2024, 2, 2501−2508

water in this range (0.48 cm^{-1} at 980 nm) can induce undesired heating effects, limiting the use of 980 nm laser sources in water-rich environments.[16,17] Therefore, as an alternative for Tm^{3+} UC excitation, sources operating at 808 nm have been considered due to their well-established technology in manufacturing high-performance and low-cost diode laser, as well as their lower absorption by water molecules, which can be contained in the host matrix.[17,18] This strategy typically involves significant Nd^{3+} absorption at around 800 nm, where the absorption by water is 20 times lower than that at 980 nm, followed by energy transfer to the emitter ion. Nevertheless, the incorporation of Yb^{3+} in these systems can significantly enhance the UC efficiency due to highly efficient ET from excited Nd^{3+} to Yb^{3+}, followed by a second transfer to Tm^{3+}.[18−1920] Consequently, Yb^{3+} plays a crucial role in these systems, serving as an energy-transfer bridge between the donor (Nd^{3+}) and an acceptor ion (Tm^{3+}).[21]

The selection of an appropriate host material is essential for designing an efficient UC emitter device. In particular, the development of photonic glasses has emerged as a relevant topic of focus in laser research, particularly for the potential application of new RE^{3+}-based fiber lasers in solid-state devices.[22−24] Among the various glass matrices, phosphate glasses have attracted considerable interest due to their suitable optical properties, especially the good transparency across the UV−vis−NIR spectrum.[25,26] Moreover, the addition of metal oxide tends to improve the chemical and thermal stabilities of phosphate glasses. The introduction of Al_2O_3, for example, facilitates cross-links between [PO_4] tetrahedra within the glass network, thereby enhancing resistance to aqueous and moisture environments and improving their durability.[27,28] Furthermore, the addition of alkaline-metal oxides such as Na_2O and K_2O enhances the solubility of RE^{3+} within the matrix, enabling the use of high dopant concentrations.[29,30] This, coupled with a reduction in the glass synthesis melt temperature, results in more favorable characteristics for processes such as fiber drawing or shaping, in general.[28,31−33]

In this sense, this work focuses on the synthesis and luminescence studies of aluminum-phosphate glasses and optical fibers doped with varying concentrations of Tm^{3+}, Nd^{3+}, and Yb^{3+} to investigate blue UC luminescence under an excitation wavelength of 788 and 980 nm. The glass samples containing RE^{3+} were analyzed through UV−vis−NIR absorption and photoluminescence measurements. These data aim to understand the effect of Nd^{3+} and Yb^{3+} concentrations and the excitation wavelength on the mechanisms of Tm^{3+} blue emission and evaluate the potential of this material for applications in solid-state lasers and fiber-based emitter devices.

2. EXPERIMENTAL SECTION

The glass bulks and optical fiber precursors were synthesized by the conventional melt-quenching method. The starting materials were H_3PO_4 (85 w/w%, 1.7 g/mL), Na_2CO_3 (99.9%), K_2CO_3 (99.9%), and Al_2O_3 (Aldrich, 99.99%), while RE^{3+} were supplied using ytterbium oxide, Yb_2O_3 (Lumintech, 99.9% pure), neodymium oxide, Nd_2O_3 (Lumintech, 99.99% pure), and thulium oxide, Tm_2O_3 (Lumintech, 99.9% pure). The raw materials were stoichiometrically weighted with a molar composition of $45P_2O_5$−$20Na_2O$−$20K_2O$−$15Al_2O_3$, labeled as PNKA, and different amounts of dopants were added to the basic glass composition, as described in Table 1. The powder reagents were placed in a Teflon beaker and heated to 300 °C on a hot plate. The slow addition of H_3PO_4 followed, and the mixture was heated overnight at the same temperature. Subsequently, the mixture was transferred into a Pt crucible and melted at 1100 °C for 60 min under room atmosphere to ensure complete elimination of adsorbed gases and achieve homogenization. The molten material was then casted into a preheated stainless-steel mold at 360 °C and annealed at 400 °C for 5 h before slowly cooling to room temperature to minimize residual internal stress. Finally, the obtained samples were cut and optically polished for the luminescence measurements.

Table 1. Label and Nominal Molar Concentrations of the Synthesized Doped Glass Samples

	dopant molar concentrations (mol %)			
sample label	Tm_2O_3	Nd_2O_3	Yb_2O_3	T_g (°C)
PNKA	-	-	-	400
Tm0.2	0.2	-	-	406
Tm0.2-Nd0.5	0.2	0.5	-	415
Tm0.2-Nd0.5-Yb1	0.2	0.5	1.0	408

The PNKA glass preform, measuring 5 cm in length and 16 mm in diameter, was prepared using the same procedure described above but cast in a cylindrical mold. Subsequently, the preform was drawn into the fiber under a helium gas flow using a commercial Control Interface Limited drawing tower at around 715 °C, with a feeding rate of 1.0 mm/min. The resulting single-index fiber exhibited diameters ranging between 125 and 200 μm depending on the drawing parameters.

The characteristic temperatures of undoped PNKA glass were measured by using differential thermal analysis (DTA) at a heating rate of 10 °C/min under a N_2 atmosphere. The refractive index of the PNKA glass was measured at different wavelengths using a variable angle spectroscopic ellipsometer (VASE) from J. A. WOOLLAM with a standard configuration of a rotating polarizer. A Xe light source was employed for emission with light guided to the monochromator (HS-190 model) via a ZrF_4 optical fiber. Measurements were conducted within the range of 0.4−2.50 μm while maintaining a constant incidence angle.[34]

UV−vis−NIR absorption spectra were recorded in the wavelength range of 300−1200 nm on optically polished glass pieces using a PerkinElmer spectrophotometer model Lambda 1050. Optical losses in single-index PNKA fibers were assessed using the cutback method on samples measuring 2−3 m in length. A 100 W external halogen lamp emitting within the spectral range of 0.5−5.2 μm was effectively coupled into the fiber using a mirror objective. The resulting output signal was recorded using a portable spectrometer operational within the wavelength range of 380−900 nm. Additionally, attenuation measurements within the 380−500 nm range were performed utilizing light-emitting diodes (LEDs) with tunable emission peaks around 405 and 420 nm.

Photoluminescence measurements on glass bulks were conducted in a Horiba Jobin Yvon Fluorolog-3 FL-1050 Spectrofluorometer, coupling an 808 nm laser as the excitation source, operating in a power range from 150 to 300 mW. In addition, glass bulks were excited at 980 nm using a Horiba iHR320 Photoluminescence Microspectrometer, with the laser spot diameter being maintained at 10 μm and the source power varying from 100 to 200 mW. Furthermore, UC luminescence on optical fibers was measured using a Thor Laboratories ITC4005 laser diode for the excitation at 788 nm and Thor Laboratories CLD 1015 for excitation at 980 nm, both operating at 25 °C. To collect the signal, an IFG multimode fiber with a core diameter of 400 μm and a 0.30 numerical aperture was used to measure the luminescence in transmission mode, along with a portable spectrometer operating in the range between 380 and 900 nm. Additionally, a 725 nm cutoff long-pass filter was used to remove the excitation light.

https://doi.org/10.1021/acsaom.4c00348
ACS Appl. Opt. Mater. 2024, 2, 2501−2508

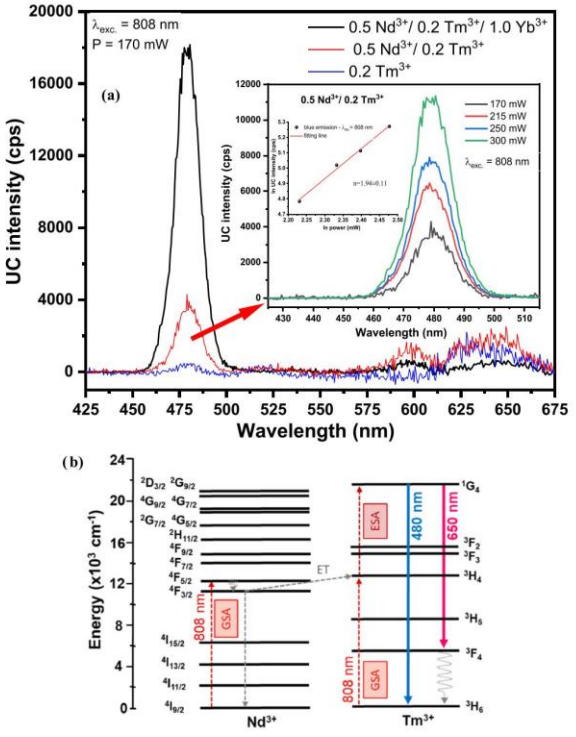

Figure 4. (a) UC spectra of Tm0.2, Tm0.2-Nd0.5, and Tm0.2-Nd0.5-Yb1 samples under 808 nm with an excitation power of 200 mW; *inset:* UC spectra of Tm0.2-Nd0.5 excited at 980 nm under different power values, and log–log plot of the integrated blue emission intensity as a function of the excitation power; (b) schematic energy-level diagram with the possible mechanism for Nd^{3+}/Tm^{3+}-codoped PNKA glasses. ET, energy transfer; GSA, ground-state absorption; ESA, excited-state absorption.

The dependence of the blue UC intensity of the Nd0.5/Tm0.2 sample on excitation power is presented in the inset of Figure 4a for source power ranging from 170 to 300 mW. The UC emission intensity is proportional to the incident excitation power as $I \propto I_{exc}^{n}$, where n represents the number of photons involved in the process for a UC emission band. By using the integrated areas of the band centered at 480 nm, linear fitting ($R^2 > 0.99$) of the log–log plot was performed, resulting in an n value of 1.94 ± 0.11, indicating that two photons are involved in the process. The mechanism can be described by two ground-state absorptions (GSAs) of Tm^{3+}: $^3H_6 \rightarrow {}^3H_4$ and Nd^{3+}: $^4I_{9/2} \rightarrow {}^4F_{5/2}$, followed by an energy transfer (ET) from $^4F_{3/2}$ of Nd^{3+} to the $^3H_4$ excited state of Tm^{3+}.[15] Then, this excited-state absorption (ESA) leads to the electron excitation to $^1G_4$ of Tm^{3+}, suggesting a two-photon mechanism, as depicted in Figure 4b.

In the triply doped system, other mechanisms can happen, including energy-transfer upconversion (ETU). In this case, Nd^{3+} serves as a sensitizer, absorbing an 808 nm photon, while Yb^{3+} acts as a bridge in the ET process between Nd^{3+} and Tm^{3+}, as already reported by Gouveia-Neto et al. in germanate glasses.[18] This enhances the efficiency of the process and contributes to the increased blue emission intensity. The dependence of the blue UC intensity on the excitation power was examined under an 808 nm excitation, with the source power varying between 170 and 300 mW, as shown in Figure 5a. Using the integrated areas of the band centered at 480 nm, linear fitting ($R^2 > 0.99$) of the log–log plot was calculated.

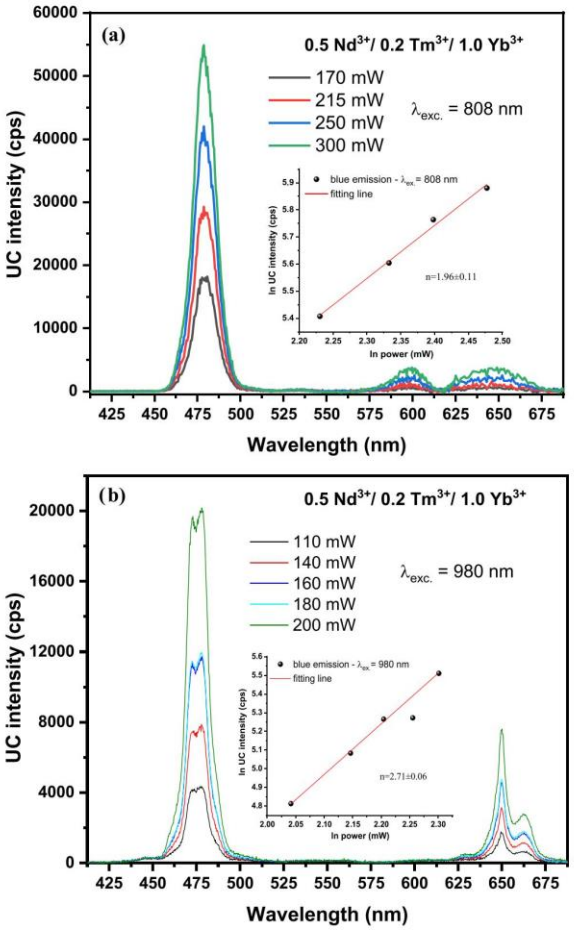

Figure 5. (a) UC spectra of the triply doped glass bulk (Tm0.2-Nd0.5-Yb1 sample) excited at 808 nm under different power values; *inset:* the log–log plot of the integrated blue emission intensity as a function of the excitation power; (b) UC spectra of Tm0.2-Nd0.5-Yb1 excited at 980 nm under different power values; *inset:* the log–log plot of the integrated blue emission intensity as a function of the excitation power (the point obtained for 180 mW was excluded of the slope calculation).

This analysis resulted in an n value of 1.96 ± 0.11, which reveals that two photons participate in the ETU mechanism when an 808 nm excitation is used.

UC luminescence for the triply doped system was also investigated under a 980 nm excitation (Figure 5b). Here, direct absorption by Yb^{3+} occurs, followed by energy transfer to the emitter ions. As expected, only samples containing Yb^{3+} (Tm0.2-Yb1 and Tm0.2-Nd0.5-Yb1) exhibited UC activity (see Figure S2). Under this excitation, a red UC emission centered at 650 nm was observed, likely related to the Tm^{3+}: $^1G_4 \rightarrow {}^3F_4$ transition. Luminescence intensity was measured by using different excitation powers from 110 to 200 mW, and a log–log plot determined the number of photons involved. For a 980 nm excitation, the calculated slope from linear fitting ($R^2 > 0.99$) showed a different value compared to an 808 nm

https://doi.org/10.1021/acsaom.4c00348
ACS Appl. Opt. Mater. 2024, 2, 2501−2508

excitation, as shown in the inset of Figure 7. Here ($n = 2.71 \pm 0.06$), it can be inferred that three photons from the excitation source are required for the UC pathway.

The UC mechanism proposed for the $Nd^{3+}/Yb^{3+}/Tm^{3+}$-codoped PNKA glasses under an 808 nm excitation is depicted in Figure 6a. Initially, both Nd^{3+} and Tm^{3+} are excited by an

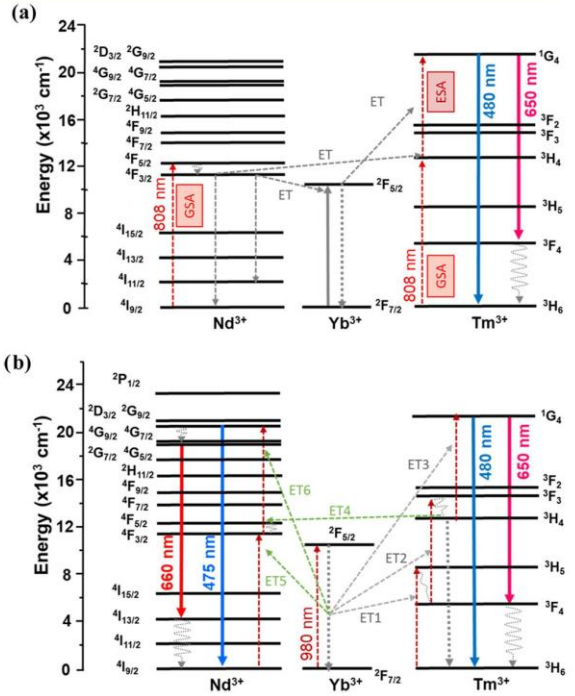

Figure 6. (a) Simplified energy-level diagram with the possible transition pathways for $Nd^{3+}/Tm^{3+}/Yb^{3+}$ triply doped PNKA glasses. ET, energy transfer; GSA, ground-state absorption; (b) simplified energy-level diagram with the proposed UC mechanism for the $Nd^{3+}/Tm^{3+}/Yb^{3+}$-tridoped PNKA glass under a 980 nm excitation.

808 nm radiation, corresponding to the Nd^{3+}: $^4I_{9/2} \rightarrow {}^4F_{5/2}$ and Tm^{3+}: $^3H_6 \rightarrow {}^3F_4$ transitions. The Nd^{3+}:$^4F_{5/2}$ excited state promptly relaxes to the next-lower $^4F_{3/2}$ state due to multiphonon relaxation, followed by an ET from Nd^{3+} to Yb^{3+} through the transitions Nd^{3+}: $^4F_{3/2} \rightarrow {}^4I_{11/2}$ and Yb^{3+}: $^2F_{5/2} \rightarrow {}^2F_{7/2}$. Afterward, the energy is transferred to the electron in the $^3H_4$ excited state of Tm^{3+}, promoting it to the $^1G_4$ level. Finally, the Tm^{3+}: $^1G_4 \rightarrow {}^3H_6$ radiative transition occurs, leading to a notably intense blue UC luminescence at around 480 nm. As previously reported in several works,[15,18−19] the Yb^{3+} plays a critical role in this kind of system, acting as a "bridging ion" between Nd^{3+} and Tm^{3+} under excitation at around 800 nm.

The properties of the host matrix can considerably influence the emission efficiency. Phosphate glasses often exhibit relatively high phonon energy (~1200 cm^{-1}), which can facilitate nonradiative relaxation and reduce luminescence efficiency in RE^{3+} ions.[42] However, glass matrices with relatively high phonon energy can also be advantageous for codoped systems, as they facilitate energy transfer between dopant ions, particularly in systems where Yb^{3+} serves as a sensitizer.[43−45] For the Yb^{3+}: $^2F_{5/2} \rightarrow {}^2F_{7/2}$ transition at 980 nm (10204 cm^{-1}), used for Tm^{3+} sensitization, nine phonons are required for complete nonradiative relaxation. Since the number of required phonons is larger than four, the contribution of nonradiative transitions becomes negligible in this process.[44]

To further elucidate the $Yb^{3+} \rightarrow Tm^{3+}$ UC energy-transfer pathway under a 980 nm excitation, an energy-level diagram is proposed in Figure 6b. Initially, Tm^{3+} ions are excited from the ground state to the $^3H_5$ level via energy transfer (ET1) from Yb^{3+}, followed by a rapid relaxation to the $^3F_4$ level. Next, most Tm^{3+} progress to the $^3F_{2,3}$ levels with Yb^{3+} assistance (ET2) before further relaxing to the $^3H_4$ metastable state. From the $^3H_4$ level, Tm^{3+} are promoted to the $^1G_4$ level via another energy transfer (ET3) from Yb^{3+}. Finally, the excited Tm^{3+} at the $^1G_4$ state emit 480 nm blue and 650 nm red lights as they return to the ground state $^3H_6$ and the $^3F_4$ level, respectively. Additionally, Nd^{3+} contributes to two side bands in the spectra through the $^4G_{9/2} \rightarrow {}^4I_{9/2}$ and $^4G_{7/2} \rightarrow {}^4I_{13/2}$ transitions, resulting in emissions at 475 and 660 nm, respectively. These Nd^{3+} emissions are also depicted in Figure 6b, where Nd^{3+} ions are initially excited from their ground state to the $^4F_{5/2}$ level through ET4 from the Tm^{3+}: $^3H_4$ level. These Nd^{3+} ions then rapidly relax to the $^4F_{3/2}$ level, which can also be populated via ET5 from the Yb^{3+}: $^2F_{5/2}$ level. Subsequently, further excitation of Nd^{3+} ions occurs from the $^4F_{3/2}$ level to the $^2G_{9/2}$ level via ET6 from Yb^{3+} ions. The Nd^{3+} ions at the $^2G_{9/2}$ level then radiate to the ground state, resulting in an intense blue emission of 475 nm. Furthermore, the 660 nm red emission occurs due to the population of the $^4G_{7/2}$ level via multiphonon relaxation from the $^2G_{9/2}$ level, followed by a radiative decay to the $^4I_{13/2}$ level.[12,46]

3.3. Blue UC on Triply Doped Optical Fibers

PNKA optical fibers were evaluated for optical losses within the range of 380−825 nm. As depicted in Figure 7, the PNKA

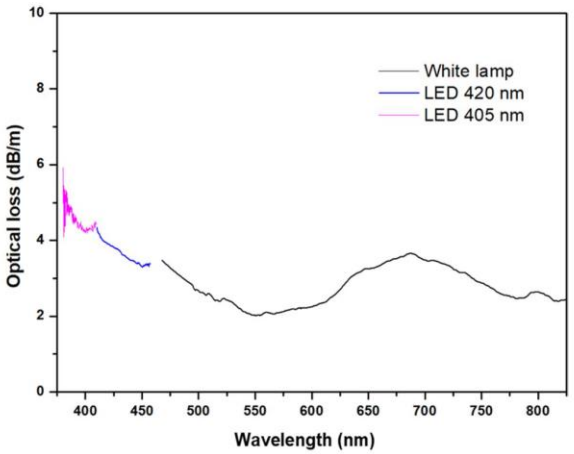

Figure 7. Optical loss curve of the PNKA optical fiber (diameter = 160 μm) using three different light sources: white lamp (gray line), 420 nm (blue), and 405 nm (pink) light-emitting diodes (LEDs).

fiber demonstrates a signal attenuation of less than 5 dB/m across the entire analyzed range. A slight increase in attenuation is observed between 600 and 750 nm, which is commonly seen in tellurite and phosphate fibers and is attributed to the presence of Pt^{4+} ions originating from the platinum crucible utilized.[41,47,48] Besides the relatively low

https://doi.org/10.1021/acsaom.4c00348
ACS Appl. Opt. Mater. 2024, 2, 2501−2508

refractive index of around 1.5 (see Figure S3), this comparatively low level of optical loss for an unclad single-index fiber indicates its suitability as a host material for blue UC applications.[49,50] Due to the high solubility of RE^{3+} in this glass matrix, only short fiber lengths are required for efficient UC measurements. Therefore, a 15 cm fiber was used in the UC measurements, resulting in a total loss of 0.3 dB.

With the aim of creating a compact system, small-femtometer fiber-coupled diodes are used in this section to excite the phosphate optical fiber. The optical fiber was excited at different wavelengths from 776 to 795 nm, and the optimum excitation wavelength was defined as 788 nm, aiming to achieve maximum intensity for blue UC (see Figure S4). Figure 8a shows the emission spectra of the PNKA optical fiber doped with $Tm^{3+}/Nd^{3+}/Yb^{3+}$ as a function of excitation power.

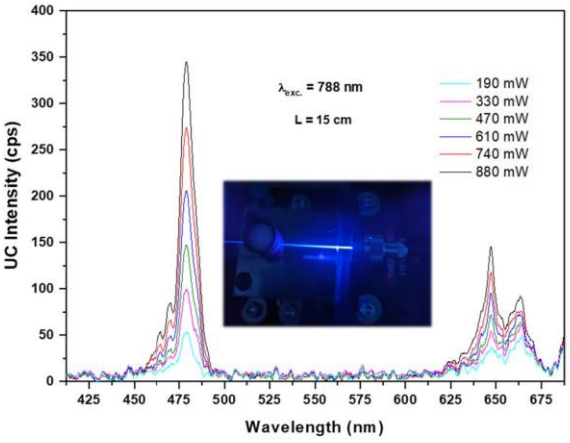

Figure 8. UC spectra of the PNKA optical fiber triply doped with $Tm^{3+}/Nd^{3+}/Yb^{3+}$ under a 788 nm excitation under different powers; *inset:* picture of the fiber emitting blue UC luminescence.

The red emission centered at 650 nm was observed under this experimental condition as well as in the measurements on bulks excited at 980 nm. As aforementioned, this emission occurs by a radiative decay to a nongrounded state, representing a competitor transition to the blue emission pathway (see Figure 6a). Nevertheless, the blue UC emission is significantly more intense than the red UC emission in the fiber's measurements, observable even to the naked eyes (see the *inset* of Figure 8), indicating the potential of $Tm^{3+}/Nd^{3+}/Yb^{3+}$ triply doped aluminum-phosphate fiber for blue laser applications. It is worth noting that the blue emission band comprises two components, which can be explained by the electron−electron interaction and spin−orbit coupling, resulting in the splitting of Stark sublevels $^1G_{4(2)}$ and $^1G_{4(1)}$.[51,52] In addition, the slight variations in the spectra of the bulk and fiber samples can be attributed to the fact that the sample thickness affects the emission spectra, particularly in fibers, where radiation trapping occurs in longer segments (>10 cm), leading to a narrowing and red shift of the emission.[53]

The UC measurements using triply doped optical fibers were also conducted under excitation at 980 nm. To evaluate the role played by Yb^{3+} ions as bridging and donor species in the Tm^{3+} UC process, the dependence of the blue emission intensity as a function of the pump wavelength at 980 nm was examined (Figure 9). A comparison of the UC spectra of the

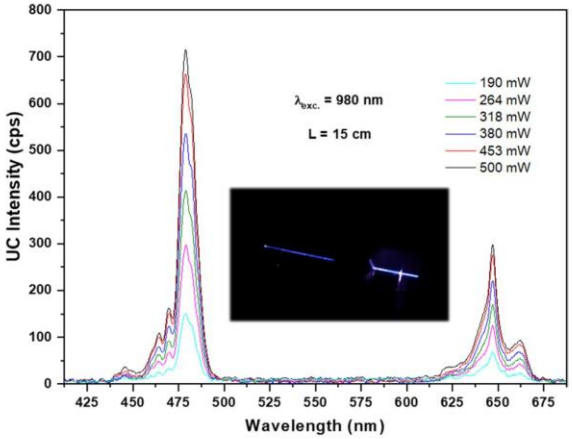

Figure 9. UC spectra of the PNKA optical fiber triply doped with $Tm^{3+}/Nd^{3+}/Yb^{3+}$ under a 980 nm excitation under different values of power (from 190 to 500 mW); *inset:* picture of the fiber emitting a blue UC luminescence.

triply doped optical fiber under excitation at 788 and 980 nm reveals that the direct excitation of Yb^{3+} leads to higher UC luminescence intensities. This can be attributed to a lack of the bridging role of Yb^{3+} when excited at 980 nm, enabling the pumped ion to transfer energy directly to the emitters. However, it is relevant to note that a bright blue UC was achievable under both excitation wavelengths using low-cost diode laser sources, with the 788 nm excitation also demonstrating significant effectiveness. Thus, these results suggest a viable alternative for systems where the use of 980 nm may be impractical or unfeasible.

4. CONCLUSIONS

This study presents the observation of a bright blue UC luminescence around 480 nm in $Nd^{3+}/Tm^{3+}/Yb^{3+}$ triply doped aluminum-phosphate glassy materials when excited at 788, 808, and 980 nm. The characterizations of PNKA glass indicate its suitability for fiber drawing, as evidenced by the successful production of single-index optical fibers exhibiting a low optical loss in the visible range.

The inclusion of Yb^{3+} in the glass composition significantly enhances the energy-transfer process, leading to an amplified blue UC luminescence from Tm^{3+}, for which mechanisms have been proposed in this work. Triply doped optical fibers containing Nd^{3+}, Tm^{3+}, and Yb^{3+} were successfully produced, a contribution that, to the best of our knowledge, is reported here for the first time in the literature.

The UC photoluminescence measurements using optical fibers were carried out under 788 and 980 nm excitations, which revealed a significant enhancement in the blue UC intensity under excitation at 980 nm. However, an intense blue UC emission was obtained even when excited at 788 nm, which provides an interesting alternative source for the 980 nm laser diode in several systems. Thus, the demonstrated capability to generate and guide the bright blue luminescence within the optical fiber signifies the promising potential of the developed material for diverse applications in solid-state lasers and photonics.

https://doi.org/10.1021/acsaom.4c00348
ACS Appl. Opt. Mater. 2024, 2, 2501−2508

■ ASSOCIATED CONTENT

Supporting Information

The Supporting Information is available free of charge at https://pubs.acs.org/doi/10.1021/acsaom.4c00348.

DTA curves of doped glass samples; UC spectra of different doped samples to evaluate the influence of Nd^{3+} in this system; refractive index of PNKA glass as a function of the wavelength; and wavelength optimization for the excitation of triply doped PNKA fibers (PDF)

■ AUTHOR INFORMATION

Corresponding Authors

Renato Grigolon Capelo − *Instituto de Química de São Carlos (IQSC), Universidade de São Paulo (USP), São Carlos, SP 13566-590, Brazil; Laboratoire Interdisciplinaire Carnot de Bourgogne (ICB), UMR 6303 CNRS-Université de Bourgogne, Dijon 21078, France;* orcid.org/0000-0001-8886-1507; Email: renatocapelo@usp.br

Danilo Manzani − *Instituto de Química de São Carlos (IQSC), Universidade de São Paulo (USP), São Carlos, SP 13566-590, Brazil;* orcid.org/0000-0001-7280-5404; Email: dmanzani@usp.br

Authors

Clément Strutynski − *Laboratoire Interdisciplinaire Carnot de Bourgogne (ICB), UMR 6303 CNRS-Université de Bourgogne, Dijon 21078, France*

Gregory Gadret − *Laboratoire Interdisciplinaire Carnot de Bourgogne (ICB), UMR 6303 CNRS-Université de Bourgogne, Dijon 21078, France*

Frédéric Désévédavy − *Laboratoire Interdisciplinaire Carnot de Bourgogne (ICB), UMR 6303 CNRS-Université de Bourgogne, Dijon 21078, France*

Frédéric Smektala − *Laboratoire Interdisciplinaire Carnot de Bourgogne (ICB), UMR 6303 CNRS-Université de Bourgogne, Dijon 21078, France*

Complete contact information is available at: https://pubs.acs.org/10.1021/acsaom.4c00348

Funding

The Article Processing Charge for the publication of this research was funded by the Coordination for the Improvement of Higher Education Personnel - CAPES (ROR identifier: 00x0ma614).

Notes

The authors declare no competing financial interest.

■ ACKNOWLEDGMENTS

The authors acknowledge grants from São Paulo Research Foundation—FAPESP (2020/12280-1, 2023/07793-6, 2021/08111-2) and Campus France for financial support. This work benefited from the facilities of the SMARTLIGHT platform funded by the Agence Nationale de la Recherche (EQUIPEX+ contract "ANR-21-ESRE-0040") and Région Bourgogne Franche-Comté.

■ REFERENCES

(1) Dorosz, D.; Kochanowicz, M.; Zmojda, J. Blue Upconversion Emission in Germanate Glass Co-Doped with Yb3+/Tm3+ Ions. *Int. J. Appl. Glass Sci.* **2014**, *5* (4), 393−400.

(2) Kochanowicz, M.; Mazerski, W.; Żmojda, J.; Czajkowski, K.; Dorosz, D. Green Upconversion Emission in Tellurite Optical Fibre Codoped with Yb3+/Er3. *Photonics Lett. Poland* **2013**, *5* (1), 35−37.

(3) Yamashita, T.; Ohishi, Y. Spectroscopic Properties of Tb3+-Yb3+-Codoped Borosilicate Glasses for Green Lasers and Amplifiers. In *Active and Passive Optical Components for Communications VI*; SPIE, 2006; Vol. *6389*, pp 283−293 DOI: 10.1117/12.685507.

(4) Tinsley, J. N.; Bandarupally, S.; Penttinen, J.-P.; Manzoor, S.; Ranta, S.; Salvi, L.; Guina, M.; Poli, N. Watt-Level Blue Light for Precision Spectroscopy, Laser Cooling and Trapping of Strontium and Cadmium Atoms. *Opt. Express* **2021**, *29* (16), 25462.

(5) Sousa, V.; Gomes, A. T. P. C.; Freitas, A.; Faustino, M. A. F.; Neves, M. G. P. M. S.; Almeida, A. Photodynamic Inactivation of Candida Albicans in Blood Plasma and Whole Blood. *Antibiotics* **2019**, *8* (4), 221.

(6) Seme, B.; Günther, K.; Winkler, N.; Wipprich, W. Blue Light-emitting Diodes for Disinfection: Is the Process Able to Improve Hygiene in Clinics and Public Buildings? *PhotonicsViews* **2021**, *18* (3), 91−95.

(7) Zou, Y.; Wang, Y.; Zhu, Z.; Li, J.; Lakshminarayana, G.; Tu, C. Crystal Growth and Infrared-to-Visible Upconversion Luminescence in Nd-Yb-Tm: CaYAlO4 Single Crystal. *J. Lumin.* **2023**, *263*, No. 120037.

(8) Sukul, P. P.; Swart, H. C. Crystal Phase Modified Blue Upconversion on Tm3+/Yb3+:BCZT Ceramic Phosphor Benefits Multifunctionality in White-Light Applications. *Dalton Trans.* **2022**, *51* (30), 11515−11525.

(9) Dutta, J.; Chakraborty, M.; Rai, V. K. Tm3+; Yb3+:Zn2TiO4 near Infrared to Blue Upconversion Phosphors for Anti-Counterfeit Applications. *RSC Adv.* **2023**, *13* (34), 23386−23395.

(10) Wu, L.; Pan, Y.; Xu, S.; Zhang, P.; Wu, W.; Hao, Y.; Ta, S.; Wang, Y.; Goodman, B. A.; Deng, W. Design and Preparation of White Light Emission from Up-Conversion Transitions in Er3+/Tm3+/Yb3+ Co-Doped Cubic Zirconia Single Crystals. *Ceram. Int.* **2023**, *49* (18), 29682−29689.

(11) Upconversion and Anti-Stokes Processes with f and d Ions in Solids | Chemical Reviews. https://pubs.acs.org/doi/10.1021/cr020357g (accessed 2023−10−26).

(12) Song, S.-A.; Kim, D.-S.; Jeong, H.-M.; Lim, K.-S. Upconversion in Nd−Tm−Yb Triply Doped Oxyfluoride Glass−Ceramics Containing CaF2 Nanocrystals. *J. Lumin.* **2014**, *152*, 75−78.

(13) Li, D.; Wang, Y.; Zhang, X.; Yang, K.; Liu, L.; Song, Y. Optical Temperature Sensor through Infrared Excited Blue Upconversion Emission in Tm3+/Yb3+ Codoped Y2O3. *Opt. Commun.* **2012**, *285* (7), 1925−1928.

(14) Soni, A. K.; Dey, R.; Rai, V. K. Stark Sublevels in Tm3+−Yb3+ Codoped Na2Y2B2O7 Nanophosphor for Multifunctional Applications. *RSC Adv.* **2015**, *5* (44), 34999−35009.

(15) Tian, Y.; Li, X.; Shen, R.; Han, C.; Wang, X.; Xu, S.; Cheng, L.; Sun, J.; Zhang, J.; Zhang, X.; Chen, B. Laser-Induced Thermal Effect and the Role of Nd3+ in Tm3+/Yb3+/Nd3+ Triply Doped LaNbO4 up-Conversion Phosphors under 808 Nm Excitation. *J. Lumin.* **2020**, *223*, No. 117201.

(16) Liu, X.; Li, T.; Zhao, X.; Suo, H.; Zhang, Z.; Zhao, P.; Gao, S.; Niu, M. 808 Nm-Triggered Optical Thermometry Based on up-Conversion Luminescence of Nd3+/Yb3+/Er3+ Doped MIn2O4 (M = Ca, Sr and Ba) Phosphors. *Dalton Trans.* **2018**, *47* (19), 6713−6721.

(17) Liu, B.; Li, C.; Yang, P.; Hou, Z.; Lin, J. 808-Nm-Light-Excited Lanthanide-Doped Nanoparticles: Rational Design, Luminescence Control and Theranostic Applications. *Adv. Mater.* **2017**, *29* (18), No. 1605434, DOI: 10.1002/adma.201605434.

(18) Gouveia-Neto, A. S.; da Costa, E. B.; dos Santos, P. V.; Bueno, L. A.; Ribeiro, S. J. L. Sensitized Thulium Blue Upconversion Emission in Nd3+/Tm3+/Yb3+ Triply Doped Lead and Cadmium Germanate Glass Excited around 800 Nm. *J. Appl. Phys.* **2003**, *94* (9), 5678−5681.

(19) Huang, X. Giant Enhancement of Upconversion Emission in ($NaYF_4$:Nd^{3+}/Yb^{3+}/Ho^{3+})/($NaYF_4$:Nd^{3+}/Yb^{3+}) Core/Shell Nanoparticles Excited at 808 Nm. *Opt. Lett.* **2015**, *40* (15), 3599−3602.
(20) Qiu, J.; Kawamoto, Y. Blue Up-Conversion Luminescence and Energy Transfer Process in Nd3+-Yb3+-Tm3+ Co-Doped ZrF4-Based Glasses. *J. Appl. Phys.* **2002**, *91* (3), 954−959.
(21) Ye, Z.-Q.; Xiao, S.-G.; Yang, X.-L. Up-Conversion of Nd3+/Yb3+/Tm3+ Tri-Doped CaTeO3 Compound under Excitation of 808 Nm. *Rare Met.* **2021**, *40* (4), 1008−1013.
(22) Anashkina, E. A. Laser Sources Based on Rare-Earth Ion Doped Tellurite Glass Fibers and Microspheres. *Fibers* **2020**, *8* (5), 30.
(23) Falconi, M. C.; Laneve, D.; Portosi, V.; Taccheo, S.; Prudenzano, F. Design of a Multi-Wavelength Fiber Laser Based on Tm:Er:Yb:Ho Co-Doped Germanate Glass. *J. Lightware Technol.* **2020**, *38* (8), 2406−2413.
(24) Vonderhaar, A.; Stone, M. P.; Campbell, J.; Hawkins, T. W.; Ballato, J.; Dragic, P. D. Concentration Quenching and Clustering Effects in Er:YAG-Derived All-Glass Optical Fiber. *Opt. Mater. Express* **2021**, *11* (10), 3587.
(25) Mura, E.; Lousteau, J.; Milanese, D.; Abrate, S.; Sglavo, V. M. Phosphate Glasses for Optical Fibers: Synthesis, Characterization and Mechanical Properties. *J. Non-Cryst. Solids* **2013**, *362*, 147−151.
(26) Manzani, D.; Montesso, M.; Mathias, C. F.; Krishanaiah, K. V.; Ribeiro, S. J. L.; Nalin, M. Visible Up-Conversion and near-Infrared Luminescence of Er3+/Yb3+ Co-Doped SbPO4-GeO2 Glasses. *Opt. Mater.* **2016**, *57*, 71−78.
(27) Filho, J. C.; Zilio, S. C.; Messias, D. N.; Pilla, V.; Almeida Silva, A. C.; Dantas, N. O.; Andrade, A. A. Effects of Aluminum Substitution by Potassium in the P2O5−Al2O3−Na2O−K2O Phosphate Glasses. *J. Alloys Compd.* **2020**, *815*, No. 152359.
(28) Brow, R. K.; Kirkpatrick, R. J.; Turner, G. L. Nature of Alumina in Phosphate Glass: II, Structure of Sodium Alurninophosphate Glass. *J. Am. Ceram. Soc.* **1993**, *76* (4), 919−928.
(29) Lakshminarayana, G.; Qiu, J.; Brik, M. G.; Kumar, G. A.; Kityk, I. V. Spectral Analysis of Er3+-, Er3+/Yb3+- and Er3+/Tm3+/Yb3+-Doped TeO2−ZnO−WO3−TiO2−Na2O Glasses. *J. Phys.: Condens. Matter* **2008**, *20* (37), No. 375101.
(30) Reddy, A. A.; Babu, S. S.; Pradeesh, K.; Otton, C. J.; Vijaya Prakash, G. Optical Properties of Highly Er3+-Doped Sodium−Aluminium−Phosphate Glasses for Broadband 1.5μm Emission. *J. Alloys Compd.* **2011**, *509* (9), 4047−4052.
(31) Zaki, R. M.; Strutynski, C.; Kaser, S.; Bernard, D.; Hauss, G.; Faessel, M.; Sabatier, J.; Canioni, L.; Messaddeq, Y.; Danto, S.; Cardinal, T. Direct 3D-Printing of Phosphate Glass by Fused Deposition Modeling. *Mater. Des.* **2020**, *194*, No. 108957.
(32) Filho, J. C.; Lourenço, S. A.; Ferreira, P. Z.; Pilla, V.; Messias, D. N.; Almeida Silva, A. C.; Dantas, N. O.; Andrade, A. A. Thermal Window of Constant Luminescence Quantum Efficiency of Nd3+-Doped Phosphate Glass. *J. Lumin.* **2016**, *180*, 81−87.
(33) Tian, Y. M.; Shen, L. F.; Pun, E. Y. B.; Lin, H. High-Aluminum Phosphate Glasses for Single-Mode Waveguide-Typed Red Light Source. *J. Non-Cryst. Solids* **2015**, *426*, 25−31.
(34) Evrard, M.; Serrano, E.; Strutynski, C.; Désévédavy, F.; Gadret, G.; Jules, J. C.; Kibler, B.; Smektala, F. (INVITED)Dispersion-Shifted Tellurite Fibers for Nonlinear Frequency Conversion. *Opt. Mater. X* **2022**, *15*, No. 100183.
(35) Tsuchida, J. E.; Ferri, F. A.; Pizani, P. S.; Martins Rodrigues, A. C.; Kundu, S.; Schneider, J. F.; Zanotto, E. D. Ionic Conductivity and Mixed-Ion Effect in Mixed Alkali Metaphosphate Glasses. *Phys. Chem. Chem. Phys.* **2017**, *19* (9), 6594−6600.
(36) Jlassi, I.; Elhouichet, H.; Ferid, M. Thermal and Optical Properties of Tellurite Glasses Doped Erbium. *J. Mater. Sci.* **2011**, *46* (3), 806−812.
(37) Wang, J. S.; Vogel, E. M.; Snitzer, E. Tellurite Glass: A New Candidate for Fiber Devices. *Opt. Mater.* **1994**, *3* (3), 187−203.
(38) Ehrmann, P. R.; Campbell, J. H.; Suratwala, T. I.; Hayden, J. S.; Krashkevich, D.; Takeuchi, K. Optical Loss and Nd3+ Non-Radiative Relaxation by Cu, Fe and Several Rare Earth Impurities in Phosphate Laser Glasses. *J. Non-Cryst. Solids* **2000**, *263*−*264*, 251−262.
(39) Ehrt, D.; Ebeling, P.; Natura, U. UV Transmission and Radiation-Induced Defects in Phosphate and Fluoride−Phosphate Glasses. *J. Non-Cryst. Solids* **2000**, *263*−*264*, 240−250.
(40) Friedrich-Schiller-Universität Jena; Ehrt, D. REVIEW: Phosphate and Fluoride Phosphate Optical Glasses — Properties, Structure and Applications. *Phys. Chem. Glasses: Eur. J. Glass Sci. Technol., Part B* **2015**, *56* (6), 217−234.
(41) Click, C. A.; Brow, R. K.; Ehrmann, P. R.; Campbell, J. H. Characterization of Pt4+ in Alumino-Metaphosphate Laser Glasses. *J. Non-Cryst. Solids* **2003**, *319* (1−2), 95−108.
(42) Malkin, B. Z. Ion-Phonon Interactions. In *Spectroscopic Properties of Rare Earths in Optical Materials*; Hull, R.; Parisi, J.; Osgood, R. M.; Warlimont, H.; Liu, G.; Jacquier, B., Eds.; Springer Series in Materials Science; Springer Berlin Heidelberg: Berlin, Heidelberg, 2005; Vol. *83*, pp 130−190 DOI: 10.1007/3-540-28209-2_3.
(43) Chen, Y.; Chen, G.; Liu, X.; Xu, J.; Zhou, X.; Yang, T.; Yuan, C.; Zhou, C. Upconversion Luminescence, Optical Thermometric Properties and Energy Transfer in Yb3+/Tm3+ Co-Doped Phosphate Glass. *Opt. Mater.* **2018**, *81*, 78−83.
(44) Rivera-López, F.; Babu, P.; Basavapoornima, Ch.; Jayasankar, C. K.; Lavín, V. Efficient Nd3+→Yb3+ Energy Transfer Processes in High Phonon Energy Phosphate Glasses for 1.0 μm Yb3+ Laser. *J. Appl. Phys.* **2011**, *109* (12), No. 123514.
(45) Sun, Y.; Yu, F.; Liao, M.; Ma, J.; Wang, X.; He, D.; Gao, W.; Knight, J.; Hu, L. Visible Emission and Energy Transfer in Tb^{3+}/Dy^{3+} Co-doped Phosphate Glasses. *J. Am. Ceram. Soc.* **2020**, *103* (12), 6847−6859.
(46) Peng, S.; Zhou, Y.; Yang, F.; Wu, L.; Qi, Y.; Wang, B. Improved Thermal Stability and Intense Blue Upconversion in Yb3+/Nd3+/Tm3+ Tri-Doped Tellurite Glasses. *Mater. Lett.* **2015**, *138*, 132−134.
(47) Kalnins, C. A. G.; Ebendorff-Heidepriem, H.; Spooner, N. A.; Monro, T. M. Enhanced Radiation Dosimetry of Fluoride Phosphate Glass Optical Fibres by Terbium (III) Doping. *Opt. Mater. Express* **2016**, *6* (12), 3692.
(48) Ebendorff-Heidepriem, H.; Kuan, K.; Oermann, M. R.; Knight, K.; Monro, T. M. Extruded Tellurite Glass and Fibers with Low OH Content for Mid-Infrared Applications. *Opt. Mater. Express* **2012**, *2* (4), 432.
(49) Galleani, G.; Ledemi, Y.; De Lima Filho, E. S.; Morency, S.; Delaizir, G.; Chenu, S.; Duclere, J. R.; Messaddeq, Y. UV-Transmitting Step-Index Fluorophosphate Glass Fiber Fabricated by the Crucible Technique. *Opt. Mater.* **2017**, *64*, 524−532.
(50) Kalnins, C. A. G.; Heidepriem, H. E.; Dowler, A.; Monro, T. M. Fabrication of Fluoride Phosphate Glass Optical Fibres for UV Applications. In *2011 International Quantum Electronics Conference (IQEC) and Conference on Lasers and Electro-Optics (CLEO) Pacific Rim incorporating the Australasian Conference on Optics, Lasers and Spectroscopy and the Australian Conference on Optical Fibre Technology*; IEEE: Sydney, Australia, 2011; pp 2051−2053 DOI: 10.1109/IQEC-CLEO.2011.6194106.
(51) Patra, A.; Ghosh, P.; Chowdhury, P. S.; Alencar, M. A. R. C.; Lozano, B. W.; Rakov, N.; Maciel, G. S. Red to Blue Tunable Upconversion in Tm3+-Doped ZrO2 Nanocrystals. *J. Phys. Chem. B* **2005**, *109* (20), 10142−10146.
(52) Liu, G.; Fu, Z.; Sheng, T.; Sun, Z.; Zhang, X.; Wei, Y.; Ma, L.; Wang, X.; Wu, Z. Investigation into Optical Heating and Applicability of the Thermal Sensor Bifunctional Properties of Yb3+ Sensitized Tm3+ Doped Y2O3, YAG and LaAlO3 Phosphors. *RSC Adv.* **2016**, *6* (100), 97676−97683.
(53) Richards, B.; Jha, A.; Tsang, Y.; Binks, D.; Lousteau, J.; Fusari, F.; Lagatsky, A.; Brown, C.; Sibbett, W. Tellurite Glass Lasers Operating Close to 2 μm. *Laser Phys. Lett.* **2010**, *7* (3), 177−193.

https://doi.org/10.1021/acsaom.4c00348
ACS Appl. Opt. Mater. 2024, 2, 2501−2508

Supporting Information

Blue up-conversion emission of $Nd^{3+}/Tm^{3+}/Yb^{3+}$ triply doped aluminophosphate optical fibers

Renato Grigolon Capelo[1,2*], Clément Strutynski[2], Gregory Gadret[2], Frédéric Désévédavy[2], Frédéric Smektala[2], Danilo Manzani[1*].

[1]*Instituto de Química de São Carlos (IQSC), Universidade de São Paulo (USP), São Carlos, SP, 13566-590 Brazil*

[2]*Laboratoire Interdisciplinaire Carnot de Bourgogne (ICB), UMR 6303 CNRS-Université de Bourgogne, Dijon, 21078, France*

*Corresponding authors:

Renato Grigolon Capelo
Instituto de Quimica de São Carlos (IQSC)
Universidade de São Paulo
São Carlos – SP – Brazil
E-mail: renatocapelo@usp.br

Danilo Manzani
Instituto de Quimica de São Carlos (IQSC)
Universidade de São Paulo
São Carlos – SP – Brazil
E-mail: dmanzani@usp.br

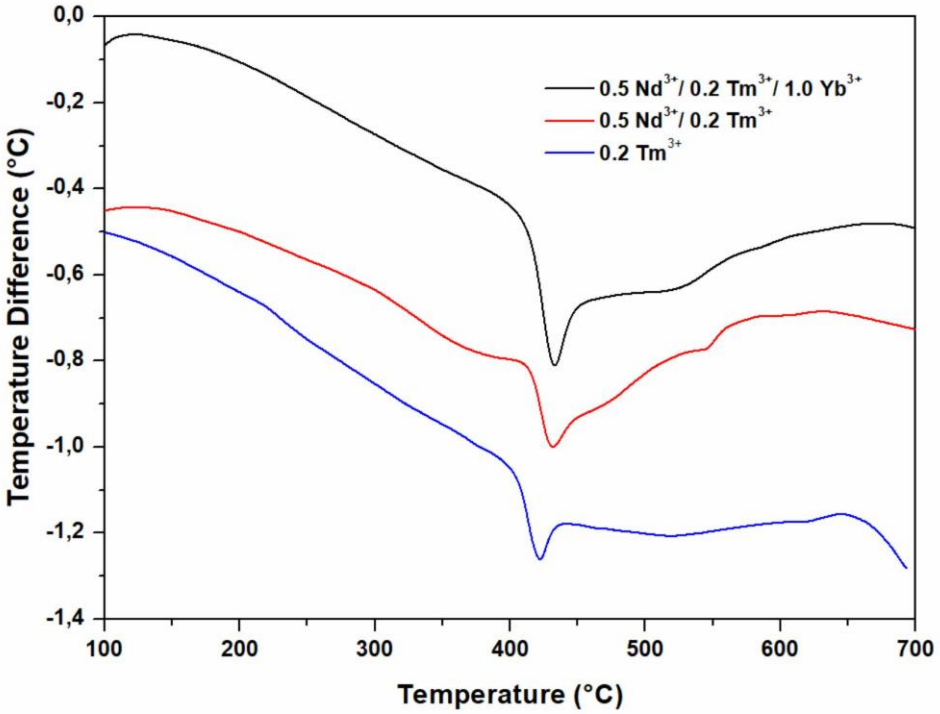

Figure S1. DTA curves of Tm0.2 (blue), Tm0.2-Nd0.5 (red), and Tm0.2-Nd0.5-Yb1 (black) samples in a range between 100 and 700 °C.

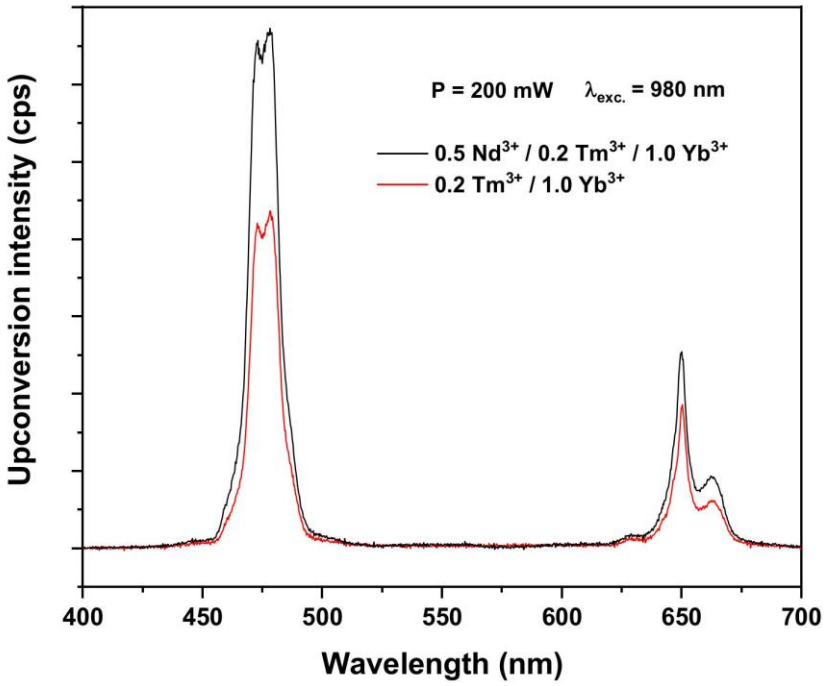

Figure S2. UC spectra of the samples Tm0.2- Yb1.0 and Tm0.2- Nd0.5-Yb1.0 under 980-nm excitation.

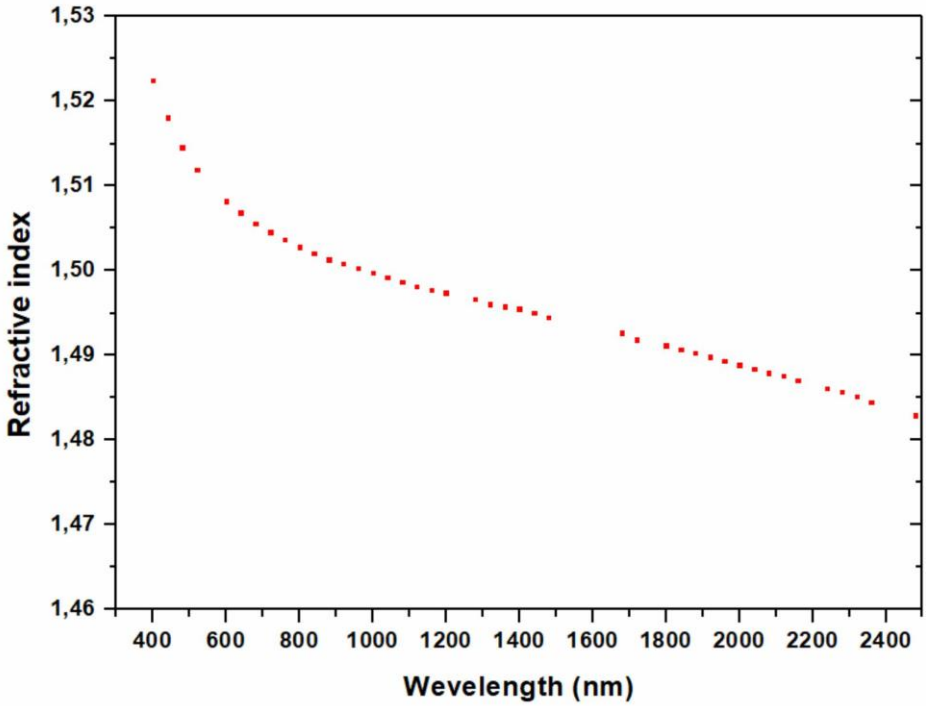

Figure S3. Refractive index of PNKA glass as a function of the wavelength in the range between 400 and 2500 nm.

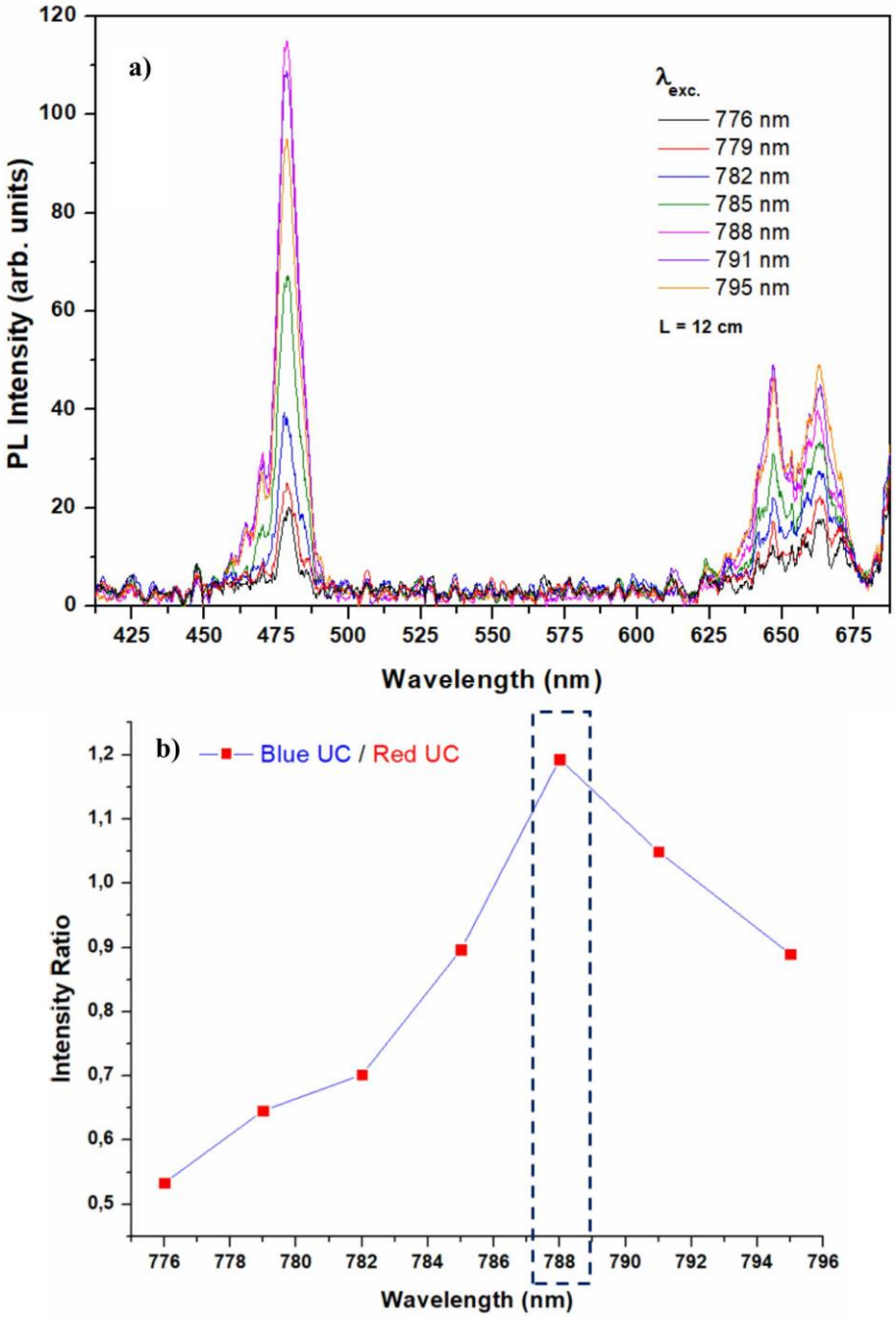

Figure S4. a) UC spectra of PNKA optical fiber triply-doped with $Tm^{3+}/Nd^{3+}/Yb^{3+}$ excited at different wavelengths; b) Intensity ratio of the emissions centered at 480 nm and 647 nm as a function of excitation wavelength.

Table of Contents (TOC) graphic

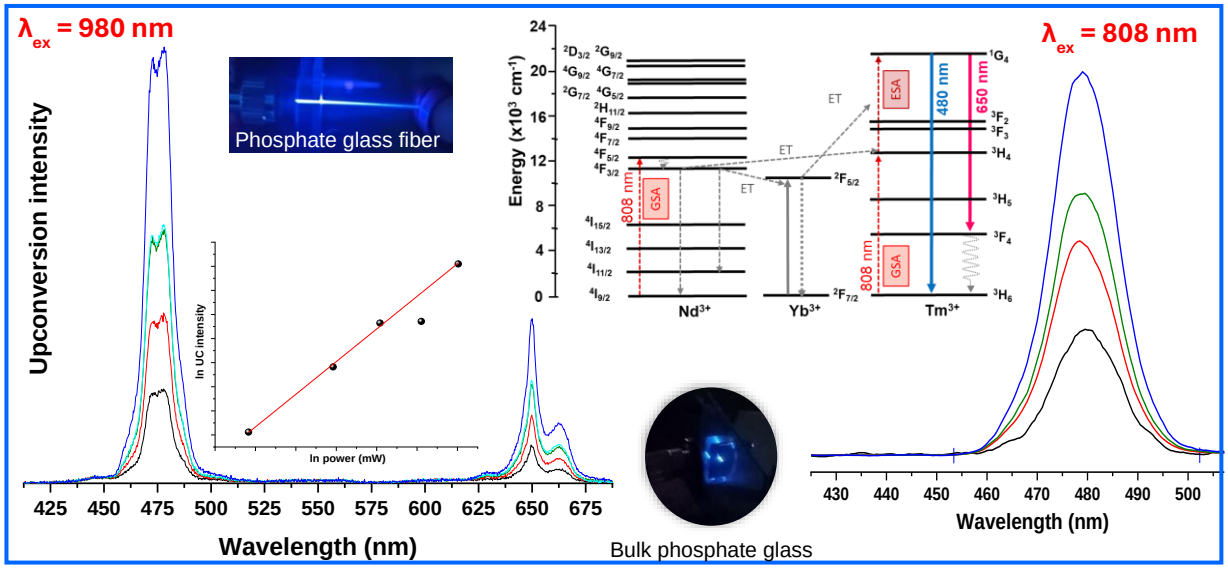

CHAPTER VII:

In situ growth of lanthanide coordination polymers on oxide glass and optical fibers: a promising material for chemical sensing

Abstract

Coordination polymers (CPs) and metal-organic frameworks (MOFs) have gained significant attention as chemical sensors due to their highly tunable porous structures, enabling selective interactions with target analytes. In particular, lanthanide-based coordination polymers (Ln-CPs) have been extensively utilized in optical sensing owing to their photoluminescent properties. However, these applications typically require deposition on stable substrates with appropriate chemical and physical characteristics. This study presents a simple, rapid, and in situ synthesis and coating process for Ln-MOFs on oxide glass bulk materials and optical fibers. Eu^{3+}-based CPs were successfully coated onto tellurite and phosphate glasses using polycarboxylic acids as ligands. Although slight deviations from previously reported crystalline structures were observed, the luminescent coatings were effectively formed and demonstrated good adhesion to the tellurite glass substrates. The optical fiber coatings showed significant potential for guiding light over long distances, facilitating remote sensing of various analytes. These materials exhibited high sensitivity, particularly in the detection of carbonyl organic compounds, with an enhanced luminescent response at low concentrations. The successful integration of Ln-CPs onto TZN-based optical fibers underscores their potential for real-time remote sensing, offering promising applications in environmental monitoring, industrial safety, and biomedical diagnostics.

Keywords: luminescence; lanthanide-coordination polymers; composites; chemical sensing.

1. Introduction

Coordination polymers (CPs) represent an advanced class of materials formed by the self-assembly of metal ions or clusters with organic linkers (1). They have garnered significant attention in recent decades, particularly those exhibiting porous structures, commonly referred to as metal-organic frameworks (MOFs) (2). These materials distinguish themselves from traditional porous materials like zeolites due to their remarkably high surface areas and tunable pore structures, which can reach up to 7000 $m^2.g^{-1}$ (3,4). CPs offer versatile functionality by combining the properties of their metal and organic components, enabling a wide range of applications (5–10).

Among CPs, those containing lanthanide ions as the metallic center (Ln-CPs) are particularly noteworthy due to the unique electronic, magnetic, and optical properties of lanthanide ions, attributed to their 4f electrons (11,12). In this context, lanthanide MOFs (Ln-MOFs) have emerged as promising multifunctional materials, characterized by high thermal stability and diverse coordination environments that allow for precise structural tuning. These materials not only possess high porosity but also exhibit exceptional luminescence properties, making them suitable candidates for applications in areas such as light-emitting diodes (LEDs), biomedical imaging, and chemical sensing (13–18).

The luminescence of Ln-MOFs can be tailored through the selection of lanthanide ions and organic linkers, positioning these materials as promising alternatives for new optical sensors (19–21). For instance, Eu^{3+}-based Ln-MOFs have been extensively studied using carboxylate ligands to form 3D networks with large pore volumes and high surface areas, while also exploring the antenna effect as a sensing mechanism (22–25). The porous nature of Eu-carboxylate MOFs allows for the selective uptake of guest molecules, which can modulate luminescence by either quenching or enhancing the emission from Eu^{3+}. This interaction facilitates molecular recognition, enabling the detection of gases, ions, and small molecules through changes in luminescent intensity or emission profile. Consequently, Ln-MOFs are promising sensors for detecting a wide range of analytes, providing a fast, efficient, and reusable platform (25).

For practical applications, MOFs must maintain stability when exposed to the chemical species of interest, typically forming a film over an appropriate substrate. In the case of Ln-MOFs, their luminescent properties are leveraged for sensing; however, an adequate supporting

material is also required to facilitate the transmission of excitation and emission light after interaction with an analyte. In this regard, oxide glasses with appropriate transparency in the ultraviolet (UV) and visible ranges can act as suitable host substrates for Ln-MOFs, as they exhibit good thermal and chemical stability along with desired optical properties (26–29). Additionally, optical fibers fabricated from these glasses represent a potential host material for Ln-MOFs, particularly in applications involving remote chemical sensing (30–32).

Although several studies report the formation of MOFs on substrates, most employ complex techniques such as dip coatings, electrochemical processes, or the incorporation of metal layers (33–35). Therefore, this study aims to investigate the *in situ* growth of Ln-CPs on the surfaces of tellurite and phosphate glasses and optical fibers, exploring their potential as chemical sensors. More specifically, we report the synthesis of various glass@Ln-CP composites combining glassy substrates and Ln-CPs based on Eu^{3+} linked to carboxylate ligands, utilizing a simple and rapid process, and examine their photoluminescent properties for detecting small organic molecules.

2. Experimental

2.1. Materials and methods

All chemicals were purchased from commercial sources and used without prior treatment. The glass samples were synthesized by conventional melt-queching method from high purity tellurium oxide (TeO_2, Aldrich 99.99%), zinc oxide (ZnO, Aldrich 99.9%), anhydrous zinc fluoride (ZnF_2, Aldrich 99.9%), and anhydrous sodium carbonate (Na_2CO_3, Aldrich 99%). The Ln-CPs precursors, 1,3,5-benzenetricarboxylic acid (H_3BTC), 2,6-pyridinedicarboxylic acid (H_2PDC), 1,2,4,5- benzenetetracarboxylic acid (H_4B4C) and $EuCl_3.6H_2O$ were purchased from Sigma Aldrich. The composites were characterized by Raman spectroscopy, X-ray diffractometry (XRD), scanning electron microscopy using a field emission gun (FEG-SEM) and photoluminescence (PL) spectroscopy to evaluate the formation of Ln-CPs on glass surfaces.

2.2. Glass Substrates Synthesis.

The glass samples were prepared by conventional melt-quenching process and the compositions and labels are shown in Table VII.1. For the tellurite glasses (TZN), the batch was heated in a furnace in a temperature range of 700-750 °C for 20 min in a gold crucible, then poured into a preheated brass mold, annealed 120 min at 250 °C, and finally cooled at a

rate of 10 °C/min down to room temperature. In the case of the aluminum-phosphate matrix (PNKA), the melting process was carried out at 1100 ºC during 40 min and then poured in a brass mold. The mold was preheated at 360 ºC and the annealing was performed at 400 ºC during 5 h, followed by a cooled process with a rate of 5 ºC. The samples were cut and polished before the coating process.

Table VII.1 - Label and nominal molar concentrations of the produced glass substrates.

Sample label	Nominal molar composition (%mol)						
	TeO_2	ZnO	ZnF_2	Na_2O	P_2O_5	K_2O	Al_2O_3
TZN	75	15	0	10			
TZNF15	75	0	15	10			
TN	90	-	-	10			
PNKA	-	-	-	20	45	20	15

The TZN glass preform for fiber drawing was prepared following the same procedure described above, but using a cylindrical mold and obtaining a preform measuring 5 cm in length with a diameter of 16 mm. Subsequently, the preform was drawn into fiber under He gas flow, on a commercial Control Interface Limited drawing tower at approximately 570 °C with a loading rate of 1.0 mm/min. Similarly, the PNKA cylindrical preform was fabricated using the melt-quenching technique, and optical fibers were drawn under analogous conditions, except for a higher temperature of around 715 ºC. Both resulting single-index optical fibers exhibited diameters ranging from 250 µm to 1 mm.

2.3. In situ growth of Ln-CPs on glass and optical fibers surfaces.

Glass coatings were initially prepared through microwave-assisted hydrothermal synthesis using a Teflon cylinder reactor at a temperature of 180°C. Following the addition of Ln-CP precursors into the reactor chamber, optical glass pieces were immersed in the reactive medium. Previously, the glass pieces were immersed in isopropanol and acetone for surface cleaning. Similarly, the *in situ* synthesis of Ln-CPs was conducted in an open system, utilizing a hotplate set to 90°C for durations ranging from 5 to 20 min with continuous stirring. This streamlined approach not only simplified the synthesis conditions but also facilitated the application of Ln-CP coatings onto optical fibers. The process involved immersing the fiber end (approximately 2-5 cm) into the solution. Specific procedures corresponding to the synthesis of each distinct Ln-CP were meticulously adhered to.

2.3.1. Synthesis of {[Eu(BTC)(PDC)]$_n$} MOF (1).

This synthesis follows the procedure described by Da Silva et al. (35), using two ligands containing carboxylate groups: H_3BTC and H_2PDC (35). H_3BTC (0.40 mmol, 84 mg) and 10 mL of deionized water were added to the reactor and the pH was adjusted to 3.6 with NaOH solution (0.5 mol. L^{-1}). Then, H_2PDC (1.20 mmol, 200 mg) and $EuCl_3.6H_2O$ (0.28 mmol, 100 mg) were added and heated for 20 min and cooled to room temperature. The same procedure was performed with a synthesis time of 10 min.

2.3.2. Synthesis of {[Eu(BTC)]$_n$} MOF (2).

This MOF was obtained using the same procedure described above, removing the H_2PDC ligand. Then, 84 mg (0.40 mmol) of H_3BTC was added in 10 mL of deionized water and the pH was adjusted to 3.6. The same amount of $EuCl_3.H_2O$ (0.28 mmol, 100 mg) was added to the Teflon reactor and heated for 20 min.

2.3.3. Synthesis of {[Eu(B4C)]$_n$} MOF (3).

This compound was synthesized by following a similar procedure to that used for Da Silva et al. (35), adapting some parameters based on procedures reported in the literature (36,37). H_4B4C (0.40 mmol, 90 mg) was dissolved in 10 mL of deionized water and the pH was adjusted to 5.0 using an aqueous solution of NaOH (0.5 mol. L^{-1}). After the $EuCl_3.6H_2O$ addition (0.28 mmol, 100 mg) addition, the reactor was sealed and heated for 20 min and then cooled to room temperature.

2.4. Characterization techniques

2.4.1. FEG-SEM

A JEOL JSM-7200F operating at a beam energy of 2.0 kV was used to obtain the scanning electron microscopy images using a field emission gun (FEG-SEM). The glass samples coated with Ln-CPs were analyzed using gold as a support, and high-resolution images of the glass-CP interface and the Ln-CP surfaces were taken.

2.4.2. X-ray diffractometry

XRD measurements were performed using a Siemens diffractometer, model D 5000, at room temperature with a wavelength corresponding to the $K_{\alpha 1}$ layer of Cu (1.54056 angstroms).

The crystallographic base ICSD (Inorganic Structure Database) was used, which presents an updated catalog of crystallographic phases already described.

2.4.3. PL spectroscopy

PL spectroscopy measurements were performed by Horiba Fluorolog-3 FL-1050 Spectrofluorometer, for the glasses coated with Ln-CPs. Luminescence spectra were recorded at room temperature from 400 to 700 nm, under excitation wavelengths varying from 300 to 395 nm and using different slit widths between 1 and 5 nm, depends on the sample. The data were collected at every nanometer with an integration time of 0.1 seconds for each step. In addition, decay time measurements were conducted in a Cary Eclipse spectrofluorometer in the phosphorescence mode, monitoring the main emission peak centered at 616 nm, under excitation at 300 nm.

2.4.4. PL measurements on optical fibers

PL measurements on coated optical fibers were performed using samples with lengths ranging from 7 to 15 cm and diameters between 250 μm and 1 mm. The Ln-CP coatings were excited using a UV lamp (254 nm) and a LED (308 nm). Emission was collected at the opposite tip of the optical fibers by a portable Hamamatsu Photonics spectrometer, model C-13555MA-5345. An integration time of 0.2 seconds was employed, with the accumulation of 100 spectra for improved signal accuracy.

2.4.5. Chemical sensing trials

The PL measurements for the sensing tests were carried out under the same conditions as described in Sections 2.4.3 for bulk samples and 2.4.4 for fiber samples. The samples were immersed in a quartz cuvette containing aqueous solutions of various organic compounds, with concentrations ranging from 0.05% to 6% by volume. The initial volume of the solution was 3 mL. PL spectra were recorded in triplicate, and the average spectrum was considered for analysis to ensure accuracy and reproducibility of the results.

3. Results and Discussion

3.1. Adhesion, morphology and structural characterization

The glass compositions of the TZN system were initially used for in situ growth of Ln-CPs, demonstrating good surface adhesion. This glass system, particularly those containing

ZnF_2, had been previously studied and exhibited a wide transparency range - from UV to mid-infrared - and good thermal stability (38). A composition without Zn (TN) was also tested to evaluate the influence of this transition metal on the coating capability of the glass. Additionally, the PNKA matrix was used as a substrate for Ln-CP growth, but the resulting coatings were less homogeneous and appeared to have weaker adhesion compared to those on TZN substrates. The composites produced in this study are described in Table VII.2, which indicates the carboxylate ligand coordinating to Eu^{3+}, the glass composition of the substrate, and its form, either as a monolith or a single-index optical fiber (OF).

Table VII.2 - Composites samples synthesized with a CP containing Eu^{3+} coated on glass substrates.

Sample label	Ligand precursor			Glass matrix	Composite form
	H_3BTC	**H_2PDC**	**H_4B4C**		
TZN@[Eu(BTC)(PDC)]	X	X		TZN	monolith
TZNF15@[Eu(BTC)(PDC)]	X	X		TZNF15	monolith
TZN@EuBTC	X			TZN	monolith / OF
TZNF15@EuBTC	X			TZNF15	monolith
TN@EuBTC	X			TN	monolith
PNKA@EuBTC	X			PNKA	monolith / OF
TZN@EuB4C			X	TZN	monolith / OF

Figure VII.1 presents images of several samples produced in this study. In panel 1(a), a photograph of TZN@[Eu(BTC)(PDC)] demonstrates a uniform coating layer on one face of the glass surface, while the other faces were polished to remove the coating. Panel 1(b) showcases the PNKA@EuBTC (transparent glass) and TZN@EuBTC (yellowish glass) samples under white light, whereas panel 1(c) displays their intense luminescence under UV light centered at 254 nm. Furthermore, panel 1(d) presents a cross-sectional image obtained via optical microscopy, allowing for the measurement of coating thickness, which averages 20 µm. Finally, panel 1(e) shows the same sample irradiated with blue LED light centered at 405 nm, revealing the intense green luminescence emitted from the film coated on the glass surface after the excitation source was removed, utilizing a bandpass filter.

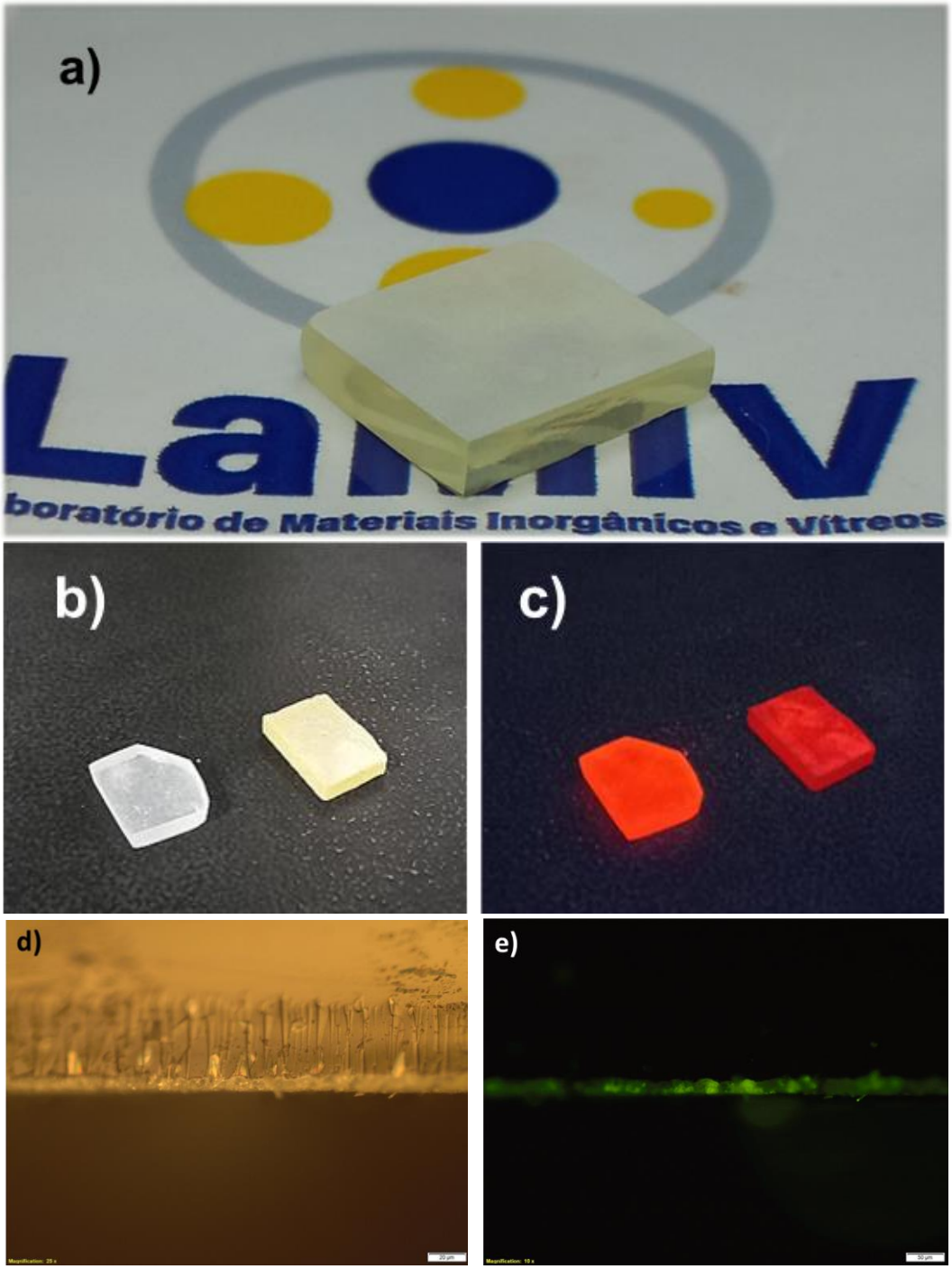

Figure VII.1 - Photographs of (a) TZN@[Eu(BTC)(PDC)]; (b) PNKA@EuBTC and TZN@EuBTC under whith light and (c) irradiated by UV-light at 254 nm; optical microscopy images of TZN@EuBTC under (d) white light and (e) blue light (405 nm).
Source: by the author

To investigate the interaction between the glass and the coordination polymer (CP), synthesis procedures were conducted using individual CP components - specifically, either the carboxylate ligand, BTC, or the Eu^{3+} precursor. Adhesion tests were performed using optical fibers as the glass substrate. Figure VII.2(a) presents optical microscopy images of the TZN@EuBTC and PNKA@EuBTC samples, revealing distinct differences in film appearance

despite identical synthesis conditions. Subsequently, TZN and PNKA substrates were exposed to the BTC ligand in an aqueous H_3BTC solution at a pH of 3.6. Figure VII.2(b) illustrates the BTC ligand coverage on the TZN fiber, resulting in a crystalline coating, while the PNKA fiber exhibited no adhesion of this species. However, exposure to EuC_3 solution resulted in a non-uniform coating on the PNKA surface, whereas no adhesion was observed on the TZN fiber (Figure VII.2(c)). This behavior suggests an interaction between the carboxyl groups and the TZN glass, as well as potential coordination of Eu^{3+} with the negatively charged groups on the PNKA surface, influenced by the glass composition and structural properties.

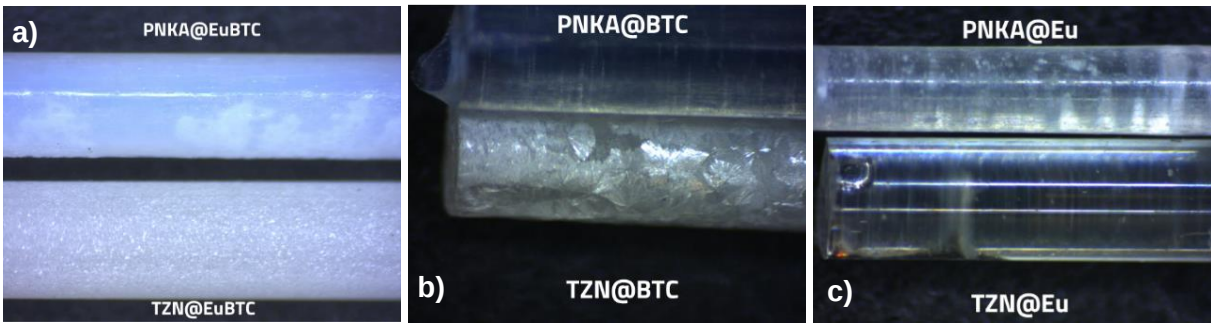

Figure VII.2 - Optical microscopy images of glass substrates after exposure to individual CP components: (a) TZN@EuBTC and PNKA@EuBTC films, showing distinct film appearances; (b) BTC ligand coating on TZN fiber with crystalline aspects and no adhesion on PNKA fiber; (c) $EuCl_3$ coating on PNKA fiber with non-uniform coverage and no adhesion on TZN fiber.
Source: by the author.

As previously reported in Chapter V and other works, aluminum-phosphate glasses exhibit good transparency in the UV-visible range but limited infrared (IR) transmission due to the high concentration of hydroxyl groups within their matrix (39). Consequently, a significant amount of hydroxyl (OH) groups is expected on the glass surfaces, which can interact with cations such as Eu^{3+} ions. In contrast, tellurite glasses are commonly used in mid-IR applications, showcasing relatively low OH concentrations alongside high network connectivity attributed to the formation of TeO_4 units. These intrinsic characteristics play an important role in understanding their interaction with carboxylate ligands.

Given the acidic conditions during the synthesis of Ln-CPs, it is plausible that a chemical attack on the glass surface may occur, leading to the removal of superficial hydroxyl groups (40). This process could expose cationic species, such as Zn^{2+}, embedded within the glass matrix, facilitating their interaction with carboxylate ligands. These cationic species may serve as coordination sites for the carboxylate groups of the ligands, as illustrated in Figure VII.3. This phenomenon may explain the formation of coatings on other tellurite glass matrices,

such as TZNF15 and TN, whereas the PNKA matrix may exhibit greater affinity for Eu^{3+} due to its higher content of hydroxyl groups.

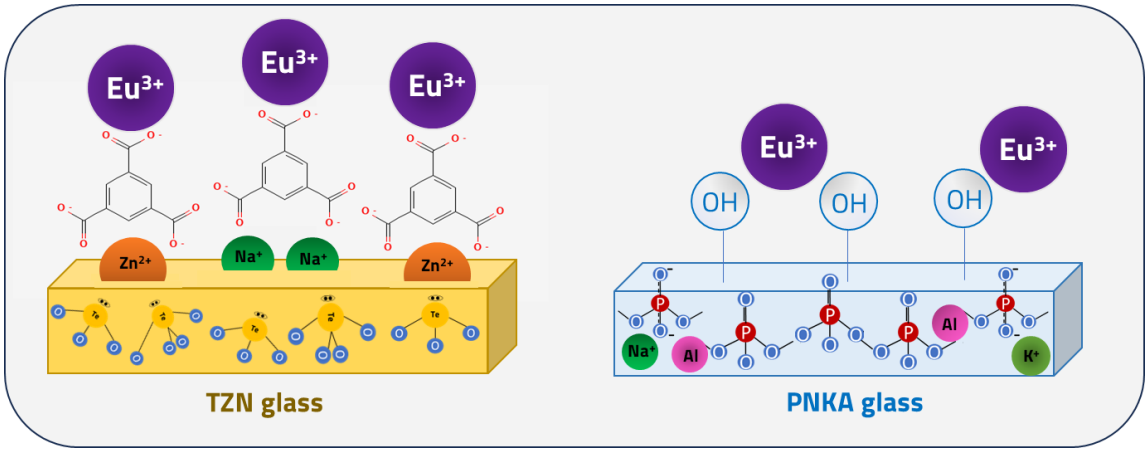

Figure VII.3 - Representative scheme for the interaction between the glass systems and the Ln-CPs components. Source: by the author.

The morphology of Ln-CPs coated on TZN glasses was analyzed using FEG-SEM in conjunction with EDX. The samples TZN@Eu(BTC)(PDC) and TZNF15@Eu(BTC)(PDC) were examined through surface imaging and elemental mapping via EDX. The images for both samples are shown in Figure VII.4. As depicted in Figure VII.4(a), the TZN@Eu(BTC)(PDC) sample exhibits the formation of typical metal-organic framework (MOF) rod-like crystals (41), indicative of a well-defined structure. Conversely, Figure VII.4(b) shows the TZNF15@[Eu(BTC)(PDC)] sample displaying an irregular structure on the glass substrate. These observations align with X-ray diffraction (XRD) findings, suggesting higher crystallinity in glasses without fluoride ions and highlighting a direct correlation between glass composition and the resultant film on the substrate. Moreover, EDX analysis maps reveal the elemental distribution for both samples, focusing on C, Eu, Te, and O. In summary, the TZN sample predominantly exhibits C, Eu, and O across its surface, indicating extensive coverage by the Ln-CP. In contrast, TZNF15@Eu(BTC)(PDC) displays regions with elevated tellurium content alongside areas rich in carbon and Eu^{3+}. Therefore, a non-homogeneous CP formation was observed in these samples, consistent with previous findings regarding the crystallinity of the synthesized layer. These combined microscopy and chemical analyses provide valuable insights into the surface characteristics and elemental composition of the Ln-CPs, underscoring the influence of fluoride ions and glass composition on film morphology and crystallinity.

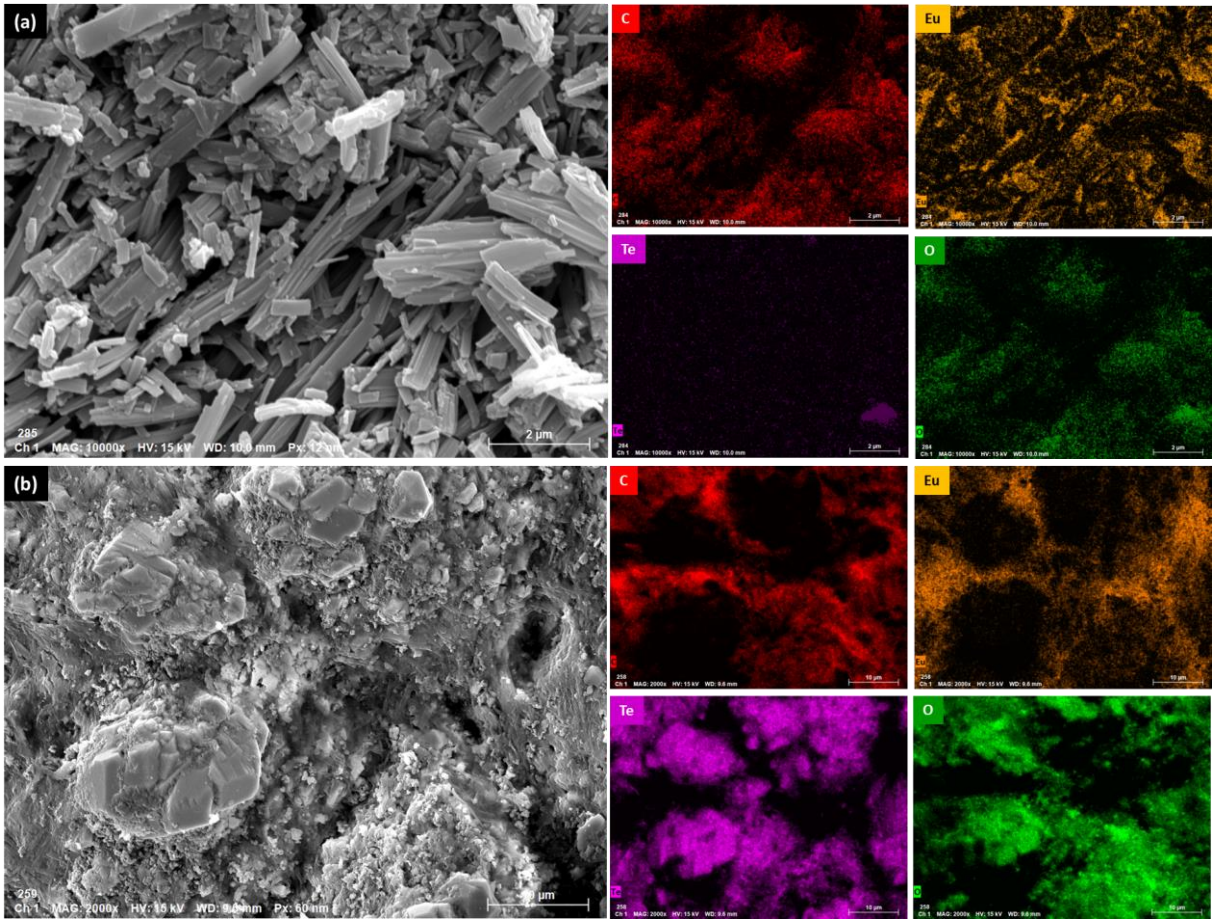

Figure VII.4 - FEG-SEM images and EDX analysis of (a) TZN@[Eu(BTC)(PDC)] and (b) TZNF15@[Eu(BTC)(PDC)] with the mapping of the elements C (red), Eu (yellow), Te (purple), and O (green). Source: by the author.

To elucidate the structures of the synthesized coatings, XRD analyses were performed on the deposited films on the glass as well as on the powders precipitated in the reactor, which were isolated by centrifugation and dried at 80 °C for 5 h. The XRD results shown in Figure VII.5 indicate that the lanthanide metal-organic framework (Ln-MOF) described by Da Silva et al. was not precisely reproduced in the synthesis conducted with the tellurite glass, as the main peaks only partially match the pattern reported in the literature (35). It is important to note that the previously reported Ln-MOF utilized only PDC species as ligands, while our procedure included the addition of the BTC ligand. The structural differences observed in the materials synthesized here may stem from the incorporation of the BTC ligand, as well as the interactions between the organic species and the glass. Additionally, considering the Ln-CP components, it is anticipated that some of the carboxylate groups from the BTC and PDC ligands coordinate with the glass surface, specifically with the metallic ions present in the matrix (42). However, the differing diffractograms for each glass matrix indicate that the glass composition impacts the formation of the CP structure. Notably, TZN@[Eu(BTC)(PDC)], which exhibits a greater

number of peaks matching the reference compound, also displays sharper peaks compared to TZNF15@[Eu(BTC)(PDC)], indicating a higher crystallinity of the obtained structure.

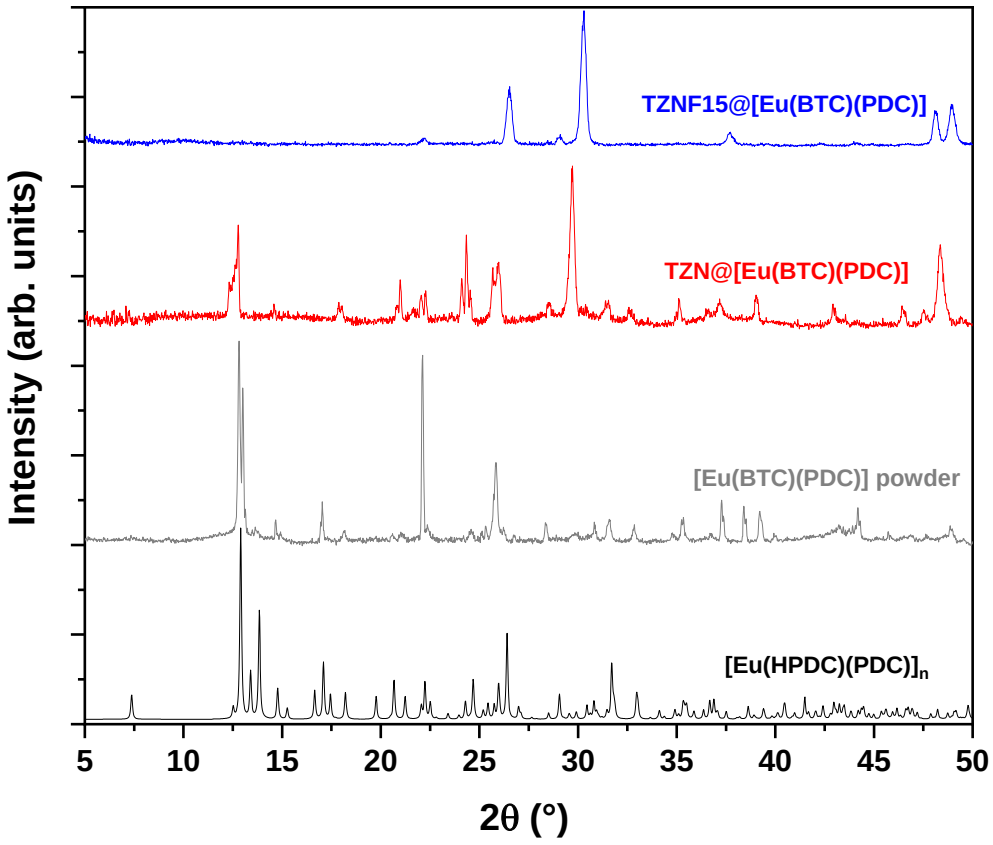

Figure VII.5 - Diffractograms of synthesized Ln-CPs with measurements of (a) precipitates obtained in the after the syntheses (in powder form) (b) coatings on the glass bulk. The results is compared with the MOF described in Da Silva et al. (35), labelled as $[Eu(HPDC)(PDC)]_n$.
Source: by the author.

To investigate the effect of synthesis time on the formation of Ln-CPs (43), the TZN@Eu(BTC)(PDC) sample was prepared following the same procedure but with the reaction time reduced to 10 min. The images obtained at the shorter reaction time reveal that the morphologies of the Ln-CPs are surprisingly different from those presented in Figure VII.4. In Figure VII.6, the sample exhibits structures with a symmetric coralloid pattern (44), and the EDX mapping confirms that these structures are composed of the CP components (C, O, and Eu). This coralloid shape is attributed to rapid nucleation of the structure and is characteristic of MOFs synthesized using BTC ligands (45, 46). Consequently, it is possible to conclude that a Ln-MOF containing primarily the BTC ligand is formed, and the coralloid structure develops quickly before transforming into rod-like crystals with an increase in synthesis time (47). Thus, synthesis time is an important parameter for the *in situ* growth of the Ln-MOFs and for the coverage of the glass surface, indicating that a more crystalline structure forms with a shorter reaction time. Another notable observation from Figure VII.6 is the presence of cubic structures

that seem to be fragments of glass detached from the bulk, reinforcing the theory of chemical attack due to the acidic pH of the reaction medium, which may also influence the adhesion of the MOFs to the substrate.

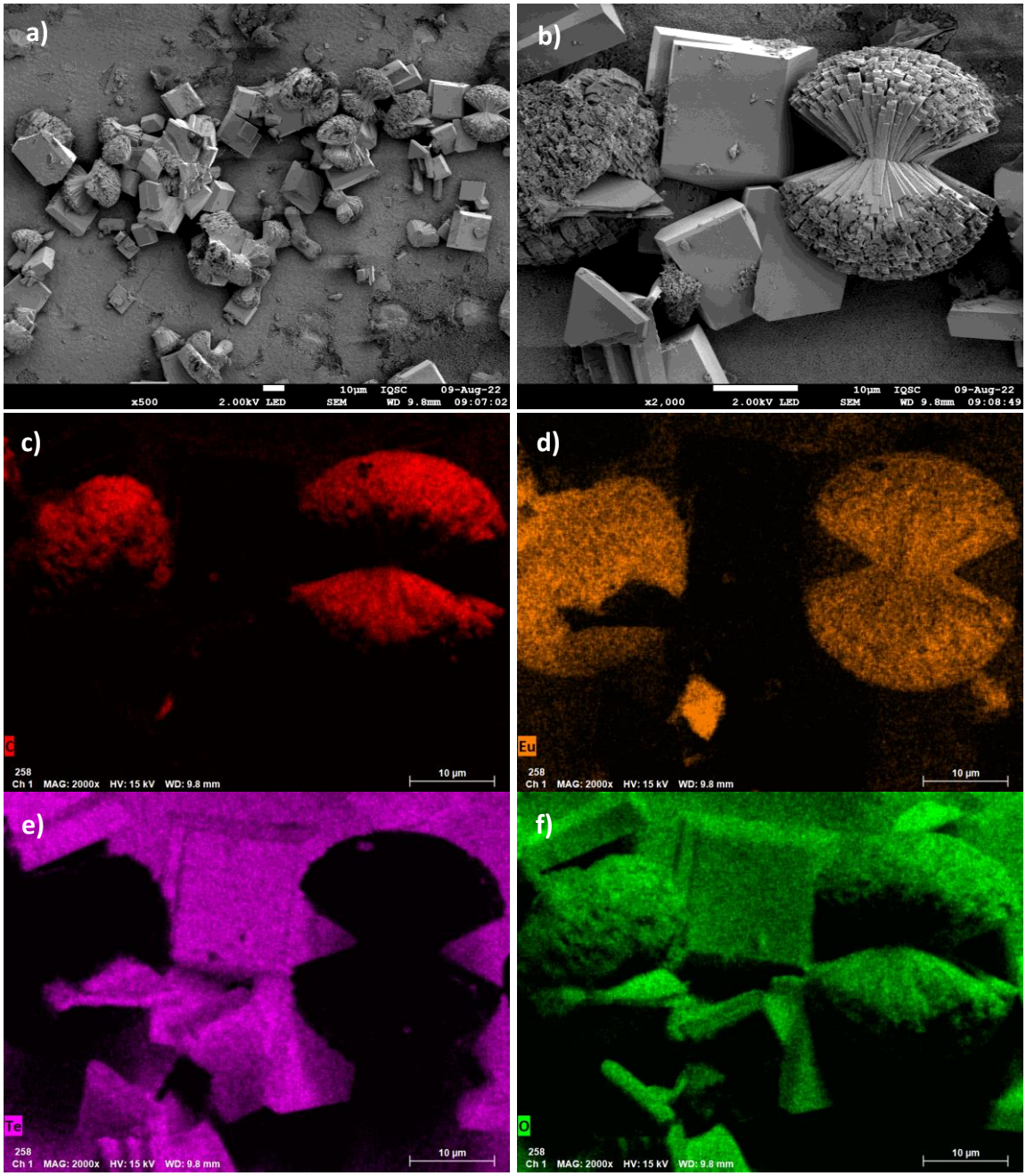

Figure VII.6 - SEM-FEG images of the surface of TZN@[Eu(BTC)(PDC)] – (a) and (b) with different magnifications; and EDX analysis with the mapping of the elements (c) C (red), (d) Eu (yellow), (e) Te (purple), and (f) O (green).
Source: by the author.

Other composites were morphologically characterized using field-emission gun scanning electron microscopy (FEG-SEM). Figure VII.7 displays the surface images of TZN@EuBTC, TN@EuBTC, and TZN@EuB4C samples. A comparison of Figures 7(a) and 7(b) reveals

similar surface morphologies between the TZN@EuBTC and TN@EuBTC samples. However, the TZN@EuBTC sample exhibits a greater amount of deposited material on its surface, suggesting stronger interactions between the BTC ligands and the TZN glass matrix, likely facilitated by the presence of Zn^{2+} ions. In contrast, the TZN matrix shows weaker ligand interactions, resulting in less material deposition. Figures 7(c) and 7(d) present the surface morphology of the TZN@EuB4C sample at different magnifications, revealing the presence of spherulitic structures. These observations indicate that the B4C ligand promotes a higher degree of crystallinity compared to the BTC ligand.

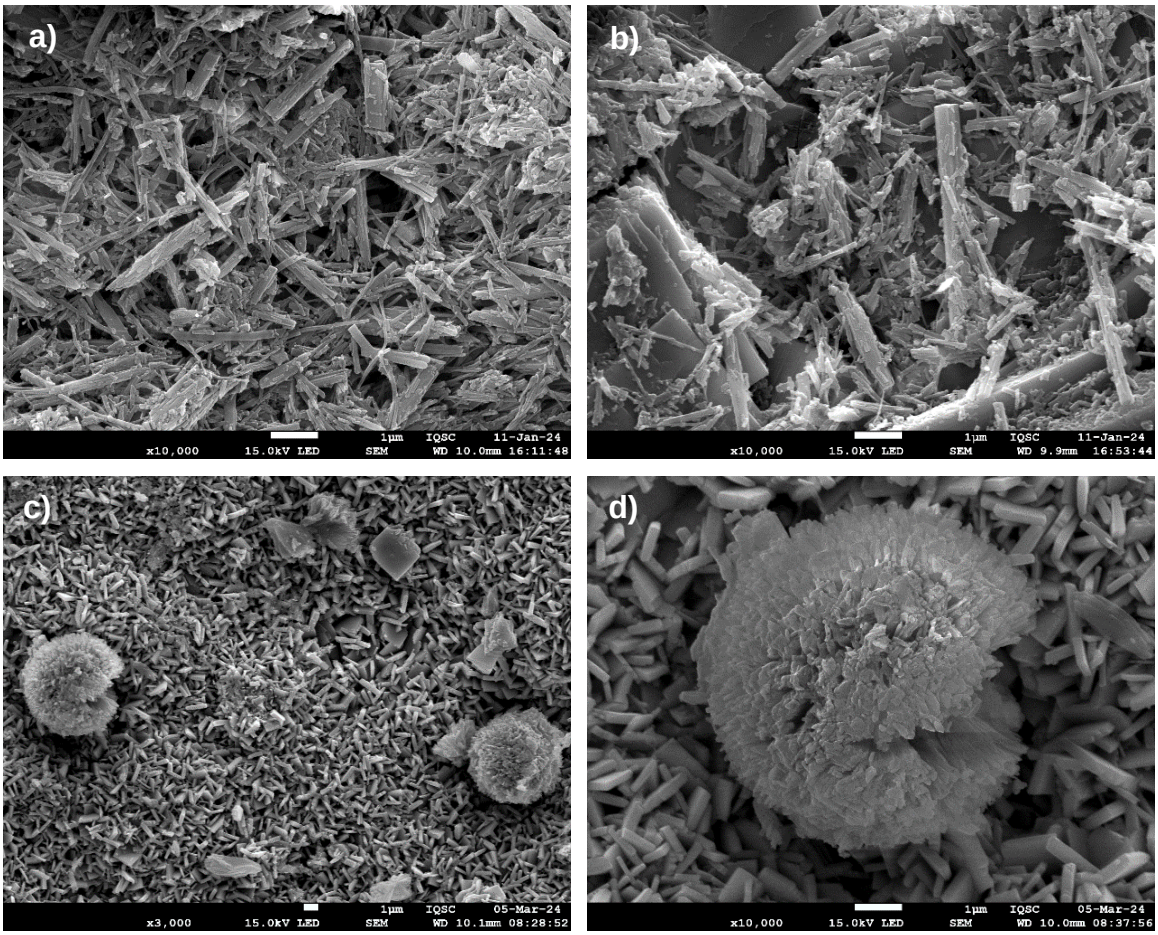

Figure VII.7 - SEM-FEG images of the surfaces of (a) TZN@EuBTC at 10,000x magnification; (b) TN@EuBTC at 10,000x magnification; (c) TZN@EuB4C at 3,000x magnification; and (d) TZN@EuB4C at 10,000x magnification.
Source: by the author.

The samples TZN@EuBTC and TZN@EuB4C were also analyzed using XRD, as shown in Figure VII.8. The TZN@EuBTC sample displays only a few peaks at positions corresponding to those of TZN@[Eu(BTC)(PDC)]. However, the diffraction pattern indicates a lower degree of crystallinity, which may be attributed to partial disorder or the presence of amorphous regions within the material. In contrast, the TZN@EuB4C sample exhibits more

pronounced crystalline behavior, characterized by sharper and narrower diffraction peaks. It is noteworthy that the MOFs were synthesized through *in situ* growth on glass substrates, meaning the XRD patterns were obtained from thin film coatings rather than conventional powder samples. This difference in sample preparation can influence the diffraction results, as thin films may exhibit preferred orientation or surface-related effects that are less prominent in powder-based analyses (48). The *in situ* growth approach potentially allows for more controlled crystal formation on the surface, but it also introduces complexities, such as substrate interactions and the influence of film thickness on the observed diffraction patterns (49,50).

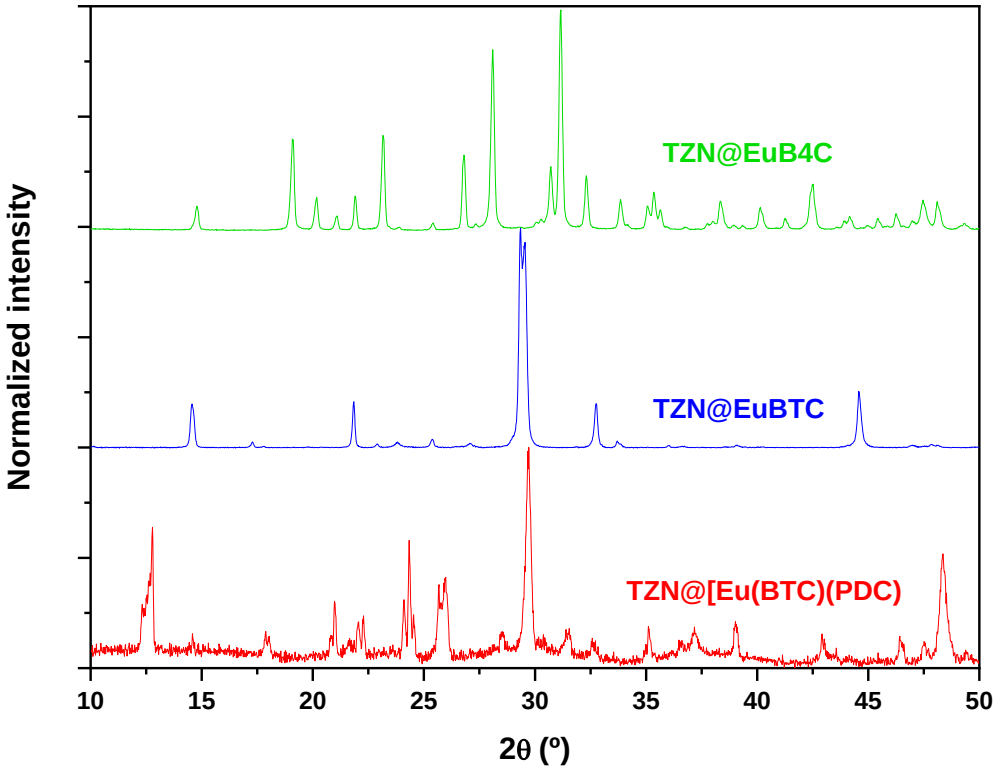

Figure VII.8 - XRD patterns of TZN@EuBTC and TZN@EuB4C samples compared to TZN@[Eu(BTC)(PDC)] pattern.
Source: by the author.

3.2. PL characterization

The photoluminescent behavior of the glass@Ln-CPs samples was investigated. First, the solid-state photoluminescence spectra of TZNF15@[Eu(BTC)(PDC)] are shown in Figure VII.9. The excitation spectrum, monitored at 617 nm, reveals a broad band centered at 301 nm, attributed to intraligand (IL) transitions, along with relatively narrow bands in the 350–550 nm region, assigned to f–f transitions. The most intense transition in this region is the $^{7}F_{0} \rightarrow {}^{5}L_{6}$

transition, centered at 394 nm. The emission spectra of TZNF15@[Eu(BTC)(PDC)] were recorded under excitation at 301 nm (red line, ligand excitation) and 394 nm (blue line, Eu^{3+} excitation), as also shown in Figure VII.9. When excited at 301 nm, the composite exhibits a broad band with a maximum at 420 nm, attributed to IL transitions, along with three bands corresponding to Eu^{3+} transitions, centered at 598 nm ($^5D_0 \rightarrow {}^7F_1$), 617 nm ($^5D_0 \rightarrow {}^7F_2$) and 700 ($^5D_0 \rightarrow {}^7F_4$) nm. This indicates the occurrence of antenna effect by energy transfer from the ligand to the metallic center (51,52). This behavior is highly desirable for various applications involving Ln-MOFs, particularly for chemical sensing of different analytes (53). Furthermore, the PL spectra obtained with excitation at 394 nm show, in addition to the previously observed characteristic Eu^{3+} emissions, two additional f–f transitions at 580 nm ($^5D_0 \rightarrow {}^7F_0$) and 653 nm ($^5D_0 \rightarrow {}^7F_3$), although these are less intense. In both excitation scenarios, the most intense transition is the $^5D_0 \rightarrow {}^7F_2$ transition, which dominates due to the low-symmetry environment of the Eu^{3+} centers (54,55). The presence of the $^5D_0 \rightarrow {}^7F_0$ emission, a symmetry-forbidden transition, further suggests a non-centrosymmetric site around the Eu^{3+} (56). Additionally, the decay time of the emission at 617 nm (inset of Figure VII.9) was fitted to a double-exponential function, indicating the existence of different chemical environments around the Eu^{3+} centers in the sample.

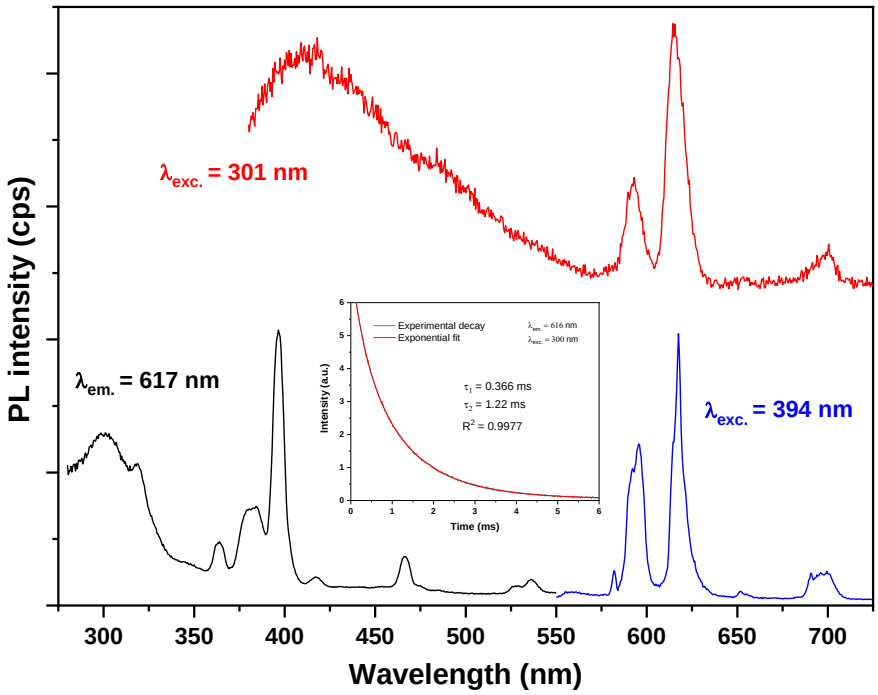

Figure VII.9 - Photoluminescent spectra of the TZNF15@[Eu(BTC)(PDC)]; the emission at 617 nm was monitored in the excitation spectra (black) and two emission spectra were recorded under excitation at 394 nm (blue) and 301 nm (red). *Inset:* experimental decay and exponential fit curves of the decay time for this sample. Source: by the author.

Figure VII.10 presents the PL spectra for the two different glass matrices coated with [Eu(BTC)(PDC)], revealing significant differences between the samples deposited on the TZN matrix and those containing ZnF_2. Specifically, when excited at 394 nm, the emissions between 585–600 nm ($^5D_0 \rightarrow {}^7F_1$, J =1) and 617-630 nm ($^5D_0 \rightarrow {}^7F_2$, J =2) display well-resolved peaks in the TZN@[Eu(BTC)(PDC)] sample, whereas an overlap of these regions is observed for TZNF15@[Eu(BTC)(PDC)]. This difference in emission behavior suggests that the TZN matrix provides a more asymmetric chemical environment around the Eu^{3+}, as indicated by the clear resolution of the $^7F_1$ and $^7F_2$ levels, which exhibit minimal degeneracy in their sublevels (2J+1) (57). In contrast, the broad emission profile seen in the TZNF15 matrix implies that the emitting centers are in coordination environments with higher symmetry than those in the TZN glass (54).

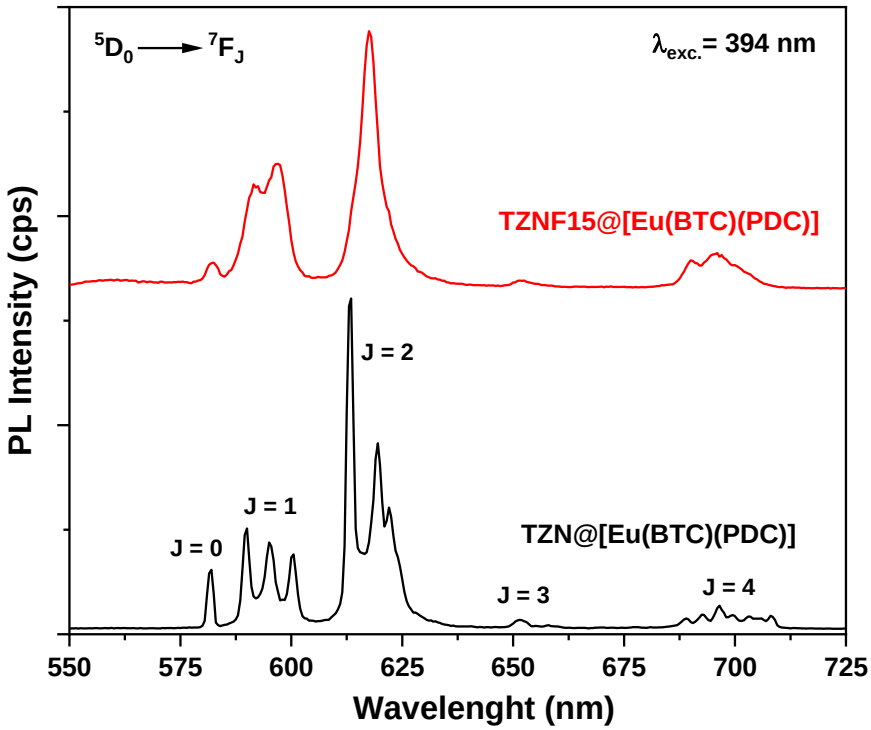

Figure VII.10 - Emission spectra of the Ln- CPs coating on TZN and TZNF15 glasses excited at 394 nm. Source: by the author.

The photoluminescent properties of the TZN@EuBTC and TZN@EuB4C samples were also investigated. Figure VII.11 presents the excitation spectra of both samples, with the emission wavelength monitored at 616 nm. In addition to the characteristic Eu^{3+} f-f transitions, a broad ligand excitation band is observed around 300 nm, with maxima at 295 nm for TZN@EuBTC and 310 nm for TZN@EuB4C. Despite this slight difference in excitation maxima, it is noteworthy that the ligand excitation band is significantly more intense for the

EuB4C sample, both in absolute terms and in comparison, to the excitation intensity of the Eu^{3+} $^7F_0 \rightarrow {}^5L_6$ transition centered at 395 nm. This suggests a stronger contribution of the ligand to the energy transfer process involved in the monitored emission, indicating a more effective antenna effect in the EuB4C composition.

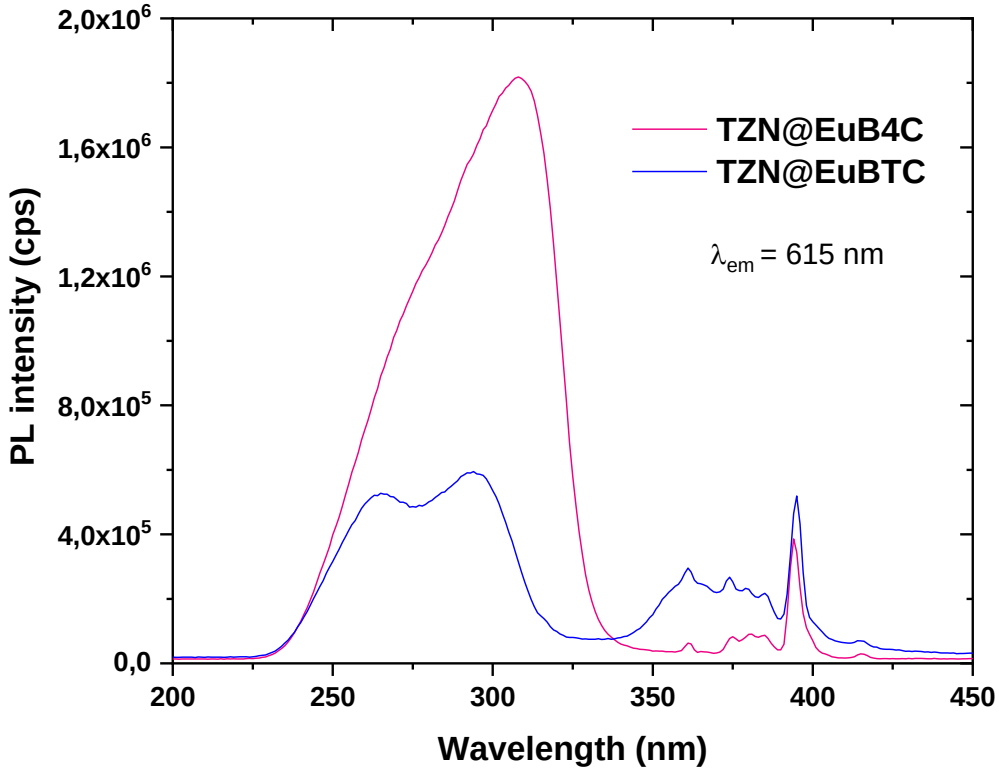

Figure VII.11 - Excitation spectra of TZN@EuBTC and TZN@EuB4C samples monitored at 616 nm. Source: by the author.

The effectiveness of the antenna effect is further demonstrated in the emission spectra shown in Figure VII.12. Both samples were excited at three different wavelengths: 310 nm (ligand excitation), 360 nm (an intermediate region between ligand and Eu^{3+} excitation), and 395 nm (direct Eu^{3+} excitation). For the TZN@EuBTC sample (Figure VII.12(a)), the emission intensity is similar when excited at both 310 nm and 395 nm. However, for the TZN@EuB4C sample (Figure VII.12(b)), a significant enhancement in emission is observed with excitation at 310 nm, showing an intensity approximately five times higher than that achieved with direct Eu^{3+} excitation at 395 nm. This considerable increase highlights the efficiency of the antenna effect in this composition, where the Eu^{3+} luminescence, typically originating from forbidden f-f transitions, is significantly amplified when the coordination polymer ligand is excited first, and this energy is subsequently transferred to the Eu^{3+}. Therefore, the TZN@EuB4C sample exhibits the greatest potential for chemical sensing applications due to its highly effective antenna effect. This substantial increase highlights the efficiency of the antenna effect in this

composition, where the Eu^{3+} luminescence, typically arising from forbidden f-f transitions, is significantly amplified when the coordination polymer ligand is excited first, and the energy is subsequently transferred to the Eu^{3+}. Consequently, the TZN@EuB4C sample exhibits the greatest potential for chemical sensing applications due to its highly effective antenna effect. To further understand the electronic transition mechanisms between the ligand and the lanthanide ion in the CP, lifetime measurements were performed. The insets of Figure VII.12(a) and VII.12(b) display the experimental decay curves and their exponential fits. The decay times for the TZN@EuBTC and TZN@EuB4C samples were calculated as 0.175 ms and 0.298 ms, respectively. These results reinforce the conclusion that the antenna effect is more efficient in the TZN@EuB4C sample, as longer decay times are typically associated with enhanced energy transfer processes, making this composition more suitable for sensing applications (58).

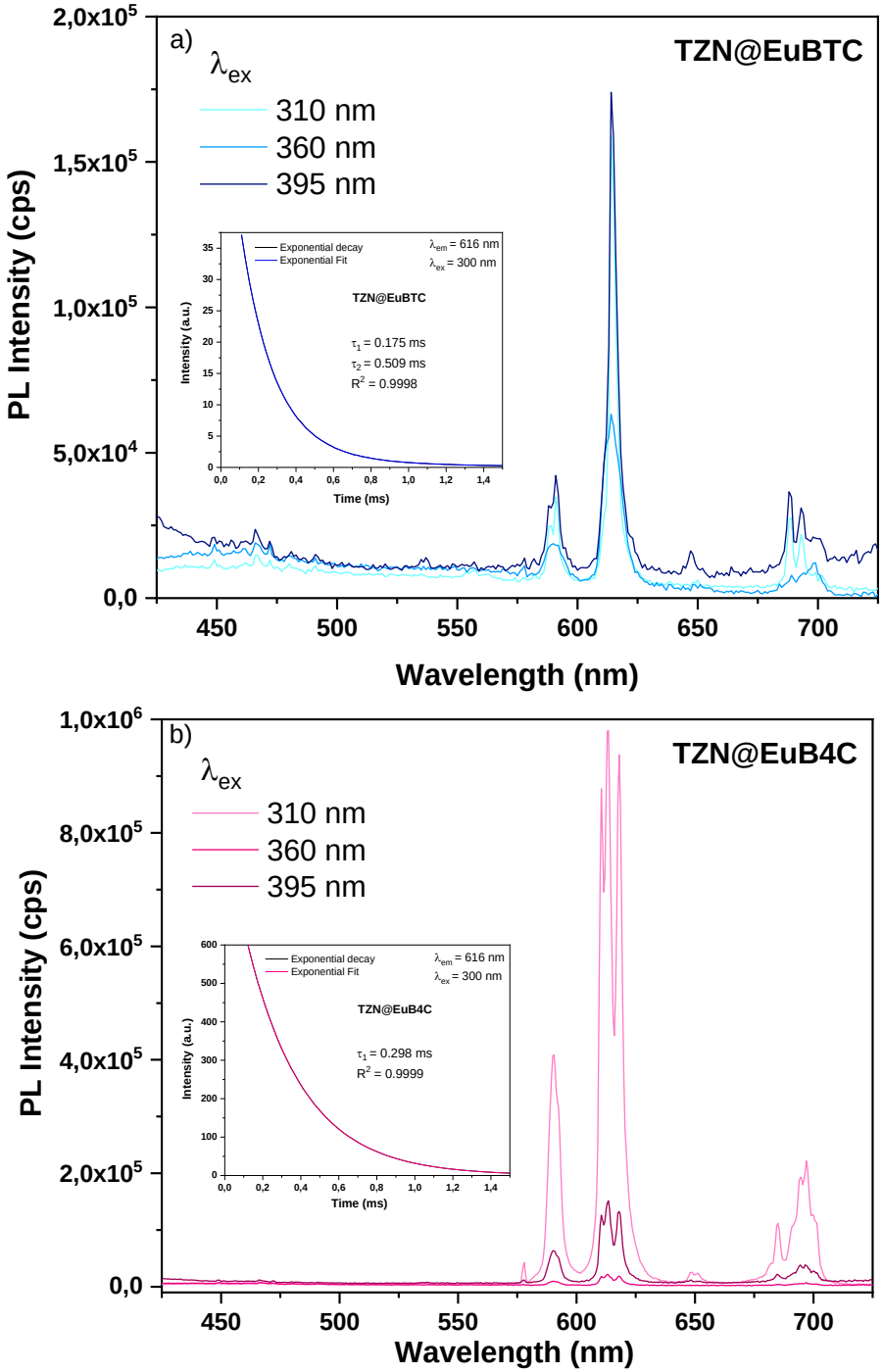

Figure VII.12 - (a) Emission spectra of TZN@EuBTC excited at 310 nm, 360 nm, and 395 nm; (b) emission spectra of TZN@EuB4C under the same excitation wavelengths. *Insets*: experimental decay curves and their corresponding exponential fits, with decay times of 0.175 ms for TZN@EuBTC and 0.298 ms for TZN@EuB4C. Source: by the author.

3.3. Luminescent sensing of small organic molecules

Sensing tests for various volatile organic compounds were performed using a Horiba fluorometer. A sealed quartz cuvette with a plastic lid was employed to minimize analyte

evaporation. The sample was positioned diagonally within the container to ensure optimal exposure and measurement accuracy. The TZN@EuBTC sample was exposed to vapors from different analytes, as illustrated in Figure VII.13(a). The figure shows that acetone and methanol vapors induced a noticeable change in the luminescence response. Upon reviewing the physicochemical properties of these compounds, it becomes clear that both acetone and methanol have the highest vapor pressures among the tested analytes and exhibit similar refractive indices (59). Therefore, the observed changes in the emission spectrum may result from alterations in the refractive index of the medium in the presence of these vapors, rather than a specific interaction between the composite and the analytes. Subsequently, the TZN@EuBTC sample was immersed in each of the organic solvents and excited at 300 nm, as shown in Figure VII.13(b). In this scenario, a complete suppression of Eu^{3+} luminescence was observed in acetone, which could be attributed to the intrinsic absorption properties of acetone in this spectral range (60).

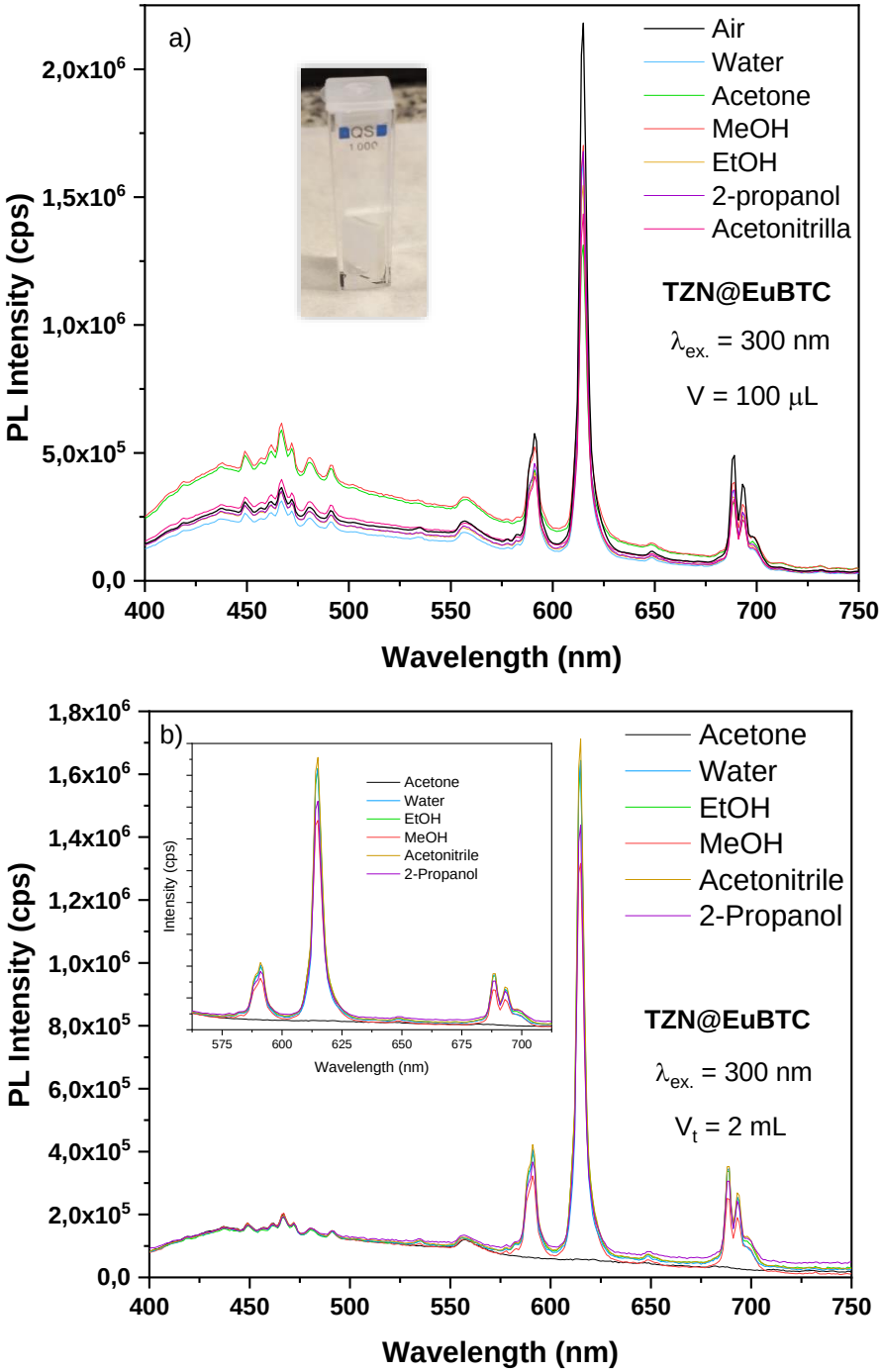

Figure VII.13 - (a) Luminescence response of the TZN@EuBTC sample when exposed to vapors of various analytes; *inset*: picture of the sealed quartz cuvette containing the TZN@EuBTC sample (b) Luminescence suppression of the TZN@EuBTC sample when immersed in organic solvents and excited at 300 nm, showing complete suppression in acetone.
Source: by the author.

To further examine the effect of acetone on the luminescence of the TZN@EuBTC sample, the sample was immersed in aqueous solutions containing varying low concentrations (volume %) of the analyte, and its photoluminescence spectrum was recorded under 300 nm excitation. Figure VII.14(a) demonstrates an exponential suppression of luminescence with increasing acetone concentration. In Figure VII.14(b), within a lower concentration range, a

pronounced linear decrease in luminescence intensity is observed for higher analyte concentrations. This suggests a direct correlation between luminescence intensity and analyte concentration. However, as mentioned earlier, this sensing mechanism likely relates to acetone absorption in the medium, which diminishes the effective intensity of the excitation beam reaching the coordination polymer. This phenomenon corresponds to the "inner filter effect," which is well described in the literature (61).

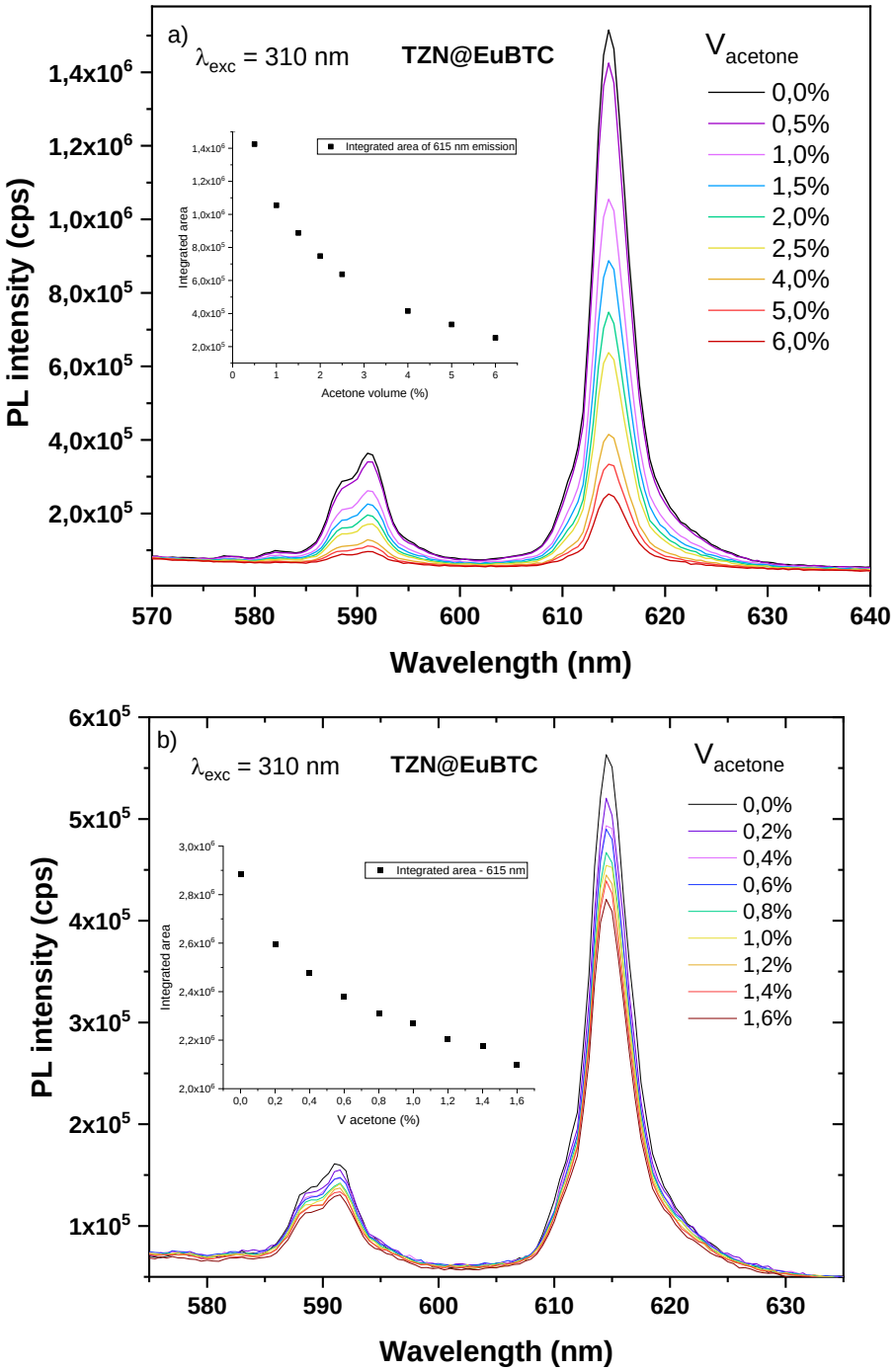

Figure VII.14 - (a) Luminescence in the TZN@EuBTC sample with increasing volumes of acetone (up to 6.0%) under 300 nm excitation. (b) Linear decrease in luminescence intensity at lower concentrations of acetone, from 0.2 to 1.6%.
Source: by the author.

Acetone absorption was analyzed across a concentration range of 0 to 1.75% by volume. As shown in Figure VII.15, the absorbance at 310 nm exhibits a linear increase at concentrations above 0.40% by volume, facilitating a stable comparison with the luminescent response of the composite. In this range, a quasi-linear quenching pattern in luminescence is observed between 0.6% and 1.6% acetone concentration. By correlating these results, it becomes evident that the inner filter effect significantly influences the changes in luminescence intensity. This suggests that the luminescent response of the sensor is closely tied to the intrinsic absorption properties of the analyte.

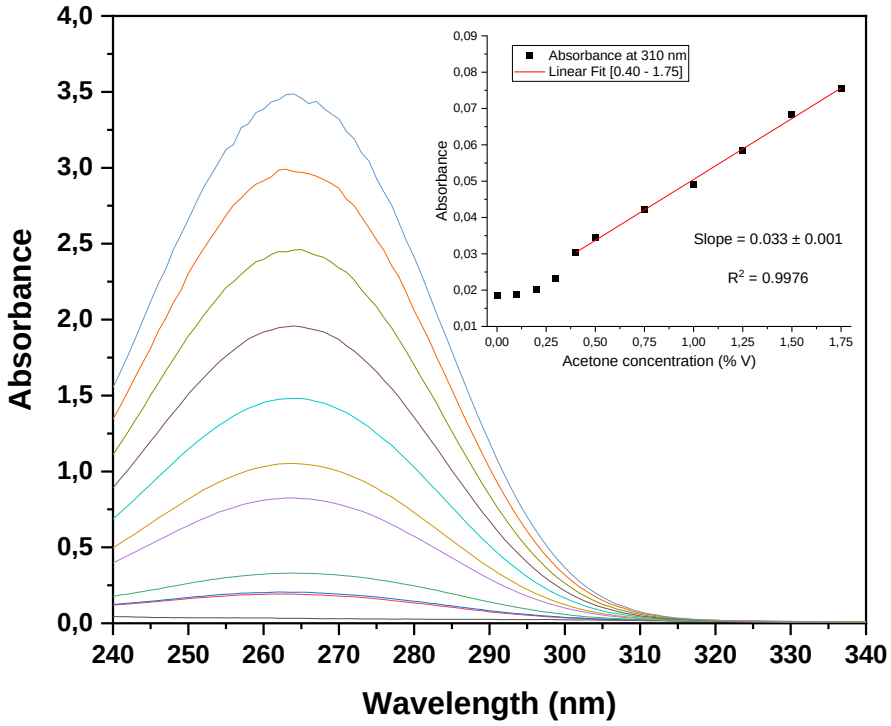

Figure VII.15 - Absorption spectra of acetone in aqueous solution in a concentration range between 0 and 1.75% by volume. Inset: absorbance values at 310 nm as function of acetone concentration and linear fit from 0.40% to 1.75%.
Source: by the author.

In contrast to the behavior observed for TZN@EuBTC, where acetone absorption led to an inner filter effect by reducing excitation light intensity, the TZN@EuB4C sample demonstrated a luminescence enhancement when exposed to low acetone concentrations (up to 1.0% by volume), as shown in Figure VII.16(a). This enhancement suggests that acetone is adsorbed within the CP pores, facilitating direct energy transfer to the Eu^{3+} and thereby increasing luminescence through a guest-induced phenomenon (62–64). At higher concentrations (Figure VII.16(b)), the Eu^{3+} emission intensity begins to decrease but remains higher than the initial spectra obtained with the sample immersed in water. This behavior indicates that both enhancement of luminescence — due to energy transfer from adsorbed

acetone molecules — and quenching, caused by the inner filter effect from acetone in solution, are occurring simultaneously at these higher acetone concentrations.

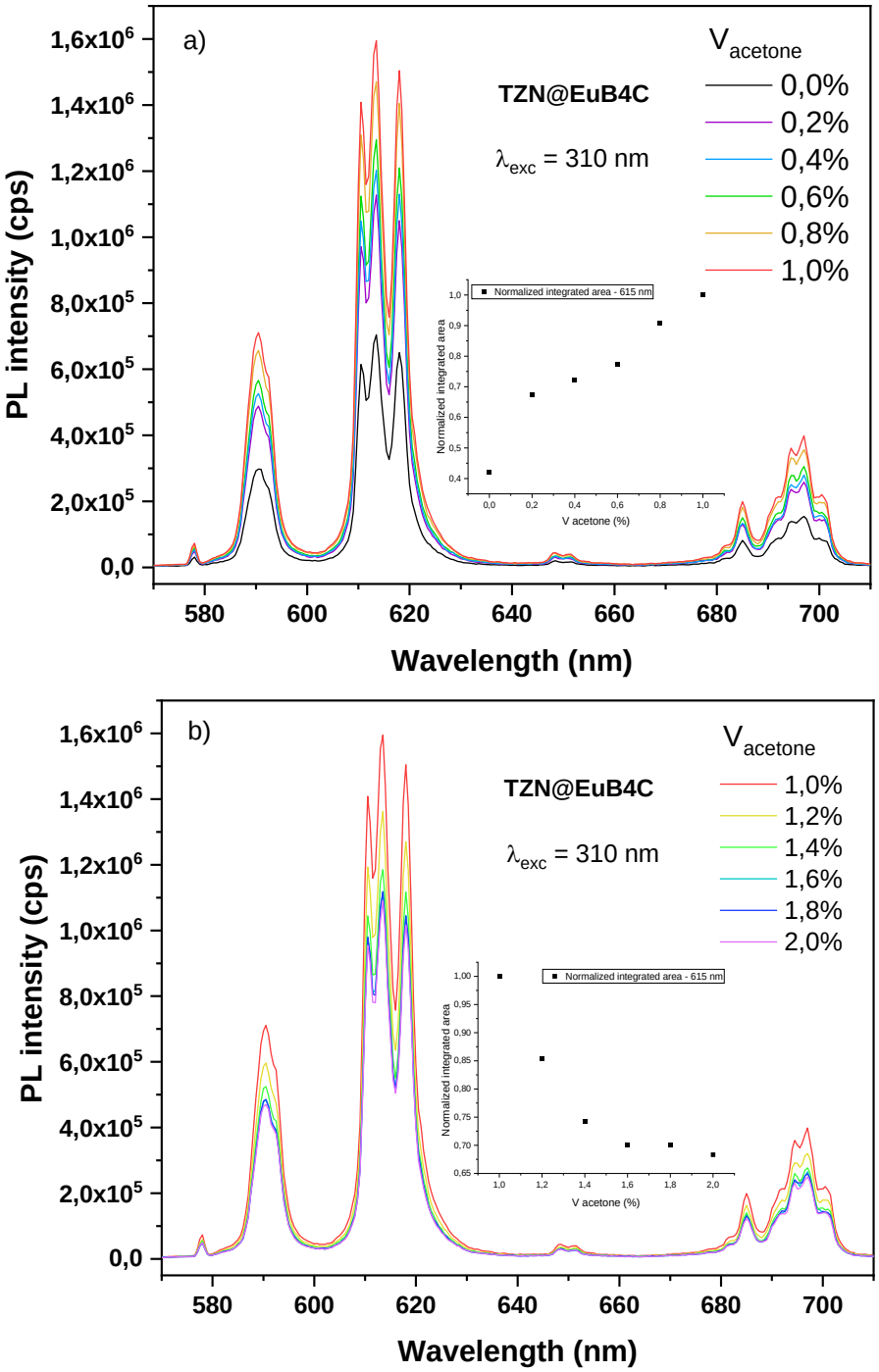

Figure VII.16 - (a) Enhanced luminescence response of TZN@EuB4C to low concentrations (up to 1.0% by volume) of acetone; and (b) decrease of Eu^{3+} emission intensity at higher concentrations, both excited at 310 nm. Source: by the author.

To elucidate the sensing mechanism observed for acetone, a proposed model is illustrated in Figure VII.17. As previously mentioned, when acetone molecules are adsorbed onto the CP layer, they can efficiently absorb the excitation light. Due to the proximity of the

S_1 state of the B4C ligand (see the energy diagram in Figure VII.17), the analyte enhances the excitation process of the CP through a turn-on effect (65). This suggests that the antenna effect is more efficient under these conditions, leading to an increase in Eu^{3+} luminescence. As the pores of the CP become saturated, excess acetone remains in solution, resulting in an increased absorption of excitation light — similar to the inner filter effect reported to TZN@EuBTC sample. Consequently, acetone sensing in the TZN@EuB4C sample shows a dynamic interplay between the turn-on and inner filter effects. Initially, this competition results in an enhancement of luminescence intensity as adsorption progresses. However, once analyte saturation is reached, further luminescence quenching occurs, driven by the absorption of the excitation light by free acetone molecules in the solution.

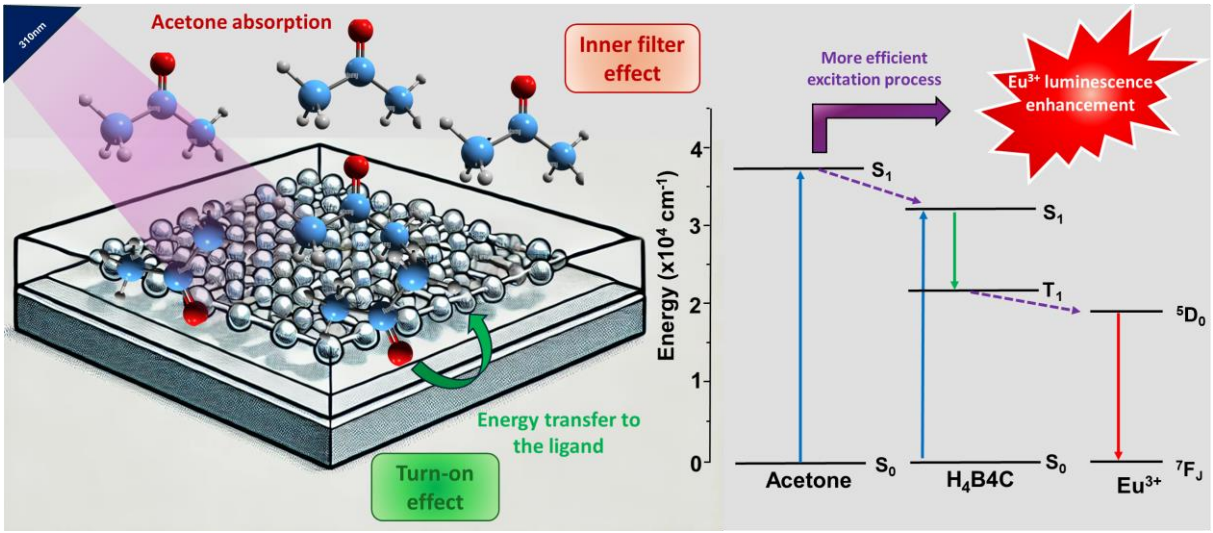

Figure VII.17 - Proposed sensing mechanism for acetone in the TZN@EuB4C sample. The scheme illustrates the interaction between acetone molecules both adsorbed on the CP layer and in solution, highlighting the competition between the turn-on and inner filter effects. The energy diagram shows the proximity of the S_1 states of the B4C ligand and acetone, facilitating efficient excitation and enhancing the antenna effect, which results in increased Eu^{3+} luminescence.
Source: by the author.

Following the procedure applied with acetone, trace amounts of 2-pentanone in water were also tested for detection, as shown in Figure VII.18. At low concentrations of 2-pentanone, an increase in luminescence was observed, with the emission intensity peaking at 0.4% by volume, followed by a decline at higher concentrations. This behavior mirrors that seen with acetone, suggesting similar underlying mechanisms. These results highlight the potential of this system for practical sensing applications of carbonyl compounds. The observed luminescence response mechanisms demonstrate high selectivity and sensitivity, particularly for detecting ketones at low concentrations, which is crucial since certain ketones can serve as biomarkers for diseases such as cancer (66–69).

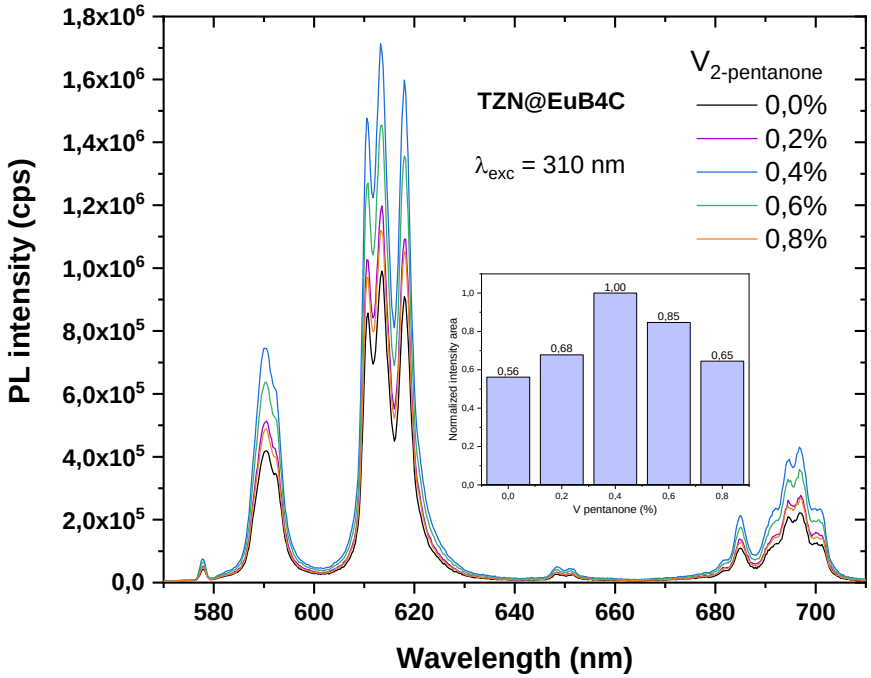

Figure VII.18 - Luminescent response of TZN@EuB4C to low concentrations of 2-pentanone excited at 310 nm. Source: by the author.

In addition, acetylacetone, a diketone, was analyzed for its luminescence response, as shown in Figure VII.19. A strong quenching effect was observed at very low concentrations, specifically below 0.15% by volume. Repeated tests confirmed that this quenching was irreversible, likely due to the coordination of acetylacetone with Eu^{3+}, leading to a modification of the CP structure. This irreversible structural alteration compromises the material's suitability for sensing diketones, as the changes prevent a reliable, reversible luminescent response.

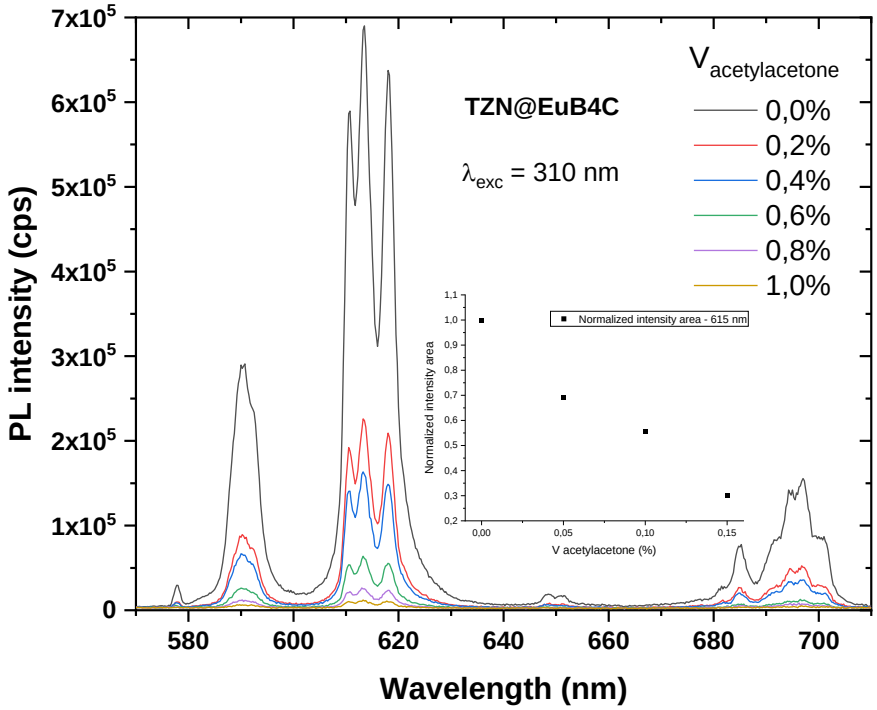

Figure VII.19 - Luminescent response of TZN@EuB4C sample to low concentrations of acetylacetone excited at 310 nm.
Source: by the author.

3.4. Luminescent sensing using coated optical fibers

Figure VII.20 shows images of TZN optical fibers coated with [Eu(B4C)]. In Figure VII.20(a), the optical microscopy image reveals a visually homogeneous coating on the optical fiber. Additionally, Figure VII.20(b), which shows the fiber's cross-section, confirms the presence of a uniform layer surrounding the fiber. Finally, the coating morphology was analyzed by SEM, as seen in Figure VII.20(c), where Ln-CP coatings are clearly visible on the fiber's surface. The coating thicknesses were measured using optical microscopy with a 100x magnification objective lens. Figure VII.21 displays images of TZN@EuB4C) fibers coated with different synthesis times, ranging from 5 to 60 min. As expected, the coating thickness increases with longer synthesis times; however, all samples exhibit thicknesses of less than 10 µm, varying from 2.7 to 9.6 µm. In comparison to the coatings on glass, the fiber coatings are thinner, which may be advantageous for applications as optical fiber sensors, as this thinner coating facilitates the efficient excitation of the Ln-CP by the guided light.

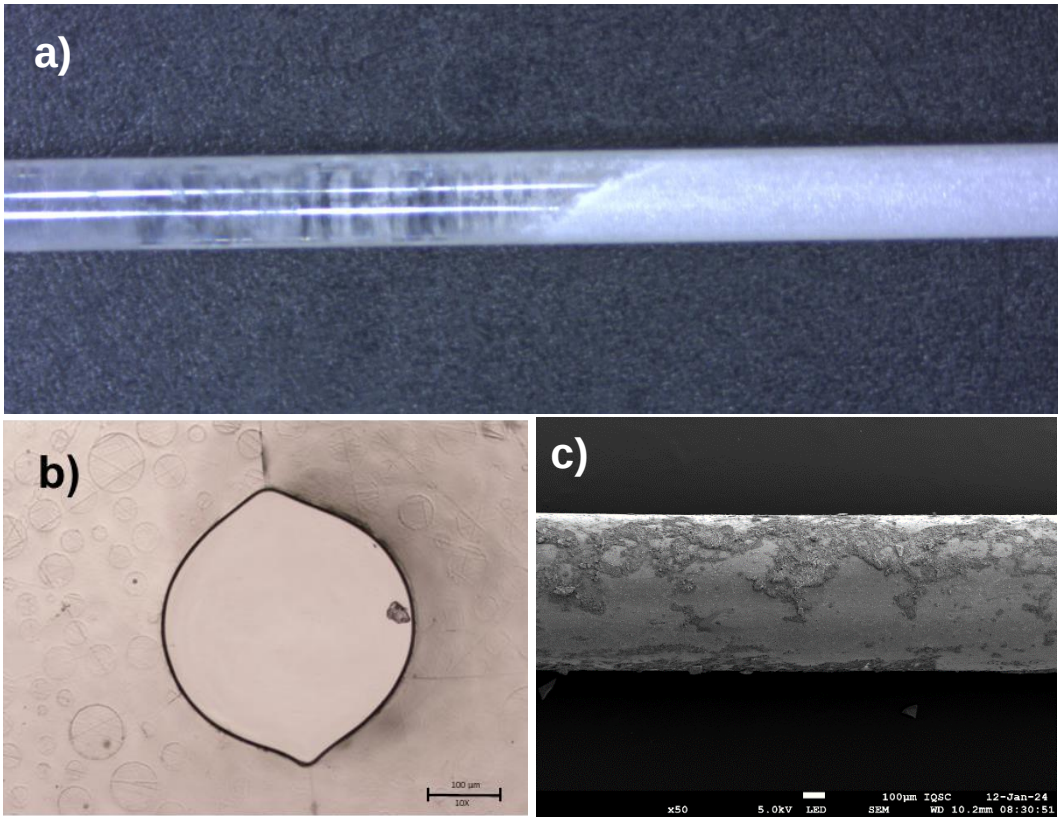

Figure VII.20 - (a) optical microscopy image of TZN fibers coated with [Eu(B4C)]; (b) TZN@EuB4C cross-section visualized with 10X magnification; (c) SEM image of the coated fiber's end with 81X magnification.
Source: by the author.

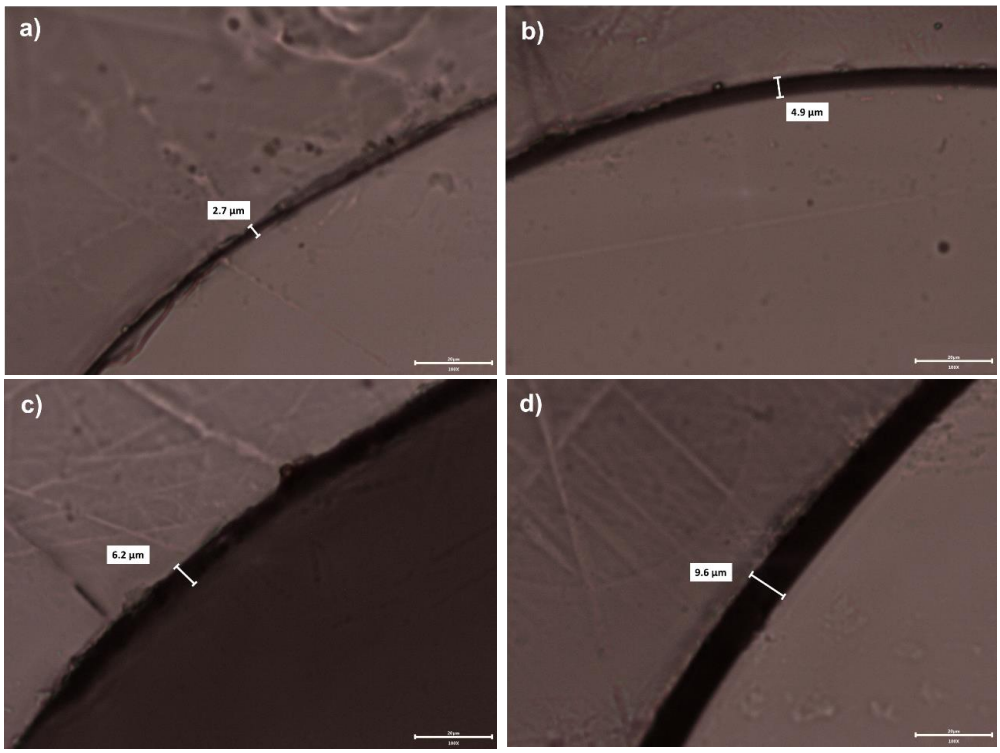

Figure VII.21 - Optical microscopy images of TZN@EuB4C fibers cross-section synthesized with different durations: (a) 5 min; (b) 10 min; (c) 20 min; and (d) 60 min.
Source: by the author.

Figure VII.22(a) shows the attenuation curves for single-index TZN optical fibers with a diameter of 170 µm, melted in different types of crucibles. The curves reveal relatively low optical loss in the 550–700 nm range, enabling their use for guiding Eu^{3+} emission. The coating's luminescence was measured in a 15 cm long optical fiber with varying diameters to demonstrate the luminescence signal, as illustrated in Figure VII.22(b). The coating was illuminated using a UV lamp at 254 nm, and a portable spectrometer was coupled to the opposite end of the fiber with a commercial ZrF_4 fiber to collect the signal. The results revealed the characteristic emissions of Eu^{3+}, with the most prominent being the $^5D_0 \rightarrow {}^7F_2$ transition with a maximum at 612 nm and an improvement of the signal intensity for fibers with larger diameters (from 270 µm to 1 mm).

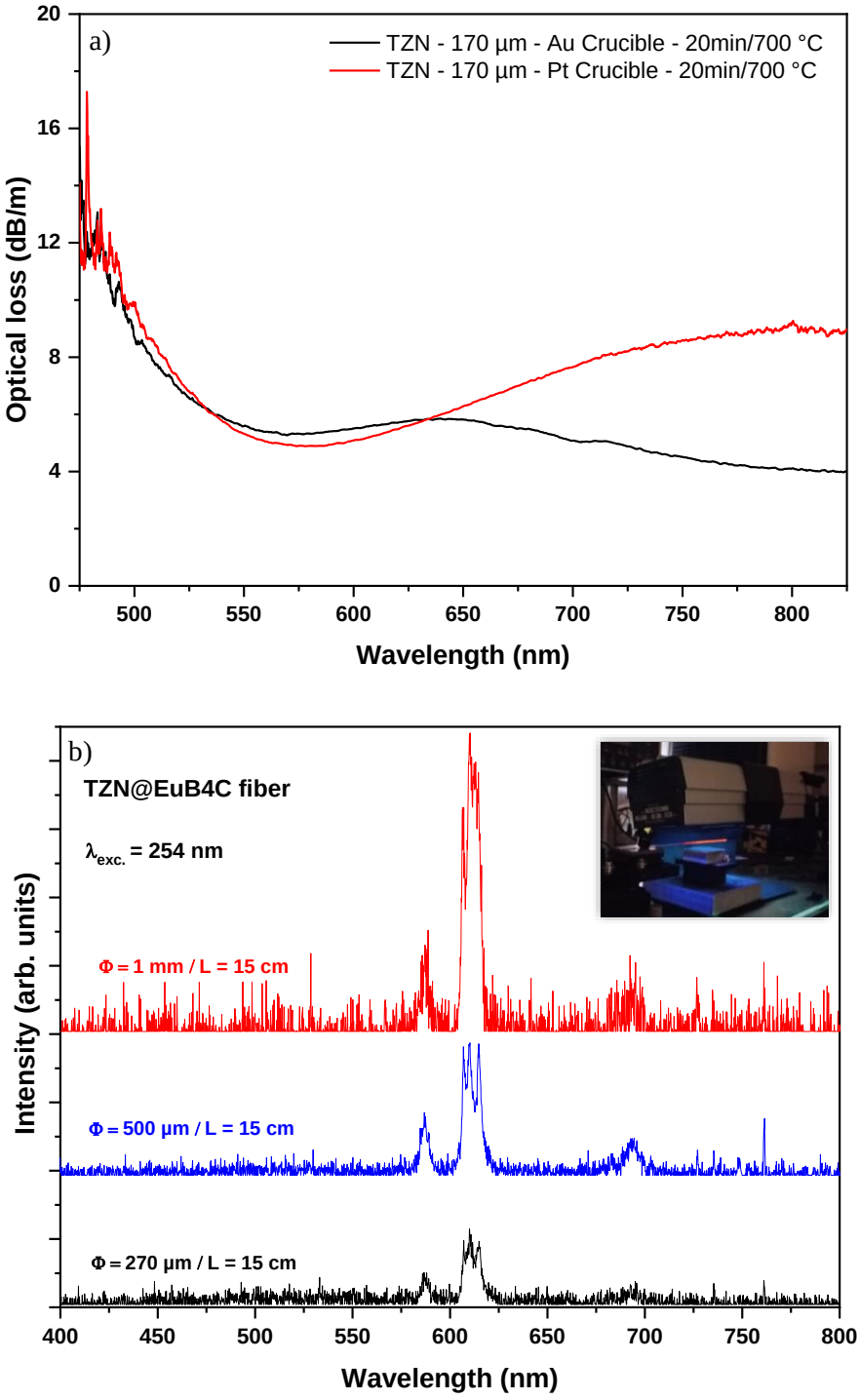

Figure VII.22 - (a) Attenuation curves of TZN fibers prepared in Au and Pt crucibles; (b) luminescent spectra of TZN@EuB4C optical fibers under excitation at 254 nm. *Inset:* coated fiber illuminated by UV lamp.
Source: by the author.

To perform sensing measurements using 1 mm optical fibers coated with Ln-CPs, we established an experimental setup that enables the immersion of the fiber's tip into the analyte solution while connecting it to a spectrometer for luminescent signal collection. Two different configurations were employed based on the type of fiber used, as illustrated in Figure VII.23. Figures VII.23(a) and VII.23(b) depict the setup for tests utilizing commercial silica fibers with

a 1 mm diameter, which can be bent into a small curvature. In contrast, Figure VII.23(c) shows the configuration used for 1 mm TZN fibers, which are not bendable. In this case, the spectrometer was positioned vertically to collect the signal from the tip immersed in the cuvette, with the fiber directly coupled to the spectrometer entrance.

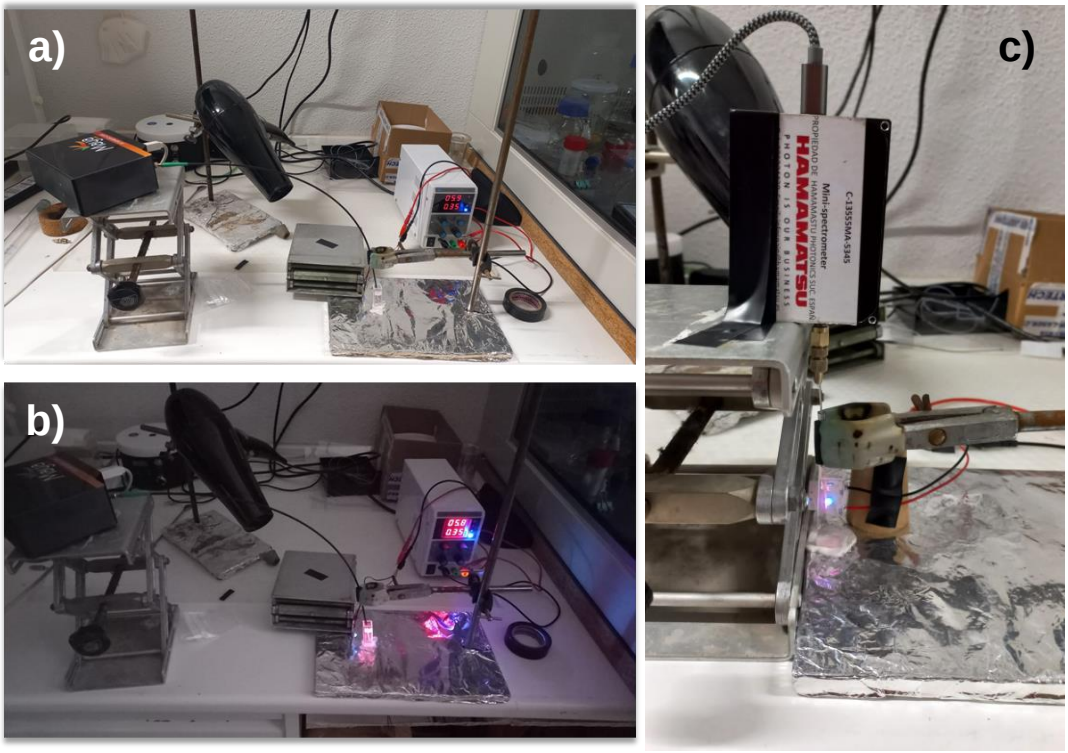

Figure VII.23 - Experimental setups for sensing measurements using optical fibers coated with Ln-CPs: (a) and (b) show the setup for commercial silica fibers (1 mm diameter); (c) setup for TZN fibers, with 1 mm diameter as well.
Source: by the author.

The initial test using optical fibers involved commercial silica fibers coated with [EuB4C]. It is noteworthy that the coating on the silica fiber surface appeared thinner and exhibited weaker adhesion compared to the TZN fibers. Nevertheless, it was possible to observe and collect the luminescent signal from the fiber's tip. This sample was subsequently tested for acetone detection, with the luminescent response to varying concentrations shown in Figure VII.24. The luminescence intensity decreased as the acetone concentration in the solution increased, displaying behavior that diverges from that observed in the coated bulk samples. This discrepancy may be attributed to the chemical characteristics of the silica fiber, particularly its high content of OH groups on surface (70). These OH groups tend to repel the carboxylate ligands, thereby reducing their adhesion to the surface. As a result, Eu^{3+} may interact directly with the OH groups rather than with the organic ligands, a phenomenon noted in previous studies. Consequently, the observed luminescence quenching is primarily attributed to the inner filter effect caused by acetone absorption.

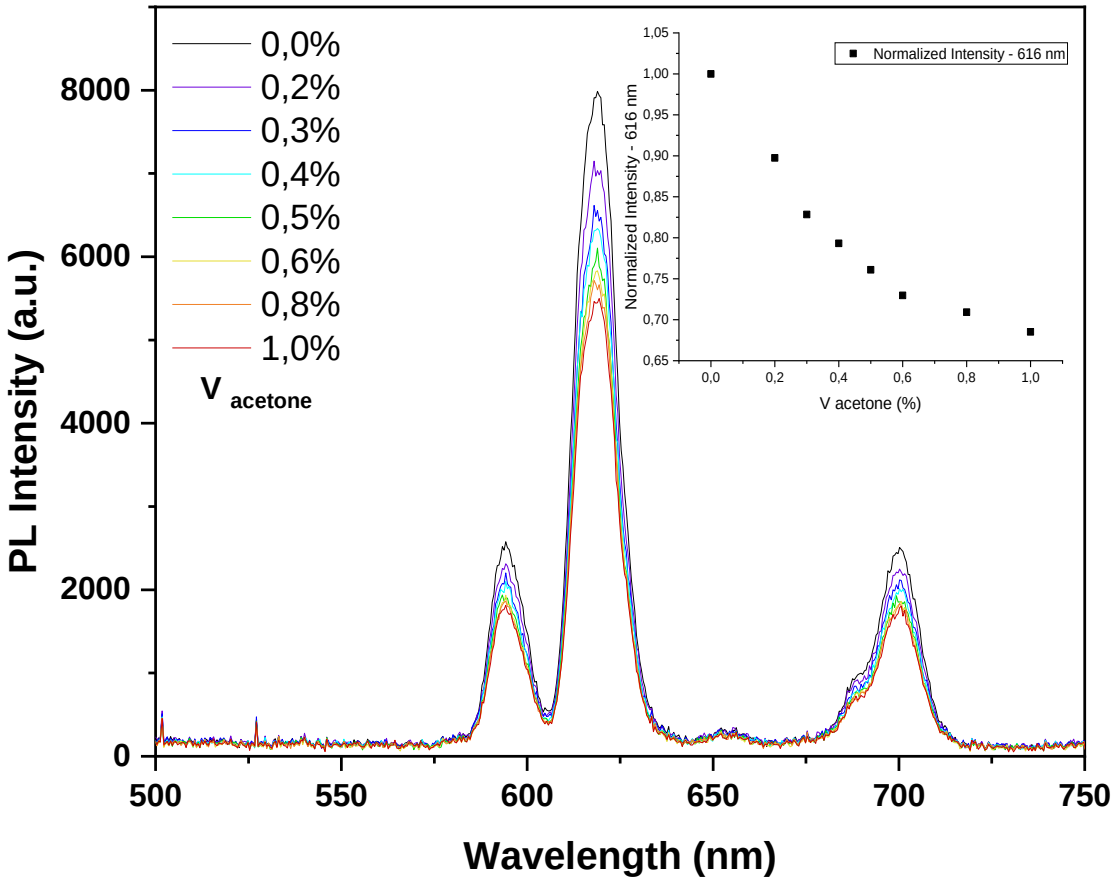

Figure VII.24 - Luminescent response of commercial silica fibers coated with [EuB4C] to varying concentrations of acetone up to 1,0% in volume.
Source: by the author.

Subsequently, the TZN@EuB4C fiber sample was immersed in a cuvette filled with water and connected to a vertically positioned spectrometer. Small increments of acetone were added to the cuvette, starting at 0.05% for the initial measurements. Figures VII.25(a)-(c) illustrate the luminescence intensity response as the acetone concentration increases, revealing a maximum emission at a concentration of 1.0% by volume. At higher concentrations, a decrease in emission intensity is observed, which can be attributed to the saturation of analyte adsorption and its increased presence in solution, leading to greater absorption of the excitation light. Finally, Figure VII.25(d) presents the linear dependence of emission intensity at 616 nm with acetone concentration within the range of 0.05% to 0.30% by volume, showing a slope of 0.25 ± 0.01. This result demonstrates the prototype material's effective response for sensing low concentrations of acetone.

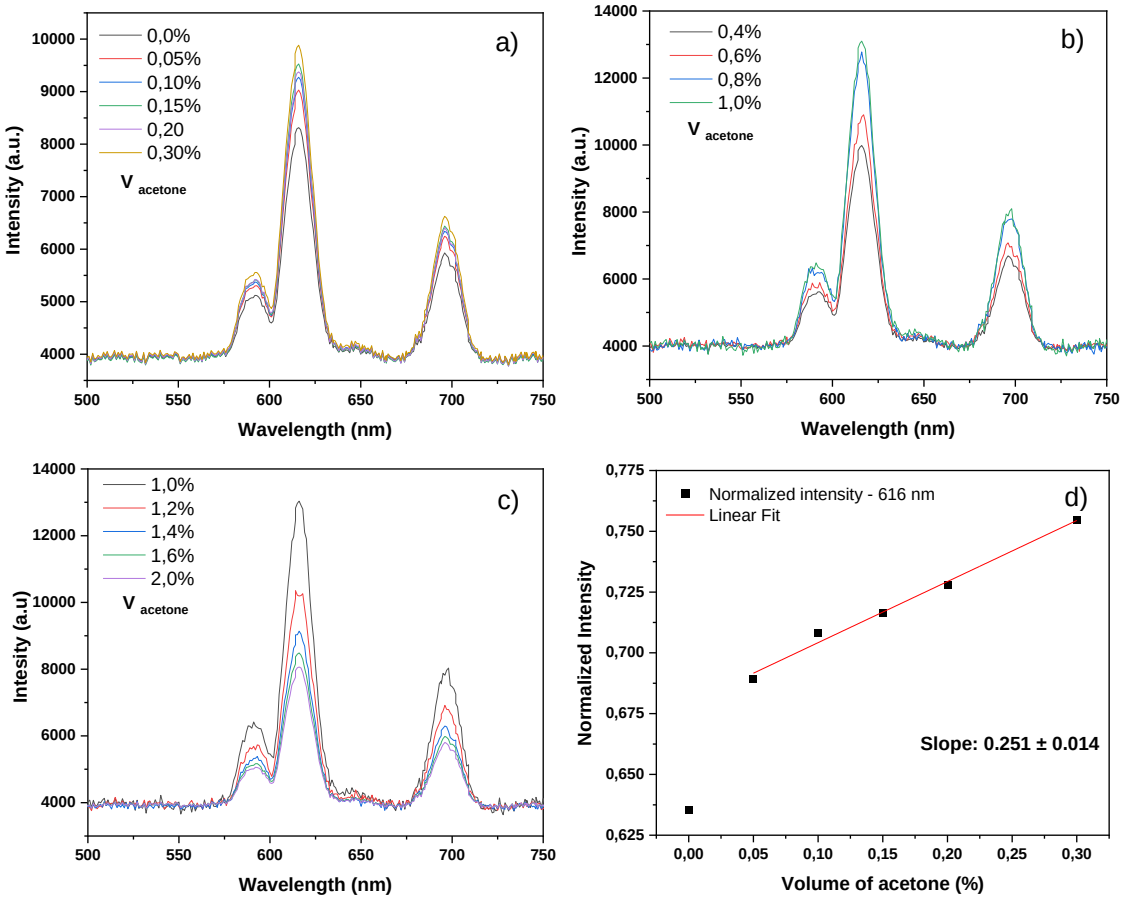

Figure VII.25 - Luminescence intensity response of the TZN@EuB4C fiber with varying acetone concentrations, in different ranges: (a) from 0.00% to 0.30%; (b) from 0.40% to 1.0%; and (c) from 1.0 to 2.0% by volume; (d) linear dependence between emission intensity at 616 nm and acetone concentration in the range of 0.05 to 0.30% by volume.
Source: by the author.

The same sample was also tested for the detection of 2-pentanone, following the previously described procedure. Figure VII.26(a) shows an enhancement in Eu^{3+} emission intensity, consistent with the behavior observed in earlier tests. In this case, the maximum intensity was recorded at 0.70%, which is slightly higher than the values measured for bulk samples. Despite this difference and the noted non-linearity in the response, a clear pattern of increasing emission intensity with the gradual addition of the analyte up to a certain concentration was evident. At concentrations above 0.80% (Figure VII.26(b)), luminescence quenching was observed, again linked to the increased presence of free analyte in solution and its intrinsic absorption in the UV region. Notably, a flat region is observed between 0.90% and 1.40%, which was not present in other tests. A plausible explanation for this anomaly could involve a competition between the enhancement and quenching effects of luminescence related to analyte adsorption and its energy transfer to the emitting center. Despite this non-linearity, it can be confirmed that the material developed during the PhD project demonstrates sensitivity

and an optical response to the presence of carbonyl compounds, particularly the ketones tested (propanone and 2-pentanone).

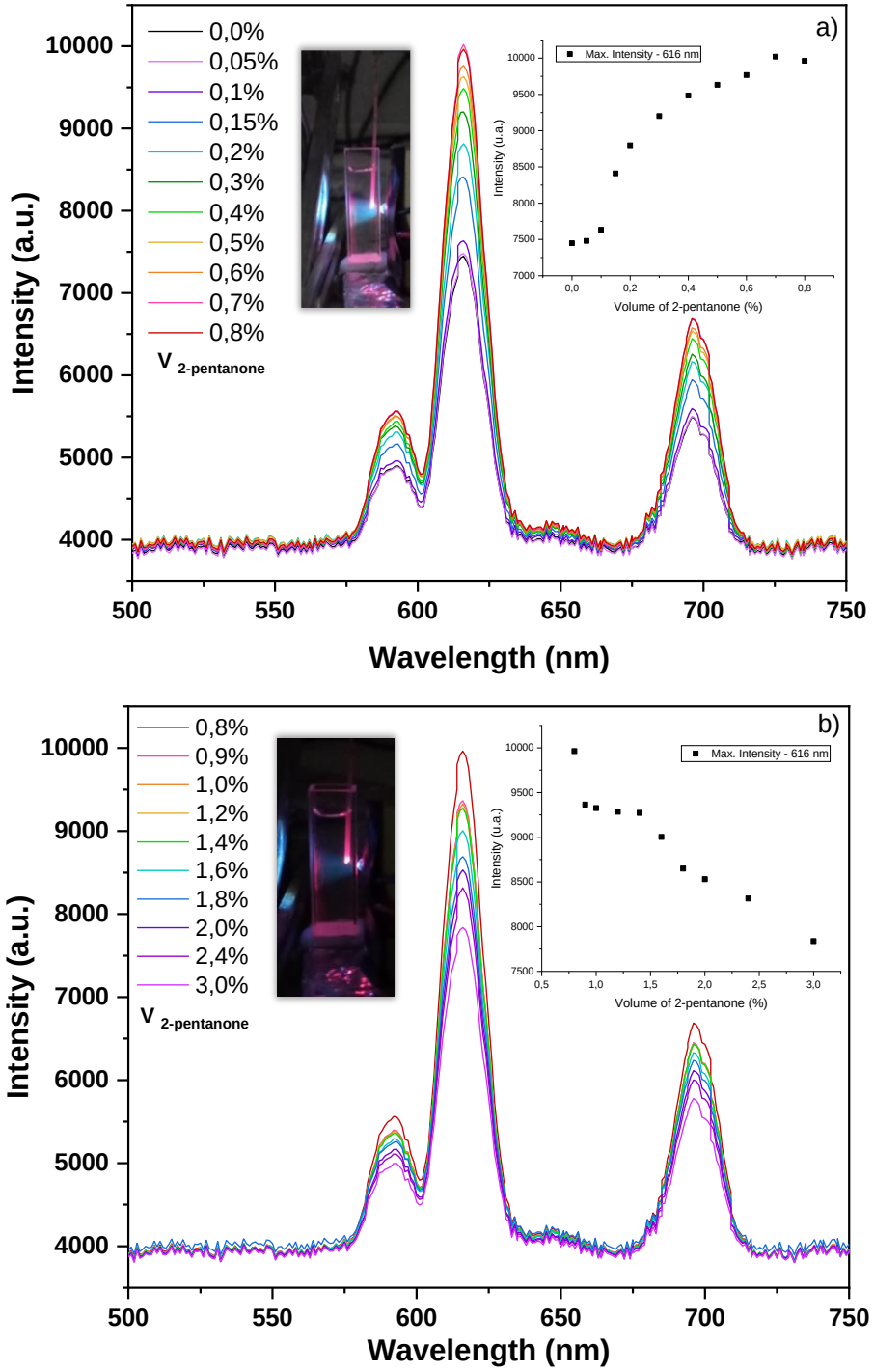

Figure VII.26 - Luminescence response of the TZN@EuB4C fiber to 2-pentanone: (a) enhancement of emission intensity with varying concentrations of 2-pentanone, with the maximum intensity at 0.70%; (b) quenching of luminescence at concentrations above 0.80%.
Source: by the author.

4. Conclusions

In conclusion, this final chapter of the thesis presents a rapid synthesis process for new and stable glass@Ln-CPs and optical-fibers@Ln-CPs composites. Although the crystalline forms obtained do not exactly match those described in the literature, luminescent Ln-CPs coatings combining Eu^{3+} and carboxylate ligands were successfully formed and demonstrated good adhesion to the tellurite glass substrates. Moreover, the coated optical fibers represent a promising material due to their ability to guide optical signals over long distances, enabling the development of remote sensors for various analytes. The findings underscore the significant potential of these materials for chemical sensing applications, particularly in the detection of carbonyl organic compounds.

The successful integration of Ln-CPs onto optical fibers, especially TZN-based fibers, has shown the feasibility of using these materials in real-time remote sensing applications. The enhanced luminescent response observed at low concentrations of ketones highlights the sensitivity of these composites, while the linear response within specific concentration ranges confirms their reliability for quantitative detection. These characteristics position them as good candidates for challenging demands, such as industrial monitoring, environmental analysis, and particularly for the detection of biomarkers in health monitoring and disease diagnostics (71,72).

Additionally, this research provides opportunities for further optimization, including enhancing the adhesion of CPs to fiber surfaces and exploring alternative fiber materials to improve sensor performance. Future studies could focus on increasing the selectivity of these sensors for a broader range of analytes, as well as assessing their long-term stability and efficacy under real-world conditions. The outcomes of this project not only provide valuable insights into chemical sensing but also offer perspectives for developing optical sensors based on a new type of composite material, combining the luminescent properties of metal-organic compounds with the light-guiding capabilities of optical fibers.

References

[1]LI, B.; WEN, H. M.; CUI, Y.; QIAN, G.; CHEN, B. Multifunctional lanthanide coordination polymers. **Progress in Polymer Science**, Oxford, v. 48, p. 40–84, 2015.

[2]MAURIN, G.; SERRE, C.; COOPER, A.; FÉREY, G. The new age of MOFs and of their porous-related solids. **Chemical Society Reviews**, v. 46, n. 11, p. 3104–3107, 2017.

[3]CUI, Y.; CHEN, B.; QIAN, G. Lanthanide metal-organic frameworks for luminescent sensing and light-emitting applications. **Coordination Chemistry Reviews**, Amsterdam, v. 273–274, p. 76–86, 2014.

[4]KONDO, M.; YOSHITOMI, T.; MATSUZAKA, H.; KITAGAWA, S.; SEKI, K. Three-dimensional framework with channeling cavities for small molecules: {M_2(4, 4′-bpy)$_3$(NO_3)$_4$·xH_2O}$_n$ (M = Co, Ni, Zn). **Angewandte Chemie International Edition in English**, Weinheim, v. 36, n. 16, p. 1725–1727, 1997.

[5]XUE, D.-X.; BELMABKHOUT, Y.; SHEKHAH, O.; JIANG, H.; ADIL, K.; CAIRNS, A. J.; EDDAOUDI, M. Tunable rare earth fcu-MOF platform: access to adsorption kinetics driven gas/vapor separations via pore size contraction. **Journal of the American Chemical Society**, Washington, v. 137, n. 15, p. 5034–5040, 2015.

[6]YANG, D.; GATES, B. C. Catalysis by metal organic frameworks: perspective and suggestions for future research. **ACS Catalysis**, Washington, v. 9, n. 3, p. 1779–1798, 2019.

[7]OTAKE, K.; CUI, Y.; BURU, C. T.; LI, Z.; HUPP, J. T.; FARHA, O. K. Single-atom-based vanadium oxide catalysts supported on metal–organic frameworks: selective alcohol oxidation and structure–activity relationship. **Journal of the American Chemical Society**, Washington, v. 140, n. 28, p. 8652–8656, 2018.

[8]KRENO, L. E.; LEONG, K.; FARHA, O. K.; ALLENDORF, M.; VAN DUYNE, R. P.; HUPP, J. T. Metal–organic framework materials as chemical sensors. **Chemical Reviews**, Washington, v. 112, n. 2, p. 1105–1125, 2012.

[9]ORELLANA-TAVRA, C.; MARSHALL, R. J.; BAXTER, E. F.; ABÁNADES LÁZARO, I.; TAO, A.; CHEETHAM, A. K.; FORGAN, R. S.; FAIREN-JIMENEZ, D. Drug delivery and controlled release from biocompatible metal–organic frameworks using mechanical amorphization. **Journal of Materials Chemistry B**, London, v. 4, n. 47, p. 7697–7707, 2016.

[10]CUI, Y.; LI, B.; HE, H.; ZHOU, W.; CHEN, B.; QIAN, G. Metal–organic frameworks as platforms for functional materials. **Accounts of Chemical Research**, Washington, v. 49, n. 3, p. 483–493, 2016.

[11]ROY, S.; CHAKRABORTY, A.; MAJI, T. K. Lanthanide–organic frameworks for gas storage and as magneto-luminescent materials. **Coordination Chemistry Reviews**, Amsterdam, v. 273–274, p. 139–164, 2014.

[12]CHEN, Y.; MA, S. Microporous lanthanide metal-organic frameworks. **Reviews in Inorganic Chemistry**, Berlin, v. 32, n. 2–4, p. 81–100, 2012.

[13]LI, Q.; QIAN, J.; ZHOU, J.; DU, L.; ZHAO, Q. Highly chemically and thermally stable lanthanide coordination polymers for luminescent probes and white light emitting diodes. **CrystEngComm**, Cambridge, v. 22, n. 15, p. 2667–2674, 2020.

[14]CHEN, W.; FAN, R.; ZHANG, H.; DONG, Y.; WANG, P.; YANG, Y. Tunable white-light emission PMMA-supported film materials containing lanthanide coordination polymers: preparation, characterization, and properties. **Dalton Transactions**, London, v. 46, n. 13, p. 4265–4277, 2017.

[15]LI, X.; LU, S.; TU, D.; ZHENG, W.; CHEN, X. Luminescent lanthanide metal–organic framework nanoprobes: from fundamentals to bioapplications. **Nanoscale**, London, v. 12, n. 28, p. 15021–15035, 2020.

[16]TANG, G.; GAO, J.; WANG, C.; TAN, H. Luminescent lanthanide coordination polymer as a platform for DNA colorimetric detection. **Sensors and Actuators B: Chemical**, Amsterdam, v. 244, p. 571–576, 2017.

[17]ZHU, X.; WU, X.; LIU, J.; ZOU, L.; YE, B.; LI, G. Lanthanide coordination polymers used for fluorescent ratiometric sensing of H_2O_2 and glucose. **Inorganic Chemistry Communications**, Amsterdam, v. 144, p. 109849, 2022.

[18]FENG, X.; SHANG, Y.; ZHANG, H.; LIU, X.; WANG, X.; CHEN, N.; WANG, L.; LI, Z. Multi-functional lanthanide-CPs based on tricarboxylphenyl terpyridyl ligand as ratiometric luminescent thermometer and highly sensitive ion sensor with turn on/off effect. **Dalton Transactions**, London, v. 49, n. 15, p. 4741–4750, 2020.

[19]QIN, J.; MA, B.; LIU, X. F.; LU, H. L.; DONG, X. Y.; ZANG, S. Q.; HOU, H. Aqueous- and vapor-phase detection of nitroaromatic explosives by a water-stable fluorescent microporous MOF directed by an ionic liquid. **Journal of Materials Chemistry A**, Cambridge, v. 3, n. 24, p. 12690–12697, 2015.

[20]BANERJEE, D.; HU, Z.; LI, J. Luminescent metal–organic frameworks as explosive sensors. **Dalton Transactions**, London, v. 43, n. 28, p. 10668–10685, 2014.

[21]HU, Z.; DEIBERT, B. J.; LI, J. Luminescent metal–organic frameworks for chemical sensing and explosive detection. **Chem. Soc. Rev.**, London, v. 43, n. 16, p. 5815–5840, 2014.

[22]IRIKURA, K.; PERINI, J. A. L.; FLOR, J. B. S.; FREM, R. C. G.; ZANONI, M. V. B. Direct synthesis of $Ru_3(BTC)_2$ metal-organic framework on a Ti/TiO_2NT platform for improved performance in the photoelectroreduction of CO_2. **Journal of CO_2 Utilization**, Amsterdam, v. 43, p. 101364, 2021.

[23]SILVA, B. C. E.; IRIKURA, K.; FREM, R. C. G.; ZANONI, M. V. B. Effect of Cu(BDC-NH_2) MOF deposited on Cu/Cu_2O electrode and its better performance in photoelectrocatalytic reduction of CO_2. **Journal of Electroanalytical Chemistry**, Amsterdam, v. 880, p. 114856, 2021.

[24]KUNG, C.-W.; WANG, T. C.; MONDLOCH, J. E.; FAIREN-JIMENEZ, D.; GARDNER, D. M.; BURY, W.; KLINGSPORN, J. M.; BARNES, J. C.; VAN DUYNE, R.; STODDART, J.

F.; WASIELEWSKI, M. R.; FARHA, O. K.; HUPP, J. T. Metal–organic framework thin films composed of free-standing acicular nanorods exhibiting reversible electrochromism. **Chemistry of Materials**, Washington, v. 25, n. 24, p. 5012–5017, 2013.

[25]WADE, C. R.; LI, M.; DINCĂ, M. Facile Deposition of Multicolored Electrochromic Metal-Organic Framework Thin Films. **Angewandte Chemie International Edition**, Weinheim, v. 52, n. 50, p. 13377–13381, 2013.

[26]JHA, A.; RICHARDS, B. D. O.; JOSE, G.; FERNANDEZ, T. T.; HILL, C. J.; LOUSTEAU, J. Review on structural, thermal, optical and spectroscopic properties of tellurium oxide based glasses for fibre optic and waveguide applications. **International Materials Reviews**, London, v. 57, n. 6, p. 357–382, 2012.

[27]GALLEANI, G., SANTAGANELLI, S.H., LEDEMI, Y., MESSADDEQ, Y., JANKA, O., POTTGEN, R., ECKERT, H. Ultraviolet upconversion luminescence in a highly transparent triply-doped Gd^{3+}-Tm^{3+}-Yb^{3+} fluoride-phosphate glasses. **Journal of Physical Chemistry C**, Washington, v. 122, n. 4, p. 2275–2284, 2018.

[28]MANZANI, D.; SOUZA-JUNIOR, J. B.; REYNA, A. S.; SILVA-NETO, M. L.; BAUTISTA, J. E. Q.; RIBEIRO, S. J. L.; ARAUJO, C. B. Phosphotellurite glass and glass-ceramics with high TeO_2 contents: thermal, structural and optical properties. **Dalton Transactions**, London, v. 48, n. 18, p. 6261–6272, 2019.

[29]PISARSKI, W. A., PISARKA, J., MACZKA, M., RYBA-ROMANOWSKI, W. Europium-doped lead fluoroborate glasses: Structural, thermal and optical investigations. **Journal of Molecular Structure**, Amsterdam, v. 792–793, p. 207–211, 2006.

[30]WU, J.; ZHANG, W.; WANG, Y.; LI, B.; HAO, T.; ZHENG, Y. JIANG, L.; CHEN, K.; CHIANG, K.S. Nanoscale light–matter interactions in metal–organic frameworks cladding optical fibers. **Nanoscale**, London, v. 12, n. 18, p. 9991–10000, 2020.

[31]DING, L.; RUAN, Y.; LI, T.; HUANG, J.; WARREN-SMITH, S. C.; EBENDORFF-HEIDEPRIEM, H.; MONRO, T. M. Nitric oxide optical fiber sensor based on exposed core fibers and CdTe/CdS quantum dots. **Sensors and Actuators B:** chemical, Amsterdam, v. 273, p. 9–17, 2018.

[32]HEIDEMANN, B. R.; CHIAMENTI, I.; OLIVEIRA, M. M.; MULLER, M.; FABRIS, J. L. Plasmonic optical fiber sensors: enhanced sensitivity in water-based environments. **Applied Optics**, Washington, v. 54, n. 27, p. 8192, 2015.

[33]CHAUDHARI, A. K.; SOUZA, B. E.; TAN, J. C. Electrochromic thin films of Zn-based MOF-74 nanocrystals facilely grown on flexible conducting substrates at room temperature. **APL Materials**, Melville, v. 7, n. 8, 2019.

[34]MILIUTINA, E.; GUSELNIKOVA, O.; CHUFISTOVA, S.; KOLSKA, Z.; ELASHNIKOV, R.; BURTSEV, V.; POSTNIKOV, P.; SVORCIK, V.; LYUTAKOV, O. Fast and all-optical hydrogen sensor based on gold-coated optical fiber functionalized with metal–organic framework layer. **ACS Sensors**, Washington, v. 4, n. 12, p. 3133–3140, 2019.

[35]DA SILVA, C. M.; ELLENA, J.; FREM, R. C. G. Chemical transformation of a luminescent two-dimensional Eu(III) coordination polymer in the aqueous phase. **New Journal of Chemistry**, Cambridge, v. 44, n. 24, p. 10146–10152, 2020.

[36]FABELO, O.; PASÁN, J.; LLORET, F.; JULVE, M.; RUIZ-PÉREZ, C. Structural versatility in cobalt(ii) complexes with 1,2,4,5-benzenetetracarboxylic acid (H_4bta) and 4,4′-bipyridine-N,N′-dioxide (dpo). **CrystEngComm**, Cambridge, v. 9, n. 9, p. 815, 2007.

[37]LAHOUD, M. G.; FREM, R. C. G.; MARQUES, L. F.; ARROYOS, G.; BRANDÃO, P.; FERREIRA, R. A. S.; CARLOS, L. D. A novel near monochromatic red emissive europium(III) metal-organic framework based on 1,2,4,5-benzenetetracarboxylate: from synthesis to photoluminescence studies. **Journal of Solid State Chemistry**, Amsterdam, v. 253, p. 176–183, 2017.

[38]CAPELO, R. G.; BALTIERI, R. S.; OLIVEIRA JR, M.; MANZANI, D. Exploring the influence of ZnF_2 on zinc-tellurite glass: unveiling changes in OH content, structure, and optical properties. **ACS Omega**, Washington, v. 8, n. 38, p. 35266–35274, 2023.

[39]FILHO, J. C.; ZILIO, S. C.; MESSIAS, D. N.; PILLA, V.; SILVA, A. C. A.; DANTAS, N. O.; ANDRADE, A. A. Effects of aluminum substitution by potassium in the P_2O_5–Al_2O_3–Na_2O–K_2O phosphate glasses. **Journal of Alloys and Compounds**, Amsterdam, v. 815, p. 152359, 2020.

[40]ZHANG, A.; LIN, A.; WANG, J. S.; TOULOUSE, J. Multistage etching process for microscopically smooth tellurite glass surfaces in optical fibers. **Journal of Vacuum Science & Technology B, Nanotechnology and Microelectronics: Materials, Processing, Measurement, and Phenomena**, Melville, v. 28, n. 4, p. 682–686, 2010.

[41]JAMALI, A.; TEHRANI, A. A.; SHEMIRANI, F.; MORSALI, A. Lanthanide metal–organic frameworks as selective microporous materials for adsorption of heavy metal ions. **Dalton Transactions**, London, v. 45, n. 22, p. 9193–9200, 2016.

[42]SARKAR, A.; ADHIKARY, A.; MANDAL, A.; CHAKRABORTY, T.; DAS, D. Zn-BTC MOF as an adsorbent for iodine uptake and organic dye degradation. **Crystal Growth & Design**, Washington, v. 20, n. 12, p. 7833–7839, 2020.

[43]FENG, X.; WANG, Y.; MUHAMMAD, F.; SUN, F.; TIAN, Y.; ZHU, G. Size, shape, and porosity control of Medi-MOF-1 via growth modulation under microwave heating. **Crystal Growth & Design**, Washington, v. 19, n. 2, p. 889–895, 2019.

[44]CHEN, L.; SHEN, Y.; BAI, J.; WANG, C. Novel symmetrical coralloid Cu 3D superstructures: Solid-state synthesis from a Cu-carboxylate MOF and their in-situ thermal conversion. **Journal of Solid State Chemistry**, Amsterdam, v. 182, n. 8, p. 2298–2306, 2009.

[45]KESHMIRI, N.; NAJMI, P.; RAMEZANZADEH, M.; RAMEZANZADEH, B. Designing an eco-friendly lanthanide-based metal organic framework (MOF) assembled graphene-oxide with superior active anti-corrosion performance in epoxy composite. **Journal of Cleaner Production**, Amsterdam, v. 319, p. 128732, 2021.

[46]LIU, K.; ZHENG, Y.; JIA, G.; YANG, M.; SONG, Y.; GUO, N.; YOU, H. Nano/micro-scaled La(1,3,5-BTC)(H_2O)$_6$ coordination polymer: Facile morphology-controlled fabrication and color-tunable photoluminescence properties by co-doping Eu^{3+},Tb^{3+}. **Journal of Solid State Chemistry**, Amsterdam, v. 183, n. 10, p. 2309–2316, 2010.

[47]HU, Y.; CHEN, K. Crystal splitting in the growth of β-FeO(OH). **Journal of Crystal Growth**, Amsterdam, v. 308, n. 1, p. 185–188, out. 2007.

[48]WANG, J.-L.; HOU, K. L.; BAI, F. Y.; XING, Y. H.; SHI, Z. Hydrothermal synthesis, crystal structure, and photoluminescence of novel lanthanide metal organic frameworks constructed from 1,4-benzene-dicarboxylic acid and 1,2,4,5-benzenetetracarboxylic acid as ligands. **Structural Chemistry**, New York, v. 23, n. 1, p. 275–285, 2012.

[49]BOUDERBALA, M.; HAMZAOUI, S.; AMRANI, B.; RESHAK, A. H.; ADNANE, M.; SAHRAOUI, T.; ZERDALI, M. Thickness dependence of structural, electrical and optical behaviour of undoped ZnO thin films. **Physica B: Condensed Matter**, Amsterdam, v. 403, n. 18, p. 3326–3330, 2008.

[50]PRASADA RAO, T.; SANTHOSHKUMAR, M. C. Effect of thickness on structural, optical and electrical properties of nanostructured ZnO thin films by spray pyrolysis. **Applied Surface Science**, Amsterdam, v. 255, n. 8, p. 4579–4584, 2009.

[51]UH, H.; PETOUD, S. Novel antennae for the sensitization of near infrared luminescent lanthanide cations. **Comptes Rendus Chimie**, Paris, v. 13, n. 6–7, p. 668–680, 2010.

[52]JI, G.; LIU, J.; GAO, X.; SUN, W.; WANG, J. Z.; ZHAO, S.; LIU, Z. L. A luminescent lanthanide MOF for selectively and ultra-high sensitively detecting Pb^{2+} ions in aqueous solution. **Journal of Materials Chemistry A**, Cambridge, v. 5, n. 21, p. 10200–10205, 2017.

[53]CUI, Y.; YUE, Y.; QIAN, G.; CHEN, B. Luminescent functional metal–organic frameworks. **Chemical Reviews**, Washington, v. 112, n. 2, p. 1126–1162, 2012.

[54]BÜNZLI, J.-C. G.; ELISEEVA, S. V. Basics of lanthanide photophysics. *In*: **Lanthanide luminescence: photophysical, analytical and biological aspects**. Springer Nature, Berlin, p. 1–45, 2011.

[55]ABAD-GALÁN, L.; CIESLIK, P.; COMBA, P.; GAST, M.; MAURY, O.; NEUPERT, L.; ROUX, A.; WADEPOHL, H. Excited state properties of lanthanide(III) complexes with a nonadentate bispidine ligand. **Chemistry – A European Journal**, Weinheim, v. 27, n. 40, p. 10303–10312, 2021.

[56]WEN, T.; ZHOU, Y.; YANG, B.; WANG, Y. Controllable synthesis, polymorphism and structure-dependent photoluminescence properties of europium oxyfluorides. **European Journal of Inorganic Chemistry**, Weinheim, v. 2017, n. 44, p. 5121–5126, 2017.

[57]CASCALES, C.; BALDA, R.; FERNÁNDEZ, J.; ARRIANDIAGA, M. A.; FDEZ-NAVARRO, J. M. Fluorescence line narrowing spectroscopy of Eu^{3+} in TeO_2–TiO_2–Nb_2O_5 glass. **Optical Materials**, Amsterdam, v. 31, n. 7, p. 1092–1095, 2009.

[58]BINNEMANS, K. Lanthanide-based luminescent hybrid materials. **Chemical Reviews**, Washington, v. 109, n. 9, p. 4283–4374, 2009.

[59]HOWARD, P. H. **Handbook of Physical Properties of Organic Chemicals**, Part 1. Boca Raton: CRC Press, 1996

[60]KOCH, J. D.; GRONKI, J.; HANSON, R. K. Measurements of near-UV absorption spectra of acetone and 3-pentanone at high temperatures. **Journal of Quantitative Spectroscopy and Radiative Transfer**, Oxford, v. 109, n. 11, p. 2037–2044, 2008.

[61]SAI, L.; WANG, X.; CHANG, Q.; SHI, W.; HUANG, L. Selective determination of acetone by carbon nanodots based on inner filter effect. **Spectrochimica Acta Part A: Molecular and Biomolecular Spectroscopy**, Amsterdam, v. 216, p. 290–295, 2019.

[62]YAN, B. Luminescence response mode and chemical sensing mechanism for lanthanide-functionalized metal–organic framework hybrids. **Inorganic Chemistry Frontiers**, Cambridge, v. 8, n. 1, p. 201–233, 2021.

[63]ALLENDORF, M. D.; BAUER, C. A.; BHAKTA, R. K.; HOUK, R. J. T. Luminescent metal–organic frameworks. **Chemical Society Reviews**, Cambridge, v. 38, n. 5, p. 1330, 2009.

[64]ZHAO, Y.; LI, D. Lanthanide-functionalized metal–organic frameworks as ratiometric luminescent sensors. **Journal of Materials Chemistry C**, Cambridge, v. 8, n. 37, p. 12739–12754, 2020.

[65]YANG, X. L.; CHEN, X.; HOU, G. H.; GUAN, R. F.; SHAO, R.; XIE, M. H. A multiresponsive metal-organic framework: direct chemiluminescence, photoluminescence, and dual tunable sensing applications. **Advanced Functional Materials,** Weinheim**,** v. 26, 3, p. 393-398, 2016.

[66]FERNÁNDEZ DEL RÍO, R.; O'HARA, M. E.; HOLT, A.; PEMBERTON, P.; SHAH, T.; WHITEHOUSE, T.; MAYHEW, C. A. Volatile biomarkers in breath associated with liver cirrhosis — comparisons of pre- and post-liver transplant breath samples. **EBioMedicine**, Amsterdam, v. 2, n. 9, p. 1243–1250, 2015.

[67]MONDAL, P.; MISRA, D.; CHOWDHURY, S. K.; MANDAL, V.; DUTTA, T.; BAILDYA, N.; KHAN, A. A.; MANDAL, M.; REZA, R.; AHMED, M.; GHOSH, N. N. Exhaled volatile organic compounds (VOCs): a potential biomarkers for chronic disease diagnosis. **Scientific Journal of Biology**, Hyderabad, v. 4, n. 1, p. 5–028, 2021.

[68]SANTOS, P. M.; DEL NOGAL SANCHEZ, M.; POZAS, Á. P. C.; PAVÓN, J. L. P.; CORDERO, B. M. Determination of ketones and ethyl acetate—a preliminary study for the discrimination of patients with lung cancer. **Analytical and Bioanalytical Chemistry**, Berlin, v. 409, n. 24, p. 5689–5696, 2017.

[69]MOCHALSKI, P.; LEJA, M.; ŚLEFARSKA-WOLAK, D.; MEZMALE, L.; PATSKO, V.; AGER, C.; KRÓLICKA, A.; MAYHEW, C. A.; SHANI, G.; HAICK, H. Identification of key volatile organic compounds released by gastric tissues as potential non-invasive biomarkers for gastric cancer. **Diagnostics**, Basel, v. 13, n. 3, p. 335, 2023.

[70]OKHRIMENKO, D. V.; NIELSEN, C. F.; LAKSHTANOV, L. Z.; DALBY, K. N.; JOHANSSON, D. B.; SOLVANG, M.; DEUBENER, J.; STIPP, S. L. S. Surface reactivity and dissolution properties of alumina–silica glasses and fibers. **ACS Applied Materials & Interfaces**, Washington, v. 12, n. 32, p. 36740–36754, 2020.

[71]SAASA, V.; MALWELA, T.; BEUKES, M.; MOKGOTHO, M.; LIU, C. P.; MWAKIKUNGA, B. Sensing technologies for detection of acetone in human breath for diabetes diagnosis and monitoring. **Diagnostics**, Basel, v. 8, n. 1, p. 12, 2018.

[72]BUSZEWSKI, B.; GRZYWINSKI, D.; LIGOR, T.; STACEWICZ, T.; BIELECKI, Z.; WOJTAS, J. Detection of volatile organic compounds as biomarkers in breath analysis by different analytical techniques. **Bioanalysis**, London, v. 5, n. 18, p. 2287–2306, 2013.

GENERAL CONCLUSIONS AND PERSPECTIVES

This PhD thesis has explored the development of innovative luminescent materials and composites for applications in optical sensing and photonics. Through systematic research, several novel glass matrices, optical fibers, and composites were synthesized, characterized, and evaluated, resulting in significant contributions to the fields of glass science, lanthanide coordination polymers (Ln-CPs), and fiber-optic-based sensors. The research's interdisciplinary nature has led to the creation of materials with enhanced optical properties and advanced sensing capabilities, positioning them for potential applications in different fields.

The initial phase of this research focused on the synthesis and characterization of tellurite and phosphotellurite glass matrices, including the introduction of various network modifiers like Na_2O, ZnO, NaF, and ZnF_2. These studies revealed that the incorporation of fluoride into tellurite glasses notably altered their structure, leading to a broader transparency range while maintaining similar thermal stability. Specifically, fluoride-modified matrices demonstrated a significant reduction in hydroxyl content and an improved ability to dissolve rare-earth ions (RE^{3+}). The structural and optical investigations, using techniques like solid-state NMR, Raman spectroscopy, and absorption spectroscopy, provided a comprehensive understanding of how different compositional changes affected the glass networks. These insights guided the selection of compositions with high potential for photonic applications, such as light-emitting materials and fiber-optic devices.

The next phase of the project extended the focus to the development of optically active phosphate glasses co-doped with RE^{3+}, such as Er^{3+}, Yb^{3+}, Nd^{3+}, and Tm^{3+}. These glasses exhibited promising upconversion (UC) luminescence when excited in the NIR range. The research demonstrated that Ag-NPs could significantly amplify the UC emission of Er^{3+}/Yb^{3+}-co-doped glasses, a result that has potential applications in photonic devices like data storage and solid-state lighting. Furthermore, aluminum-phosphate glasses doped with Nd^{3+}, Tm^{3+}, and Yb^{3+} displayed intense blue UC luminescence when excited at different wavelengths, and the ability to guide this luminescence through optical fibers was successfully demonstrated. These findings highlight the potential of such materials for applications in solid-state lasers and other photonic technologies.

The final phase of the research focused on the development of glass@Ln-CP composites and their application in chemical sensing. The integration of Ln-CPs onto glass substrates and

optical fibers was achieved through an *in situ* growth process, resulting in stable luminescent coatings with strong adhesion in tellurite glass substrates. These composites exhibited a high sensitivity to carbonyl compounds, such as acetone and 2-pentanone, making them particularly promising for chemical sensing. The ability of the coated fibers to guide optical signals over long distances enables the development of advanced sensors capable of real-time detection and quantification of analytes. This aspect of the research underscores the potential of combining advanced glass matrices with luminescent Ln-CPs to create highly sensitive and selective optical sensors.

Overall, this thesis has made substantial contributions to the field of luminescent and fiber-optic materials, addressing both fundamental and applied aspects of glass and composite development. The systematic characterization of glass matrices, optimization of their compositions for optical fiber production, and enhancement of their luminescent properties through dopants and surface modifications can established a strong basis for future research in this area. The successful synthesis of glass@Ln-CP composites and their demonstrated sensing capabilities represent a significant advancement in the field of optical sensing, offering promising perspectives for the development of new photonic devices.

Looking forward, the results of this project present several opportunities for further exploration. Improving the adhesion of Ln-CPs to optical fiber surfaces and experimenting with alternative glass compositions could enhance sensor performance. Additionally, expanding the range of detectable analytes and evaluating the long-term stability of these materials under practical conditions are essential steps toward the commercialization of these technologies. This research contributes to the development of a new class of luminescent glass-based sensors, with potential applications across diverse fields, including environmental analysis, public health monitoring, and industrial safety.

In conclusion, this PhD project has made substantial contributions to the design and application of luminescent materials, with potential applications in solid-state lighting and optical sensing. The findings and methodologies developed provide a deeper understanding of the relationships between glass structure, optical and thermal properties, and luminescence capability. Additionally, the optically active materials reported in this manuscript represent a promising foundation for future advancements in photonic technologies.

APPENDIX A – Academic activities

1. List of publications in the period (2021-2024).

1.1. CAPELO, R. G.; ALMEIDA, J. M. P.; FRANCO, D. F.; POIRIER, G. Y.; MENDONÇA, C. R.; NALIN, M.; MANZANI, D..; Controlled formation of metallic tellurium nanocrystals in tellurite glasses using femtosecond direct laser writing. **Jornal of Materials Research and Technology**, v. 13, p. 1296-1304, 2021. https://doi.org/10.1016/j.jmrt.2021.05.037

1.2. DOS SANTOS, G. A.; CAPELO, R. G.; LIU, C.; MANZANI, D. In-situ synthesis of luminescent CdS quantum dots embedded in phosphate glass. **Journal of Non-crystalline Solids**, v. 587, p. 121599, 2022. http://dx.doi.org/10.1016/j.jnoncrysol.2022.121599

1.3. CAPELO, R. G.; GERDES, J. M.; REHFUß, U.; SILVA, L. D.; HANSEN, M. R. ; VAN WÜLLEN, L. ; ECKERT, H.; MANZANI, D. Structural characterization of a new fluorophosphotellurite glass system. **Dalton Transactions**, v. -, p. -, 2023. http://dx.doi.org/10.1039/D2DT03292A

1.4. CAPELO, R. G.; RUBIO, T. I.; CALDERÓN, G. L.; DE MORAES, D. A.; JUNIOR, E. M.; NALIN, M.; MANZANI, D. Effect of silver nanoparticles on the visible upconversion emission of Er3+/Yb3+ co-doped SbPO4-GeO2 glasses. **Optical Materials**, v. 135, p. 113234, 2023. http://dx.doi.org/10.1016/j.optmat.2022.113234

1.5. CAPELO, R. G.; BALTIERI, R. S.; OLIVEIRA Jr., M.; MANZANI, D. Exploring the Influence of ZnF_2 on Zinc-Tellurite Glass: Unveiling Changes in OH Content. **Structure, and Optical Properties. ACS Omega**, v. 8, 38, p. 35266-35274, 2023. https://doi.org/10.1021/acsomega.3c05010

1.6. FRANCISCO, D. S.; CAPELO, R. G.; BALTIERI, R. S.; MANZANI, D. Optical Fibers Sensors for Detection of SARS-CoV-2 Infection. *In:* **COVID-19 Metabolomics and Diagnosis: Chemical Science for Prevention and Understanding Outbreaks of Infectious Diseases**, Springer, Berlin, p. 91-109, 2023. https://doi.org/10.1007/978-3-031-15889-6_5

1.7. REHFUß, U.; GERDES, J. M.; CAPELO, R. G.; MANZANI, D.; HANSEN, M. R.; ECKERT, H.; VAN WÜLLEN, L. WITHDRAWN: Ultra wideline dipolar NMR spectroscopy: Combining SEDOR and WURST-CPMG. **Solid State Nuclear Magnetic Resonance**, p. 101948, 2024.

1.8. CAPELO, R. G.; STRUTYNSKI, C.; GADRET, G.; DÉSÉVÉDAVY, F.; SMEKTALA, F.; MANZANI, D. Blue upconversion emission of $Nd^{3+}/Tm^{3+}/Yb^{3+}$ tryply doped aluminophosphate optical fibers. **ACS Applied Optical Materials**, v. 2, 12, p. 2501-2508, 2024.

2. Training courses attended

2.1. Physics of materials (18/08/2020 – 03/12/2020) – IFSC/USP – 225h.

2.2. Spectroscopy methods on inorganic chemistry: fundamentals and applications (18/08/2020 – 03/12/2020) – IQ/USP – 120h.

2.3. Techniques for scientific writing in English (23/03/2021 – 01/06/2021) – IFSC/USP - 150h.

2.4. Topics on inorganic chemistry (05/04/2021 – 13/06/2021) – IQSC/USP - 60h.

2.5. Ricardo Rodrigues School of Synchrotron Light (12/07/2021 – 23/07/2021) – LNLS/CNPEM – 72h.

2.6. 1st Machine Learning School for Materials @Ilum (05 to 07/09/2022) – CNPEM.

2.7. 1st Short Course on Pair Distribution Function in Electron Diffraction (ePDF) (10 and 11/12/2022) – LNNano/CNPEM.

2.8. Scientific integrity in research professions (31/08/2024) – MOOC/UBFC – 15h.

2.9. ISIS – Cleaning, splicing and processing optical fibers – (24 and 25/06/2024) FEMTO-ST/UBFC – 14h.

2.10. Advanced topics on solid materials characterization and its applications (23/08/2024 – 14/11/2024) – IQSC/USP - 180h.

3. Presentations at conferences and scientific meetings

3.1. 45th Brazilian Chemical Society Annual Meeting (RASBQ 2022). Maceió-AL, Brazil - 03/06/2022. Poster presentation: *Functionalized tellurite and fluorotellurite glasses with lanthanide metal-organic frameworks (Ln-MOFs) for optical gas sensing.*

3.2. XX Brazilian Materials Research Society Meeting (SBPMat 2022). Foz do Iguaçu-PR, Brazil – 29/09/2022. Oral presentation: *Synthesis and structural characterization of a new fluorophosphotellurite glasses.*

3.3. 1st International Conference on Spectroscopy in Materials Science (ICOSIMS 2023). Virtual – 22/06/2023. Oral presentation: *Luminescent lanthanide-MOFs coatings on oxide glasses for sensing applications.*

3.4. European Optical Society Annual Meeting (EOSAM 2023). Dijon, France – 14/09/2023. Oral presentation: *Lanthanide-MOFs coatings on oxide glasses and optical fibers for sensing applications.*

3.5. 10th International Workshop on Photoluminescence in Rare Earths: Photonic Materials and Devices (PRE'24). Trento, Italy (15/05/2024). Oral presentation: *In-situ synthesis of lanthanide-MOFs on tellurite glasses and optical fibers for sensing of volatile organic compounds.*

3.6. XXII Brazilian Materials Research Society Meeting (SBPMat 2024). Santos-SP, Brazil – 03/10/2024. Poster presentation: *Blue up-conversion emission of $Nd^{3+}/Tm^{3+}/Yb^{3+}$ triply doped aluminophosphate optical fibers.*

3.7. XXII Brazilian Materials Research Society Meeting (SBPMat 2024). Santos-SP, Brazil – 03/10/2024. Oral presentation: *In-situ growth of lanthanide metal-organic frameworks on oxide glass and optical fibers: a promising material for chemical sensing.*

4. Co-supervisions completed

4.1. Giulia Alves dos Santos - Undergraduate student (IQSC-USP) - Supervisor: Danilo Manzani.
Period: Sep. 2020 – Aug. 2021.
Project: *Light-emitting glasses for photonic applications: In-situ synthesis and photoluminescence studies of quantum dots (class II-VI) in phosphate glasses*.

4.2. Vihanga Ravindu Bandara – Master's degree in Physics, Photonics and Nanotechnology (ICB-uB) – Supervisor: Frédéric Désévédavy.
Period: Jan. 2023 – Jun. 2023.
Project: *Tm^{3+} and Ho^{3+} doped tellurite glasses and fibres for lasing at 2 µm.*

5. Other academic activities

5.1. Internship in the Teaching Improvement Program (PAE) – IQSC/USP – Subject: Inorganic Chemistry I – Supervisor: Danilo Manzani – 1st semester of 2021. Project: *Use of technological tools and educational games for the study of symmetry and molecular orbitals in "Inorganic Chemistry I"*

5.2. Internship in the Teaching Improvement Program (PAE) – IQSC/USP – Subject: Technological Inorganic Chemistry Laboratory – Supervisor: Danilo Manzani - 2nd semester of 2021. Project: *Experiments for the synthesis of nanomaterials and their connections to theoretical concepts of Inorganic Chemistry.*

5.3. Graduate Student Representative on the Council of the Department of Molecular Chemistry and Physics – SQM at the Instituto de Química de São Carlos from 03/31/2021 to 03/30/2022.

5.4. Student Representative on the Graduate Comission (CPG) at the Instituto de Química de São Carlos from 07/08/2021 to 06/08/2023.